EXPERIMENTAL PETROLOGY OF METEORITES: PHOSPHORUS AND OXYGEN ISOTOPES IN OLIVINE

by

JOSEPH S. BOESENBERG

A Dissertation submitted to the

Graduate School-New Brunswick

Rutgers, The State University of New Jersey

in partial fulfillment of the requirements

for the degree of

Doctor of Science

Graduate Program in the Geological Sciences

written under the direction of

Dr. Roger H. Hewins

and approved by

_____

_____

_____

_____

New Brunswick, New Jersey

May, 2007

ABSTRACT OF THE DISSERTATION

Experimental Petrology of Meteorites:

Phosphorus and Oxygen Isotopes in Olivine

By JOSEPH S. BOESENBERG

Dissertation Director:
Dr. Roger H. Hewins

Experiments have been conducted to investigate the exchange and behavior of phosphorus and oxygen isotopes in olivine of extraterrestrial materials. The first project concentrated on determining the conditions necessary for the formation of phosphoran olivine in pallasite meteorites. Results indicate that phosphoran olivine forms during rapid crystallization and not subsolidus diffusion. Phosphoran olivine does not persist if the system closely approaches equilibrium. Models proposing that pallasites represent samples of a core-mantle boundary of a differentiated asteroid are inconsistent with these results.

The second and third projects involved the exchange of oxygen isotopes in chondrules at nebular pressures and temperatures, first observing gas-melt exchange, then olivine-melt exchange. In the gas-melt exchange experiments, a low pressure flow of carbon monoxide gas was reacted with an olivine-normative melt to simulate exchange with a nebular gas in the early solar system. No isotopic exchange between carbon monoxide and olivine-rich melt was detected. However, the experiments did demonstrate

for the first time, the kinetic evaporation of oxygen. It was proposed that water vapor was likely the major oxygen-bearing species to exchange oxygen in the early solar nebula and carbon monoxide contributed to this only through reactions with the water vapor or ambient hydrogen. The final experiments involved exchange of oxygen between relict chondrule olivine, their overgrowths, and the chondrule melt. It was determined that Fe-Mg diffusion can obscure relict grains during chondrule crystallization. However, the original oxygen isotopic composition of those grains will remain intact. Durations of weeks at high temperature are required to obscure the oxygen signature by diffusion. Relict olivine grains are more prevalent than previously estimated and probably occur in more than 30% of all chondrules.

DEDICATION

For my family and friends

ACKNOWLEDGEMENTS

I would like to gratefully thank and acknowledge the following people for their enormous amount of support, assistance, encouragement and generosity during the years it has taken me to complete this dissertation. It has been a privilege to work with and learn from such an extraordinary group of individuals.

Marc Chaussidon, CRPG-CNRS, Nancy, France
Nehru Cherukupalli, Brooklyn College
Harold Connolly, Kingsborough College
Mariana Cosarinsky, University of California, Los Angeles
Jeremy Delaney, Rutgers University
Denton Ebel, American Museum of Natural History
Mark Feigensen, Rutgers University
Robert Fogel, NASA Headquarters
Jon Friedrich, Fordham University
Mickey Gunter, University of Idaho
George Harlow, American Museum of Natural History
Roger Hewins, Rutgers University
Charles Mandeville, American Museum of Natural History
Edmond Mathez, American Museum of Natural History
Kevin McKeegan, University of California, Los Angeles
Martin Prinz (deceased), American Museum of Natural History
James Webster, American Museum of Natural History
Michael Weisberg, Kingsborough College
Ed Young, University of California, Los Angeles
Karen Ziegler, University of California, Los Angeles

TABLE OF CONTENTS

LIST OF TABLES

LIST OF ILLUSTRATIONS

APPENDICES

OVERVIEW

Olivine [$(Mg,Fe)_2SiO_4$] is one of the most abundant minerals in terrestrial and extraterrestrial rocks. It (or its high pressure equivalent) is a major constituent in the mantle of the earth and is contained in nearly every chondrite and achondrite meteorite group, including their components, such as chondrules and matrix. Olivine is now known to be abundant also in the cometary samples returned by the Stardust mission (Weisberg et al., 2006). Mineralogically, olivine is among the simplest silicate structures, having an orthorhombic symmetry and consisting of independent silica tetrahedra linked by divalent atoms in six-fold coordination (Deer et al., 1993). Olivine is quite restrictive in its mineralogic behavior, being compatible with a relatively small number of elements (Brown, 1980). Within olivine are two elements which are often overlooked in petrology. First is oxygen, because it is ubiquitous and comprises typically 31 to 45 wt% of the olivine structure (and a substantially higher volume proportion), and the second is phosphorus, since it is rarely present above a few hundred parts per million (Koritnig, 1965; Henderson, 1968). Both elements, however are important in understanding olivine's role during planet and asteroid formation in the early solar system

The two main topics of this dissertation are: 1) what can the oxygen isotopic composition of olivine tell us about chondrule formation in the early solar nebula and 2) what can phosphorus substitution in olivine tell us about the mantles of differentiated asteroids (pallasites). Though the two questions may seem somewhat disparate, the processes and principles which govern oxygen and phosphorus distribution and function within olivine are largely the same. They are controlled by the geologic processes of melting, olivine crystallization, diffusion, and atom exchange. Oxygen isotopic

systematics, along with phosphorus chemistry in olivine, should provide a record of the interactions between solids (minerals), liquids (melt) and gases during the first tens of millions of years of the solar system. Fortunately, one of the fundamental principles in geology is the present is that the key to the past, which states that the physiochemical and geologic processes we observe today are the same processes that occurred throughout time. Therefore, these unresolved questions about the early solar system can be investigated (within limits) through experimentation in the laboratory with some hope of simulating conditions that may have occurred 4.6 billion years ago, with the only major constraints being time and the complexity of the formation processes.

REFERENCES

Brown G. E., Jr. (1980) Olivines and silicate spinels. In *Reviews in Mineralogy, 5: Orthosilicates* (ed. P. H. Ribbe), Ch. 11, pp. 275-382. Mineralogical Society of America.

Deer W. A., Howie R. A. and Zussman J. (1993) An Introduction to Rock-Forming Minerals. Longman Scientific and Technical, Essex England, 696 pp.

Henderson P. (1968) The distribution of phosphorus in the early and middle stages of fractionation of some basic layered intrusions. *Geochimica et Cosmochimica Acta* **32**, 897-911.

Koritnig S. (1965) Geochemistry of phosphorus – I. The replacement of Si^{4+} by P^{5+} in rock-forming silicate minerals. *Geochimica et Cosmochimica Acta* **29**, 361-371.

Weisberg M., Connolly H., Zolensky M., Bland P., Bradley J., Brearley A., Bridges J., Brownlee D., Butterworth A., Dai Z., Ebel D., Genge M., Gounelle M., Graham G., Grossman J., Grossman L., Harvey R., Ishii H., Kearsley A., Keller L., Krot A., Langenhorst F., Lanzirotti A., Leroux H., Matrajt G., Messenger K., Mikouchi T., Nakamura T., Ohsumi K., Okudaira K., Perronnet M., Simon S., Stephan T., Stroud R., Taheri M., Tomeoka K., Toppani A., Tsou P., Tsuchiyama A., Velbel M., Weber I., Westphal A., Yano H., and Zega T. (2006) Stardust (Comet) Samples and the Meteorite Record. *American Geophysical Union*, Fall Meeting, P51E-1243 (abstract).

CHAPTER 1

AN EXPERIMENTAL STUDY OF PHOSPHORAN OLIVINE AND ITS SIGNIFICANCE IN MAIN GROUP PALLASITES.

INTRODUCTION

Pallasites are stony-iron meteorites consisting of olivine and minor phases, such as troilite, chromite, phosphates and schreibersite, all within an FeNi metal matrix (Urey, 1956; Mason, 1962). For a long time, pallasites have been divided into two groups, the Main Group (~65 separate meteorites) and the Eagle Station trio, based on their oxygen isotopic signatures and forsterite compositions (Scott, 1977; Clayton, 1978, 1993). In recent years, interpretations of pallasites have become more complicated. As of this writing, no less than five oxygen isotopically distinct parent bodies are required to explain the newly studied samples. [On the oxygen three isotope diagram, developed by Clayton and Mayeda in the early 1970s, $\delta^{18}O$ (a ratio of $^{18}O/^{16}O$) is plotted against $\delta^{17}O$ (a ratio of $^{17}O/^{16}O$). Parent bodies are distinguished from one another by having different 0.52 mass fractionation slopes.] In addition to their unusual oxygen isotopic signatures, their mineralogy has become increasingly diverse and interesting. Boesenberg et al. (2000) studied the pyroxene pallasites, Vermillion and Yamato 8451, finding pyroxene (both high- and low-Ca) at the 2% level (by volume). Before this study, pyroxene was known only in a few Main Group pallasites as part of rare symplectic intergrowths (Buseck, 1977). Jones et al. (2003) studied the unusual pallasite, Milton, which contains unusually iron-rich olivine (Fo_{83}), similar to that seen in the Eagle Station trio, but without the same oxygen isotopic signature. Finally, Bunch et al. (2005) studied the

pallasite, Zinder, where they found pyroxene also, but no longer as a minor component, instead representing 28% of the volume of the meteorite, and pushing the limits on the definition of a pallasite. Perhaps the most revealing aspect of this broadening view of pallasites is that large silicate and metal assemblages must occur as a natural consequence of the differentiation process in asteroidal-sized bodies. Therefore, a drastic change in the classic view of pallasites must occur. Models (Mason, 1962, 1963; Anders, 1964; Scott, 1977) have always assumed olivine and metal would immediately density-separate (as in Earth) into mantle and core during differentiation. To form the pallasite texture however, subsequent mixing of the separated components (metal and olivine) at a boundary layer has always been envisioned (Fig. 1.1). Based on the increasing commonality of the simple olivine (or silicate) - metal texture, this basic assumption appears to be false

A complication in the classic pallasite model, which will be explored here, involves the occurrence of phosphoran olivine within several Main Group pallasites (Buseck, 1977; Buseck and Clark, 1984). In phosphoran olivine, phosphorus replaces silicon within the olivine structure. Up to 4.9 wt% P_2O_5 has been found in several olivine crystals within the pallasites Brahin, Springwater, Rawlinna 001, and Zaisho. Buseck (1977) interpreted these olivines to form by subsolidus reaction between olivine and phosphorus-bearing FeNi metal. He observed that texturally the phosphoran olivine occurs as zones or thick rims on the edges of non-phosphoran “normal” olivine crystals (as large as 200 microns wide and several millimeters long). Also, the contacts between phosphoran and non-phosphoran areas were straight, sharp and abrupt. There were no compositional gradients. He also observed that phosphoran olivine occurred in pallasites that contained rounded olivine as well as those that contained fractured olivine. This

interpretation was broadly consistent with the ideas of Mason (1962, 1963), Anders (1964) and Scott (1977).

Since then, there have been additional reports on the occurrence of phosphoran olivine. These reports come from both terrestrial and extraterrestrial samples, as well as man-made objects. Phosphoran olivine has been found in the silicate inclusions in an iron-carbon alloy from Disko Island, Greenland (Goodrich, 1984); in a syenitic intrusion into an early Tertiary volcanic country rock in Pine Canyon, Utah (Agrell et al., 1998); as dendritic crystals in melt inclusions in a shergottite Martian meteorite (Goodrich 2003); at a 2300-year-old sacrificial burning site in Tyrol, Austria (Tropper et al., 2004) and in slag inclusions from the wrought iron hull of the Civil War warship, *USS Monitor* (Boesenberg, 2006). These latter occurrences are quite different from the rim-forming texture seen in the pallasites and despite coming from varied sources have all been interpreted as the result of rapid crystallization from a phosphorus-rich melt. In addition, Miyamoto (1997) and Hsu (2003) have carried out trace and minor element profile analyses across pallasite olivines where they find inverted U-shaped patterns. They propose that pallasite olivine cooled quickly from high temperatures, but more slowly at lower temperatures. This suggestion is difficult to reconcile with the Mason (1962, 1963), Anders (1964) and Scott (1977) interpretations, where cooling must occur very slowly over a long period of time. Thus, the Buseck (1977) interpretation concerning how phosphoran olivine and pallasites formed becomes problematic and a series of questions must be addressed. First, is phosphoran olivine a stable phase? Second, is the petrologic setting for the phosphoran olivine in pallasites consistent with their formation by subsolidus reaction between olivine and metal or alternatively by rapid crystallization?

Third, are the existing compositional data for phosphoran olivine and the inferred substitution systematics for silicon by phosphorus correct?

EXPERIMENTAL PROCEDURE

Experimental charges composed of powders of 50% FeP or 50% magnesium pyrophosphate ($Mg_2P_2O_7$) were mixed with 50% San Carlos olivine (Fo_{92}) (See Table 1.1 for calculated bulk compositions). Both FeP and $Mg_2P_2O_7$ are unstable compounds at high temperatures (~1000°C) and will dissociate releasing either elemental phosphorus or P_2O_5. Thus, both make excellent starting materials as the phosphorus is not preferentially bonded to any specific ion at the initiation of the experiment. The only problem encountered using these starting materials was estimating the temperature and oxygen fugacity conditions at which sufficient melt would be produced to allow phosphoran olivine crystallization.

The powders were ground separately before mixing so that no grains exceeded 75 micrometers in diameter. The powders were then mixed and pressed into pellets (4mm diameter). Because of the abundance of phosphorus within each experiment and the rapid reaction between phosphorus and metals, wire loop experiments could not be run. (All of the initial test experiments using various types of wire metal loops failed. The phosphorus reacted with the wire, formed a low temperature phosphide, melted, and dropped the experiment). Instead, dunite (Fo_{91}) crucibles were cut from the Twin Sisters Range, Washington dunite. The crucibles were cubes, one centimeter in length, containing a five millimeter wide, seven millimeter deep drill hole. The pellets were placed at the bottom of the hole and covered in additional San Carlos olivine powder to minimize the

volatilization of phosphorus during each experiment. The cube was then placed on an alumina disk that could be lowered into the furnace. The experiments were run in a vertical muffle tube Deltech furnace where the temperature reproducibility was +/-2ºC and the oxygen fugacity was controlled by a mixture of CO and CO_2 gases (Nafziger et al., 1971). Oxygen fugacity reproducibility is easily controlled within +/-0.1 log units.

The run conditions varied depending on the experimental composition and predicted result. Temperatures ranged from 900°C to 1350°C, while durations varied from one to 15 days, and oxygen fugacities were regulated between one log unit below the fayalite-magnetite-quartz buffer (FMQ-1) to three log units below the iron-wustite buffer (IW-3). Both isothermal and dynamic crystallization experiments were completed. The experiments were quenched by removing the run products from the furnace and dropping them into water. Because of the size of the dunite crucible, drop quenching directly from inside the furnace was not possible. Fortunately, because phosphate-rich glass does not crystallize easily, only rare quench products were ever found. All experiments and their run conditions are listed in Table 1.2.

ANALYTICAL TECHNIQUES

The completed experiments were sliced vertically, embedded in epoxy and both halves prepared as polished mounts. They were characterized using a petrographic reflected light microscope and the Cameca SX-100 electron microprobe located in the Department of Earth and Planetary Sciences at the American Museum of Natural History. Qualitative analysis was performed using both backscattered electron imaging and energy dispersive analysis. Quantitative analyses were performed using wavelength dispersive

analysis. An accelerating voltage of 15 kV and a beam current of 10nA was employed with 40 second counting times for all elements. Data correction on all analyses was carried out using data reduction of the PAP procedures (Pouchou and Pichoir, 1991). Both natural and synthetic minerals were used as standards (Appendix I).

RESULTS

The typical run product mineralogy consisted of forsterite or fayalite (formed by diffusion of Fe into the pre-existing forsterite), surrounded by an overgrowth of phosphoran olivine (either Fe- or Mg-rich depending on the starting materials and the duration of the experiment), plus a phosphate-rich glass, +/- tridymite, +/- metal, +/- phosphide. No phosphate phase [such as graftonite ($Fe_3P_2O_8$) or farringtonite ($Mg_3P_2O_8$)] crystallized in any of the experiments. The mineralogy was produced when FeP or magnesium pyrophosphate was oxidized and reacted with the San Carlos olivine. A phosphate-rich melt was produced, caused the activity of silica to rapidly rise to unity within the melt, and resulted in the rapid crystallization of abundant tridymite. The San Carlos olivine that escaped initial melting by the reaction with FeP or magnesium pyrophosphate experienced Fe-Mg diffusion and left occasional relict San Carlos forsterite cores intact. Phosphoran olivine overgrowths then crystallized around the diffused olivine. Metal and phosphide were present in the FeP experiments run below the IW buffer and were found as intimate intergrowths. In the experiments where phosphoran olivine was identified, the olivine was normally zoned in Fe-Mg. Zoning of P-Si was present as well, with phosphorus decreasing from the inner to outer edge of the

overgrowths (Fig. 1.2). Based on simple partitioning calculations and the phase assemblages, it is clear few experiments reached chemical equilibrium.

The experiments showed one major unpredicted result. Because of the size of the dunite crucible and slight variations in temperature from the top to the bottom of the crucible, as well as volatilization effects of phosphorus, many of the experimental charges became layered. At the top of the experiment, where it was cooler, and within the overlying San Carlos olivine powder, phosphoran olivine was often found, indicating volatilization (and probable loss) of some of the phosphorus from the underlying assemblage. In the experiments where the oxygen fugacity was below the iron-wustite buffer, metal and iron phosphide often formed single complex assemblages near the base of the pelletized charge. Metal and phosphide were rarely seen in the upper half of the pellets. Tridymite was commonly found throughout the pellet. All areas of the charge were examined, however the main emphasis of analysis and interpretation was placed on the pellet within the crucible as well as any reactions at the base of the crucible (in or very near the hotspot of the experiment). Reactions within the overlying San Carlos olivine powder were noted but not explored in detail.

The first set of experiments (Experiments 95, 96 and 87) consisted of isothermal runs using San Carlos olivine and $Mg_2P_2O_7$ at 1300°C and at an oxygen fugacity of FMQ-1.0 (Fig. 1.2 and 1.3). The durations were the only variable, ranging from 24 to 150 hours. The predominant resulting mineralogy consisted of angular to subrounded forsterites surrounded by one to ten micron overgrowths of phosphoran forsterite within a phosphate glass. Generally, thinner overgrowths with lower P_2O_5 abundances were found around the olivines as the duration increased. In the 24 hour experiment (#95), the rims

contained between 0.1 and 9.0 wt% P_2O_5, but the majority of overgrowths had compositions containing 1 to 5 wt% P_2O_5. In the 41.5 hr experiment (#96), the overgrowths contained between 0 and 5.9 wt% P_2O_5. The majority of overgrowths had compositions containing ~1 wt% P_2O_5. In contrast, the 150 hour experiment (#87) contained up to 5.5 wt% P_2O_5 in the overgrowths, with the overwhelming majority having a mere 0.05 to 0.3 wt% P_2O_5 (Fig 1.3). Round tridymite blebs or necklaces, generally one micron or less in size, were commonly found in the glass immediately adjacent to the phosphoran forsterite overgrowths.

The second set of experiments (Experiments 70, 71, 89, 91 and 92) also consisted of isothermal runs but contained an Fe-rich composition and were run at an oxygen fugacity of IW-1 (Fig. 1.2 and 1.4). Experiments 70 and 71 are nearly identical. They were run for about 165 hours and both contain abundant phosphoran olivine, which occurs both as overgrowths and individual grains with up to 27 wt% P_2O_5. The only notable difference between the two experiments is their different Fe/(Fe+Mg) ratios. In experiment 70, the Fe/(Fe+Mg) ratios are ~55-70 and in experiment 71 the Fe/(Fe+Mg) ratios are ~70-80. Experiment 70 appears to have lost a fraction of its melt composition (i.e. iron) through a fracture in the dunite crucible. The durations for experiments 92, 89 and 91 are roughly twice those of experiments 70 and 71, resulting in only rare phosphoran olivine overgrowths with less than 0.1 wt% P_2O_5. A major mineralogic difference between the long and short duration experiments is that the long experiments also contain phosphoran low-Ca pyroxene. Phosphoran pyroxene forms because the longer experiments more closely approach equilibrium. Tridymite is more abundant in the short duration experiments. With increasing duration, tridymite is resorbed back into

the phosphate glass, which alters the melt to a more silica-rich composition. When the melt subsequently crystallizes, some pyroxene is formed. Most of the phosphoran pyroxene occurs as rare individual grains or overgrowths surrounding fayalite. Compositionally, they usually contain only 1 to 5 wt% P_2O_5, although there are rare pyroxene overgrowths containing up to 31.5 wt % P_2O_5.

The third group of experiments (Experiments 99, 100, 101, 98) were dynamic crystallization runs. They were initially placed in the furnace for 10 minutes at 1350ºC and an oxygen fugacity of IW-1. The experiments were then cooled at rates of 1, 5, 20 or 25ºC per hour down to 830ºC. The results show a good correlation between decreasing cooling rate and decreasing average P_2O_5 content in olivine (Fig. 1.5). The FeO content of the olivine meanwhile shows a dramatic inverse correlation with cooling rate. Because slower cooling allows a closer approach to equilibrium conditions, results indicate incompatibility of FeO and P_2O_5 in olivine (Fig 1.5b.). Silica was found in the experiments cooled at 5, 20 and 25ºC per hour, but not in the experiment cooled at 1 ºC per hour.

The final set of experiments (Experiments 88, 71, 86, 95) were used to determine the oxygen fugacity range over which phosphoran olivine could be produced. Successful runs produced phosphoran olivine from FMQ-1 to IW-3. The experiments were run using a diverse range of compositions, temperatures, and durations. The simplest interpretation is that phosphoran olivine can be made under the same conditions (temperature, oxygen fugacity or composition) in which phosphorus-free olivine can be produced (Fig. 1.6). Because of the reduced nature of experiment 88, it produced both phosphoran olivine and

pyroxene. The olivine contains only up to 2.5 wt% P_2O_5, but the pyroxene contains 23 wt% P_2O_5.

DISCUSSION

Stability and Formation

Phosphoran olivine (like phosphoran pyroxene) is kinetically controlled and its presence is indicative of rapid crystallization from a phosphorus-rich olivine-normative melt that has not equilibrated. This conclusion is supported by two major pieces of experimental evidence. First, in the isothermal experiments, olivine overgrowth thicknesses and the P_2O_5 content of those overgrowths decrease with increasing duration. (Fig. 1.3 and 1.4) Second, the P_2O_5 content of the olivine overgrowths decreases as the cooling rate decreases in the dynamic crystallization experiments (Fig. 1.5). Both of these suggest that as durations are increased and equilibrium is more closely approached, the phosphorus in olivine approaches a minimum. Phosphorus behaves as if it were compatible, if not highly compatible, within the first few tens of hours of the experiments to highly incompatible on a days to weeks timescale. This is further supported by and reconfirms the phase diagrams of Wojciechowska and Berak (1959), which show no solid solution or intermediate phases between forsterite and farringtonite (Fig. 1.7), and the crystal-liquid distribution coefficients for phosphorus in olivine determined by Anderson and Greenland (1969) of 0.02-0.04.

The composition of phosphoran olivine can vary greatly both in Fe-Mg and Si-P depending on the bulk composition of the melt. Table 1.3 shows the theoretical extreme

endmember compositions, while Table 1.4 shows a few sample phosphoran olivine compositions generated in the experiments.

There are four requirements needed to produce phosphoran olivine: 1) enrichment of phosphorus in the melt, 2) depletion of SiO_2 in the melt, 3) rapid crystallization from a melt or recrystallization in an unequilibrated system, and 4) olivine as the liquidus phase at the time of crystallization. Goodrich (1984) and (Agrell et al., 1998) suggested a fifth requirement - that calcium be depleted in the melt as well. The present low-CaO experiments do not offer any direct proof of this suggestion. However, the phosphoran olivines always contained higher proportions of CaO than their non-phosphoran counterparts. The CaO limit suggested would largely impose compositional restraints on the stability of olivine and not specifically phosphoran olivine. Thus, it would seem consistent that as long as olivine is a liquidus phase at the time of crystallization, the amount of CaO present could influence the amount of phosphorus that is soluble in the olivine. Goodrich (1984) further suggested a sixth requirement that in order to produce phosphoran olivine the oxygen fugacity be near the IW buffer. This is unnecessary. Oxygen fugacity controls phosphoran olivine formation only to the extent of influencing the composition of the melt. Fugacity will not have any direct effect on the phosphorus ion while the liquid of the bulk composition remains in the olivine stability field, as its charge will remain +5. Phosphoran olivine was produced in these experiments from just below FMQ-1 to IW-3.

Significance in Main Group Pallasites

There are four pallasites known to contain phosphoran olivine – Brahin, Zaisho, Springwater and Rawlinna 001. All four have phosphoran olivine compositions that are quite similar (Table 1.5), with only minor variations in the Fa content. Although they are considered part of the Main Group based on oxygen isotopes, petrologically the four exhibit somewhat diverse and disparate characteristics. Brahin contains angular olivines with an average "normal olivine" composition of Fa_{12}, while Zaisho, Springwater and Rawlinna contain round olivines with average "non-typical olivine" compositions of Fa_{18}, Fa_{18}, and Fa_{16}, respectively. Thus, no obvious correlation between phosphoran olivine and either olivine composition or texture appears to exist.

Based on the experimental evidence, the phosphoran olivine found within pallasites forms as a result of rapid late stage crystallization from phosphorus-rich melt pockets, and not as a result of subsolidus reaction between phosphorus-bearing metal and olivine as suggested by Buseck (1977). If a subsolidus reaction had occurred between metal and olivine, diffusional gradients of phosphorus should be present in the olivine from rim to core and in the metal immediately surrounding the olivine. These do not exist. Further, if phosphorus replaced silicon during a subsolidus reaction, an excess of both silicon and magnesium (or iron) should exist. What happens to this silicon and magnesium that must be removed from the olivine? How is it accomodated by the pallasite mineralogy? For silicon to enter the metal, oxygen fugacities approaching and probably exceeding IW-5 would be required (Moore, 1993). However, pallasites have been calculated to form at ~IW-0.5 (Righter et al., 1990) and no silica phase has yet been observed in them.

The presence of phosphoran olivine places further constraints on pallasite formation times and conditions. Assuming that pallasite olivine formed near the core-mantle boundary as envisioned by Mason (1962, 1963) and Anders (1964), once the crystallization of the phosphoran olivine took place, the phosphoran olivine could not have remained at depth for more than a few hours to days, as equilibration at high temperature would have erased the phosphorus enrichment. If however pallasite olivines formed as either residues of extensive partial melting or as cumulates from fractional crystallization of melted chondritic precursors (Urey, 1956, Mittlefehldt, 1980), the olivine could be formed at more shallow levels. Whether the formation of olivine and metal was contemporaneous or if the metal and olivine formed separately but were mixed subsequently to create the pallasite texture is still highly debated (Anders, 1964; Buseck and Goldstein 1969; Davis, 1977; Scott and Taylor, 1990). Either way, rapid cooling from high temperature could occur, with perhaps a regolith blanket forming subsequently to allow the slow cooling recorded by the Widmanstätten pattern of the metal (Hsu, 2003). This asymptotic decrease of temperature would also be consistent with Hsu (2003) and Miyamoto (1997) who did profiles across pallasite olivines using the ion microprobe and electron microprobe. They determined that the olivines are zoned and contain high core concentrations but low edge concentrations of the minor and trace elements Ca, Cr, Ni, Ti, and V. These profiles would be flat if slow cooling rates had persisted from high to low temperature. Metallographic cooling rates for pallasites (estimated to be ~2-10ºC per million years) are consistent with slow cooling at low temperatures (below 900ºC), but could easily support either model.

For a model to be completely consistent with pallasite formation, a fundamental change in how differentiation is thought to occur in small planetary bodies appears to be needed. The new model envisioned looks at the effect of inefficient differentiation, to produce a pallasite-style texture in the mantle of an asteroidal body (Fig. 1.8).

The assumption that solid olivine and molten metal can density separate in a very low gravity environment may be wrong (Takahashi 1983, 1984). A simple observation of museum and university collections around the world supports this idea. There are several hundred differentiated meteorites containing high metal/silicate ratios including the five pallasite types, mesosiderites, IAB-IIICD irons, IVA irons and numerous ungrouped or anomalous meteorites.

Stevenson (1990) and Arculus et al. (1990) have pointed out that surface tension effects play an important role in metal-silicate interactions when gravity is low. The surface tension between solid olivine and molten FeNi metal is approximately 40 times that of water on quartz (Su et al., 2005; Li et al., 2005; Brooks and Quested, 2005). Because of this very high value, molten metal does not easily release olivine from within it unless the olivine is either outright melted or sufficient silicate (or sulfide) melt is present to act as a lubricating medium between the two phases. Silicate melt and molten metal have very low surface tension and can easily separate. Thus, when a chondritic body partially melts and differentiates, three phases are likely to be present: solid olivine, silicate melt and molten FeNi metal. The silicate melt should easily rise and percolate up from the molten metal and olivine (Takahashi 1983, 1984) to become a basaltic crust. Meanwhile, some molten iron, that is free of olivine, will presumably become a core simply because temperatures in excess of the olivine solidus will melt any silicates

initially located deep in the parent asteroid. This leaves a pallasite texture in the mantle, where olivine exists as a solid and metal as a dense liquid.

If the parent body started with a bulk chondritic composition, extensive fractional crystallization (~80%) (Scott, 1977) of the metal is required to produce a metal composition similar to that seen in the pallasite meteorites. This appears to be possible in the inefficient differentiation model as long as crystallization proceeded from the bottom up (i.e. solid inner core, liquid outer core – more evolved metal compositions would reside at more shallow depths).

Phosphoran olivine could be explained by simple convection within such a model. Tiny amounts of P-enriched late-stage melt that was trapped between the olivine and molten metal, following the removal of most of the basaltic melt (i.e. the crust of the parent body), would be brought to shallow depths where they would rapidly crystallize. [based on partitioning, P prefers liquid silicate and liquid metal and would be enriched in such areas].

Convection would further explain the existence of both angular and rounded olivines in pallasites. The olivine being crushed and fractured in cooling metal at shallow depths, while olivine at depth is recrystallized and rounded.

Finally, the inverted U-shaped patterns in minor and trace elements in olivine found by Miyamoto (1997) and Hsu (2003) would be in complete agreement with this model. The olivine would cool relatively quickly through high temperatures, during which time it would develop a flat pattern. As cooling slowed at lower temperatures, diffusion of the trace and minor elements out of the olivine would occur leaving the patterns seen. Presumably, most of the trace and minor elements are likely incorporated

into either forming late-stage phosphates, sulfides, or diffusing into the metal. The slow cooling would be reflected in the cooling rates calculated from the metal (Goldstein and Short, 1967; Buseck and Goldstein, 1969).

Charge Balance and Stoichiometry

The question of charge balance of phosphorus in olivine has been addressed by every researcher who has written on phosphoran olivine (Buseck, 1977; Buseck and Clark, 1984; Goodrich, 1984; Agrell et al., 1998; Self and Buseck, 1983; Boesenberg, 2006). Buseck (1977) left charge balance an open question, suggesting interstitial anions, cation site vacancies, or substituting ions. Buseck and Clark (1984) initially suggested charge balance by the addition of lithium, but ion probe work showed insufficient lithium abundances and no correlation with P. They then suggested "charge balance by having vacant octahedral sites". Goodrich (1984) agreed with Buseck and Clark (1984) that octahedral site vacancies charge balance the phosphorus in the tetrahedral site, because octahedral cation totals were consistently low for the structural formula. Self and Buseck (1983) did high resolution structure determination and confirmed the negative correlation between Si and P, but had no convincing evidence for an octahedral site vacancy. They suggested that in addition to $M + 2Si \leftrightarrow 2P$ substitution, a tetrahedral vacancy involving $5Si \leftrightarrow 4P + {}^{VI}[]$ may occur. The difficulty faced by Self and Buseck (1983), Buseck and Clark (1984), and Goodrich (1984) mainly hinges on the relatively low P_2O_5 content in natural samples (less than 6 wt%). The experimental phosphoran olivine (Fo_{20}) produced in experiment 71, however, contains 27% P_2O_5, very near the maximum amount possible in the olivine structure. This represents 69% of the tetrahedral sites being replaced by P

[The maximum is 70%. Beyond this level of substitution, the olivine structure destabilizes and the Fe-Mg phosphates, graftonite and farringtonite $(Fe,Mg)_3P_2O_8$, exist. It is not know whether a silico-phosphate version of graftonite and farringtonite can form]. These experimental data confirm the vacancy of the octahedral site and its correlation with the M site cation deficiency (Fig. 1.9). The latter $5Si \leftrightarrow 4P$ scheme is not present. The charge balancing scheme for phosphoran olivine is (more formally written): $4^{VI}M^{+2} + 2Si^{+4} \leftrightarrow 3^{VI}M^{+2} + 2P^{+5} + {}^{VI}[\ ]$. Mineralogically, the phosphoran olivine formula is a solid solution varying between $(Mg,Fe)_2SiO_4$ and $(Mg,Fe)_{1.65}[]_{0.35}Si_{0.3}P_{0.7}O_4$.

CONCLUSIONS

The presence of high phosphorus in olivine is an indication of a disequilibrium assemblage under all conditions of temperature and oxygen fugacity. Phosphoran olivine can form for brief intervals when rapid crystallization of olivine occurs and there is sufficient phosphorus within the melt. Its presence in pallasites indicates that these meteorites could not have remained at high temperature for longer than perhaps a few days. They are therefore unlikely to have formed deep inside a large differentiated asteroid near the core-mantle boundary. The standard pallasite formation models are unsatisfactory. A new model looking at the inefficient differentiation of an asteroid appears compatible with pallasite formation. Unfortunately, this model hinges on the poorly-understood physical interactions between crystalline olivine and molten metal in a low gravity environment.

REFERENCES

Agrell S. O., Charnley N. R. and Chinner G. A. (1998) Phosphoran olivine from Pine Canyon, Piute Co., Utah, *Mineralogical Magazine* **62**, 265-269.

Anders E. (1964) Origin, age and composition of meteorites. *Space Science Reviews* **3**, 583-714.

Anderson A. T. and Greenland L. P. (1969) Phosphorus fractionation diagram as a quantitative indicator of crystallization differentiation of basaltic liquids. *Geochimica et Cosmochimica Acta* **33**, 493-505.

Arculus R.J., Holmes R.D., Powell R. and Righter K. (1990) Metal-silicate equilibria and core formation. In *Origin of the Earth* (ed. H. C. Newsom and J. H. Jones), pp.251-271. New York: Oxford University Press.

Brooks R. F. and Quested P. N. (2005) The surface tension of steels. *Journal of Materials Science* **40**, 2233-2238.

Buseck P. R. (1977) Pallasite meteorites - mineralogy, petrology and geochemistry. *Geochimica et Cosmochimica Acta* **41**, 711-740.

Buseck P. R. and Clark J. (1984) The Zaisho pallasite, a bearer of pyroxene and phosphoran olivine. *Mineralogical Magazine* **48**, 229-235.

Buseck P. R. and Goldstein J. I. (1969) Olivine compositions and cooling rates of pallasitic meteorites. *Geological Society of America Bulletin* **80**, 2141-2158.

Clayton R. N. and Mayeda T. K. (1978) Genetic relations between iron and stony meteorites. *Earth and Planetary Science Letters*, **40**, 168-174.

Clayton R. N. (1993) Oxygen isotopes in meteorites. *Annual Review of Earth and Planetary Sciences*, **21**, 115-149

Goldstein J. I. and Short J. M. (1967) Cooling rates of 27 iron and stony-iron meteorites. *Geochimica et Cosmochimica Acta* **31**, 1001-1002.

Goodrich C. A. (1984) Phosphoran pyroxene and olivine in silicate inclusions in natural iron-carbon alloy, Disko Island, Greenland. *Geochimica et Cosmochimica Acta* **48**, 1115-1126.

Goodrich C. A. (2003) Petrogenesis of olivine-phyric shergottites Sayh al Uhaymir 005 and Elephant Moraine 79001A lithology A. *Geochimica et Cosmochimica Acta* **67**, 3735-3771

Goodrich C. A. and Barnes S. (1984) Is phosphorus predictably incompatible in igneous processes? *Conference on the Origin of the Moon*, Kona, Hawaii.

Henderson P. (1968) The distribution of phosphorus in the early and middle stages of fractionation of some basic layered intrusions. *Geochimica et Cosmochimica Acta* **32**, 897-911.

Hsu W. (2003) Minor element zoning and trace element geochemistry of pallasites. *Meteoritics & Planetary Science* **38**, 1217-1240.

Koritnig S. (1965) Geochemistry of phosphorus – I. The replacement of Si^{4+} by P^{5+} in rock-forming silicate minerals. *Geochimica et Cosmochimica Acta* **29**, 361-371.

Li Z., Mukai K., Zeze M. and Mills K. C. (2005) Determination of the surface tension of liquid stainless steel. *Journal of Materials Science* **40**, 2191-2195.

Mason B. (1962) *Meteorites*. New York: Wiley, 274 pp.

Mason B. (1963) The pallasites. *American Museum Novitiates,* **2163**.

McSween H. Y. (1999) Meteorites and their Parent Planets. Cambridge University Press, 324 pp.

Mittlefehldt D. W. (1980) The composition of mesosiderite olivine clasts and the implications for the origins of pallasites. *Earth and Planetary Science Letters* **51**, 29-40.

Miyamoto M. (1997) Chemical zoning of olivine in several pallasites. *Journal of Geophysical Research* **102**, 21613-21618.

Moore J. J. (1993) *Chemical Metallurgy*. London: Butterworths, 435 pp.

Nafziger R. H., Ulmer G. C. and Woerman E. (1971) Gaseous buffering for control of oxygen fugacity at one atmosphere. In *Research Techniques for High Pressure and High Temperature* (ed. G. C. Ulmer), pp. 9-41. New York: Springer-Verlag.

Pouchou J. and Pichour F. (1991) Quantitative analysis of homogeneous or stratified microvolumes applying the model "PAP". In *Electron Probe Quantitation* (eds. K. F. J. Heinrich and D. E. Newbury), Plenum Press, New York, 31-75.

Righter K., Arculus R. J., Delano J. W., and Paslick C. (1990) Electrochemical measurements and thermodynamic calculations of redox equilibria in pallasite meteorites: Implications for the eucrite parent body. *Geochimica et Cosmochimica Acta* **54**, 1803-1815.

Scott E. R. D. (1977) Pallasites – metal composition, classification and relationships with iron meteorites. *Geochimica et Cosmochimica Acta* **41**, 349-360

Scott E. R. D. and Taylor G. J. (1990) Origins of pallasites at the core-mantle boundaries of asteroids. *Lunar and Planetary Science Conference* **XXI**, 1119-1120.

Self P. G. and Buseck P. R. (1983) High-resolution structure determination by ALCHEMI. *Proceedings of the 41st Annual Meeting of the Electron Microscopy Society of America*, San Francisco Press.

Stevenson D. J. (1990) Fluid dynamics of core formation. In *Origin of the Earth* (ed. H. C. Newsom and J. H. Jones), pp. 231-249. New York: Oxford University Press.

Su. Z., Li. K. and Mills K. C. (2005) Equation to estimate the surface tensions of stainless steels. *Journal of Materials Science* **40**, 2201-2205.

Takahashi E. (1983) Melting of a Yamato L3 chondrite (Y-74191) up to 30 kbar. *Proceedings of the Eighth Symposium on Antarctic Meteorites, National Institute of Polar Research* **30**, 168-180.

Takahashi E. (1984) On the origin of pallasite. *Antarctic Meteorites* **IX**, 63.

Tropper P., Recheis A. and Konzett J. (2004) Pyrometamorphic formation of phosphorous-rich olivines in partially molten metapelitic gneisses from a prehistoric sacrificial burning site (Otz Valley, Tyrol, Austria) *European Journal of Mineralogy* **16**, 631-640.

Urey H. C. (1956) Diamonds, meteorites and the origin of the solar system. *The Astrophysical Journal* **124**, 623-627.

Wojciechowska J. and Berak J. (1959) *Roczniki Chem.* **33**, 24-27.

FIGURE CAPTIONS

Figure 1.1. Standard model of Mason (1962, 1963), Anders (1964), and Scott (1977) envisioning pallasite formation as the product of mixing of olivine and metal, following core-mantle differentiation. Within the standard models, pallasites are thought to have metal compositions similar to more evolved members of the IIIAB iron meteorites. To produce pallasite metal from an average chondrite, the metal is required to undergo approximately 80% fractional crystallization. The diagram is from McSween (1999).

Figure 1.2. Backscattered electron images of phosphoran olivine in iron-rich experiment #71 (a) and magnesium-rich experiment #87 (b). In photo A, fayalite cores (light gray) are surrounded by phosphoran olivine overgrowths (medium gray) in a phosphate glass (slightly darker medium gray – large patch in lower right corner). Thousands of small phosphoran olivines were generated in this experiment. A large tridymite (black) is also visible. Many of small round black areas are pore spaces. In photo B, thin phosphoran olivine overgrowths (light gray) are seen around forsterite (medium gray) within a phosphate glass (white). Silica blebs (black) and necklaces ring the forsterite in the phosphoran olivine overgrowth. There are no pore spaces showing in this experiment.

Figure 1.3. Bar graph showing the a) progressive decrease of P_2O_5 abundance and b) increase in FeO in the olivine overgrowths with duration for the isothermal experiments run with magnesium pyrophosphate. Although using the percentage of the total number of analyses is not a quantitatively accurate method for determining the modal proportions of the phases, it is sufficient to obtain a general estimation for the abundance of phosphoran olivine present within the experiment.

Figure 1.4. Bar graphs showing the disappearance of P_2O_5 in the olivine overgrowths when the duration is doubled from ~160 to ~320 hours for the isothermal experiments run with the iron phosphide.

Figure 1.5. Bar graphs of the dynamic crystallization experiments run with iron phosphide showing the progressive decrease of (a) P_2O_5 and (b) FeO abundance in the olivine overgrowths as a function of cooling rate.

Figure 1.6. Bar graphs showing the wide range of P_2O_5 abundances in olivine overgrowths produced in experiments run at various oxygen fugacity conditions.

Figure 1.7. In A and B, the phase diagrams of Wojciechowska and Berak (1959) show the relationships between farringtonite ($Mg_3P_2O_8$) and forsterite. There are no existing phase diagrams for the iron-rich endmembers, graftonite-fayalite, but presumably are similar. In C and D, phosphoran olivine compositions are plotted on graphs of Si/(Si+P) versus Fe/(Fe+Mg), which mimic the farringtonite-forsterite binary in A. Graph C shows the range of phosphoran olivine compositions produced in experiment #71. Graph D shows the approach towards equilibrium in experiment #89 and the absence of any phosphoran olivine.

Figure 1.8. A model of pallasite formation by inefficient differentiation. Upon partial melting of a chondritic body, liquid silicate separates to become a crust, while molten metal and solid olivine are unable to be disentangled resulting in a pallasite mantle. High temperatures, in excess of the olivine solidus, produce an olivine-free core.

Figure 1.9. Overlapping graphs of P vs. Si (blue) and P vs. M cations (red) in phosphoran olivine in atoms per formula unit (a. p. f. u.) from experiment #71. P vs. Si shows the depletion from full tetrahedral site occupancy where P + Si = 1 (green line). P vs. M cations show progressive depletion of the octahedral sites with increased P. One M must be removed (along with two Si) for every two P added to the olivine (complete removal of one M is shown by the green line).

Table 1.1. Starting compositions. Compositions were produced using San Carlos olivine with either iron phosphide or magnesium pyrophosphate. Iron and phosphide have been recalculated as oxides. Note the drastic difference in Fe/(Fe+Mg) ratios of the starting compositions. These compositions in reality were both more magnesian and olivine normative than the compositions indicate due to the reaction of the experimental charge with the wall of the dunite crucible. Higher values of Cr are also likely as chromite was a constituent of the dunite.

	50% San Carlos / 50% FeP	50% San Carlos / 50% $Mg_2P_2O_7$
P_2O_5	30.87	31.84
SiO_2	15.42	20.38
Cr_2O_3	0.14	0.18
FeO	34.85	4.77
MnO	0.05	0.07
MgO	18.67	42.76
100*Fe/(Fe+Mg)	51.2	5.9
100*Si/(Si+P)	54.1	60.2

Table 1.2.

I. Isothermal Experiments

	Exp#	Composition	Temp	$F(O_2)$	Duration	P-oliv present
A.	95	Fo+Mg_2P2O_7	1300	FMQ-1.0	24 hrs	yes
	96	Fo+Mg_2P2O_7	1300	FMQ-1.0	41.5 hrs	yes
	87	Fo+Mg_2P2O_7	1300	FMQ-1.0	150 hrs	yes
B.	92	Fo+FeP	1100	IW-1.0	336+ hrs (lost power)	No
	89	Fo+FeP	1010	IW-1.0	311.5 hrs	No
	91	Fo+FeP	975	IW-1.0	356.5 hrs	No
	71	Fo+FeP	1000	IW-1.0	169.5 hrs	Yes
	70	Fo+FeP	975	IW-1.0	162 hrs	Yes

II. Dynamic Crystallization Experiments

Exp#	Composition	Temp	$F(O_2)$	Duration
98	Fo+FeP	1350	IW-1	20 hrs (25C/hr) down to 830C
101	Fo+FeP	1350	IW-1	26 hrs (20C/hr) down to 830C
100	Fo+FeP	1350	IW-1	103 hrs (5C/hr) down to 830C
99	Fo+FeP	1350	IW-1	220 hrs (1C/hr) lost power ~1130C

III. Oxygen Fugacity Range Experiments

Exp#	Composition	Temp	$F(O_2)$	Duration
88	Fo+Mg_2P2O_7	1325	IW-3.0	72 hrs
71	Fo+FeP	1000	IW-1.0	169.5 hrs
86	Fo+Mg_2P2O_7	1275	IW-0.5	240+ hrs
95	Fo+Mg_2P2O_7	1300	FMQ-1.0	24 hrs

Table 1.3. Theoretical endmember phosphoran olivine compositions for both fayalite and forsterite.

	Fayalite	P-Fayalite	Forsterite	P-Forsterite
P_2O_5	0	26.67	0	37.01
SiO_2	29.49	9.68	42.70	13.43
FeO	70.51	63.65	0	0
MgO	0	0	57.30	49.56

Table 1.4. Sample analyses demonstrating the compositional range of experimental phosphoran olivines.

	Exp96	Exp87	Exp71	Exp71	Exp70	Exp100	Exp101	Exp95
P_2O_5	3.94	0.80	26.97	19.88	24.59	3.15	13.79	4.11
SiO_2	37.82	40.38	10.37	16.50	15.27	33.29	25.63	38.82
TiO_2	0.02	0.01	0.03	0.00	0.03	0.00	0.00	0.00
Al_2O_3	0.01	0.04	0.01	0.00	0.10	0.05	0.00	0.00
Cr_2O_3	0.01	0.13	0.02	0.04	0.02	0.07	0.10	0.00
FeO	6.37	8.26	55.70	54.13	42.54	34.59	32.12	4.33
MnO	0.06	0.08	0.19	0.13	0.03	0.06	0.09	0.11
MgO	50.58	50.78	6.76	9.85	17.92	28.82	28.02	52.56
CaO	0.09	0.04	0.30	0.03	0.03	0.00	0.06	0.12
Na_2O	0.06	0.00	0.00	0.00	0.00	0.01	0.01	0.18
NiO	0.36	0.00	0.00	0.06	0.01	0.00	0.00	0.23
Total	99.31	100.51	100.35	100.62	100.53	100.04	99.72	100.46
P	0.08	0.02	0.68	0.50	0.57	0.07	0.31	0.08
Si	0.91	0.98	0.30	0.49	0.42	0.92	0.69	0.91
Ti	0.00	0.00	0.00	0.00	0.00	0.00	0.00	0.00
Al	0.00	0.00	0.00	0.00	0.00	0.00	0.00	0.00
Cr	0.00	0.00	0.00	0.00	0.00	0.00	0.00	0.00
Fe	0.13	0.17	1.38	1.34	0.98	0.80	0.72	0.09
Mn	0.00	0.00	0.00	0.00	0.00	0.00	0.00	0.00
Mg	1.83	1.83	0.30	0.44	0.74	1.18	1.12	1.86
Ca	0.00	0.00	0.01	0.00	0.00	0.00	0.00	0.00
Na	0.00	0.00	0.00	0.00	0.00	0.00	0.00	0.00
Ni	0.00	0.00	0.00	0.01	0.00	0.00	0.00	0.00

Table 1.5. Sample analyses of phosphoran olivines measured in pallasites.

	Brahin[1]	Rawlinna 001[1]	Springwater[1]	Zaisho[2]
P_2O_5	3.82	4.91	4.14	4.36
SiO_2	36.5	35.9	35.5	36.5
FeO	13.7	14.3	16.2	15.9
MnO	0.30	0.26	0.45	0.40
MgO	43.2	44.8	43.0	42.9
100*Fe/(Fe+Mg)	15.1	15.2	17.4	17.2
100*Si/(Si+P)	95.7	94.5	95.3	95.1

[1] from Buseck (1977)
[2] from Buseck and Clark (1984)

Figure 1.1.

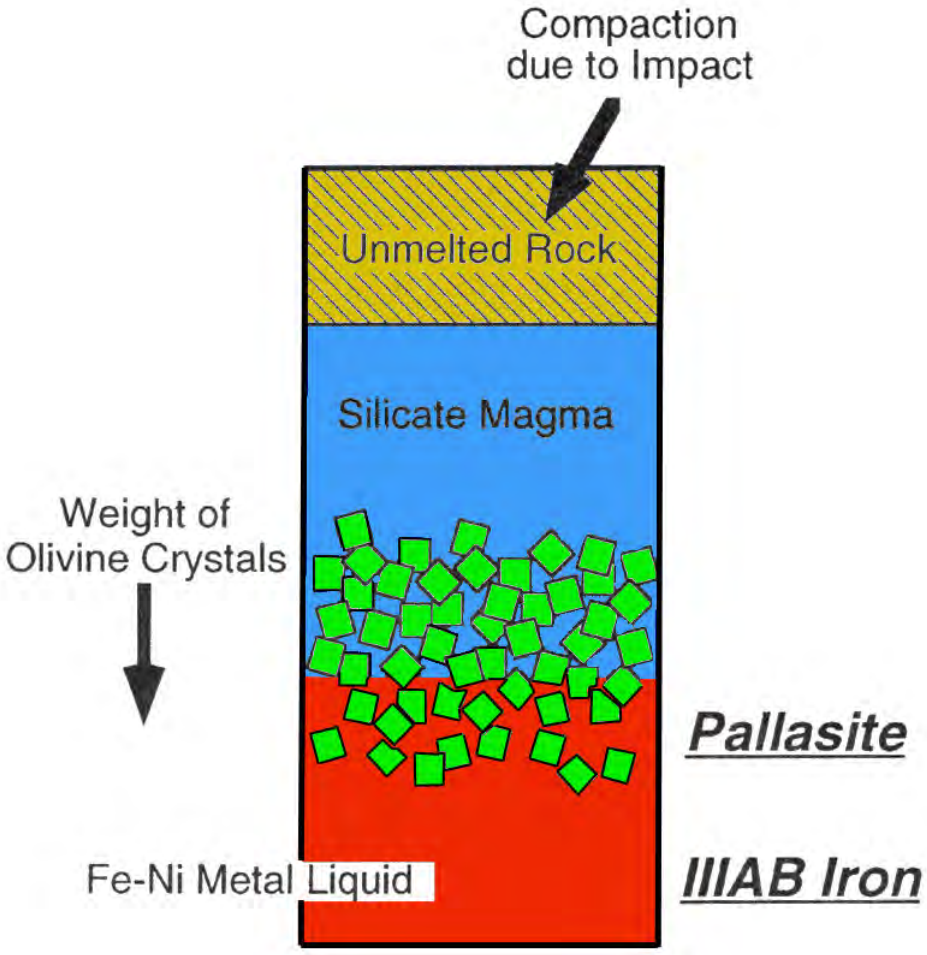
Compaction
due to Impact
Unmelted Rock
Silicate Magma
Weight of
Olivine Crystals
Pallasite
Fe-Ni Metal Liquid
IIIAB Iron

Figure 1.2a.

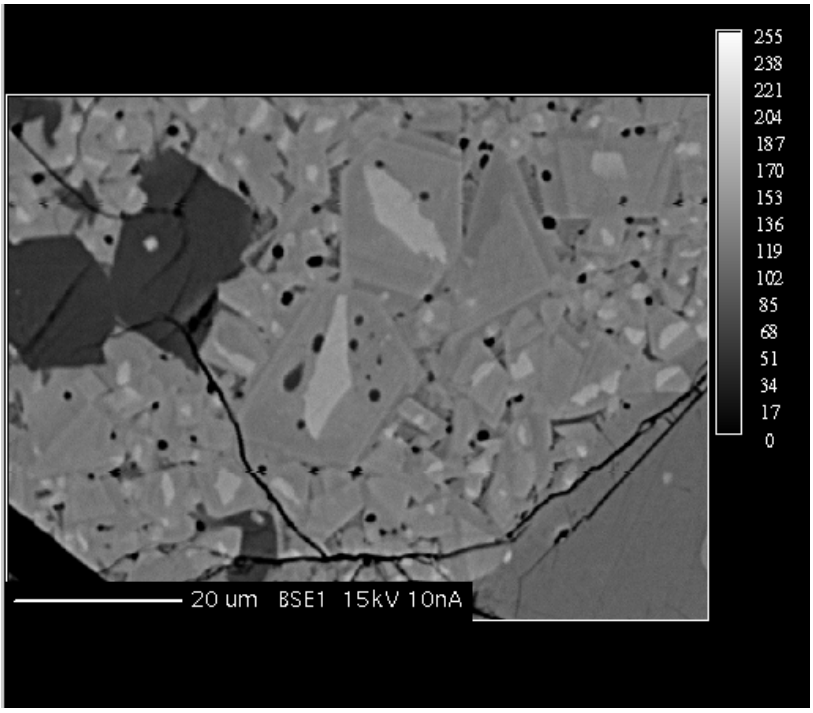

Figure 1.2b.

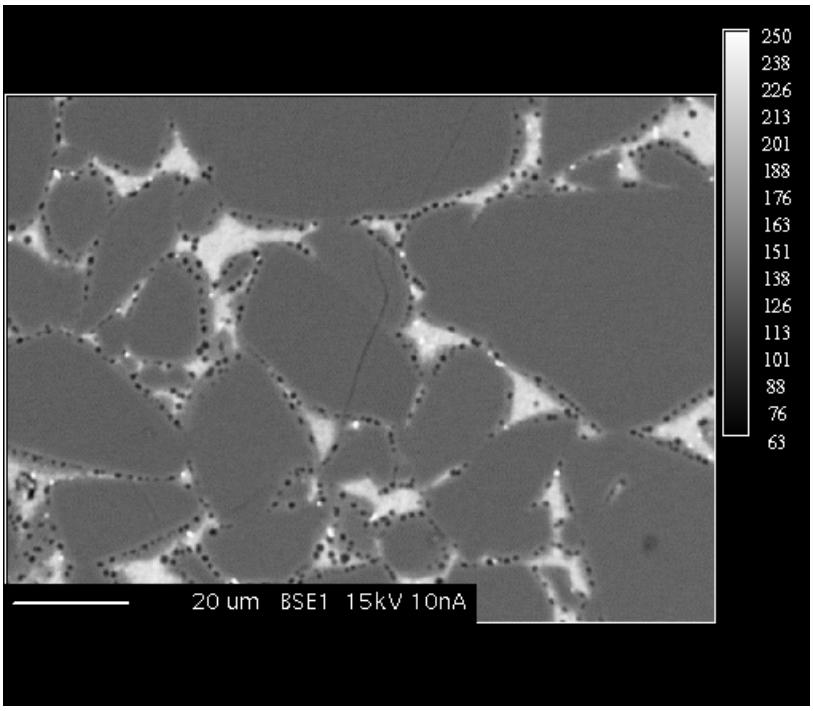

Figure 1.3a.

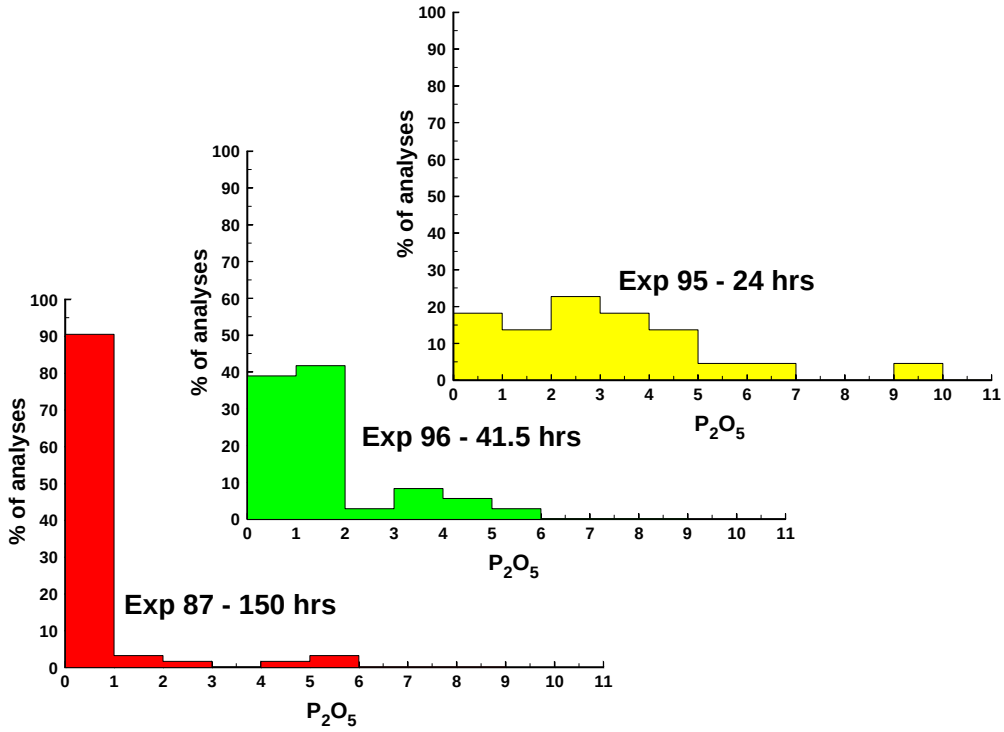

Figure 1.3b.

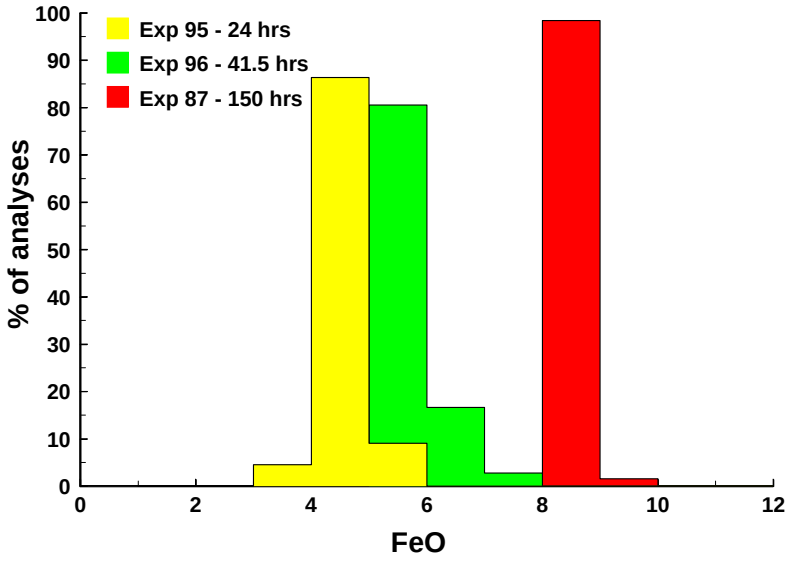

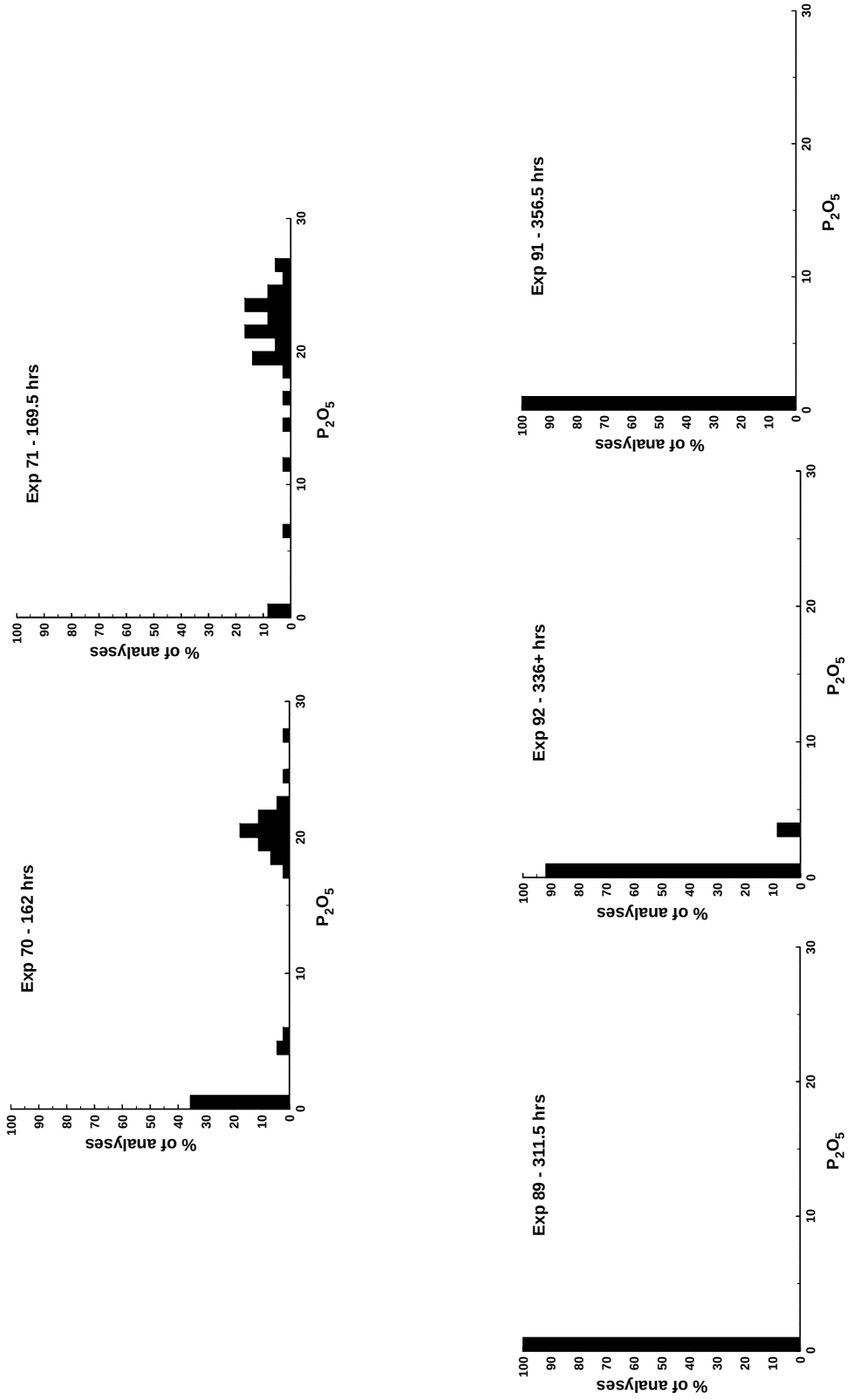
Exp 70 - 162 hrs
Exp 71 - 169.5 hrs
Exp 89 - 311.5 hrs
Exp 91 - 356.5 hrs
Exp 92 - 336+ hrs
% of analyses
P_2O_5

Figure 1.4.

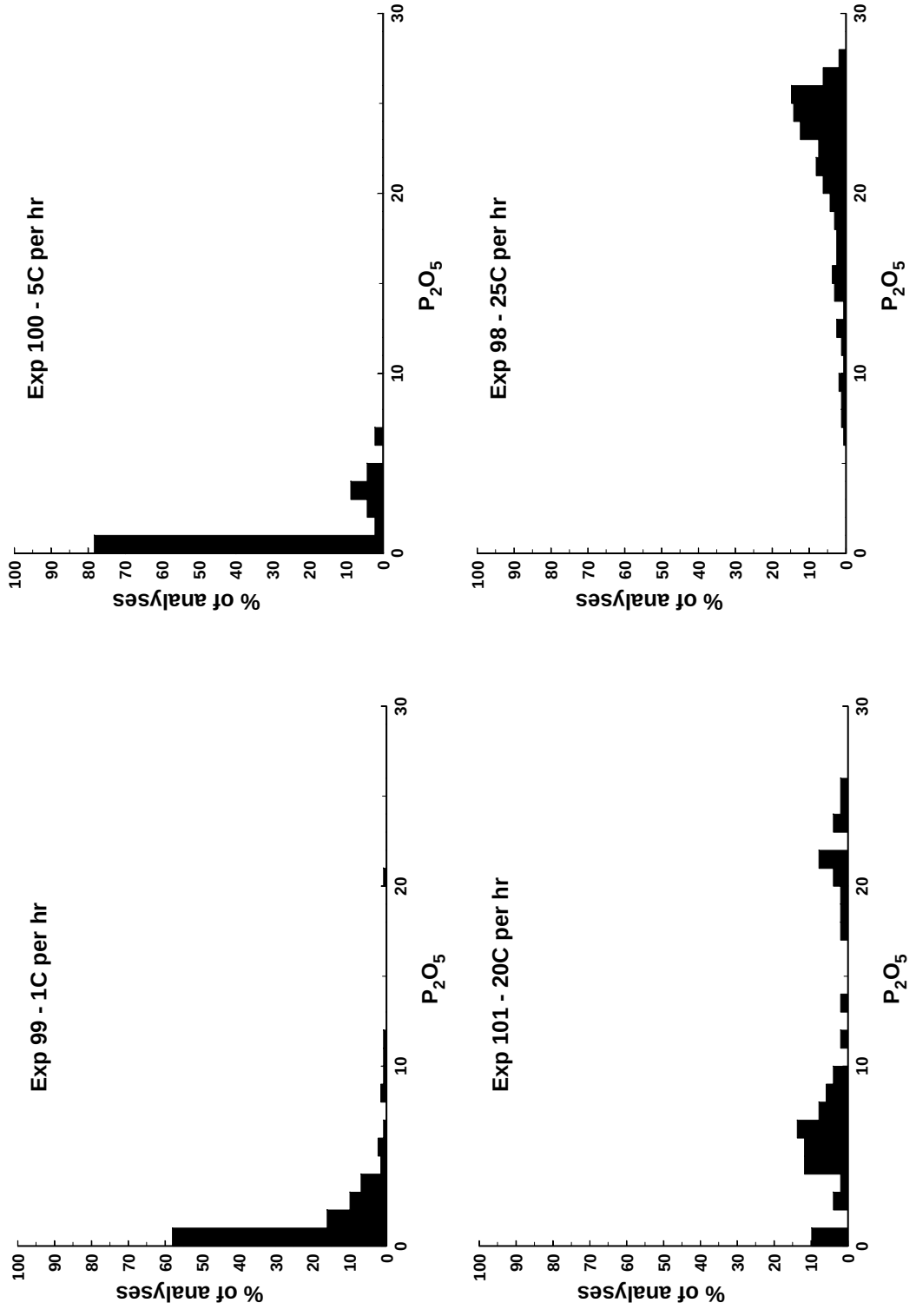
Exp 100 - 5C per hr
Exp 98 - 25C per hr
Exp 99 - 1C per hr
Exp 101 - 20C per hr
% of analyses
P_2O_5
0
10
20
30
40
50
60
70
80
90
100

Figure 1.5a.

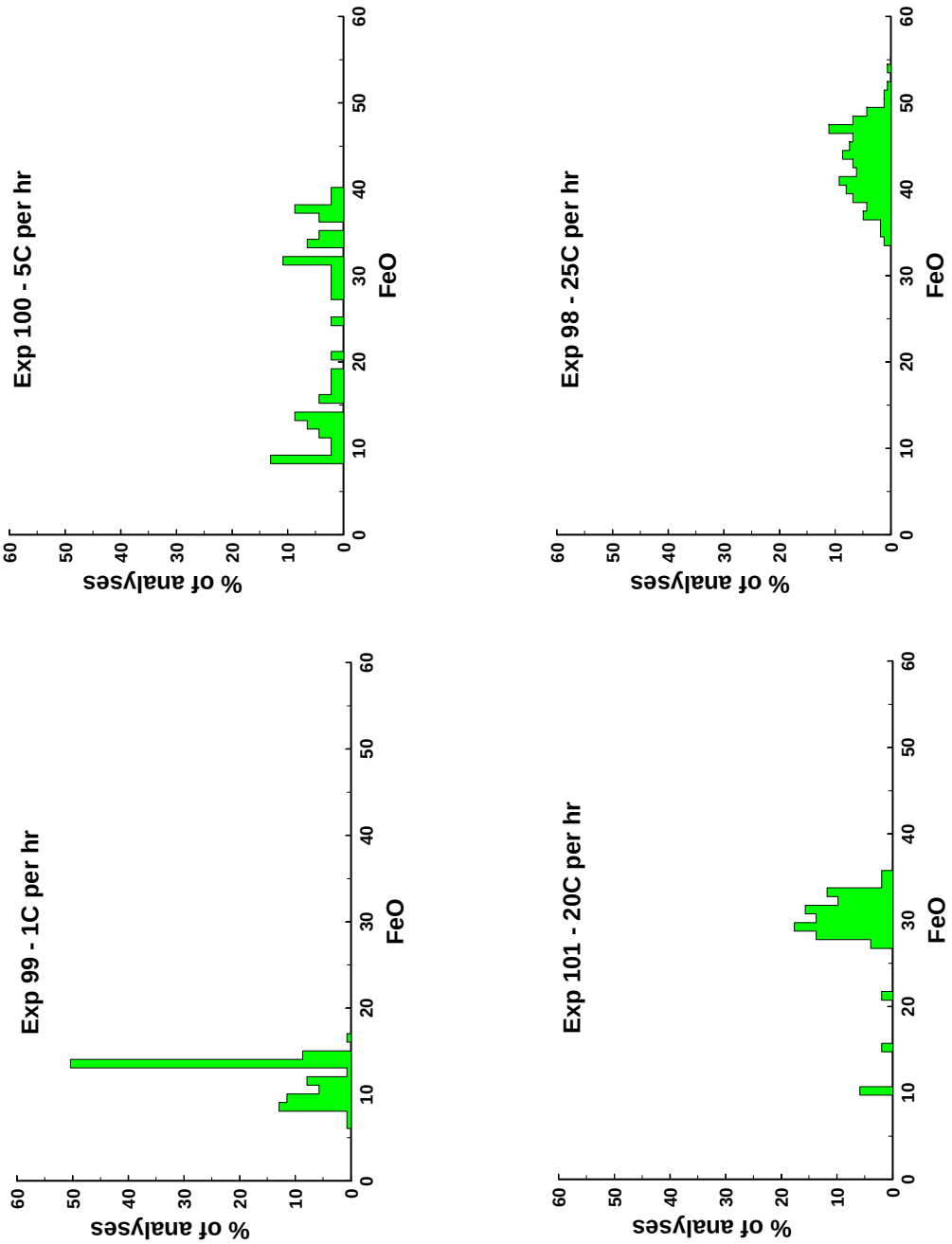
Exp 100 - 5C per hr
Exp 98 - 25C per hr
Exp 99 - 1C per hr
Exp 101 - 20C per hr
% of analyses
FeO
0
10
20
30
40
50
60

Figure 1.5b.

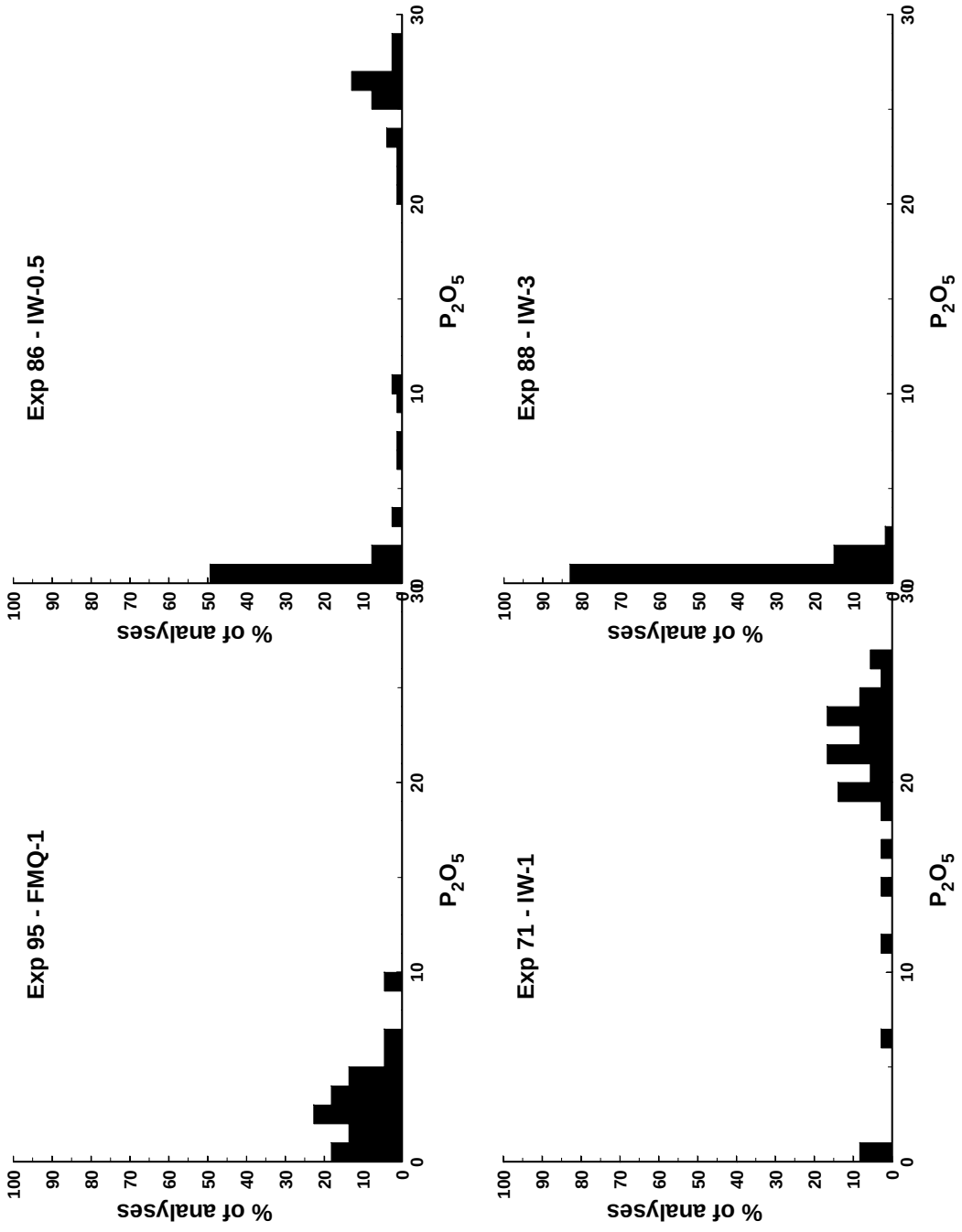
Exp 86 - IW-0.5
Exp 88 - IW-3
Exp 95 - FMQ-1
Exp 71 - IW-1
% of analyses
P_2O_5
0
10
20
30
40
50
60
70
80
90
100

Figure 1.6.

Figure 1.7a.

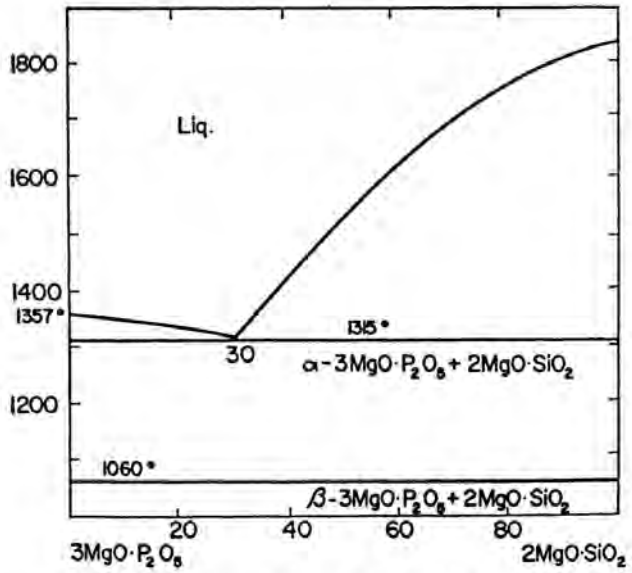

FIG. 728.—System $2MgO \cdot SiO_2$–$3MgO \cdot P_2O_5$.

Jadwiga Wojciechowska and Józef Berak, *Roczniki Chem.*, **33**, 26 (1959).

Figure 1.7b.

MgO–SiO_2–P_2O_5

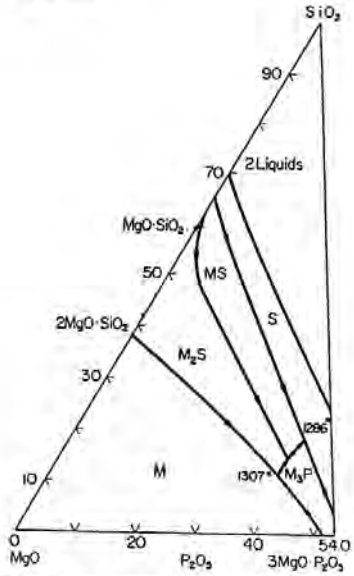

FIG. 725.—System MgO–$3MgO \cdot P_2O_5$–SiO_2. M = MgO, P = P_2O_5, S = SiO_2.

Jadwiga Wojciechowska and Józef Berak, *Roczniki Chem.*, **33**, 27 (1959).

Figure 1.7c.

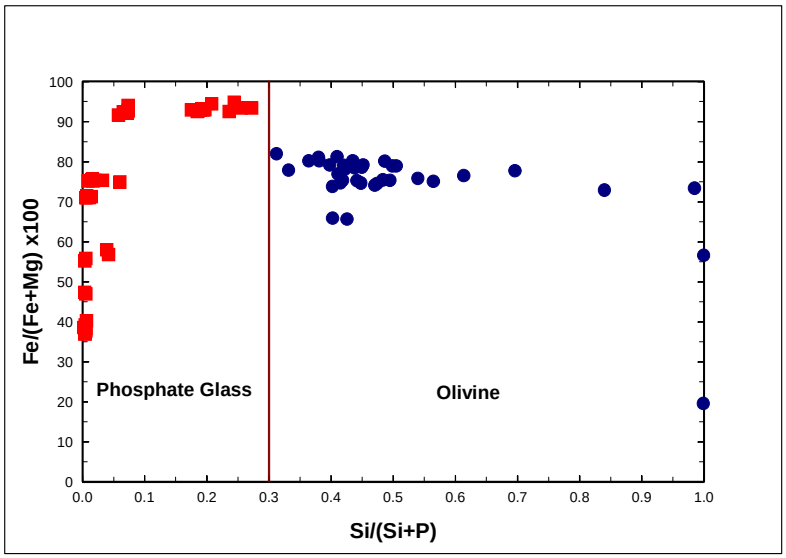

Figure 1.7d.

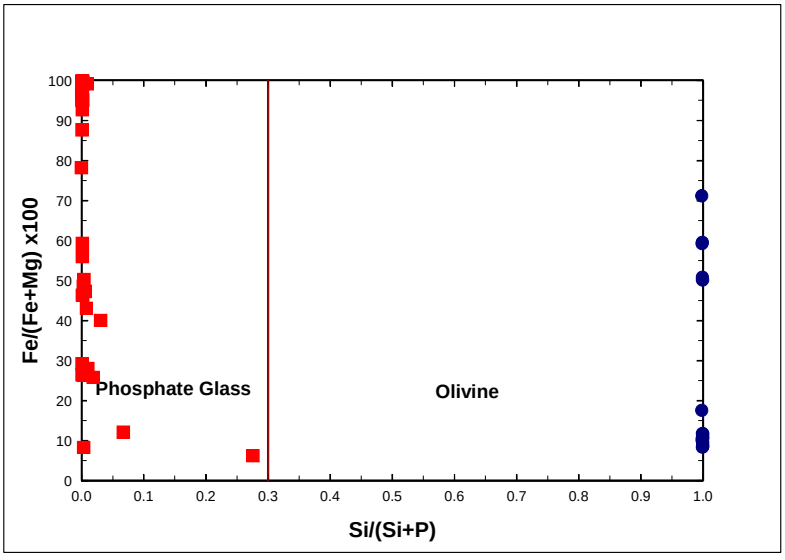

Figure 1.8.

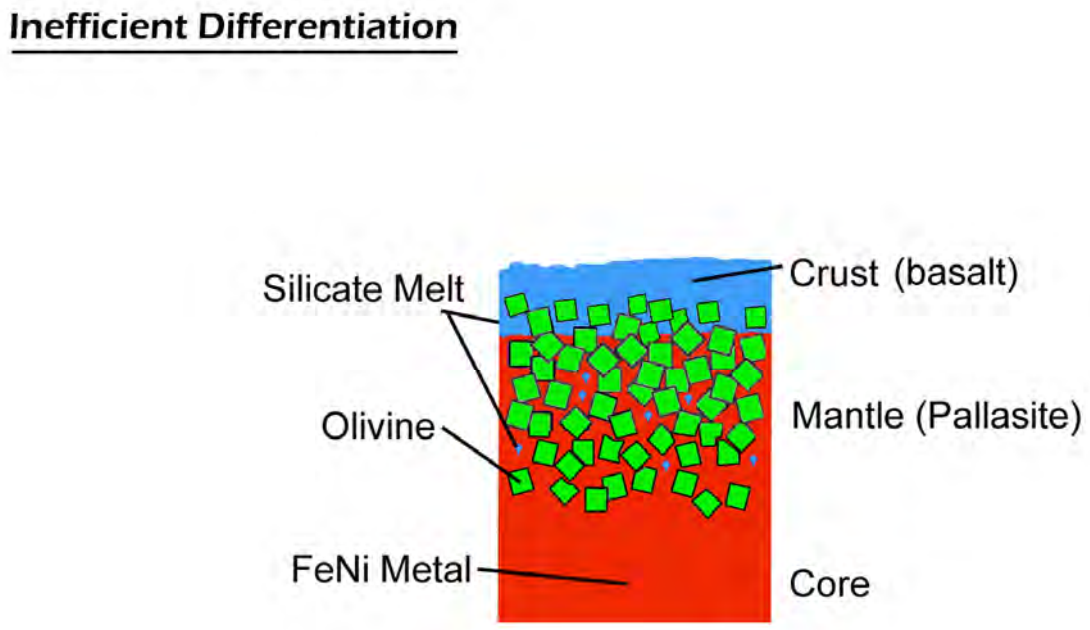

Figure 1.9

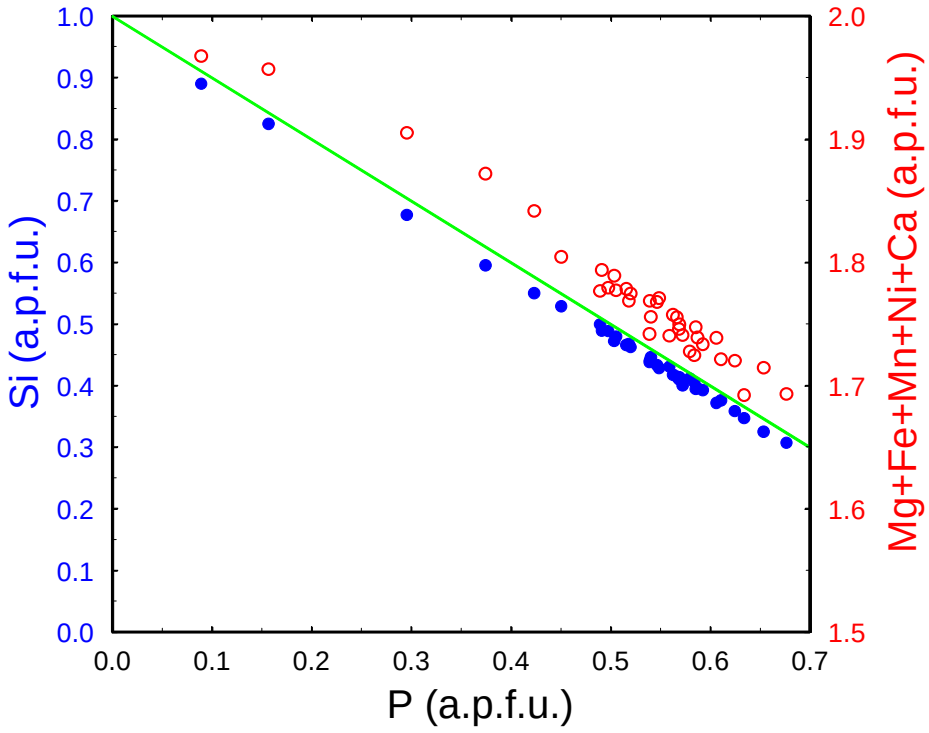

CHAPTER 2

THE VACUUM FURNACE:

CONSTRUCTION AND EXPERIMENTAL TECHNIQUES

INTRODUCTION

The experiments discussed in the following chapters involved oxygen isotopic reactions between solid, melt and gas. To minimize the contamination by the terrestrial atmosphere, the experiments were run in a specialized furnace where very low pressures of specific gas species, quantities and known isotopic compositions could be maintained. Yu et al. (2003) constructed a suitable furnace to do potassium isotopic evaporation experiments in silicate melts, and this furnace was utilized for the oxygen experiments.

Because of various problems that arose during the earliest stages of repairing and testing the furnace, the final version of the furnace differs in many details from the original (See Appendix III for the furnace construction details). The overhauled and redesigned version was dubbed by the author the "Angry Mountain" vacuum furnace (the English translation of the author's last name).

EXPERIMENTAL TECHNIQUE

The procedures for running experiments in the vacuum furnace deviate slightly from those used in a standard Deltech one atmosphere furnace. To begin, the experimental charge is placed on Pt or Re wire loops and suspended on the sample rod. The sample rod is then inserted in the quartz dome sample holder and held in position by the magnetic support system. The quartz tube and sample rod are subsequently carefully

positioned over the furnace and lowered so that the KF flanges connecting the sample holder and the furnace can be tightened, closing off the chamber to be evacuated. The experiment's initial position is well above the hotspot of the furnace in an area which experiences temperatures of no more than 200ºC. The muffle tube-quartz dome chamber is then evacuated to a pressure of ($1.3x10^{-2}$ torr) using a mechanical pump. Thereafter, a turbopump is turned on to evacuate the chamber to ~10^{-6} torr. Typically 12-16 hours were allotted for pumping to thoroughly degas the interior surfaces. During pumping, the temperature in the furnace is slowly cycled between 1000ºC and 1550ºC. Temperature cycling was utilized for two reasons. First, the cycling introduces far less structural stress on the muffle tube hotspot than having the furnace remain at very high temperatures for long time periods. Second, the cycling allowed the turbopump a more efficient method for removal of any degassing of adsorbed materials in the chamber than just constant temperature alone (lower pressure could be achieved at lower temperature). Following the pump down, the starting temperature was achieved and computer recording of the pressure began. Argon was then bled into the furnace at flowrates of ~10^{-4} liters per minute through the gas inlet for 30 minutes preceding each experiment to minimize atmospheric oxygen contamination. At the end of the 30 minutes, the argon was either adjusted to the appropriate flowrate (typically 2.3 x 10^{-4} liters per minute) to achieve the proper pressure or the argon was discontinued and a different gas was turned on (such as carbon monoxide). The new flow would then be allowed to run for 15 minutes. Finally, the experiment would be lowered into the hotspot. The experiments were typically run at pressures of 10^{-2}-10^{-3} torr (measured in a cold portion of the furnace and recalculated for conditions experienced by the sample in the hotspot). Generally the sample would

evaporate all of its volatile components within the first four minutes, during which time the pressure temporarily and proportionally would increase and then decrease. After four minutes, the pressure would return to its original setting. Run durations varied from seconds to hours. When the experiment was complete, the sample was either removed from the hotspot (when possible) or the furnace was rapidly reduced in temperature and then the sample was removed. Because of equipment limitations caused by the vacuum, drop quenching is not possible in this furnace. The combination of dropping temperature and then removing the sample was necessary for very low viscosity melts (olivine-rich), as even a slight tug on the sample rod could dislodge the melt from the sample wire. As a result of these limitations, quench products, such as melt-grown olivines, were often produced. Once the sample was removed from the hotspot, the pressure recording via computer was terminated and the vacuum pumps were turned off (first the turbo pump, then the mechanical pump). The quartz dome could then be removed from the furnace, the experiment extracted and another loaded for the following day.

Deviations from these procedures will be noted in the Experimental Procedure sections of subsequent chapters, as will specific details about compositions, gases, run durations and conditions.

REFERENCES

Yu Y., Hewins R. H., Alexander C. M. O'D. and Wang J. (2003) Experimental study of evaporation and isotopic mass fractionation of potassium in silicate melts. *Geochimica et Cosmochimica Acta* **67**, 773-786.

CHAPTER 3

EVAPORATION AND THE ABSENCE OF OXYGEN ISOTOPIC EXCHANGE BETWEEN SILICATE MELT AND CARBON MONOXIDE GAS AT NEBULAR PRESSURES

INTRODUCTION

Clayton et al. (1973, 1976) developed the hypothesis that primitive nebular solids were ^{16}O-rich and became progressively ^{16}O-poor through mixture with an ^{16}O-poor gas, particularly during chondrule formation (Some of the mixing was presumably the result of isotopic exchange reactions with oxygen-bearing gaseous species in the early solar nebula). The two major species in the early solar nebula at high temperature (~1300-1600°C) were carbon monoxide (~50-60 vol%) and water vapor (~35-50 vol%) (Ebel, 2006). Yu et al. (1995) demonstrated that when a 50 mg chondrule analog charge (composed of the carbonaceous chondrites Allende or Ornans) is melted near its liquidus and reacts an H_2 and H_2O (water vapor) (at a gas ratio of 2:1 by volume, respectively) at one atmosphere total pressure, and an oxygen fugacity of IW-0.5, about 50% of the oxygen atoms in the experimental melt exchanged with the gas within 5 minutes. They argued that at nebular pressures (~10^{-3} to 10^{-6} torr, 1 atm = 760 torr) exchange could take nearly 10 hours, depending on surface kinetics and exchange probability. This is consistent with the textural and Fe-Mg zoning experiments of Jones and Lofgren (1993) and Weinbruch et al. (1998), which suggest that chondrule formation occurred over a time period of hours to days rather than minutes to hours. The main aim of this project is to determine the extent to which carbon monoxide alone exchanges with the melt and to test whether long exchange durations may be required for chondrule formation. An initial

expectation, based purely on the masses of CO and H_2O and simple kinetic constraints, CO should have an effect less than that of water vapor.

Additional reactions have also been experienced by chondrules (to varying degrees) during their formation, including evaporation. High temperatures (>1200°C) have been shown to rapidly vaporize several elements, particularly sodium and potassium, (Humuyan and Clayton, 1995; Yu and Hewins, 1998; Alexander et al., 2000; Yu et al., 2003; Alexander and Grossman, 2005) and nebular pressures only make these rates more pronounced. Minor evaporation of elements, such as iron (Alexander and Wang 2001, Zhu et al., 2001; Mullane et al., 2003a, 2003b; Kehm et al., 2003), magnesium (Hashimoto, 1990; Galy et al., 2000; Nguyen et al., 2000; Young et al., 2002) and silicon (Clayton et al., 1991) also occur in chondrules. However, because of equipment limitations, the conditions and rates at which these elements evaporate have been precisely measured in only a few laboratories to date (Davis et al., 1990; Hashimoto, 1990; Tsuchiyama, 1999; Wang et al., 2001; Cohen et al., 2004; Ozawa and Nagahara, 2005). Evaporation rates will be determined for these experiments (where possible) and first order comparisons made with chondrules to try to further constrain some part of their formational history.

EXPERIMENTAL PROCEDURE

The oxygen isotopic exchange experiments were run in the “Angry Mountain” vacuum furnace at the Department of Geological Sciences in Rutgers University. The experimental starting composition is a IIAB chondrule composition (liquidus 1504°C)

(Table 3.1, Starting Comp.) that was composed from ten oxides and carbonates and ground to a fine powder (<50 microns).

At 1515°C, the initial 40 mg IIAB experiments were run for durations of 4 to 128 minutes on platinum and rhenium wires. A gas flow of argon ($3x10^{-4}$ liters per minute) was introduced into the furnace for 30 minutes preceding the experiment to minimize the amount of terrestrial atmospheric contamination. After the 30 minutes expired, the argon was shut off and isotopically labeled CO gas was turned on at a rate of 2.3×10^{-4} liters per minute for 15 minutes. [The calculated composition of the CO gas was $\delta^{18}O \sim -995$, $\delta^{17}O \sim -27$. Isotec, the manufacturer of the gas, did not have an exact composition of all three oxygen isotopes. They could only report that the composition was >99.96% for ^{16}O and $^{17}O >> ^{18}O$. The final $\delta^{18}O$ and $\delta^{17}O$ values were calculated assuming $^{16}O = 99.96\%$, $^{17}O = 0.039\%$ and $^{18}O = 0.001\%$]. This rate maintains a constant pressure at the hotspot of $3x10^{-3}$ torr ($4x10^{-6}$ atmospheres). After 15 minutes, the recording of the experiment began, the CO gas was maintained and the experimental charge lowered into the hotspot. Following the experimental duration, the furnace temperature was lowered from 1515°C to 1425°C at a rate of 60°C per minute to cool the charge. (There is no detectable effect on pressure during this decrease in temperature. The detection limit of the gauge in the 10^{-3} torr range is about $+/-1 \times 10^{-4}$ torr). If the temperature were not lowered, the low viscosity charge would easily drop off the sample wire while being moved out of the hotspot. It is therefore necessary to allow the charge to cool ~80°C, whereby it maintains its shape and position on the wire.

It is important to recognize that all experiments run in this furnace are in an open system, since a constant low pressure and gas flow are maintained. Therefore,

equilibrium conditions are only rarely attained and effects, such as evaporation, are exaggerated.

The oxygen fugacity of the hotspot in the furnace at a temperature of 1515ºC can only be estimated based on the results of the experiments and several calculations and considerations. First, the pressure in the furnace (as measured at the gauge and at a temperature of 50ºC) preceding the start of experiment and without flowing gas was $2x10^{-5}$ torr or $2.6x10^{-8}$ atmospheres. Adjustment for a temperature of 1515ºC at the hotspot yields a pressure of $(2.6x10^{-8})(1515) / 50 = 7.878 \times 10^{-7}$ atmospheres. As oxygen in the atmosphere is 21%, 1.654×10^{-7} atmospheres oxygen exist in the furnace [$(7.878 \times 10^{-7}$ atmospheres)(0.21)]. The vacuum within the furnace was then increased to $1x10^{-4}$ torr (or 1.315×10^{-7} atmospheres) with the addition of argon (also measured at 50ºC). Adjusting for the hotspot temperature of 1515ºC makes the pressure 3.98×10^{-6} atmospheres. Thus, the amount of argon in the furnace is the difference between the final and starting pressures (3.98×10^{-6} atmospheres - 7.878×10^{-7} atmospheres) or 3.19×10^{-6} atmospheres argon.

The percentage of oxygen in the furnace when argon is added is [1.654×10^{-7} atmospheres oxygen / (1.654×10^{-7} atmospheres oxygen + $3.19 x10^{-6}$ atmospheres argon) = 0.049] or 4.9% atmospheres oxygen (assuming the argon gas is pure). To determine the amount of oxygen present while the argon is ON and flowing into the furnace we multiply $0.049 \times 1.654 x10^{-7} = 8.1 \times 10^{-9}$ atmospheres oxygen. The log $f(O_2)$ value is therefore:

$$\log 8.1 \times 10^{-9} = -8.09 \text{ log units}$$

Calculating the iron-wüstite (IW) buffer at a temperature of 1515ºC for comparison and based on the equations from Nafziger et al. (1971) yields:

$$\log f(O_2) = -27215 / (273.15 + 1515) + 6.57$$

$$\log f(O_2) = -8.65 \text{ log units} = \text{IW buffer at } 1515ºC$$

Thus, the furnace with argon flowing has an $f(O_2)$ relative to the IW buffer of -8.09 - (-8.65) = IW+0.56. However, since carbon monoxide replaces argon before the start of the experiments, and at the same pressure (3.19×10^{-6} atmospheres CO); AND carbon monoxide will react with some of the available O_2 in the furnace [$CO + 1/2\ O_2 = CO_2$], the final oxygen fugacity value must be lower than IW+0.56, depending on the efficiency of this reaction.

Assuming the reaction converts all of the oxygen (8.1×10^{-9} atmospheres) to CO_2, thus making a $CO\text{-}CO_2$ equivalent buffering system, and the tables for one atmosphere $CO\text{-}CO_2$ oxygen fugacity controls (Deines et al., 1974) are realistic at these pressures (this is quite doubtful), the lowest possible $f(O_2)$ would be -12.1 log units or IW-3.45. However, the experiments do not reflect this rather extremely low oxygen fugacity, based on only the moderate loss of FeO and Cr_2O_3. A more reasonable estimate would seem to indicate the experiments experienced a fugacity of about IW-0.5 ± 0.5. There is a good chance that the charges are in fact self-buffered, as the system is not in equilibrium. It is likely the charges simply lose oxygen to the vacuum over time.

Note that the oxygen fugacity in the furnace increases drastically at the beginning of each experiment, because of the initial vaporization of the volatile carbonate-rich components, but decreases with time. Fugacity stabilizes after about 6-8 minutes when all

volatiles (and alkalis) have been removed, and the pre-experiment pressure is re-establishment. A subsequent decrease in the $f(O_2)$ likely continues by stripping of oxygen directly from the experimental charge.

EXPERIMENTAL ANALYSIS

Microprobe Analysis

Following each experimental run, the glass charges were removed from their rhenium or platinum wires and placed in temporary mounts. The samples were cut in half, polished, and their bulk compositions analyzed by electron microprobe. Analyses used a Cameca SX-100 electron microprobe located in the Department of Earth and Planetary Sciences at the American Museum of Natural History. Qualitative analysis was performed using backscatter electron imaging and energy dispersive analysis (EDS). Quantitative analysis was performed using wavelength dispersive analysis (WDS). Ten elements (Si, Ti, Al, Cr, Fe, Mn, Mg, Ca, Na and K) were analyzed. An accelerating voltage of 15 kV and a beam current of 10nA were employed with 40 second counting times for all elements. A diffuse 15 micron spot size beam was used. Data correction on all analyses was carried out using the PAP procedure (Pouchou and Pichoir, 1991). Both natural and synthetic minerals were used as standards (Appendix I). The charges were composed of glass with occasional interspersed olivine quench crystals. Between 70 and 100 systematic, equally-spaced analyses were performed across both halves of the experimental charge and averaged to determine a bulk composition of each experiment.

Laser Fluorination Oxygen Isotopic Analysis

Following microprobe analysis, the experimental charges were removed from their temporary mounts, cleaned of any remaining residue and sent to Ed Young and Karen Ziegler at the Sciences Stable Isotope Laboratory in the Department of Earth and Space Sciences at University of California, Los Angeles. The bulk glass samples were analyzed using a 25 watt CO_2 laser that heats the sample in an atmosphere of 40 mbar of purified F_2. The oxygen extracted by laser-fluorination is purified by freezing to a 13X molecular sieve at -190ºC followed by elution of the O_2 from the first sieve at -130ºC to a second five angstrom molecular sieve at -190ºC. In this procedure trace amounts of NF_3 are retained on the first sieve, permitting separation of O_2 and NF_3 and ensuring that the analyte O_2 is free from interferences that compromise the accuracy of $\Delta^{17}O$ measurements (NF^+ is an isobar for $^{33}O_2$ on the gas-source mass spectrometer). Measurements of the isotope ratios are made on a Finnigan DeltaPlus mass spectrometer. The oxygen isotope ratios are calibrated against the isotopic composition of air O_2 and San Carlos olivine. Tropospheric oxygen yielded $\delta^{18}O$ and $\delta^{17}O$ values of 23.51 +/– 0.01‰ and 11.97 +/– 0.03‰ respectively (the negative $\Delta^{17}O$ of tropospheric air relative to rocks is well known). A typical analysis of San Carlos olivine in their lab gives $\delta^{18}O$ = 5.32 +/– 0.01‰ and $\delta^{17}O$ = 2.75 +/– 0.04‰. The UCLA laboratory verified the accuracy and precision for samples by comparing results from various pallasite meteorite samples from the UCLA collection with results published previously by R. N. Clayton and colleagues at the University of Chicago, and obtained by bulk chemical analytical methods. These results include: the Brenham pallasite for which they obtained $\delta^{18}O$ = 3.12 +/– 0.06‰ and $\delta^{17}O$ = 1.37 +/– 0.05‰ compared with 3.18 and 1.33‰,

respectively, reported by Clayton and Mayeda (1996); the Giroux pallasite for which they obtained $\delta^{18}O$ = 3.02 +/– 0.01‰ and $\delta^{17}O$ = 1.27 +/– 0.04‰ compared with values of 3.13 and 1.33 reported by Clayton and Mayeda (1996).

RESULTS

All experimental products consisted of both glass and fine-grained olivine quench crystals. Bulk compositions were determined by microprobe analysis (Table 3.1). There were three types of experimental results produced: 1) those that were run on rhenium wire and remained as spherical charges (Exp 537, 538, 539, 541 and 545), 2) those that were run on platinum wire (534 and 536), and 3) those charges that did not behave as predicted and migrated along the wire to form flattened disks (pancakes) (533, 535 and 540).

Runs on rhenium wire show the progressive depletion of approximately 6 wt% FeO and 0.4 wt% Cr_2O_3 over a time period of 4 to 128 minutes. The FeO loss appears to follow a simple linear loss rate of 0.05 wt% FeO per minute, while Cr_2O_3 obeys a power law ($y = x^{-0.7}$) for evaporation (Fig. 3.1). The evaporation of carbonates in the first 4-8 minutes of the experiments will massively oxidize the system and perhaps stabilizes $Cr^{6+}(CrO_3)$, which is volatile at these temperatures (Graham and Davis, 1971). The FeO loss rate of 0.05 wt% per minute however, is probably somewhat deceiving as it will likely decrease once the system begins to reach a steady state condition within the furnace environment. A power curve probably better represents the FeO loss over much longer periods of time as evaporation is not a linear process, but rather an asymptotic one. The pancake runs show more drastic FeO and Cr_2O_3 depletions than their rhenium wire

counterparts, as do the platinum wire runs. None of the glasses from any experiments contained globular or interspersed Fe-metal. There is however Fe-metal present at low levels (0.1-0.25 wt% Fe) within the platinum wire of run #534. In run #536 (8 minute, platinum wire) the FeO concentrations in the sample may have been slightly out of position in the furnace and did not reach peak temperature with the result that FeO variations are not consistent with other charges.

There is complete loss of Na and K by volatilization within all of the experiments. Based on pressure gauge measurements (Fig. 3.2), Na and K are completely lost within the first 4 to 8 minutes. By the time 8 minutes have passed, the pressure has returned to the initial starting pressure of the experiment.

The oxygen isotopic results were unexpected (Table 3.2). Despite having a labeled CO gas of extreme composition reacting with the melt, no apparent oxygen isotopic exchange was measured. The initial starting test glass compositions plot on the terrestrial fractionation (TF) line at a $\delta^{18}O \sim 12$, while the endmember CO gas plots towards an extremely negative $\delta^{18}O$ value (-995), but only a slightly negative $\delta^{17}O$ value (-27). The experiments would therefore move to the left of their starting compositions, in the direction of the reacting gas, in the case of exchange (Fig. 3.3). However, the rhenium wire experiments have $\delta^{18}O$ values between 14 and 16, plot on a line with a slightly shallower slope than the TF, and show a correlation towards progressively heavier isotopic compositions with duration.

The three pancake experiments plot on essentially the same line as the rhenium wire-glass sphere experiments but show more extreme fractionations compared to their durations (Fig. 3.4). Similar results are seen in the platinum wire experiments, where the

4 and 8 minute duration runs fall in the same range as the 16 to 32 minute duration runs of the rhenium wire glass-sphere run (Fig. 3.5).

DISCUSSION

The experiments conducted yielded unexpected yet interesting results. Bulk isotopic exchange between the CO gas and melt at high temperature was expected, but no exchange with the gas occurred. Small isotopic mass fractionations consistent with evaporation are clearly seen (Fig. 3.3).

Absence of Oxygen Isotopic Exchange

The experiments conducted here are unique in that only labeled carbon monoxide (enriched $C^{16}O$) was used. The reaction with an olivine-normative silicate melt (similar to a Type IIAB chondrule) was expected to demonstrate unambiguous gas-solid exchange. Exchange experiments have been conducted using only CO_2 reacting with a basaltic melt (Canil and Meuhlenbachs, 1990; Wendlandt, 1991). There is a distinct lack of previous exchange experiments involving only CO with either melts or solids.

The lack of oxygen isotopic exchange between silicate melt and CO gas may be consistent with the idea of Yu et al. (1995) that long durations (>10 hours) are required for oxygen isotopic exchange at nebular pressures, but seems to indicate that even substantially longer times (days to weeks) or much higher pressures may be needed if carbon monoxide is the major gaseous oxygen-bearing species in the exchange reaction (though this idea now seems unlikely). This of course assumes that non-mass dependent

photochemical reactions with the CO gas prior to reaction with the silicate melt surfaces are not involved in the exchange (Thiemens and Heidenreich, 1983).

Comparison of these experiments with Yu et al. (1995) suggest the possibility that the sole controlling factor of oxygen isotopic exchange within the solar nebula gas may be the proportion of water vapor it contains (or water vapor produced by reaction between CO and H_2 gas). Water contains weaker bonds than carbon monoxide. Any carbon monoxide that is present may only react in the first step of a two step reaction (See below). In the first step, water and CO exchange. In the second step, the reacted water and silicate melt (SiO_2 written as $Si^{16}O^{16}O$) exchange.

1) $H_2{}^{16}O + C^{18}O \rightarrow H_2{}^{18}O + C^{16}O$

2) $H_2{}^{18}O + Si^{16}O^{16}O \rightarrow H_2{}^{18}O + Si^{18}O^{16}O$

or

$$H_2{}^{18}O + Mg^{16}O \rightarrow H_2{}^{18}O + Mg^{18}O$$

Therefore, water vapor would be a rate limiting component facilitating the exchange with the carbon monoxide that would otherwise be acting as an inert, yet diluting, gas.

Water vapor dissociates much more rapidly than carbon monoxide at temperatures above 600℃ (Moore, 1993). Thus, despite carbon monoxide representing 50-60 vol% of the oxygen-bearing gaseous species in the nebula, water vapor that is present at 35-50 vol% (Ebel, 2006) would likely react with a substantially larger proportion of nebular components (i.e. chondrules and CAIs). An interesting set of experiments that should perhaps be run in the future are low pressure experiments involving labeled CO_2 + H_2 rather than labeled CO, so that a CO + H_2O environment would be produced and could be simultaneously reacted with silicate melt.

Elemental Evaporation

Sodium, potassium, iron and chromium in the starting composition all experienced evaporation during the experiments. Because potassium and sodium completely volatilized from the charges, no data can be obtained concerning their rates of evaporation. Their evaporation is so fast, all that is known is that it coincides with the volatilization of the carbonate components from several of the starting ingredients (Na_2CO_3 and K_2CO_3). Thus no useful conclusions can be drawn.

However, the progressive evaporation of iron and chromium can allow some conclusions to be extracted. Chondrules in general display a wide range of bulk compositions and there is still no consensus on whether the chemical variations are inherited from precursor materials or generated as a result of chondrule formation itself. Type I chondrules have bulk depletions relative to CI chondrites of Fe, Cr, Mn, Na and K, while having corresponding enrichments of Ca, Al, Ti and Mg. These variations suggest that element volatility is the controlling factor of the chondrule bulk composition (Larimer and Anders, 1967; Davis et al., 2005) and could be consistent with some loss by evaporation. In these experiments, approximately 25% of the bulk iron has evaporated. In chondrules however, the depletions are probably greater (~40%) ASSUMING all chondrules had a chondritic starting composition and the depletions seen are the result of the chondrule-forming process The problem however is that evaporation is usually accompanied by isotopic mass dependent fractionation. Evaporation enriches the heavy isotopes in the residue in a process known as Rayleigh fractionation. However, if a process such as slow diffusion occurs mass loss and elemental fractionation can occur and no isotopic effects may be seen (Lauretta et al., 2006). Further, it has been

demonstrated that high ambient gas pressures or high dust/gas ratios during evaporation can suppress isotopic fractionation and/or the evaporation rates (Richter et al., 2002). In chondrules, there is evidence of isotopic fractionation. Kong et al. (1999) and Humayun et al. (2002) both found evidence for evaporative loss of iron in CR2 chondrules in the meteorite Renazzo, while Alexander (1995) found indications of evaporation and recondensation of iron in chondrules of the ordinary chondrites Semarkona, Bishunpur, Chainpur and Krymka. However, isotopic analysis so far shows that the fractionations are small. Chainpur chondrules have ~0.2‰ mass fractionations (Alexander and Wang, 2001; Zhu et al., 2001; Mullane et al. 2003b), Tieschitz (H3.4) chondrules have 0.15‰ fractionations (Kehm et al, 2003). The Allende (CV3) chondrules have the largest iron isotopic fractionations so far and even they are still quite small at 0.6 and 1.1‰ (Zhu et al., 2001; Mullane et al. 2003b). Similar degrees of evaporation can also be seen in Mg, Si and K [see Davis et al. (2005) and Lauretta et al. (2006) for recent excellent summaries and lists of extensive references].

While isotopic measurements have been made on iron, no isotopic measurements have yet been made to indicate the evaporation of Cr in chondrules. Chromium is more volatile and more easily reduced than iron, but is its depletion in chondrule bulk compositions is negligible. Therefore it is doubtful chromium will show any substantial isotopic fractionation. Chromium does differ from iron in an important way however, that may yield informative results in the future. When Fe-metal or FeO evaporate, the iron gaseous species evaporating is the same species as that found in the solid or melt [i.e., Fe-metal (melt) evaporates and becomes Fe-metal (vapor)]. However, when chromium evaporates, the solid or liquid species evaporating is not necessarily the same as the one

that is coming off in gaseous form. Therefore, depending on the oxygen fugacity, the solid could be Cr_2O_3, while the gaseous species could be predominantly CrO_3 or Cr metal. Which form dominates in the gaseous state is dependent on the ambient oxygen fugacity (Graham and Davis, 1971). The $P(O_2)$ crossover point where the evaporating species changes from CrO_3 to Cr metal is ~ 10^{-12} atmospheres [Example: Cr_2O_3 at an $f(O_2)$ ~ 10^{-10} atmospheres evaporates predominantly as CrO_3, and minorly as Cr metal, but at 10^{-14} atmospheres it evaporates predominantly as Cr metal with minor CrO_3]. The lack of extensive Cr depletion in chondrules (even in Type I chondrules where there is a larger Cr depletion than Type II chondrules, the amount is only about 10-15% relative to CI abundances) argues for much higher nebular pressures.

The absence of substantial systematic isotopic fractionations in chondrules implies that chondrules were melted either in open systems (Sears et al., 1996) and the evaporation occurred in such a manner that elemental fractionation did not effect isotopic fractionation (Galy et al 2000) (i.e. Rayleigh fractionation did not occur) or that chondrules formed in a closed system environment and inherited their volatile-depleted compositions from precursor materials (Grossman and Wasson, 1983).

Oxygen Isotopic Evaporation

Along with the elements Fe and Cr, there is also a distinct shift in the oxygen isotopic compositions of the experiments with time. Evaporative isotopic fractionation is a mass dependent fractionation reaction that is unidirectional and kinetically driven. The mass-dependent fractionation laws that describe the partitioning of isotopes (in this case, ^{16}O, ^{17}O and ^{18}O) are different for kinetic and equilibrium reactions (Young et al., 2002).

For the general case, isotopic mass fractionation laws can be written $(\alpha_{2/1}) = (\alpha_{3/1})^{\beta}$, where α is the fractionation factor for the element of interest; subscripts 1, 2, and 3 are the three isotopes; and β the exponent. For oxygen, the equation would be: $(\alpha_{17/16}) = (\alpha_{18/16})^{\beta}$. For the general equilibrium reaction, the exponent $\beta = (1/m_1 - 1/m_2) / (1/m_1 - 1/m_3)$ where m_i = isotopic masses, and $m_1<m_2<m_3$. Thus for oxygen: $m_1 = m(^{16}O)$, $m_2 = m(^{17}O)$ and $m_3 = m(^{18}O)$. Inserting the isotopic masses for the three oxygen isotopes and solving the equation shows that for an equilibrium reaction involving oxygen, $\beta = 0.528$. This differs from the kinetic reactions, like evaporation, where the exponent $\beta = \ln (M_1/M_2) / \ln (M_1/M_3)$ (Young et al., 2002). The major difference between the two processes is that during equilibrium all that is needed to describe the mass-dependent fractionation is the isotopic masses of the element of interest. However, in kinetic mass-dependent fractionation, the masses of isotopic species and their motions are necessary. To describe the motions, the masses of the molecules to which the isotopes are bonded AND the frequencies of vibration involving those isotopes are also needed. Thus, the change in the notation from “m” to “M” in the equations. “M” is similar to “m” in that it can represent the atomic masses of the isotopes, however it also can represent reduced or molecular masses. Reduced masses are used in situations where bonds are being broken (i.e. evaporation), while molecular or atomic masses are used for transport processes. Because of this change in the “masses” (i.e. atomic to reduced), the kinetic reaction value varies depending on the circumstances. Generally, the kinetic value for β is less than the equilibrium value. In these experiments, we can estimate the ideal value of β based on the molecular masses of the species of the dominant gas in the furnace, namely carbon

monoxide: $M_1 = M(^{12}C^{16}O) = 28$, $M_2 = M(^{12}C^{17}O) = 29$, $M_3 = M(^{12}C^{18}O) = 30$. Inserting these masses into the kinetic reaction equation gives $\beta = 0.508$. It is important to realize however that this value does NOT describe the motion (frequencies of vibration) and essentially calculates the reaction as if the molecules were attached to a fixed point. It is therefore expected that there will be a deviation from this ideal value. Unfortunately, there is no means of calculating the reduced masses, simply because we don't know exactly what they are and experimentation is required to determine the exact β value(i.e. the reactants and the evaporative products are not the same). On a three-isotope oxygen plot, the β value is equal to the slope of the line drawn through the isotopic compositions of reactants. A more complete discussion of kinetic and equilibrium processes is given by Young et al. (2002).

Kinetic evaporation was first demonstrated by Davis et al. (1990) for magnesium isotopes in forsterite. The experiments run here are the first demonstration of kinetic evaporation for oxygen isotopes (Fig. 3.6) (pers. comm. Ed Young, 2006). The experiments lie on a line with a slope of 0.511, very near the estimated value of 0.508 (Fig. 3.6). The experiments rapidly evaporate within the first 8 minutes and get approximately 2.5‰ heavier in $\delta^{18}O$ or -0.15‰ in $\Delta^{17}O$. Thereafter, the rate of change as a result of evaporation appears linear in $\Delta^{17}O$ and continues at an average of -0.0017‰ per minute [within the conditions of 1515ºC, $3x10^{-3}$ torr, a predominantly CO atmosphere and an oxygen fugacity of ~IW-0.5 and for a duration of up to two hours]. This rate also correlates linearly with both duration and *mg#* (Fig. 3.7A and 3.7B) and suggests that iron loss (as well as other evaporation or redox reactions) may influence the oxygen isotopic composition in chondrules if all other factors remained constant.

It would appear that evaporation during chondrule formation must have been a negligible effect for the following reason. Peak heating temperatures for chondrules are estimated to be between 1550ºC and 1900ºC (Hewins and Connolly, 1996), well above the temperatures achieved here. Chondrule cooling rates are estimated to be between 5ºC and 100ºC per hour (Jones and Lofgren, 1993; Weinbruch et al., 1998). The chondrule precursors (and subsequently the chondrules themselves) would have therefore been exposed to the nebular environment for at least several hours to several days during the chondrule-forming event. Yet, there is a complete lack of isotopic evidence in chondrules for substantial effects in Fe, Mg, Si and K, and oxygen shows little deviation from the 0.528 slope line on a three-isotope plot. The simplest explanation looks to be that the region of chondrule formation must lie towards the upper limits of estimated pressures (1.8×10^{-3} to 2×10^{-6} atmospheres) (Cuzzi and Weidenschilling, 2006) or that subsequent recondensation occurred to mask any substantial evidence the evaporation process may have left (Davis et al., 2005).

Effects of Wire Composition and Charge Shape

Two interesting secondary conditions of the experiments that magnified the effects of evaporation and oxygen isotopic fractionation were 1) experiments in which platinum wire was used instead of rhenium and 2) experiments that did not remain as spheres, but flattened into disks. The platinum wire acted to enhance the reduction process and remove a greater proportion of iron from the silicate melt than the rhenium wire experiments over the same amount of time. The iron appears to have alloyed with the platinum, preventing some of its evaporation (there were small but measurable

amounts of iron in the platinum wire), but there was a definite increase in the $\delta^{18}O$ and $\delta^{17}O$ oxygen isotopic composition of the experiments compared to those run on rhenium wire. Loss of Fe to the wire, of necessity, liberates oxygen from the charge. Since the Fe was added as an oxide, and iron oxides typically are ^{16}O-rich (based on oxygen isotope fractionation factors) (Chacko et al., 2001) it seems plausible, that the oxygen liberated was also ^{16}O-rich, leaving behind a heavier isotopic composition in the melt.

The other evaporation phenomena seen in the experiments was the effect that shape (probably surface area to volume ratio, however there is essentially no difference in volume between experiments) had on the oxygen isotopic composition and the extent of iron loss evaporation. Both were more extreme in the experiments where the charges formed flattened disks (pancakes). Simple measurements of the charges show that the quenched pancakes have radii of 2.8 to 3.2 millimeters and are much less than one millimeter in thickness. The quenched spheres have radii of 1.6 to 1.9 millimeters. Doing simple surface area calculations for disks (area=$2\pi r^2$) [although in reality, disks are truly thin cylinders, the charges were so thin the height dimension is negligible] and spheres (area=$4\pi r^2$) quickly shows the spheres have areas of 32 to 44 sq. mm, while the pancakes have areas of 49 to 64 sq. mm. The pancakes have roughly a 1/3 larger surface area. The effect of surface area and volume on the oxygen isotopic composition has been seen before in chondrules from Dhajala (H3.8) by Clayton et al. (1991), where small chondrules were found to be isotopically heavier than larger ones. This appears to make sense, though assumes all other factors must remain equal. Based on the literature, pure surface area effects in chondrules are rare.

Possible exchange?

Despite the absence of evidence that exchange between melt and CO gas occurred, the data seem to hint there *might* have been minor exchange. The experiments plot below the TF line on a line having a 0.511 slope (Fig. 3.8). If the experiments and the initial starting glasses underwent ONLY evaporation, the starting glasses should lie on the same 0.511 slope line as the experiments. They do not. Using the experiments to trace backwards to what should be the starting $\delta^{18}O$ composition (where the slope 0.511 line intersects the TF), we arrive at a $\delta^{18}O$ value of ~ 4. However, the real value of the starting glasses is $\delta^{18}O \sim 12$. To account for this discrepancy, some exchange reaction must have occurred. However, what components exchanged? The starting glasses do not appear to be contaminated. They differ from the experimental product glasses in that they were never in a low pressure environment, but produced in a one atmosphere furnace in air. There is nothing apparent in the one atmosphere furnace that could have altered both starting glasses (there were two separate glass beads made) to the same degree. One possible solution is that the labeled CO gas has a $\delta^{17}O$ composition substantially lower than -27. The gas composition was never analyzed, as the UCLA lab (Ed Young) could not obtain a proper gas standard to run against it and Isotec (the company where the gas was purchased) could only report the purity of the ^{16}O component of the gas as greater than 99.96 and the ^{18}O component very near zero. The calculated CO composition is based on the assumption that $^{16}O = 99.96$, $^{17}O = 0.039$, $^{18}O = 0.001$. If however, the gas composition was such that the $\delta^{17}O$ value fell below the TF line and intersected the 0.511 evaporation slope, it would be possible that minor exchange (perhaps 2‰), combined with the evaporation could explain the results (blue arrow in Fig. 3.8). A second

possibility is that there was a progressive change in the evaporation slope. This would be possible if the products being evaporated changed with time. This idea seems plausible as the experimental charge initially volatilizes dominantly sodium and potassium, then as the oxygen fugacity decreases begins to evaporate dominantly chromium and iron. With the products changing, the reduced masses (the species evaporating and their frequencies of vibration) would progressively change. Finally, interactions with the mullite muffle tube may also be occurring. Mullite is mostly alumina plus minor amounts of silica and CaO. A possibility is that the mullite is evaporating independently of the experimental charge, and is subsequently mixing with it somehow. An unaltered portion of the muffle tube was analyzed and determined to have a terrestrial composition of $\delta^{18}O \sim 18$. If mullite evaporates, its composition gets heavier in both $\delta^{17}O$ and $\delta^{18}O$. Its $\delta^{18}O$ composition would likely be ~25 and its $\delta^{17}O$ would drop below the TF line just like the experiment. Estimating the slope of evaporating alumina gives a β~0.502. It is known that mullite turns to a fine powder when heated for long durations at very high temperature (1500ºC+). It is conceivable that small amounts of mullite dust could become dislodged from the muffle tube and redeposited on the experimental charge. The charge and mullite could then mix oxygen isotopic compositions. The mixing MAY reduce the $\delta^{17}O$ of the experimental glasses sufficiently to move them off an obvious regression line linking them to the starting glasses. A future in-depth investigation of this phenomenon will be required to determine the final cause.

CONCLUSIONS

1) The apparent lack of oxygen isotopic exchange between melt and gas appears to be consistent with the idea of Yu et al. (1995) that long durations are required for exchange at nebular pressures. However, these results indicate that days to weeks are required for exchange rather than the just the suggested “greater than 10 hours”. Perhaps much higher pressures are necessary as well.

2) Oxygen isotopic exchange may be controlled by the proportion of CO to H_2O within the nebula. H_2O dissociates more rapidly than CO above 600°C and contributes a substantially larger proportion of O_2 or O^{-2} to the nebular environment.

3) Reactions involving (only) carbon monoxide at low pressure are likely NOT to be the chief oxygen exchange mechanism in the early solar system, if CO photodissociation is not a dominant process.

4) There is a possibility that minor exchange between melt and CO gas DID occur. Measurement of the CO gas composition and additional experiments are necessary to verify this.

5) The elemental and isotopic evaporation effects seen in the experiments are not seen to the same degree in chondrules, yet the conditions in the experiments are relatively mild compared to some estimates of the solar nebula. Therefore, chondrules could not have formed in a very low pressure nebula, but must have formed in nebular environments that contained higher gas pressures or in areas where recondensation minimized any significant evaporation reactions.

REFERENCES

Alexander C. M. O'D., Grossman J. N., Wang J., Zanda B., Bourot-Denise M., and Hewins R. H. (2000) The lack of potassium-isotopic fractionation in Bishunpur chondrules. *Meteoritics and Planetary Science* **35**, 859-868 .

Alexander C. M. O'D. (1995) Trace element contents of chondrule rims and interchondrule matrix in ordinary chondrites. *Geochimica et Cosmochimica Acta* **59**, 3247-3266.

Alexander C. M. O'D. and Grossman J. N. (2005) Alkali elemental and potassium isotopic compositions of Semarkona chondrules. *Meteoritics and Planetary Science* **40,** 541-556.

Alexander C. M. O'D. and Wang J. (2001) Iron isotopes in chondrules: Implications for the role of evaporation during chondrule formation. *Meteoritics and Planetary Science* **36**, 419-428.

Canil D. and Muehlenbachs K.(1990) Oxygen diffusion in a Fe-rich basalt melt. *Geochimica et Cosmochimica Acta* **54**, 2947-2951.

Chacko T., Cole D. R. and Horita J. (2001) Equilibrium oxygen, hydrogen and carbon isotope fractionation factors applicable to geologic systems. In *Stable Isotope Geochemistry* (J. W. Valley and D. R. Cole, eds.) pp. 1-81. Reviews in Mineralogy and Geochemistry **43**, Washington D.C.

Clayton R. N., Grossman L., and Mayeda T. K. (1973) A component of primitive nuclear composition in carbonaceous meteorites. *Science* **182**, 485-488.

Clayton R. N. and Mayeda T. K. (1996) Oxygen isotope studies of achondrites. *Geochimica et Cosmochimica Acta* **60**, 1999-2017.

Clayton R. N., Mayeda T. K., Goswami J. N. and Olsen E. J. (1991) Oxygen isotope studies of ordinary chondrites. *Geochimica et Cosmochimica Acta* **55**, 2317-2337.

Clayton R. N., Onuma N., and Mayeda T. K. (1976) A classification of meteorites based on oxygen. isotopes. *Earth and Planetary Science Letters* **30**, 10-18.

Cohen B. A. and Hewins R. H. (2004) An experimental study of the formation of metallic iron in chondrules. *Geochimica et Cosmochimica Acta* **68**, 1677-1689.

Cuzzi J. N. and Weideschilling S. J. (2006) Particle-gas dynamics and primary accretion. In *Meteorites and the Early Solar System II* (ed. D. S. Lauretta et al.) pp. 353-382. University of Arizona Press, Tucson.

Davis A. M., Alexander C. M. O'D., Nagahara H. and Richter F. M. (2005) Evaporation and condensation during CAI and chondrule formation. In *Chondrites and the Protoplanetary Disk* (A. N. Krot et al. eds.) pp. 432-455. Astronomical Society of the Pacific, Volume **341**, San Francisco.

Davis A. M., Hashimoto A., Clayton R. N. and Mayeda T. K. (1990) Isotope mass fractionation during evaporation of Mg_2SiO_4. *Nature* **347**, 655-658.

Deines P., Nafziger R. H., Ulmer G. C. and Woermann E. (1974) Temperature-oxygen fugacity tables for selected gas mixtures in the system C−H−O at one atmosphere total pressure *Bulletin #88 of the Earth and Mineral Sciences Experiment Station* (Pennsylvania State University), 129 pp.

Ebel, D. S. (2006) Condensation of rocky material in astrophysical environments. In *Meteorites and the Early Solar System II* (ed. D. S. Lauretta et al.) pp. 253-277. University of Arizona Press, Tucson.

Galy A., Young E. D., Ash R. D. and O'Nions R. K. (2000) The formation of chondrules at high gas pressures in the solar nebula. *Science* **290**, 1751-1753.

Graham H. C. and Davis H. H. (1971) Oxidation/Vaporization of Cr_2O_3. *Journal of the American Ceramic Society* **54**, 89-93.

Grossman J. N. and Wasson J. T. (1983) The composition of chondrules in unequilibrated chondrites: An evaluation of models for the formation of chondrules and their precursor materials. In *Chondrules and Their Origins* (E. A. King, ed.) pp. 88-121. Lunar and Planetary Institute, Houston.

Hashimoto, A. (1990) Evaporation kinetics of forsterite and implications for the early solar nebula. *Nature*, **347**, 53-55.

Hewins R. H. and Connolly H. C. Jr. (1996) Peak temperatures of flash melted chondrules. In *Chondrules and the Protoplanetary Disk* (R. H. Hewins et al., ed.) pp. 197-204. Cambridge University Press, Cambridge.

Humayun M., and Clayton R. N. (1995) Potassium isotope cosmochemistry: Genetic implications of volatile element depletion. *Geochimica et Cosmochimica Acta* **59**, 2131-2148.

Humayun M., Campbell A. J., Zanda B. and Bourot-Denise M. (2002) Formation of Renazzo chondrule metal inferred from siderophile elements *Lunar and Planetary Science* **XXXIII**, abstract #1965 (CD-ROM).

Jones R. H. and Lofgren G. E. (1993) A comparison of FeO-rich, porphyritic olivine chondrules in unequilibrated chondrites and experimental analogues. *Meteoritics* **28**, 213-221.

Kehm K., Hauri E. H., Alexander C. M. O'D. and Carlson R. W. (2003) High precision iron isotope measurements of meteoritic material by cold plasma ICP-MS. *Geochimica et Cosmochimica Acta* **67**, 2879-2891.

Kong P. Ebihara M. and Palme H. (1999) Distribution of siderophile elements in CR chondrites: Evidence for evaporation and recondensation during chondrule formation. *Geochimica et Cosmochimica Acta* **63**, 2637-2652.

Lauretta D. S., Nagahara H., Alexander C. M. O'D. (2006) Petrology and origin of ferromagnesian silicate chondrules. In *Meteorites and the Early Solar System II* (eds. D. S. Lauretta and H. Y. McSween, Jr.) pp. 431- 459. University of Arizona Press, Tucson.

Larimer J. W. and Anders E. (1967) Chemical fractionation in meteorites. II. Abundance patterns and their interpretation. *Geochimica et Cosmochimica Acta* **31**, 1239-1270.

Moore J. J. (1993) *Chemical Metallurgy*. London: Butterworths, 435 pp.

Mullane E., Russell S. S., Gounelle M. and Mason T. F. D.(2003a) Iron isotope composition of Allende and Chainpur chondrules: Effects of equilibration and thermal history. *Lunar and Planetary Science* **XXXIV**, abstract #1027 (CD-ROM).

Mullane E., Russell S. S., Gounelle M. and Mason T. F. D.(2003b) Iron isotope composition of Allende matrix, CAIs and chondrules. *Meteoritics and Planetary Science* **38**, A66.

Nafziger R. H., Ulmer G. C. and Woerman E. (1971) Gaseous buffering for control of oxygen fugacity at one atmosphere. In *Research Techniques for High Pressure and High Temperature* (G. C. Ulmer, ed.), pp. 9-41, Springer-Verlag, New York.

Nagahara H. and Ozawa K. (1996) Evaporation of forsterite in H 2 gas. *Geochimica et Cosmochimica Acta* **60**,1445-1459.

Nguyen L. -A., Alexander C. M. O D., Carlson R. W. (2000) Mg isotope variation in bulk meteorites and chondrules. *Lunar and Planetary Science* **XXXI**, abstract #1841(CD-ROM).

Ozawa K. and Nagahara H. (2005) Kinetics of diffusion-controlled evaporation of Fe-Mg olivine: experimental study and implication for stability of Fe-rich olivine in the solar nebula. *Geochimica et Cosmochimica Acta* **64**, 939-955.

Pouchou J. and Pichour F. (1991) Quantitative analysis of homogeneous or stratified microvolumes applying the model "PAP". In *Electron Probe Quantitation* (eds. K. F. J. Heinrich and D. E. Newbury), Plenum Press, New York, 31-75.

Richter F. M., Davis A. M., Ebel D. S. and Hashimoto A. (2002) Elemental and isotopic fractionation of Type B calcium-aluminum-rich inclusions: Experiments, theoretical considerations, and constraints on their thermal evolution. *Geochimica et Cosmochimica Acta* **66**, 521-540.

Sears D. W. G., Huang S. and Benoit P. H. (1996) Open-system behavior during chondrule formation. In *Chondrules and the Protoplanetary Disk* (R. H. Hewins et al, eds.) pp. 221-232, Cambridge University Press, New York.

Thiemens M. H. and Heidenreich J. E. (1983) The mass-independent fractionation of oxygen - A novel isotope effect and its possible cosmochemical implications. *Science* 219, 1073-1075.

Tsuchiyama A. (1999) Evaporation of forsterite in the primordial solar nebula; rates and accompanied isotopic fractionation. *Geochimica et Cosmochimica Acta* **63**, 2451-2466.

Tsuchiyama A., Osada Y., Nakano T. and Uesugi K. (2004) Experimental reproduction of classic barred olivine chondrules: Open-system behavior of chondrule formation. *Geochimica et Cosmochimica Acta* **68**, 653-672.

Wang J., Davis A. M., Clayton R. N., Mayeda T. K. and Hashimoto A. (2001) Chemical and isotopic fractionation during the evaporation of the FeO-MgO-SiO_2-CaO-Al_2O_3-TiO_2 rare earth element melt system. *Geochimica et Cosmochimica Acta* **65**, 479-494.

Weinbruch S., Buettner H., Holzeid, A., Rosenhauer M., and Hewins R. H. (1998) On the lower limit of chondrule cooling rates: The significance of iron loss in dynamic crystallization experiments. *Meteoritics and Planetary Science* **33**, 65-74.

Wendlandt R. W. (1991) Oxygen diffusion in basalt and andesite melts: Experimental results and discussion of chemical versus tracer diffusion. *Contributions to Mineralogy and Petrology* **108**, 463-471.

Young E. D., Galy A. and Nagahara H. (2002) Kinetic and equilibrium mass-dependent isotope fractionation laws in nature and their geochemical and cosmochemical significance. *Geochimica et Cosmochimica Acta* **66**, 1095-1104.

Yu, Y. and Hewins R. H. (1998) Transient heating and chondrule formation - evidence from Na loss in flash heating simulation experiments. *Geochimica et Cosmochimica Acta* **62**, 159-172.

Yu Y., Hewins R. H., Clayton R. N., and Mayeda T. K. (1995) Experimental study of high temperature oxygen isotope exchange during chondrule formation. *Geochimica et Cosmochimica Acta* **59**, 2095-2104.

Yu Y., Hewins R. H., Alexander C. M. O'D. and Wang J. (2003) Experimental study of evaporation and isotopic mass fractionation of potassium in silicate melts. *Geochimica et Cosmochimica Acta* **67**, 773-786.

Zhu X. K., Guo Y., O'Nions R. K., Young E. D. and Ash R. D. (2001) Isotopic homogeneity of iron in the early solar nebula. *Nature* **412**, 311-313.

FIGURE CAPTIONS

Figure 3.1. Net evaporative loss of FeO and Cr_2O_3 following each experiment shown as a function of time. FeO decreases linearly at a rate of 0.05 wt% FeO per minute, while Cr_2O_3 decreases as a power law ($y=x^{-0.7}$). Cr_2O_3 is more susceptible to the low oxygen fugacity than FeO.

Figure 3.2. The first ten minutes of run #538 (1515°C, 32 minutes, Re wire) showing the complete evaporation of sodium, potassium and carbonate components. Approximately 8 minutes into the run, the system has returned to its original pressure. Note: The stepwise-like decrease is not real, but rather a function of the incremental measuring ability of the pressure gauge and a skew of the y-axis.

Figure 3.3. Three isotope oxygen plot of the rhenium wire-glass sphere experiments showing progressive evaporation with duration.

Figure 3.4. Three isotope oxygen plot of the pancake experiments showing exaggerated effects relative to the rhenium wire-glass sphere experiments. Because of higher surface area, the pancake experiments evaporate (and fractionate) faster (and farther).

Figure 3.5. Three isotope oxygen plot of the platinum wire experiments showing exaggerated effects relative to the rhenium wire-glass sphere experiments.

Figure 3.6. Simple comparison of the exponent β factor (the slope of the line) for kinetic mass fractionation as calculated (0.508) using CO as the dominant gaseous species (and assumed reduced species) compared to the regression line placed through the actual experiments (0.511).

Figure 3.7. Experimental glasses showing evaporation correlations between $\Delta^{17}O$ and both (a) mg# of the melt and (b) duration following the initial 8 minutes. Reactions in the first 8 minutes as yet are still somewhat unexplained.

Figure 3.8. Three isotope oxygen plot of the rhenium wire-glass sphere experiments with a regression line (red line with slope 0.511) passing through them but not through the two replicate starting glasses. One possible explanation is that the CO gas (blue arrow direction) has an oxygen isotopic composition with a greater depletion in $\delta^{17}O$ than calculated (green arrow direction) allowing a minor amount of mixing. Because of mixing, the net isotopic starting composition would plot slightly below the TF line, on the regression line.

Table 3.1. Bulk compositions of starting and experimental glasses.

	SiO_2	TiO_2	Al_2O_3	Cr_2O_3	FeO	MnO	MgO	CaO	Na_2O	K_2O	Total
Starting Comp 1 atm, 5 min	50.92	0.18	0.89	0.40	21.52	0.42	22.89	1.07	1.79	0.22	100.22
Re (sphere)											
8 min	51.15	0.16	0.93	0.25	20.52	0.43	24.78	0.99	0.01	0.00	99.22
16 min	51.79	0.17	0.81	0.09	20.43	0.40	25.05	0.95	0.01	0.00	99.70
32 min	52.78	0.18	0.79	0.08	19.81	0.40	25.23	0.99	0.00	0.00	100.27
64 min	53.11	0.17	0.78	0.06	18.21	0.39	26.11	1.01	0.01	0.00	99.91
128 min	54.71	0.17	0.80	0.02	15.49	0.42	26.92	1.01	0.01	0.00	99.56
Pancake (disk)											
4 min, Pt	50.38	0.15	0.70	0.11	21.26	0.40	24.04	0.91	0.01	0.01	97.95
8 min, Pt	51.47	0.15	0.72	0.07	20.81	0.41	25.14	0.91	0.01	0.00	99.69
64 min, Re	53.28	0.16	0.84	00.0	15.26	0.37	27.38	0.99	0.00	0.00	98.30
Pt (sphere)											
4 min, Pt	51.80	0.14	0.75	0.06	19.89	0.44	24.51	0.92	0.11	0.04	98.65
8 min, Pt	51.12	0.16	0.72	0.24	21.50	0.45	25.02	0.97	0.01	0.01	100.19

Table 3.2. Oxygen isotopic compositions of starting and experimental glasses.

	$\delta^{18}O$	$\delta^{17}O$	$\Delta^{17}O$
Starting Comp #1 1 atm, 5 min	11.82	6.35	0.20
Starting Comp #2 1 atm, 5 min	12.14	6.44	0.35
Re (sphere)			
8 min #1	14.36	7.30	-0.287
8 min #2	14.21	7.29	-0.214
16 min	15.39	7.95	-0.175
32 min	15.08	7.77	-0.192
64 min #1	15.66	7.99	-0.261
64 min #2	14.99	7.65	-0.287
128 min	15.42	7.78	-0.363
Pancake (disk)			
4 min, Pt	15.13	7.75	-0.242
8 min, Pt	15.67	8.12	-0.149
64 min, Re	16.80	8.60	-0.270
Pt (sphere)			
4 min, Pt	15.09	7.77	-0.199
8 min, Pt	15.29	7.84	-0.232

$\Delta^{17}O = \delta^{17}O-(0.52)\delta^{18}O$

Figure 3.1.

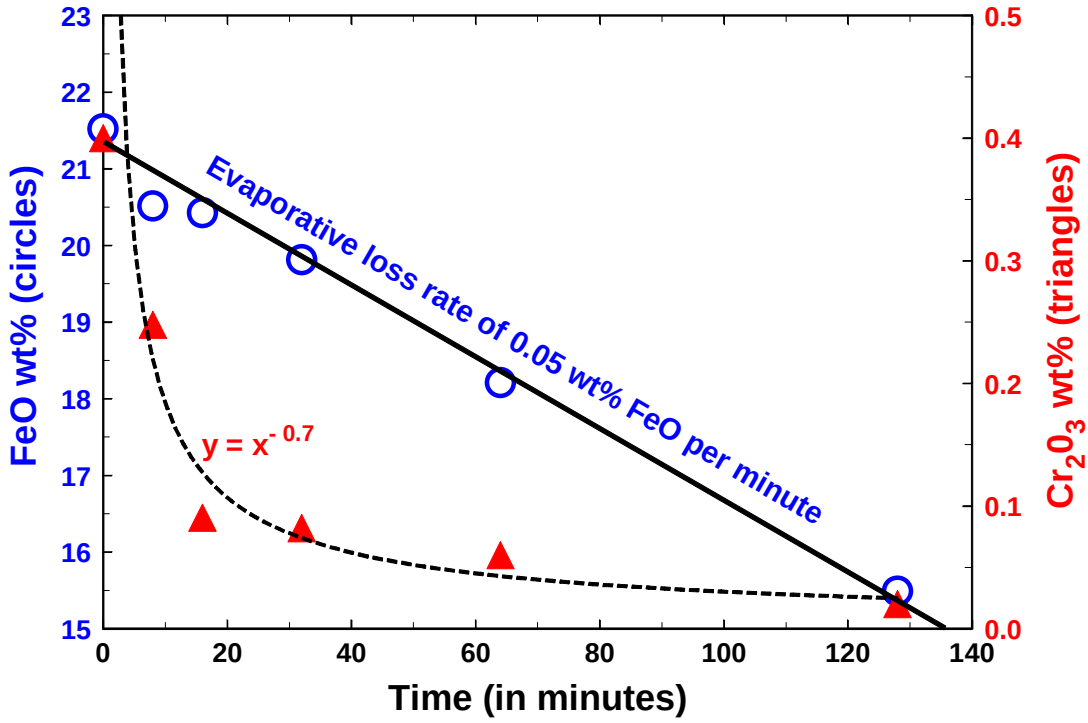

Figure 3.2.

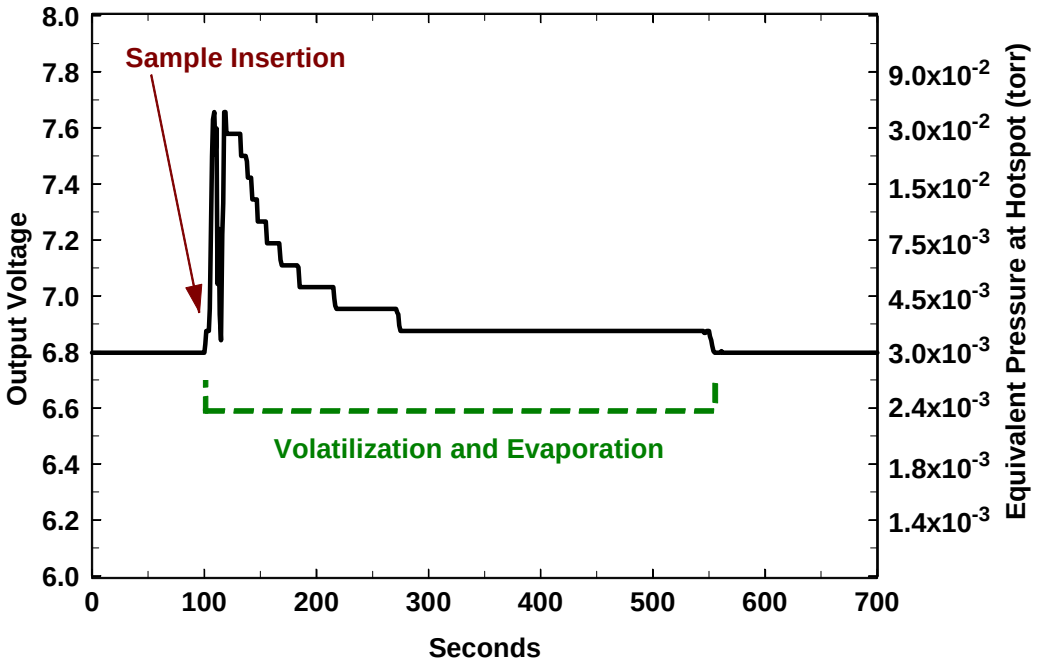

Figure 3.3.

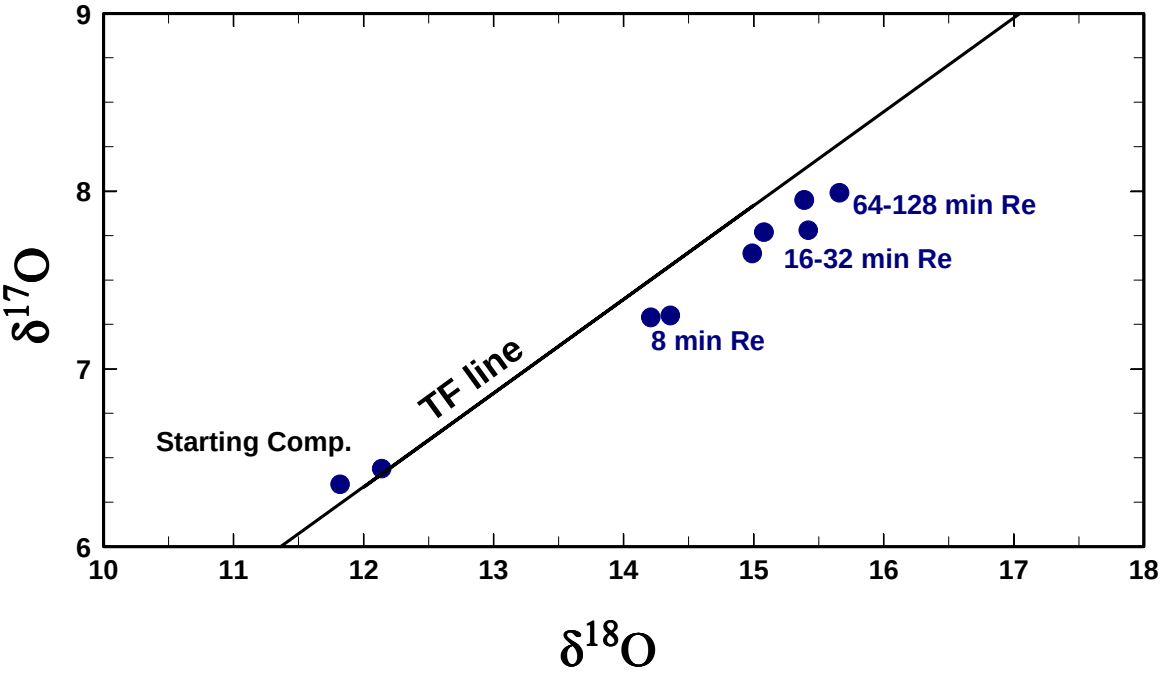

Figure 3.4.

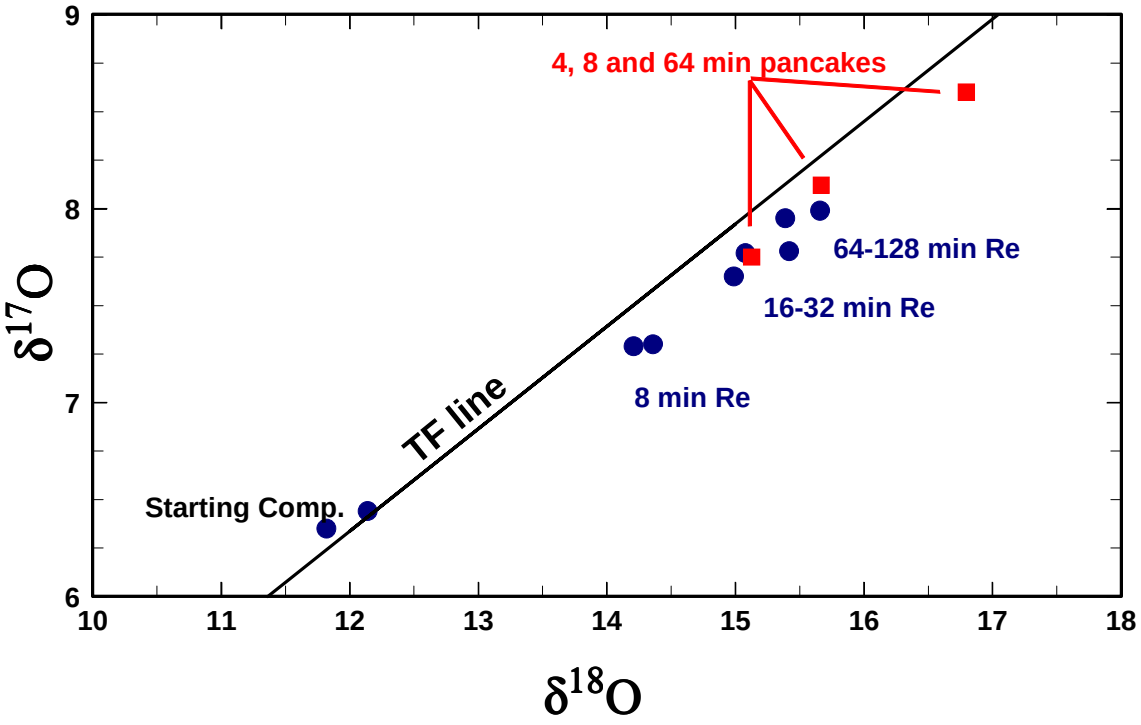

Figure 3.5.

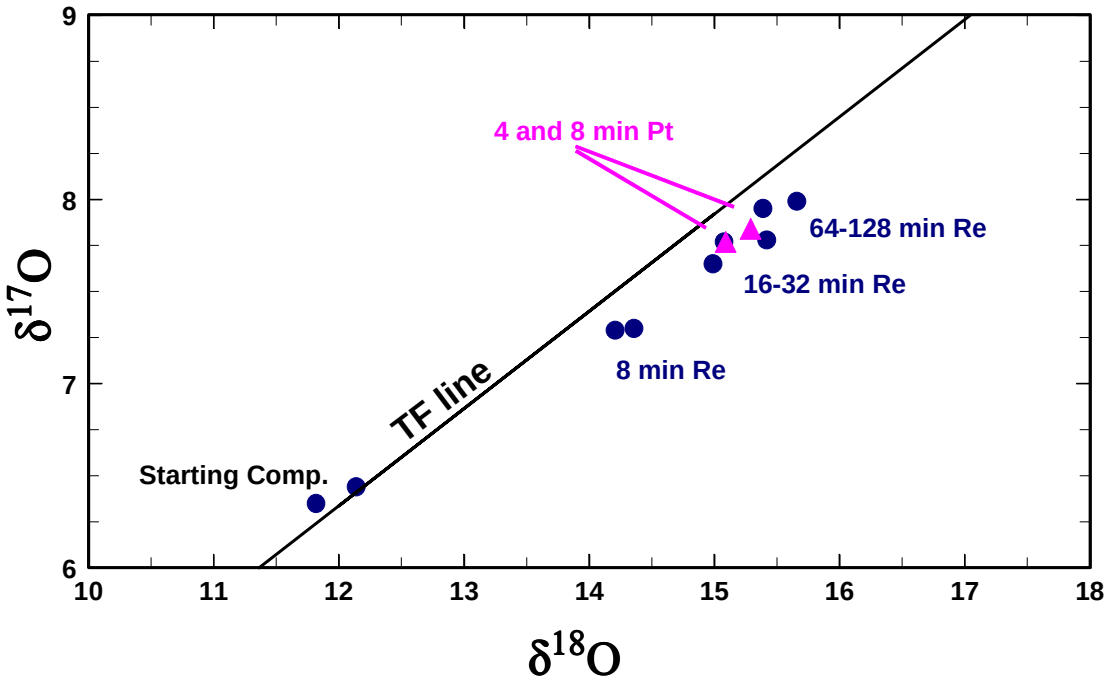

Figure 3.6.

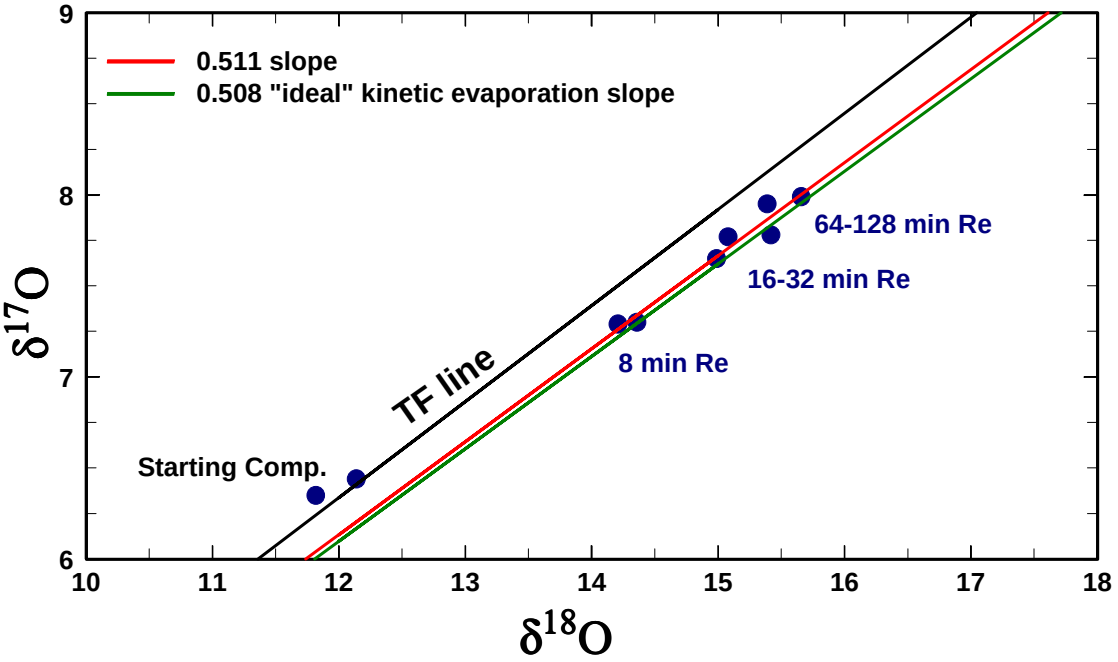

Figure 3.7a.

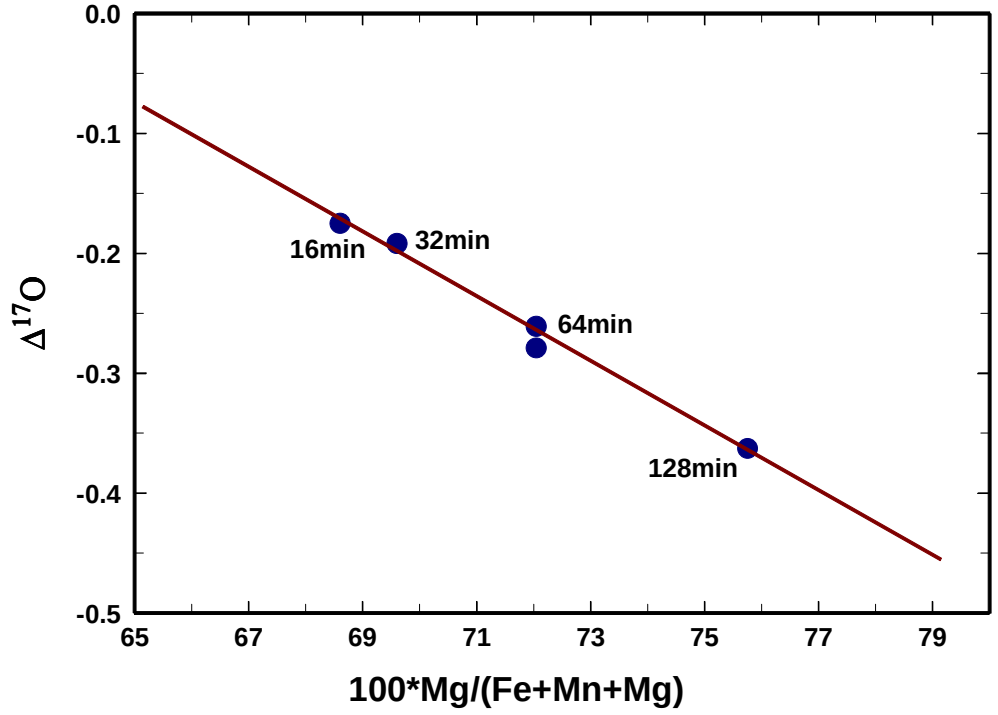

Figure 3.7b

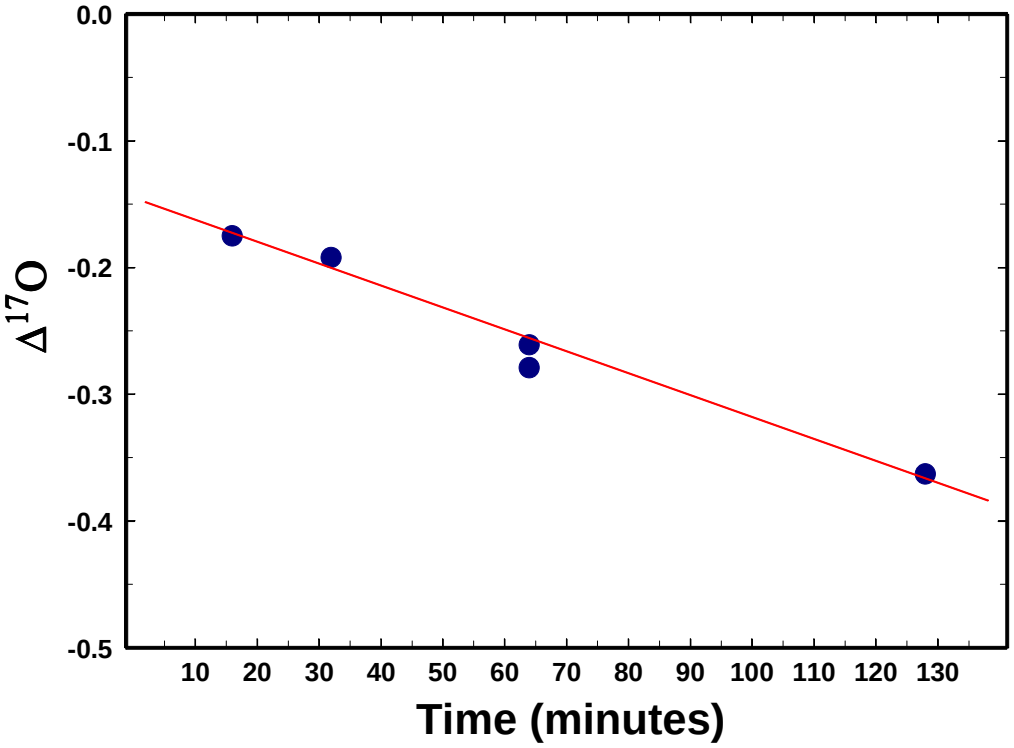

Figure 3.8.

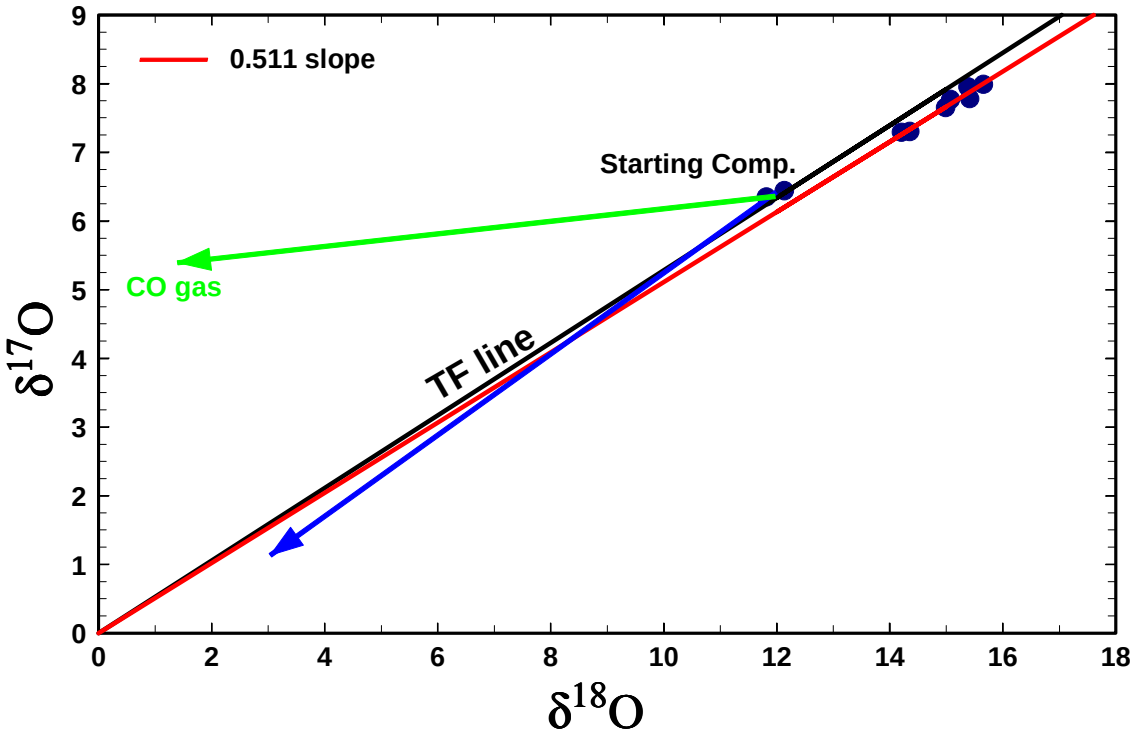
0.511 slope
Starting Comp.
CO gas
TF line
δ17O
δ18O
0
1
2
3
4
5
6
7
8
9
0
2
4
6
8
10
12
14
16
18

CHAPTER 4

OXYGEN ISOTOPIC AND FE-MG EXCHANGE BETWEEN OLIVINE AND SILICATE MELT: IMPLICATIONS FOR RELICT GRAINS AND CHONDRULES

INTRODUCTION

Chondrules are silicate spheres largely composed of olivine, pyroxene, metal, sulfides and glass which formed when precursor material was melted and subsequently crystallized. Chondrule formation occurred multiple times during relatively brief, high temperature events in the first few million years of the solar nebula (Nagahara, 1983). Occasionally, grains within chondrules have been found which have textural contrast with the surrounding minerals (Nagahara, 1981), an unusual compositional zoning pattern and/or a formational history which is inconsistent with that deduced for the host chondrule (Steele,1986, 1988, 1989; Rambaldi, 1981). These distinctive grains are called relicts and are thought to be mineral fragments that formed in a prior generation of chondrules (Jones, 1996; Kunihiro et al., 2004) and then escaped complete dissolution when they were incorporated and reheated in the present chondrule generation. However, some relict grains may have once been portions of CAIs (calcium-aluminum inclusions) (Misawa and Fujita, 1994), precursory matrix (Jones, 1992) or mineral grains originally formed directly by condensation (Weinbruch et al., 2000). It is important to note that there are also other types of relict material found in chondrites that will not be discussed here, such as relict chondrules or refractory inclusions (AOAs - amoeboid olivine aggregates or CAIs).

Nearly all relict grains within chondrules reported to date are olivines. There are three common types. 1) The first are refractory (FeO-poor) olivines found within high-FeO chondrules. These are quite common in porphyritic chondrules of type 3 ordinary and carbonaceous chondrites and typically have a sharp transitional boundary between the core and normally zoned rim. These olivines include the blue olivines (Steele, 1986, 1988, 1989; Palme et al., 1986; Kracher et al., 1984), which have a spectacular blue cathodoluminescence because of high abundances of trace Ti, Al and Ca. 2) The second type are the so-called "dusty" olivines, where low-FeO chondrules with olivine phenocrysts contain cores with submicron to 10 micron inclusions of low-Ni, metallic Fe and appear dusty when viewed in a microscope using transmitted light. It is thought that these grains, which were richer in FeO than the surrounding grains initially, experienced reduction of FeO during chondrule heating (Nagahara, 1981, 1983; Rambaldi, 1981; Kracher at al., 1984). 3) The final type of relict grains are found in enstatite chondrites. These are olivines located within enstatite laths in the chondrules. The olivines exhibit reverse zoning, contain FeO-rich cores and magnesian rims (Rambaldi and Wang, 1982; Leitch and Smith, 1982).

Relict grains are important for several reasons. First, they are the main evidence of recycling in the solar nebula. Second, they indicate that chondrule formation was not a single event, but rather a series of events or processes that probably occurred over a time period of several thousand to perhaps several million years. They therefore give us a small sampling of the precursor material. Finally, by their presence and composition, they provide constraints concerning the conditions in the solar nebula at the time of their formation AND at the subsequent time of formation when they became trapped within

the chondrule. Relict grains supply constraints on the temperature, oxygen fugacity, grain size, and bulk and isotopic compositions within the nebula.

Although no single extensive study of the oxygen isotopic compositions of relicts has yet been undertaken, the limited studies up to now indicate very few predictive relationships between chondrules and relict grains. In the ordinary chondrites, dusty relict olivines and the chondrule phenocrysts are indistinguishable from one another isotopically and have overlapping oxygen isotopic compositions (Ruzicka et al., 2005). However, FeO-poor relict olivines have been found to be ^{16}O-rich in some chondrules, while not in others, with both types being about equally prevalent (Ruzicka et al., 2005; Sears et al., 1999; Saxton et al., 1998; Sears et al., 1998). In general, carbonaceous chondrite chondrule relicts tend to be more ^{16}O-rich than their ordinary chondrite chondrule counterparts. For the CO chondrite chondrules, most relicts are ^{16}O-rich and FeO-poor, while the chondrule phenocrysts are ^{16}O-poor and FeO-rich. There are a few cases where the reverse is true, but they seem more rare than in the ordinary chondrite chondrules (Kunihiro et al., 2003; 2004; 2005; Wasson et al., 2004; Jones et al., 2000; Yurimoto and Wasson 2002). For the CV chondrite chondrules, only ^{16}O-rich and FeO-poor olivines have been found (Hervig and Steele, 1992; Saxton et al., 1998; Hiyagon, 1997). The same holds true for the one CR chondrite chondrule containing a relict that has been analyzed (in the meteorite, Renazzo)(Leshin et al., 1998). Thus, predictions and expectations for the larger chondrule population are difficult.

When predictions are difficult, experimentation or a much wider survey are necessary to try to deconvolve complicating issues. In this case, experimentation will be completed to address the following questions: 1) What profiles of Fe-Mg and oxygen

isotopes in relict olivine are expected based on their inferred isothermal or dynamic crystallization history? 2) What is the time required to erase a relict oxygen signature? 3) Can relict olivine be camouflaged from detection by Fe-Mg equilibration, but yet maintain its relict oxygen signature? 4) How common should relicts be in chondrules? 5) Does diffusion or dissolution play a larger role in obscuring or erasing a relict signature? 6) Are the isotopic signatures in the overgrowths on relict grains the result of crystallization from a melt? 7) Should heterogeneity be expected in relict grains or their overgrowths? 8) Are there evaporation effects seen in relicts – if so, what are they; if not, what might be expected?

EXPERIMENTAL PROCEDURE

The oxygen isotopic exchange experiments were run in the "Angry Mountain" vacuum furnace at the Department of Geological Sciences in Rutgers University. The experimental starting composition was composed of two components. The first was a IIAB chondrule analog (liquidus 1504°C) (Table 4.1) which was produced from ten oxides and carbonates and was ground to a fine powder (<50 micron). The analog glass oxygen isotopic composition was measured by Ed Young at UCLA using a laser fluorination technique (see previous chapter for details) and determined to have an average terrestrial composition of $\delta^{18}O = 11.98$, $\delta^{17}O = 6.40$. The chondrule glass analog was then mixed with equant chips of olivine (Fo_{80}) from the Eagle Station pallasite ($\delta^{18}O = -2.78$, $\delta^{17}O = -5.96$) (Clayton et al., 1996). The chips ranged in size from 125 to 425 microns in diameter. A gas flow of argon ($3x10^{-4}$ liters/minute) was introduced into the furnace from 30 minutes preceding the experiment until its completion, to minimize the

amount of terrestrial atmospheric contamination as well as control the pressure within the furnace. This rate maintains a constant pressure at the hotspot of $3x10^{-3}$ torr ($4x10^{-6}$ atmospheres). Two sets of experiments were run with different conditions. The first set were isothermal runs, while the second were dynamic crystallization runs.

The isothermal experiments were run at 1515°C, 1500°C, 1400°C and 1300°C for durations up to 128 minutes (depending on the temperature) (Table 4.2) and consisted of a mix of 30 mg chondrule analog and 10 mg Eagle Station olivine. Following the experimental duration, the high temperature runs (1515°C and 1500°C) were lowered to 1425°C at a rate of 60°C per minute (maximum cooling rate achievable within the vacuum furnace) to cool the charge sufficiently so it could be removed from the hotspot. The extremely low viscosity of the charge at high temperature made it unstable on the sample wire. It was therefore necessary to allow the charge to cool ~80°C, whereby it was able to maintain its shape and position on the wire. These experiments were run on platinum wire (Despite the relatively short run times, the platinum wire alloyed with the iron within the charge to a greater degree than expected by the author, and therefore rhenium wire was used in the dynamic crystallization experiments).

The dynamic crystallization experiments consisted of 20 mg IIAB chondrule analog glass and 20 mg Eagle Station olivine and were run on rhenium wire loops. Each experiment was run at 1515°C for 15 minutes and then allowed to cool at a rate between 5°C and 2000°C per hour down to 1000°C, after which each was removed from the hotspot.

Experimental charges run in this furnace are in an open system, since a low pressure and constant gas flow are maintained throughout the experimental duration.

Therefore, equilibrium conditions were only rarely attained and effects such as evaporation can be seen.

EXPERIMENTAL ANALYSIS

Microprobe Analysis

After the experiments were run in the furnace they were prepped for analysis. The samples were removed from their rhenium or platinum holding wires and mounted in epoxy. The samples were then sectioned in half and remounted in aluminum disks, suitable for both electron microprobe and ion probe analysis. The sections were analyzed by electron microprobe three times. First, a general analysis was run to determine the mineral and glass compositions as well as their textural and zoning features. They were then sent for ion probe analysis. When they returned, microprobe analysis was done again directly adjacent to the ion probe analysis spots and profiles. This allowed direct comparison between isotopic and petrologic features. The third time they were analyzed to quantify a bulk composition for the mesostasis. The microprobe analysis was carried out using a Cameca SX-100 electron microprobe located in the Department of Earth and Planetary Sciences at the American Museum of Natural History. Qualitative analysis was performed using backscattered electron imaging and energy dispersive analysis (EDS). Quantitative analysis was performed using wavelength dispersive analysis (WDS). An accelerating voltage of 15 kV and a beam current of 20nA were employed with 40 second counting times for point analyses. An accelerating voltage of 15 kV and a beam current of 40nA were employed with 40 second counting times and a 50 micron wide rastered beam to determine the bulk mesostasis compositional data for the high temperature

isothermal experiments. Data correction of all analyses was carried out using the PAP procedures (Pouchou and Pichoir, 1991). Both natural and synthetic minerals were used as standards (Appendix I).

Ion Microprobe Oxygen Isotopic Analysis – CRPG-CNRS, Nancy, France

The oxygen isotopic compositions of olivines, pyroxenes and mesostasis in the isothermal experiments were measured in situ with the CRPG-CNRS Cameca IMS 1270 ion microprobe operated in multi-collection mode (Analysis done by Marc Chaussidon). ^{16}O and ^{18}O were measured using Faraday cups; ^{17}O was measured using the axial electron multiplier. A Cs+ primary beam of 10 nA was used to produce ion probe sputter pits approximately 20–30 microns in diameter. Each analysis was preceded by 3 minutes of pre-sputtering to remove the gold coat and to check peak centering and sputtering conditions. With such conditions, the count rate was ~1 x 10^6 counts per second for ^{16}O. A normal-incidence electron flood gun was used to compensate the sample charge. Corrections for instrumental mass fractionation (IMF), counting statistics, and uncertainty in standard compositions were applied where possible. The IMF was corrected using the three isotopically distinct standards, Eagle Station pallasite olivine, San Carlos olivine and a well-characterized quartz standard. Oxygen isotopic compositions are reported as per mil (‰) deviations from SMOW (Standard Mean Ocean Water) ($\delta^{18}O$ and $\delta\ ^{17}O$) and as ^{16}O excesses relative to the terrestrial fractionation line [$\Delta^{17}O = \delta^{17}O - (0.52)(\delta^{18}O)$]. Under the analytical conditions employed, the total precision (2σ) of individual oxygen isotopic analyses is 1.62‰ for $\delta^{18}O$ and 1.43‰ for $\delta^{17}O$. Following oxygen isotopic measurements, each experiment was examined on the

electron microprobe using backscattered electrons to verify the locations of the sputtered craters and phases analyzed.

Ion Microprobe Oxygen Isotopic Analysis – University of California, Los Angeles

The oxygen-isotopic compositions of olivines from the dynamic crystallization experiments were measured in situ with the UCLA Cameca IMS 1270 ion microprobe at the W. M. Keck Foundation National Center for Isotope Geochemistry and operated in multi-collection mode (^{16}O and ^{18}O were measured simultaneously) (Analysis by Kevin McKeegan and Mariana Cosarinsky). ^{16}O and ^{18}O were measured at low mass resolving power of 2000 using a Faraday cup and an electron multiplier. A Cs+ primary beam of 10 nA was used to produce sputter pits of ~20 um in diameter. With such conditions, count rates were typically ~10^7 counts per second for ^{16}O and ~10^4 counts per second for ^{18}O. Each analysis was preceded by 3 minutes of pre-sputtering to remove the gold coat, and to check peak centering and sputtering conditions. Measurements consisted of 15 integration cycles of 10 seconds each. A normal incidence electron flood gun was used for charge compensation. Oxygen-isotopic compositions are reported as per mil (‰) deviations from Standard Mean Ocean Water (SMOW). The instrumental mass fractionation was corrected for the two day session using olivine from the Eagle Station pallasite, which was measured every four or five analyses. The pallasite olivine was mounted in the same blocks as the unknowns, thereby requiring no change of conditions at any time. Under the analytical conditions employed, the internal precision (2σ) of individual oxygen-isotopic analyses was 0.42‰ for $\delta^{18}O$. Following oxygen isotopic measurements, each experiment was examined on the electron microprobe using

backscattered electrons to verify the locations of the sputtered craters and phases analyzed.

Ion Microprobe Error Analysis

Because of difficulties encountered during the ion microprobe analysis of the experiments, it is necessary to address the potential errors within and limitations of the data. The isothermal experimental data from CNRS were collected over six sessions and over a period of two years. Difficulties within the data derive from mechanical problems with the ion probe which were encountered on five of the six sessions. These include charge buildup on the sample, electron multiplier damage, and massive contamination of the instrument by a previous user. The result is that the error bars for the precision of the data are much larger than expected (see above for the 2σ). Also because of the mechanical problems and the time over which all the data were collected, we could not normalize the data between sessions. To minimize these problems, only analyses from individual experiments that were generated in a single session were used. Cross session analyses of the same experiment were eliminated as they were often more confusing than helpful. Therefore, comparison of minor details and absolute values between isothermal experiments should not be automatically considered real differences, but may be caused by error and uncorrectable artifacts of the analysis. A second problem are the matrix effects within the glass. Because appropriate glass standards were not available additional errors may be present for the glass analyses. These errors may be as large as ~0.5‰. The final problem concerns time and distance. Because of the demands on the instrument, the breakdowns that occurred, and the distance between Rutgers and CNRS, the author was

unable to be present for 99% of the analyses. The result is that the analyses are more random than preferred, and there are substantially fewer profile analyses than desired. Therefore, caution concerning the lack of representative sampling of each experiment is justified. In most cases, a single profile across one olivine grain into glass with perhaps a few additional random analyses is the extent of analysis of one experiment.

The UCLA ion microprobe data suffer from fewer introduced errors, but have similar limitations to the CNRS data, when it comes to interpretation. First, because of communication errors, only ^{16}O and ^{18}O data were generated. ^{17}O was not analyzed. Therefore, the main advantages of using Eagle Station olivine in the experiments (it is not on the terrestrial fractionation line and would have distinct mixing line characteristics) were largely nullified. Second, because of matrix fractionation effects, glass was not analyzed and only olivine data was generated. Therefore, we did not determine the bulk exchange between glass and olivine. Finally, as with the CNRS data, I was not present at the analysis and the amount of data generated is limited for all of the experiments. In this case, most experiments contain one or two profiles across olivines, but may not be representative of the entire experimental charge. On the positive side however, the UCLA data quality is excellent, as the data were all collected over a single two day session and the data were calibrated and corrected every ~5 analyses using unreacted Eagle Station olivine.

Fortunately, because of the nature of the experiments and the extent of exchange (either quite large or non-existent) any errors in either set of runs do not greatly influence the final interpretation of the data.

RESULTS

Isothermal Experiments

The isothermal experiments produced some textures which were unintended and the result of mechanical limitations of using the vacuum furnace. Because of the need to seal off the furnace, rapid quenching of the run products is virtually impossible as there is no way to rapidly break the vacuum and quench the experiment before some quench crystallization proceeds. A second difficulty is that the experiments have an extremely low viscosity when near or above their liquidus. The viscosity is so low that the experimental charge cannot be moved without the charge dropping off the supporting wire it is suspended from. The best solution to the problem (as mentioned in the Experimental Procedure) was to reduce the temperature in the furnace by ~80°C before moving the 1515°C and 1500°C experiments from the hotspot. Texturally, the result was the formation of quench crystals and melt-grown olivine and pyroxene during cooling, which under ideal conditions would either not be present (quench crystals) or would be present in much lower abundance (melt-grown olivine and pyroxene). Test experiments were run in a one atmosphere furnace to understand the crystallization textures and kinetics that were occurring in the vacuum furnace as a result of the quenching process. Figure 4.1a shows the results from a complete simulation of the vacuum furnace procedure for an 8 minute experiment. Following 8 minutes at 1500°C, the furnace was reduced in temperature at 60°C per minute to 1425°C, after which the charge was removed from the hotspot and allowed to cool radiatively. The results are abundant quench crystals, thick melt-grown overgrowths around the relicts and many melt-grown olivines and pyroxenes. Figure 4.1b shows the ideal case where the charge was heated to

1500ºC for 8 minutes and is immediately quenched in water. There are no quench crystals and only very minor melt-grown olivines and pyroxenes. Figure 4.1c shows the effect of only the 75ºC temperature decrease. In this case, the furnace was left at 1500ºC for 8 minutes and then reduced in temperature at 60ºC per minute to 1425ºC followed by a water quench. Substantial overgrowths are already developing (such as the reversely zoned rim in Fig. 4.1a), quench crystals are forming, and melt-grown olivine and pyroxene are quite prevalent. It is important to recognize these textural artifacts are necessary to run the experiment, but are not expected to occur during actual relict entrapment and chondrule formation.

The isothermal experiments (Figures 4.2a-s and 4.3a-s) contain relict (no detectable change in Fe-Mg) rounded Eagle Station olivine cores surrounded by euhedral to subhedral, melt-grown overgrowths of olivine or rare pyroxene (orthopyroxene). Within the mesostasis, euhedral to subhedral melt-grown olivines and pyroxenes are common and quench crystals are abundant. There appears to be a fairly uniform decrease in the average size of the relict olivines, as expected, with increasing temperature and duration. Average sizes were not calculated or measured directly, as the random cut through the experimental charges revealed abundant relicts in some instances and only a few in others. However, calculations of the amount of dissolved Eagle Station olivine within the glass were done for six of the 1500ºC and 1515ºC experiments (Table 4.2, Appendix III). Over a hundred electron microprobe rastered beam analyses of the mesostasis (including glass + quench crystals + melt-grown crystals) were averaged for each experiment to determine a bulk mesostasis composition. The amount of Eagle Station dissolved in the melt and the amount of iron lost (to either the platinum wire or

evaporation) were then determined. For the 2, 8 and 32 minute 1500ºC experiments (4ºC below the calculated liquidus of the mesostasis) between 1 and 8% Eagle Station olivine dissolved into the melt, and up to 0.5 wt% FeO was lost. For the 2, 8 and 32 minute 1515ºC experiments (9ºC above the mesostasis liquidus) between 10 and 20% Eagle Station olivine dissolved into the melt, and up to 3.2 wt% FeO was lost. Estimates could not be made for the lower temperature experiments (1300ºC and 1400ºC) as there was insufficient melt or too much heterogeneity within the mesostasis to produce accurate results.

The relict Eagle Station olivines within the isothermal experiments do not show any exchange of oxygen by diffusion even at their edges. Fe-Mg diffusion does occur but appears to be limited to the outer edges of the grains. With increased duration and temperature, there is a slight increase in the effective thickness and MgO content of the outer edges of the relicts. This could be caused by either FeO stripping of the edges by reaction with the melt and/or normal diffusion between the relict edge and the melt (most likely, equilibration with the melt should increase the Fo content of the olivine).

The high temperature experiments contained fairly homogenized mesostasis based on the Fe-Mg distribution and the rastered analysis, however the oxygen isotopic compositions were still mildly heterogeneous. It is not known whether this is a real difference or due to the presence of quench crystals within the melt. The melt-grown olivines and pyroxenes as well as the quench process overgrowths and quench crystals all have the oxygen isotopic composition of the mesostasis. The mesostasis gets more Mg-rich with time as a result of FeO evaporation in all but the 1300ºC experiments. The 1300ºC experiments simply did not produce measurable melt. These experiments are

largely still composed of their original starting materials. Note that because the quench crystallized Mg-rich olivines and pyroxenes, the melt, analyzed by electron microprobe and reported within Table 4.3 and plotted in many profiles of Figure 4.3 (g, h and k particularly), is falsely and substantially more Fe-rich than it should be (or was during the actual experiment). The oxygen compositions also get progressively isotopically heavier with duration. Although the dissolution of Eagle Station should make them more isotopically light, the effects of evaporation are more strongly influencing the net isotopic composition of the liquid during the experiments.

In addition to slow but progressive loss of FeO by evaporation, the mesostasis in all experiments experienced complete loss of Na_2O and K_2O. The loss occurs in less than 8 minutes and like the experiments in Chapter 3, is reflected by the return of the pressure within the furnace to its original setting (3×10^{-3} torr).

Dynamic Crystallization Experiments

The dynamic crystallization runs typically consist of Eagle Station (Fo_{80}) olivine relict cores, Mg-rich olivine overgrowths, melt-grown olivine, melt-grown pyroxene (orthopyroxene) and mesostasis (Figure 4.4). In the experiments with cooling rates of 200℃ per hour or less, silica (tridymite) and a second pyroxene, augite, are also present.

The relict Eagle Station olivine cores and the Mg-rich overgrowths form an apparent reverse zoning pattern (Fe-rich core, Mg-rich rim) (Figures 4.4 and 4.5). This however is not because of an unusual crystallization sequence but rather because the melt had an initial *mg#* of 65 (and this is a minimum *mg#*, as it assumes no FeO is lost to either the platinum wire or evaporation) and crystallizes equilibrium olivine of Fo_{86}

[assuming a $K_{D\ (Fe\text{-}Mg\ for\ ol\text{-}lq)} = (X_{Fe\text{-}ol}/X_{Fe\text{-}lq})/(X_{Mg\text{-}ol}/X_{Mg\text{-}lq}) = 0.30$], more magnesian than the original Fo_{80} Eagle Station cores. The relicts become more rounded with duration, while the overgrowths surrounding them become more equant. The overgrowths, though initially more Mg-rich than the relict and quite obvious in the short duration experiments, become much more diffuse in Fe-Mg in the longer experiments as equilibrium is approached (though not attained).

Melt-grown olivine abundance initially increases during the first 2.5 hours but decreases thereafter as FeO evaporation effects dominate the bulk composition in favor of a more silica-rich composition. Melt-grown augite and tridymite though not in experiments of less than 2.5 hours, are both present and grow in abundance in the long duration ones. As in the isothermal runs, all Na_2O and K_2O is lost from the mesostasis, even in the shortest duration experiment. Tridymite and melt-grown pyroxenes dominate along the edges of the charge. The silica and pyroxenes appear to insulate the interior of the charge and may slow the rate of FeO loss by evaporation.

Isotopically, the relict Eagle Station olivines show no change in $\delta^{18}O$ composition (Figure 4.5 and Table 4.4). The melt-grown olivine overgrowths on relicts have increasing $\delta^{18}O$ away from relict boundaries. No other phases were analyzed. It is presumed (based on the isothermal experiments) that the melt-grown olivines and pyroxenes have $\delta^{18}O$ compositions close to that of the mesostasis and the quartz has a $\delta^{18}O$ composition heavier than the mesostasis (based on equilibrium isotopic fractionation factors) (Chacko et al., 2001).

Within the $\delta^{18}O$ data for the melt-grown olivines, there is an unusual signal which is discussed later. The highest $\delta^{18}O$ value measured in each experiment should allow an

estimate of the amount of evaporation that has occurred. The $\delta^{18}O$ value should progressively increase with duration. However, the highest value ($\delta^{18}O$=12.66) in fact occurs in the experiments cooled at 50ºC per hour (Figure 4.5h, Table 4.4). The experiments with cooling rates slower than 50ºC per hour (and longer durations) show a continued decrease in $\delta^{18}O$ (down to $\delta^{18}O$=9.32), while the experiments with cooling rates of 2000ºC per hour ($\delta^{18}O$ = 9.41) to 50ºC per hour get progressively heavier with increasing duration. The only break in the trend is at a cooling rate of 100ºC per hour where the value is lower than expected (Figure 4.6). However, given the limited number of oxygen analyses in that experiment (8 analyses), the fact that one experiment doesn't follow the trend probably indicates poor sampling during analysis rather than a true disruption in the trend.

DISCUSSION

The isothermal and dynamic crystallization experiments show Fe-Mg exchange evidence for evaporation, however they show almost no evidence for the exchange of oxygen isotopes between relict olivine and melt. Some of the charges have evolved beyond "normally" observed chondrule characteristics [very high silica (tridymite) contents] [Krot et al. (2004) did report the presence of silica in Al-rich chondrules, but not at the abundance found in these experiments], however the gross chemical and textural evolution of the charges is relevant to chondrules and the timescales (Desch and Connolly, 2002) consistent with their formation. The isothermal experiments shed light on reactions that occur during melting, dissolution, and diffusion of relict grains in chondrules and during evaporation of chondrule liquids. [In this case, ***melting*** is defined

as occurring above the melting point of ALL components/phases. *Dissolution* is defined as being below the melting point of one phase (olivine), but above the melting point of the second phase (mesostasis). The reaction of the high temperature phase in contact with the low temperature phase causes the high temperature phase to be progressively dissolved, like a solute in a solvent]. The dynamic crystallization experiments meanwhile show relationships that should result from crystallization, diffusion, and evaporation.

Dissolution plus crystallization versus diffusion

One of the difficult questions in interpreting relict grains within chondrules is how the overgrowth surrounding the relict grain was produced. Was it formed by a combination of dissolution of the relict (presumably during the heating/melting stage of chondrule formation) followed by cooling and recrystallization or is the overgrowth simply the reactive edge of the original relict grain that has undergone some degree of Fe-Mg exchange with the surrounding melt? The dynamic crystallization experiments produced relict Eagle Station olivines surrounded by magnesian, melt-grown overgrowths. These overgrowths are produced primarily by crystallization from the liquid. The overgrowths formed reversely zoned core to rim sequences because of the evaporation of FeO from the melt during crystallization (eg. Fig 4.4b). Although the type of zoning is not significant, what is important is that the relicts can be distinguished from the overgrowths because they still contain their original oxygen isotopic composition. Based on the isothermal experiments, when the relicts are being dissolved into the mesostasis, there is essentially no additional diffusion of oxygen into the melt, other than that portion of the relict that dissolves. Dissolution far outpaces isotopic diffusion of

oxygen. When cooling occurred in the dynamic crystallization experiments, the overgrowths have the isotopic composition of the mesostasis (original mesostasis plus the dissolved portion of the relicts). This differs from the Fe and Mg exchange results. Fe-Mg diffusion between relict olivine and mesostasis appears to barely outpace the dissolution of the olivine, resulting in slight Mg-enrichment at the extreme edges of the relicts.

The experimental results agree very well with relatively simple diffusion and dissolution calculations made here (See Appendices IV-V for calculation details) and those made by Ruzicka et al. (2007). The interdiffusion coefficients for Fe-Mg in olivine in the range of 1300-1500ºC are approximately 10^{-14}-10^{-15} m^2/s, while the volume diffusion coefficients for oxygen are 10^{-18}-$10^{-19}m^2/s$. Using the experiments and assuming a spherical 100 micron FeO-rich relict olivine grain surrounded by a Type IIAB chondrule melt, the calculations indicate that in 32 minutes at 1515ºC roughly 4 microns of the exterior sphere is dissolved into the melt (Appendix IV). However, under the same conditions Fe-Mg diffuses 5 microns, while oxygen diffuses only 0.1 microns (Appendix V). Therefore, the oxygen signatures in relict grains are essentially permanent under any reasonable chondrule formation conditions (hours to days), while dissolution and Fe-Mg diffusion compete for dominance, which is determined by heating duration and thermal conditions.

The diffusion calculations are useful in understanding the difference in magnitude between oxygen and Fe-Mg exchange between melt and relict olivine during the melting phase of both the isothermal and dynamic crystallization experiments. The calculations however can be deceiving when considering the effects of diffusion during the cooling phase of the dynamic crystallization experiments and during crystallization of the

overgrowths. The complication arises because during crystallization, the melt/overgrowth boundary is not fixed, but rather moves as a function of the crystallization rate. The crystallization rate in turn depends on the cooling history and melt composition. The result is that the actual diffusion distance is much larger than one would originally calculate based on a fixed boundary calculation.

For example in Figure 4.5f, there is a 150 micron wide Eagle Station relict olivine ($\delta^{18}O \sim -3$), which is surrounded by an overgrowth. A fixed boundary calculation for Fe-Mg diffusion in that experiment, which cooled over a ~5 hour period from 1515ºC to 1000ºC, yields a diffusion distance of only ~30 microns (this takes into account the decrease in temperature). However, the overgrowth is ~100 microns thick. This means that as the overgrowth crystallizes, diffusion is no longer possible between the melt and the relict when the overgrowth exceeds some thickness. It also means that the inner portion of the overgrowth continues to exchange with the relict, and the outer portion of the overgrowth exchanges with the melt, creating a very complicated diffusion pattern.

Figure 4.7 is a simplified diagram which shows how diffusion with a moving boundary might work for a relict grain and its overgrowth, as the overgrowth crystallizes from a surrounding melt. The model shows equally spaced time slices (A to D) of diffusion progressing as the overgrowth/melt boundary (I) crystallizes away from the relict grain (R). The diffusion rate, X, of a given species, such as oxygen or coupled diffusion such as Fe-Mg, in the example is assumed to be half the crystallization rate, 2X, of the overgrowth (In reality, crystallization is probably much faster than diffusion by nearly a magnitude, but a 1 to 2 ratio was used for simplicity). It is assumed that the species in question can diffuse both inwards (white box, black X) and outwards (black

box, white X) from the boundary (the direction of diffusion depends on the concentration gradient) and the diffusion rate is constant (which is certainly not true during cooling). For simplicity, only the diffusion from the boundaries are considered. In A, cooling has begun and the overgrowth (O_1) crystallizes around the relict (R). X shows the maximum diffusion distance atoms on the innermost edge of the overgrowth could move, as the overgrowth crystallizes outwards. No diffusion outward from boundary I_1 is considered while overgrowth O_1 crystallizes. It is important to recognize that by the time the overgrowth has finished growing in A, the relict is no longer within the range of diffusive exchange with the melt. The relict can only exchange with the overgrowth from now on. At time B, the overgrowth has extended to I_3, diffusion from the I_1 boundary can occur in both directions, and diffusion between the relict core and the innermost portion of overgrowth O_1 is possible. Note that diffusion hereafter is largely accomplishing local homogenization, not complete exchange from outermost edge of the overgrowth/melt boundary to the relict core. At the end of C, crystallization of the overgrowth ends with overgrowth O_3 forming. Although the distance diffusion can transport a given species from a boundary is now more extensive, overlapping diffusive zones occur. By the end of D, only diffusion is occurring. For the outer edge of the overgrowth (I_4) to finally start diffusing atoms with the relict grain at least 6 more time periods are required (In reality, the number of time periods required is probably much higher as diffusion rates decrease with temperature).

The diagram nicely demonstrates that homogeneity may or may not occur in the relict or the overgrowths, and that factors such as the size of the relict, the diffusion rate of the given species and the thermal history will determine the final outcome. The

greatest effect of diffusion with a moving boundary is to decrease the steepness of the concentration gradient across the overgrowth. The decrease however is NOT continuous from relict to the outermost overgrowth edge, but is likely to be divided into overlapping diffusive zones.

It was mentioned in the Results section that reverse Fe-Mg zoning was produced in the overgrowths in the dynamic crystallization experiments. The zoning was produced as a result of crystallization and diffusion with a moving boundary. In the experiments where the cooling rates were less than 100ºC per hour, diffusion began to obscure the relict-overgrowth boundary as well as erase the Fe-Mg zoning profile. Thus, the relict cores became camouflaged in Fe-Mg and even BSE observation or electron microprobe analysis would not reveal the relict. However, ion probe oxygen analyses still easily shows the location of the relict-overgrowth boundary (Figure 4.1 and 4.2). These results imply that relict grains in chondrules which have melt compositions that produce equilibrium olivines (overgrowths) similar to the relict can be obscured by Fe-Mg diffusion within the crystallization time of the chondrule (i.e. FeO–poor relicts in Type I chondrules or FeO-rich relicts in Type II chondrules). However, because oxygen diffusion is nearly two magnitudes slower than Fe-Mg (based on the calculation), the relict oxygen isotopic composition will remain intact (assuming no subsequent metamorphic effects).

Relict Grain Populations

Relict olivines have been found in chondrules of type 3 ordinary, carbonaceous, and enstatite chondrites. Estimates of their abundance within chondrules varies

depending on both the chondrule and chondrite type. On the whole, Jones (1996) estimated that 15% of all chondrules contain relict grains and Jones et al. (2005) estimated that up to 90% of the high-FeO porphyritic olivine chondrules, depending on the chondrite group, could contain relict magnesian olivine grains, based on comparisons of previous research results (Steele, 1989; Jones, 1990, 1992; Wasson and Rubin, 2003; Kunihiro et al., 2004). Rambaldi (1981) estimated roughly 50% of the porphyritic chondrules in unequilibrated ordinary chondrules contain relicts, while Nagahara (1983), Grossman et al. (1988) and Rambaldi and Wasson (1982) observed that approximately 10% of the low-FeO porphyritic chondrules contain "dusty" olivines, that are interpreted to be relict. In carbonaceous chondrites and particularly CO chondrites, forsteritic relicts are common (Jones, 1996; Kracher et al., 1984; Jones and Danielson, 1997; Metzler et al., 1992). However, dusty relicts are rare in CM and CV chondrites and uncommon in CO chondrites (Rubin et al, 1985; Jones, 1992, 1993). In the enstatite chondrite chondrules, dusty olivines have been found by Rambaldi et al. (1983) and Kitamura et al. (1988), while relict FeO-rich olivine within enstatite laths was reported by Rambaldi and Wang (1982) and Leitch and Smith (1982).

Though pyroxene is quite common in chondrules, relict pyroxenes are very rare. Relict pyroxene (enstatite) has been reported in the ordinary chondrites Semarkona (Kracher et al., 1984; Jones, 1996) and Bishnupur (Rambaldi, 1981), and the enstatite chondrites (Leitch and Smith, 1982). The enstatite chondrite relicts (which also luminesce blue) are controversial and may represent relicts or enstatites with minor element abundances that are on one end of a continuum of concentrations (McKinley et al, 1984). A survey to determine the abundance of pyroxene relicts would be useful. At

present, it would appear that pyroxene relicts are rare either because the temperatures reached during chondrule formation exceed their melting point or because the times to melt the relict by dissolution are quite long (greater than a few minutes) (Hewins, 1999).

Relict grains in chondrules that have mesostasis chemical compositions in near equilibrium with the chondrule phenocrysts, but having different oxygen isotopic compositions have rarely been recognized to date. Because measuring oxygen isotopes in situ was very difficult or imprecise until relatively recently (~5-10 years), the chemical compositional difference was the predominant means of identifying relicts. Today, oxygen scanning using nano-SIMS or SIMS machines is possible, but has not become a routine measurement employed when analyzing chondrules. Given these facts and the results of these experiments, it appears very likely that the relict grain population within chondrules is vastly greater than that previously estimated by Jones (1996). It seems likely that a population of relict grains (at least) equal in size to what has already been documented, is still yet to be found. Therefore, a conservative estimate of the proportion of chondrules containing relicts is greater than 30% of all chondrules.

Evaporation

Because of the low pressure environment within the furnace, most of the charges in both sets of experiments show signs of evaporation with respect to both their initial bulk and isotopic compositions. The isothermal experiments very nearly duplicate portions of results shown in the experiments of Chapter 3 (see Table 4.2) once the different proportions of Eagle Station olivine and IIAB melt are accounted for. In general, the effects in the isothermal experiments are minor because the durations are

quite short. However the dynamic crystallization experiments have drastic evaporation signatures. The degree of evaporation actually obscures the amount of Eagle Station olivine that has dissolved into the melt. The outer edges of the overgrowths have $\delta^{18}O$ values of 10 to 12, which is very close the initial 11.98 value of the analog IIAB chondrule melt composition. This would imply that almost no Eagle Station was dissolved. However, what has occurred in the dynamic crystallization experiments is a complex combination of evaporation, dissolution, and crystallization. Based on the isothermal experiments, the dynamic crystallization experiments must begin melting approximately 15-20% of the Eagle Station olivine in the first 15 minutes. The reason is simple. For the first 15 minutes, the dynamic crystallization experiments are held at 1515℃, duplicating the isothermal runs. During this time partial evaporation of FeO (and all of the alkalis) has begun and the melt composition begins to become more magnesian and isotopically heavier in oxygen. The cooling cycle then starts, eventually causing dissolution of the Eagle Station olivine to cease and crystallization of the olivine overgrowths around the relicts to begin. The overgrowths have nearly the same oxygen composition as the melt (based on Chapter 3 results) and therefore record the entire progressive evaporation process. The experiments crystallize by fractional crystallization and thus the most magnesian olivines form first, nearest to the relicts. This enriches the melt in FeO, and forces the melt composition in the reverse direction that evaporation is moving it. Therefore, a tug-of-war takes place in the melt as crystallization and evaporation compete. As both proceed, the melt composition fractionates to become more pyroxene-normative and (more slowly) FeO-poor. The melt also becomes segregated into pockets, slowing all reactions between melt and crystal, and melt and vapor. In

experiments having cooling rates of 200°C per hour or less, the melt (particularly that melt near the edges of the charge) fractionates to such a degree, tridymite begins to now crystallize in addition to pyroxene. Also, Fe/(Fe+Mg) profiles across relict grains and their overgrowths show nearly flat or show slightly inverted U-shaped patterns. This pattern is quite different from the V-shaped profiles produced by the $\delta^{18}O$ data versus distance (Figures 4.5b, c, d, e f, g, h, k, l and m).

Evaporation also displayed two counter-intuitive effects within the overgrowths that nearly went unnoticed until considered together. The effects were recognized when looking at the $\delta^{18}O$ versus distance profiles for four melt-grown olivines (Figure 4.5i, j, k and n) as well as the highest $\delta^{18}O$ value measured within the overgrowths for each experiment (Figure 4.6). Figure 4.6 shows that the maximum overgrowth $\delta^{18}O$ value for each experiment follows a progressive increase up the experiment cooled at 50°C per hour ($\delta^{18}O$ = 12.66) and then decreases thereafter. Normally, $\delta^{18}O$ is expected to continually increase with duration. Meanwhile, the melt-grown olivines (Figure 4.5i, j, k and n) all have relatively flat $\delta^{18}O$ profiles. U-shaped profiles would at first seem more likely, with melt-grown olivine interiors recording earlier and less severe evaporation (lighter $\delta^{18}O$), and the exterior zones recording heavier $\delta^{18}O$ values.

The explanation for these features comes in three parts. First, tridymite (and all other silica polymorphs) has oxygen isotope fractionation factors that preferentially partition for heavy oxygen (Chacko et al., 2001). Therefore, as tridymite crystallization occurs the $\delta^{18}O$ values of the remaining melt decrease (the melt becomes ^{16}O-enriched). Second, the experiments cooled at 200°C per hour down to 5°C per hour contain progressively more tridymite. Thus, as the tridymite abundance increases with duration,

the $\delta^{18}O$ in the melt decreases. The experiment cooled at 50ºC per hour is where evaporation (making the melt heavier in $\delta^{18}O$) and tridymite crystallization (making the melt lighter in $\delta^{18}O$) have their effect on the melt (and the overgrowths, since the overgrowths grow from the melt) cancel. Once the duration is increased further (as in the experiments cooled at 20ºC per hour or slower), tridymite crystallization overwhelms the evaporation evidence and continues to dominate the $\delta^{18}O$ of the melt.

Finally, the melt-grown olivines do not show U-shaped $\delta^{18}O$ patterns in experiments beyond 4-6 hours because the amount of evaporative change that actually occurs beyond this time is so small that it is within the analytical error of the ion probe analysis. Figure 4.8 (which is reproduced from Chapter 3) shows a $\delta^{18}O$ versus $\delta^{17}O$ graph plotted with the Chapter 3 experiments. In those experiments only the IIAB chondrule analog glass was used. No Eagle Station olivine was included. The graph shows roughly that with every four-fold increase in duration, $\delta^{18}O$ gets heavier by only half as much as the previous increment of time. [If one looks at Figure 4.8, in the first 8 minutes, $\delta^{18}O$ moves from 12 to 14.3 (net $\delta^{18}O$ distance = 2.3). By 32 minutes (four times longer) $\delta^{18}O$ has moved from 14.3 to 15.4 (net $\delta^{18}O$ distance = 1.1). By 128 minutes (four times longer again), it has moved from 15.4 to 15.8 (net $\delta^{18}O$ distance 0.4)]. The experiments are asymptotically approaching a steady state within the furnace, which is an open system. In nature, they would be approaching equilibrium. Extending this logic, it quickly becomes apparent that the amount of change after 4-6 hours is less than one per mil, even when durations reach 100 hours, such as those experienced by the dynamic crystallization experiments. Therefore, any experiments that evaporate more than 4-6 hours actually become indistinguishable because they are within the normal analytical

error of the ion probe. The dynamic crystallization experiments with melt-grown olivine profiles have durations between 10 and 103 hours.

Chondrule Relict Grains Versus Experimental Relict Grains

Comparison of the experiments to actual relict grains in chondrules has proven harder than originally thought. The basic problem derives from two facts. First, most of the relict grain investigations were done in the 1980's and early 90's before ion probes could measure oxygen isotopes in situ. Thus, all of that data come from electron microprobes and deal with only the chondrule chemical compositions, not the oxygen isotopic compositions. The second problem is the way in which the researchers to date have collected the oxygen data on the relict grains and associated phases. The present experiments were analyzed by both electron microprobe and ion microprobe. Profiles across the grains of interest were obtained to determine whether the oxygen isotopic and Fe-Mg systematics within the grain changed either abruptly, smoothly, or varied over time. In all of the investigations to date of meteorite relict grains, there are NO oxygen isotopic profiles across the grains (there are some Fe-Mg profiles). In addition, there are only rare analyses of the immediate surrounding mesostasis, which could help determine whether the overgrowth reflects changes occurring within the melt or the relict. The ion microprobe analyses appear to have been positioned only to determine whether the grains are in fact relicts, rather than to determine the systematic relict grain histories. The analyses therefore cannot be used to distinguish between an abrupt or smooth change in the oxygen isotopic compositions across the grains (Saxton et al., 1998; Jones et al., 2000; Wasson et al., 2004; Kunihiro et al., 2004; Kunihiro et al., 2005).

The analysis that comes closest to having an oxygen isotopic profile is by Yurimoto and Wasson (2002), who analyzed an 80 micron wide relict grain from the CO chondrite Yamato 81020. They analyzed ~15 locations dispersed throughout the grain to show it was concentrically zoned in oxygen from core (^{16}O-rich) to edge (^{16}O-poor). It is also normally zoned from core to edge in Fe-Mg. Based on my experimental results and the photographs in the Yurimoto and Wasson study, it would appear that this relict grain experienced dissolution followed by significant oxygen diffusion by remaining at relatively high temperatures for an extended period of time (probably several hundred hours). The chondrule mesostasis contains a quench texture, while the relict contains only a thin olivine overgrowth (which was not analyzed). Together, these suggest the chondrule was cooled from high to low temperature quite rapidly and therefore did not allow a significant overgrowth to crystallize.

Two spectacular candidate relict grains to analyze in the future to further test the results found here (and determine the diffusional extent of oxygen) are in chondrules in the CO3 chondrite, Acfer 094 (Kunihiro et al., 2005). Within this study are two very magnesian relicts that are surrounded by overgrowths. The first relict (60 micron in diameter) is surrounded by a 40 micron thick FeO-rich overgrowth [A4q within Kunihiro et al (2005)]. The second grain measures 100 microns by 60 microns and contains an extremely MgO-rich core surrounded by a thin 10 micron FeO-rich overgrowth [M7f within Kunihiro et al (2005)]. Other relict grains with less extreme Fe-Mg zonation can be seen in adjacent grains within the same chondrule. For the first grain, analysis determined that the relict is more ^{16}O rich than the overgrowth. This is presumably the case for the second grain as well, though no analysis of the overgrowth was made.

It is clear that a careful and systematic oxygen isotopic survey of chondrules in the major low metamorphic grade chondrite groups is needed to address questions concerning the population of relict grains, the history of those relict grains and the history of the chondrules that contain those grains. This will in turn provide fundamental information for future models and ideas concerning chondrule formation processes in the early solar nebula.

CONCLUSIONS

Relict grains are preserved in chondrules when processes such as melting, dissolution and diffusion only partially obscure or obliterate the grain. Dissolution predominantly determines the final size of the relict grain by reacting it with the chondrule melt. Subsequently, the degree of diffusion determines whether the relict can be recognized as such. In order to erase ALL traces of the relict signature from a relict olivine within a "typical" chondrule crystallization timescale, the grain must be either dissolved in the chondrule mesostasis or outright melted as the relict oxygen signature will persist. However, to simply obscure a relict from simple electron microprobe analysis (Fe-Mg), standard estimated chondrule cooling rates (<100ºC/hr) easily suffice.

As a consequence of obscuring a relict grain from electron microprobe detection, the relict grain population is likely much higher than 15%, as originally estimated by Jones et al. (1996). It is likely near or above 30%. If many relict grains have the same isotopic composition as phenocrysts, there may be fewer unrecognized relict grains.

Evaporation effects are prevalent within many of these experiments but are only minor in real chondrules. The absence of an abundant silica phase in chondrules would

argue against evaporation. However, pyroxene and silica do occur in CR and Al-rich chondrules. Evaporation within the experiments actually facilitates the tracking of the pathway taken by the isotopic compositions of the melt and overgrowths. While evaporation progressively makes the glass composition heavier in $\delta^{18}O$, silica crystallization acts to reverse the trend by *preferentially partitioning for* the heavier isotopes.

Overgrowths adopt the oxygen isotopic composition of the melt and form abrupt boundaries with the relict grains. Based on the experiments and simple minded calculations and considerations, erasure of a relict oxygen signature by diffusion with the overgrowth could occur on the order of weeks (hundreds of hours) if relatively high temperatures (~1400-1500℃) are maintained. It is more likely however that the oxygen signature over that time period will become less prevalent and simply adopt a less steep gradient with the surrounding overgrowth or mesostasis.

REFERENCES

Buening D. K. and Buseck P. R. (1973) Fe-Mg lattice diffusion in olivine. *Journal of Geophysical Research* **78**, 6852-6862.

Canil D. and Muehlenbachs K.(1990) Oxygen diffusion in a Fe-rich basalt melt. *Geochimica et Cosmochimica Acta* **54**, 2947-2951.

Chacko T., Cole D. R. and Horita J. (2001) Equilibrium oxygen, hydrogen and carbon isotope fractionation factors applicable to geologic systems. In *Stable Isotope Geochemistry* (J. W. Valley and D. R. Cole, eds.) pp. 1-81. Reviews in Mineralogy and Geochemistry **43**, Washington D.C.

Clayton R. N. and Mayeda T. K. (1996) Oxygen isotope studies of achondrites. *Geochimica et Cosmochimica Acta* **60**, 1999-2017.

Deer W. A., Howie R. A. and Zussman J. (1992) *An introduction to the rock-forming minerals*, 2nd ed., Longman, Essex, England.

Desch S. J. and Connolly H. C., Jr. (2002) A model of the thermal processing of particles in solar nebula shocks: Application to the cooling rates of chondrules. *Meteoritics and Planetary Science* **37**, 183-207.

Freer R. (1981) Diffusion in silicate minerals and glasses: A data digest and guide to the literature. *Contributions to Mineralogy and Petrology* **76**, 440-454.

Grossman J. N., Rubin A. E., Nagahara H. and King E. A. (1988) Properties of chondrules. In *Meteorites and the Early Solar System* (J. F. Kerridge and M. S. Matthews, eds.) pp. 619-659. University of Arizona Press, Tucson.

Hewins R. H. (1999) Relict pyroxene – Constraint on chondrule melting? *Lunar and Planetary Science* **XXX**, abstract #1678 (CD-ROM).

Hervig R. L. and Steele I. M. (1992) Oxygen isotopic analysis of Allende olivine by ion microprobe and implications for chondrule origin. *Lunar and Planetary Science* **XXIII**, 526-527 (abstract).

Hiyagon H. (1997) In situ analysis of oxygen isotopes and Fe/Mg ratios in olivine using SIMS: Preliminary results for an Allende chondrule. *Antarctic Meteorite Research* **10**, 249-274.

Jaoul O., Froidevaux C., Durham W. B. and Michaut M. (1980) Oxygen self-diffusion in forsterite: Implications for the high-temperature creep mechanism. *Earth and Planetary Science Letters* **47**, 391-397.

Jones R. H. (1990) Petrology and mineralogy of type-II, FeO-rich chondrules in Semarkona (LL3.0) – Origin by closed-system fractional crystallization, with evidence for supercooling *Geochimica et Cosmochimica Acta* **54**, 1785-1802.

Jones R. H. (1992) On the relationship between isolated and chondrule olivine grains in the carbonaceous chondrite ALHA 77307. *Geochimica et Cosmochimica Acta* **56**, 467-482.

Jones R. H. (1993) Effect of metamorphism on isolated olivine grains in CO3 chondrites. *Geochimica et Cosmochimica Acta* **57**, 2853-2867.

Jones R. H. (1996) Relict grains in chondrules: Evidence for chondrule recycling. In *Chondrules and the Protoplanetary Disk* (R. H. Hewins et al, eds.) pp. 163-172, Cambridge University Press, New York.

Jones R. H. and Danielson L. R. (1997) A chondrule origin for dusty relict olivine in unequilibrated chondrites. *Meteoritics and Planetary Science* **32**, 753-760.

Jones R. H., Grossman J. N. and Rubin A. E. (2005) Chemical, mineralogical and isotopic properties of chondrules: Clues to their origin. In *Chondrites and the Protoplanetary Disk* (A. N. Krot et al. eds.) pp. 251-285. Astronomical Society of the Pacific, Volume **341**, San Francisco.

Jones R. H., Leshin L. A. and Guan Y. (2002) Heterogeneity and ^{16}O-enrichments in oxygen isotope ratios of olivine from chondrules in the Mokoia CV3 chondrite**.** *Lunar and Planetary Science* **XXXIII**, abstract #1571 (CD-ROM).

Jones R. H., Saxton J. M., Lyon, I. C. and Turner G. (2000) Oxygen isotopes in chondrule olivine and isolated olivine grains from the CO3 chondrite Allan Hills A77307. *Meteoritics and Planetary Science* **35**, 849-857.

Kitamura M., Isobe H. and Watanabe S. (1988) Relict minerals and their assemblages in Yamato-691 (EH3). *Proceedings of the National Institute on Polar Research Symposium on Antarctic Meteorites* **1**, 38-50.

Kracher A., Scott E. R. D. and Keil K. (1984) Relict and other anomalous grains in chondrules: Implications for chondrule formation. *Proceedings of the 14th Lunar and Planetary Science Conference (Part 2) Journal of Geophysical Research (Supplement)* 89, B559-B566.

Krot A. N., Fagan T. J., Keil K., McKeegan K. D., Sahijpal S., Hutcheon I. D., Petaev M. I. and Yurimoto H. (2004) Ca, Al-rich inclusions, amoeboid olivine aggregates, and Al-rich chondrules from the unique carbonaceous chondrite Acfer 094: I. mineralogy and petrology. *Geochimica et Cosmochimica Acta* **68**, 2167-2184.

Kunihiro T., Rubin A. E., McKeegan K. D. and Wasson J. T. (2003) Oxygen-isotope composition of relict grains in carbonaceous-chondrite chondrules. *Meteoritics and Planetary Science* **38**, A138.

Kunihiro T., Rubin A. E., McKeegan K. D. and Wasson J. T. (2004) Oxygen-isotopic compositions of relict and host grains in chondrules in the Yamato 81020 CO3.0 chondrite. *Geochimica et Cosmochimica Acta* **68**, 3599-3606.

Kunihiro T., Rubin A. E., McKeegan K. D. and Wasson J. T. (2005) Oxygen-isotopic compositions of low-FeO relict in high-FeO host chondrules in Acfer 094, a type 3.0 carbonaceous chondrite closely related to CM. *Geochimica et Cosmochimica Acta* **69**, 3831-3840.

Leitch C. A. and Smith J. V. (1982) Petrography, mineral chemistry, and origin of Type I enstatite chondrites. *Geochimica et Cosmochimica Acta* **46**, 2083-2097.

Leshin L. A., McKeegan K. D., Engrand C., Zanda B., Bourot-Denise M. and Hewins R. H. (1998) Oxygen-isotopic studies of isolated and chondrule olivine from Renazzo and Allende. *Meteoritics and Planetary Science* **33**, A93-A94 (abstract).

McKinley S. G., Scott E. R. D. and Keil K. (1984) Composition and origin of enstatite in E chondrites. *Journal of Geophysical Research, Supplement* **89**, B567-B572.

Metzler K., Bischoff A. and Stoffler D. (1992) Accretionary dust mantles in CM chondrites: Evidence for solar nebula processes. *Geochimica et Cosmochimica Acta* **56**, 1873-1898.

Misawa K. and Fujita T. (1994) A relict refractory inclusion in a ferromagnesian chondrule from the Allende meteorite. *Nature* **368**, 723-726

Nagahara H. (1981) Evidence for secondary origin of chondrules. *Nature* **292**, 135-136.

Nagahara H. (1983) Chondrules formed through incomplete melting of the pre-existing minerals and the origin of chondrules. In *Chondrules and Their Origins* (E. A. King, ed.) pp. 211-222. Lunar and Planetary Institute, Houston.

Palme H., Spettel B. and Steele I. (1986) Trace elements in forsterite-rich inclusions in Allende. *Lunar and Planetary Science* **XVII**, 640-641 (abstract).

Pouchou J. and Pichour F. (1991) Quantitative analysis of homogeneous or stratified microvolumes applying the model "PAP". In *Electron Probe Quantitation* (eds. K. F. J. Heinrich and D. E. Newbury), Plenum Press, New York, 31-75.

Rambaldi E. R. (1981) Relict grains in chondrules. *Nature* **293**, 558-561.

Rambaldi E. R. and Wang D. (1982) Relict grains in enstatite chondrites. *Meteoritics* **17**, 272 (abstract).

Rambaldi E. R. and Wasson J. T. (1982) Fine, nickel-poor Fe-Ni grains in the olivine of unequilibrated ordinary chondrites. *Geochimica et Cosmochimica Acta* **45**, 1001-1015.

Rambaldi E. R., Rajan R. S., Wang D. and Housley R. M. (1983) Evidence for relict grains in chondrules of Qingzhen, an E3-type enstatite chondrite. *Earth and Planetary Science Letters* **66**, 11-24

Rubin A. E., James J. A., Keck B. D., Weeks K. S., Sears D. W. G. and Jarosewich E. (1985) The Colony meteorite and variations in CO3 chondrite properties. *Meteoritics* **20**, 175-196.

Ruzicka A., Hiyagon H. and Floss C. (2005) Relict olivine, chondrule recycling, and evolution of oxygen reservoirs. Oxygen in Asteroids and Meteorites Workshop, abstract #7009 (CD-ROM).

Ruzicka A., Hiyagon H., Hutson M. and Floss C. (2007) Relict olivine, chondrule recycling, and the evolution of nebular oxygen reservoirs. *Earth and Planetary Science Letters*, in press.

Saxton J. M., Lyon I. C., Turner G. (1998) Oxygen isotopes in forsterite grains from Julesburg and Allende: Oxygen-16-rich material in an ordinary chondrite. *Meteoritics and Planetary Science* **33**, 1017-1027.

Sears D. W. G., Lyon I., Saxton J. and Turner G. (1998) The oxygen isotopic properties of olivines in the Semarkona ordinary chondrite. *Meteoritics and Planetary Science* **33**, 1029-1032.

Sears D. W. G., Lyon I. C., Saxton J. M., Symes S. and Turner G. (1999) Oxygen isotope heterogeneity in the mesostasis of a Semarkona group A1 chondrule. *Lunar and Planetary Science* **XXX**, abstract #1406 (CD-ROM).

Steele I. M. (1986) Compositions and textures of relic forsterite in carbonaceous and unequilibrated ordinary chondrites. *Geochimica et Cosmochimica Acta* **50**, 1379-1395.

Steele I. M. (1988) Primitive material surviving in chondrites: Mineral grains. In *Meteorites and the Early Solar System* (J. F. Kerridge and M. S. Matthews, eds.) pp. 808-818. University of Arizona Press, Tucson.

Steele I. M. (1989) Compositions of relic forsterites in Ornans (C3O) *Geochimica et Cosmochimica Acta* **53**, 2069-2079.

Wasson J. T. and Rubin A. E. (2003) Ubiquitous low-FeO relict grains in type II chondrules and limited overgrowths on phenocrysts following the final melting event *Geochimica et Cosmochimica Acta* **67**, 2239-2250.

Wasson J. T., Rubin A. E. and Yurimoto H. (2004) Evidence in CO3.0 chondrules for a drift in the O isotopic composition of the solar nebula. *Meteoritics and Planetary Science* **39**, 1591-1598.

Weinbruch S., Palme H. and Spettel B. (2000) Refractory forsterite in primitive meteorites: Condensates from the solar nebula? *Meteoritics and Planetary Science* **35**, 161-171.

Wendlandt R. W. (1991) Oxygen diffusion in basalt and andesite melts: Experimental results and discussion of chemical versus tracer diffusion. *Contributions to Mineralogy and Petrology* **108**, 463-471.

Yurimoto H. and Wasson J. T. (2002) Extremely rapid cooling of a carbonaceous-chondrite chondrule containing very ^{16}O-rich olivine and a ^{26}Mg-excess. *Geochimica et Cosmochimica Acta* **66**, 4355-4363.

FIGURE CAPTIONS

Figure 4.1 (a-c). Backscattered electron images of the one atmosphere furnace test experiments used to determine the textural progression of the isothermal experimental runs which could not be quenched at high temperature in the vacuum furnace. Figure 4.1a shows a texture nearly identical to most of the isothermal runs, having melt-grown olivine or pyroxene surrounding the relict olivine with additional melt-grown crystals and quench crystals within the mesostasis. This was produced by holding the experiment at 1500ºC for 8 minutes and then sending the temperature down to 1425ºC at 60ºC per minute, and allowing the experiment to quench by simple radiation in air. Field of view is 600 microns. Figure 4.1b shows what the isothermal experiments would have looked like if water quenching was possible in the vacuum furnace. This texture was produced by holding the experiment at 1500ºC for 8 minutes and then drop quenching into water. Note the complete lack of quench crystals and substantially lower abundance of melt-grown olivine and pyroxene. Field of view is 1100 microns. Figure 4.1c is the intermediate step between 1a and 1b showing the effect of only sending the temperature from 1500ºC after 8 minutes down to 1425ºC at 60ºC per minute and then quenching in water. Field of view is 1600 microns.

Figure 4.2 (a-s). Backscattered electron images of the isothermal experiments with the ion microprobe analysis locations noted as yellow dots. Ion microprobe analyses match Figure 4.3 diagrams.

Figure 4.3 (a-s). Results of ion microprobe [$\delta^{18}O$] and electron microprobe [100*Fe/(Fe+Mg)] profiles across portions of the isothermal experiments. The relict portions of olivines maintain their original oxygen isotopic compositions (-2.78‰) throughout the series of experiments, however their 100*Fe/(Fe+Mg) ratio is modified with increasing duration and temperature. The melt-grown olivines and pyroxenes adopt an isotopic composition close to that of the mesostasis (Fig 4.3j is a good example). Vertical red labels are as follows: edge = olivine edge, core = olivine core, mol = melt-grown olivine, mpx = melt-grown pyroxene, meso = mesostasis +/- quench olivine and pyroxene crystals. Unlabeled points are interior regions of the olivine grain between the core and edge.

Figure 4.4 (a-n). Backscattered electron images of the dynamic crystallization experiments with the ion microprobe analysis locations noted as yellow dots. Ion microprobe analyses match Figure 4.5 diagrams.

Figure 4.5 (a-n). Results of ion microprobe [$\delta^{18}O$] and electron microprobe [100*Fe/(Fe+Mg)] profiles across portions of the dynamic crystallization experiments. The relict portions of olivines maintain their original oxygen isotopic compositions (-2.78‰) throughout the series of experiments, however their 100*Fe/(Fe+Mg) ratio is modified with decreasing cooling rate (increased duration). The melt-grown olivines and pyroxenes adopt an isotopic composition close to that of the mesostasis. Longer duration runs show definite evaporation effects (i.e. more extreme $\delta^{18}O$ glass and melt-grown olivine and pyroxene compositions) and are very comparable to those seen in Chapter 3.

Vertical red labels are as follows: edge = olivine edge, core = olivine core, mol = melt-grown olivine, mpx = melt-grown pyroxene, meso = mesostasis +/- quench olivine and pyroxene crystals. Unlabeled points are interior regions of the olivine between the core and edge. In some cases, core or edge labels are the core or edge of melt-grown olivines and not relict Eagle Station olivines.

Figure 4.6. A plot of the maximum olivine overgrowth $\delta^{18}O$ composition measured in each dynamic crystallization experiment versus duration (log scale). The inverted V-shaped pattern is produced by three competing factors: 1) dissolution of Eagle Station olivine into the melt, 2) evaporation of FeO from the experiment and 3) crystallization of tridymite. Evaporation forces the $\delta^{18}O$ composition to higher values, while dissolution and tridymite formation reduce the $\delta^{18}O$ values. On the positive slope, evaporation dominates, even though dissolution of Eagle Station is increasing with time and some minor tridymite crystallization occurs (starting at the 200℃ per hour experiment). On the negative slope, tridymite crystallization becomes so abundant (FeO loss has shifted the bulk composition to be extreme pyroxene normative), that the evaporation effect on the $\delta^{18}O$ values is equaled and exceeded. The dip in the graph at 100℃ per hour probably results from a lack of representative $\delta^{18}O$ data from the overgrowths.

Figure 4.7. Diagram showing the effect of diffusion on the relict grain when compared to the crystallization rate of the overgrowth. The model schematically shows through equally spaced time slices (A to D) diffusion progressing as the overgrowth/melt boundary (I) crystallizes away from the relict grain (R). The diffusion rate of a given species (such Fe or Mg) in the example is assumed to be half the crystallization rate of the overgrowth. For simplicity, the species in question is shown moving towards or away from a boundary. In the models, it is shown that atoms at the boundaries can only diffuse a distance of X [either inwards (white box with black X) or outwards (black box with white x). In the first time slice, once the overgrowth crystallizes beyond one distance of X, the relict becomes cut off from diffusion with the melt. The time slices show that the relict only has time to exchange with the innermost portion of the overgrowth (O_1). Despite the relatively slow diffusion, a large proportion of the overgrowth can diffuse with itself because of the moving boundary condition. However, there are still areas diffusion does not reach due to insufficient time. The moving boundary facilitates diffusion and makes the compositional gradient less steep in the overgrowth (I_1 to I_4). Only with substantial time can a species diffuse the entire distance between the relict interior and the final overgrowth (i.e. melt and relict exchange through the overgrowth).

Figure 4.8. Plot of $\delta^{18}O$ versus $\delta^{17}O$ showing the evaporation experiments of the IIAB chondrule analog glass from Chapter 3. Using these experiments, it was determined that for every four fold increase in duration there is a corresponding halving of the effective distance the melt can further fractionate in $\delta^{18}O$ as a result of evaporation. This diagram only shows isothermal experiments at 1515℃ and can only be used to guestimate the influence duration has on the dynamic crystallization experiments. The diagram does demonstrate however that evaporation asymptotically levels off with duration.

Table 4.1. Starting composition IIAB glass and Eagle Station olivine.

	$\delta^{18}O$	$\delta^{17}O$	$\Delta^{17}O$[e]	SiO_2	TiO_2	Al_2O_3	Cr_2O_3	FeO	MnO	MgO	CaO	Na_2O	K_2O	Total
IIAB analog[a]	11.98	6.39	0.16	50.92	0.18	0.89	0.40	21.52	0.42	22.89	1.07	1.79	0.22	100.3
Eagle Station olivine[b]	-2.78	-5.96	-4.51	38.21	0.00	0.00	0.03	19.01	0.16	42.23	0.03	0.00	0.00	99.67
"Isothermal" Comp.[c]	8.29	3.30	-1.01	47.74	0.13	0.67	0.31	20.89	0.35	27.73	0.81	1.34	0.16	100.13
"Dynamic" Comp.[d]	4.60	0.22	-2.17	44.56	0.09	0.45	0.22	20.27	0.29	32.56	0.55	0.90	0.11	100.00

Notes:
a - Oxygen isotopic composition analyzed by E. Young (UCLA) - see Chapter 3 for details.
b - Oxygen isotopic composition analyzed by Clayton (1996).
c - Assumes all of the Eagle Station available dissolves into the IIAB melt. By mass, Eagle station is 25%, and the IIAB melt 75% of each experimental charge in the isothermal experiments.
d - Assumes all of the Eagle Station available dissolves into the IIAB melt. By mass, Eagle station is 50%, and the IIAB melt 50% of each experimental charge in the dynamic crystallization experiments.
e - $\Delta^{17}O = \delta^{17}O-(0.52)(\delta^{18}O)$

Table 4.2. Bulk compositions of the glass (plus quench crystals and melt-grown olivines and pyroxenes) in the high temperature isothermal experiments determined by rastered beam analysis on the electron microprobe. Based on the endmember compositions in Table 4.1, the abundance of Eagle Station olivine dissolved in the melt and the amount of FeO lost (to either evaporation or the Pt wire) was determined.

	SiO_2	TiO_2	Al_2O_3	Cr_2O_3	FeO	MnO	MgO	CaO	Total	# of analyses
Starting Comp.[a]	51.81	0.18	0.91	0.41	21.89	0.43	23.29	1.09	100.00	
1500ºC 32min #512	50.57 (1.18)	-	0.85 (0.18)	-	21.33 (1.68)	-	24.75 (3.33)	1.04 (0.23)	98.54 (0.56)	107
1500ºC 8min #510	50.46 (1.67)	-	0.89 (0.24)	-	22.03 (2.33)	-	23.63 (3.56)	1.06 (0.28)	98.07 (0.81)	120
1500ºC 2min #508	51.71 (1.16)	-	0.91 (0.23)	-	21.87 (2.76)	-	23.34 (4.04)	1.08 (0.40)	98.92 (0.87)	112
1515ºC 32min #530	50.82 (1.58)	-	0.78 (0.15)	-	19.03 (1.58)	-	26.75 (3.55)	0.94 (0.20)	98.32 (0.92)	104
1515ºC 8min #531	49.48 (0.84)	-	0.82 (0.21)	-	21.51 (1.05)	-	25.83 (1.91)	0.95 (0.11)	98.59 (0.57)	124
1515ºC 2min #532	49.14 (0.90)	-	0.84 (0.20)	-	21.95 (1.55)	-	25.56 (2.84)	1.01 (0.14)	98.49 (0.65)	116

	Eagle Station Dissolved (wt %)	FeO lost	ES ^{18}O proportion	IIAB proportion	Final melt ^{18}O composition[b]
1500ºC 32min #512	8%	2% (~0.5wt% FeO)	-0.21	11.09	10.88
1500ºC 8min #510	2%	-	-0.06	11.75	11.69
1500ºC 2min #508	1%	-	-0.03	11.86	11.83
1515ºC 32min #530	20%	15% (~3.2 wt% FeO)	-0.46	9.98	9.52
1515ºC 8min #531	15%	5% (~1.1 wt%FeO)	-0.36	10.42	10.06
1515ºC 2min #532	10%	-	-0.25	10.89	10.64

Notes:
[a] Starting composition renormalized to volatile-free. TiO_2, Cr_2O_3 and MnO were not analyzed to determine extent of dissolution or FeO loss. One standard deviation is listed in the parentheses.
[b] Assumes no evaporative fractionation.

Table 4.3. Run conditions and analytical results of the isothermal experiments.

Sample	$\delta^{18}O$	$\delta^{17}O$	$\Delta^{17}O$	Dist	SiO_2	TiO_2	Al_2O_3	Cr_2O_3	FeO	MnO	MgO	CaO	Na_2O	K_2O	Total
1300ºC 128min #522															
1 oliv core	-0.33	-4.58	-4.41		39.37	0.00	0.09	0.01	19.24	0.20	42.33	0.06	0.00	0.00	101.30
2 oliv edge	-2.27	-6.55	-5.37		39.13	0.00	0.06	0.02	19.36	0.16	41.94	0.04	0.01	0.00	100.73
3 oliv edge	-0.49	-3.65	-3.40		39.27	0.00	0.09	0.01	19.13	0.15	42.01	0.08	0.00	0.00	100.75
4 oliv edge	-0.24	-2.83	-2.71		39.38	0.02	0.07	0.03	18.99	0.17	42.21	0.05	0.00	0.00	100.91
5 oliv edge	-1.50	-4.41	-3.63		39.13	0.02	0.09	0.03	20.07	0.18	41.31	0.07	0.00	0.01	100.90
6 oliv edge	11.81	7.01	0.87		39.25	0.00	0.10	0.02	19.86	0.22	41.48	0.09	0.00	0.00	101.02
1300ºC 64min #521															
P3 oliv edge	-3.17	-5.82	-4.18	0	39.31	0.00	0.01	0.02	19.09	0.20	42.30	0.00	0.00	0.00	100.92
P2 oliv interior	-2.95	-6.00	-4.47	100	38.89	0.02	0.01	0.01	20.00	0.16	41.06	0.09	0.01	0.00	100.26
P1 oliv interior	-3.11	-4.71	-3.10	160	39.11	0.00	0.00	0.02	19.01	0.17	42.33	0.01	0.00	0.00	100.66
P6 oliv core	-3.54	-5.31	-3.47	180	39.23	0.00	0.00	0.02	19.23	0.17	42.34	0.01	0.01	0.00	101.01
P5 oliv interior	-0.28	-2.24	-2.10	200	39.08	0.03	0.03	0.01	19.44	0.21	42.02	0.01	0.00	0.00	100.82
P4 oliv interior	0.54	-0.71	-0.99	220	38.06	0.00	0.02	0.01	24.34	0.39	37.86	0.06	0.01	0.01	100.75
P7 oliv interior	-0.87	-2.02	-1.57	270	38.55	0.00	0.03	0.01	24.08	0.31	37.60	0.05	0.00	0.01	100.64
P8 mesostasis	10.46	6.95	1.51	310	54.61	0.06	0.48	0.04	17.21	0.28	27.51	0.30	0.00	0.00	100.49
9 mesostasis	10.80	7.70	2.08		54.37	0.04	0.34	0.04	19.23	0.19	25.82	0.28	0.01	0.00	100.33
1300ºC 32min #520															
P2 oliv core	-3.02	-4.58	-3.01	0	37.94	0.00	0.03	0.03	24.09	0.23	38.20	0.04	0.04	0.00	100.59
P3 oliv interior	-2.64	-5.45	-4.08	70	38.77	0.01	0.00	0.02	20.68	0.20	41.10	0.01	0.03	0.00	100.84
P9 oliv core	-2.78	-5.96	-4.52	100	38.62	0.01	0.02	0.01	20.56	0.20	40.95	0.05	0.06	0.00	100.48
P8 oliv interior	-1.11	-3.47	-2.90	170	38.83	0.00	0.02	0.02	20.29	0.19	41.41	0.03	0.03	0.00	100.82
P6 oliv interior	1.08	-2.40	-2.97	190	38.81	0.04	0.04	0.02	19.92	0.18	41.49	0.04	0.02	0.00	100.56
P5 oliv edge	13.73	8.17	1.03	210	38.94	0.00	0.03	0.02	19.66	0.17	42.04	0.02	0.00	0.00	100.89
P7 oliv edge	0.38	-2.72	-2.92	230	38.95	0.00	0.01	0.02	19.23	0.17	42.17	0.03	0.01	0.00	100.59
P4 oliv edge	11.81	8.74	2.60	250	39.08	0.00	0.02	0.02	19.10	0.19	42.53	0.03	0.00	0.00	100.97

1 oliv core	-1.87	-6.81	-5.84		39.23	0.00	0.01	0.02	18.92	0.16	42.39	0.01	0.02	0.00	100.75
1300ºC 16min #519															
P1 oliv core	-2.77	-5.96	-4.52	0	39.25	0.00	0.03	0.03	18.75	0.36	42.24	0.09	0.03	0.00	100.78
P5 oliv edge	-2.23	-4.37	-3.21	20	39.19	0.00	0.07	0.04	18.15	1.08	42.21	0.11	0.05	0.00	100.89
P4 mesostasis	2.00	0.61	-0.43	40	54.53	0.04	0.11	0.29	5.85	14.37	25.47	0.41	0.14	0.00	101.21
P3 mesostasis	11.39	8.45	2.52	60	57.78	0.49	3.12	0.05	17.73	6.82	8.84	2.79	0.82	0.50	98.95
P2 silica	10.87	7.36	1.70	80	97.11	0.04	0.39	0.01	1.10	0.55	0.79	0.14	0.20	0.03	100.36
1400ºC 64min #529															
P1 oliv core	-2.72	-5.31	-3.90	0	39.37	0.01	0.00	0.04	18.32	0.20	42.85	0.02	0.01	0.00	100.80
P48 oliv interior	-4.14	-7.06	-4.91	100	39.68	0.00	0.00	0.04	17.61	0.32	43.74	0.00	0.01	0.00	101.40
P49 oliv edge	9.71	4.21	-0.84	200	39.94	0.01	0.00	0.02	16.37	0.29	44.56	0.02	0.01	0.00	101.23
3 oliv edge	-4.70	-6.75	-4.30		40.01	0.03	0.01	0.04	17.83	0.26	43.66	0.06	0.00	0.00	101.89
2 oliv edge	-2.77	-4.57	-3.13		39.60	0.00	0.00	0.02	16.95	0.31	44.25	0.04	0.00	0.00	101.18
4 mesostasis	9.97	5.50	0.32		52.05	0.30	2.90	0.09	28.08	0.74	12.67	4.12	0.11	0.06	101.12
5 melt grn oliv	8.71	5.56	1.03		39.53	0.01	0.00	0.04	18.32	0.20	42.85	0.02	0.01	0.00	100.97
6 melt grn oliv	8.39	5.19	0.82		39.94	0.00	0.00	0.03	16.46	0.31	44.41	0.01	0.01	0.00	101.17
7 melt grn pyx	6.02	2.86	-0.27		57.03	0.01	0.06	0.17	8.36	0.32	33.74	0.07	0.01	0.00	99.77
8 oliv edge	-6.27	-6.73	-3.47		39.46	0.01	0.01	0.06	16.84	0.33	44.24	0.03	0.00	0.00	100.97
1400ºC 32min #528															
P1 oliv core	-2.70	-5.95	-4.55	0	39.22	0.00	0.00	0.03	18.97	0.19	42.80	0.05	0.01	0.01	101.28
P2 oliv edge	-3.06	-6.20	-4.61	100	39.44	0.00	0.00	0.04	17.77	0.28	43.80	0.03	0.01	0.01	101.38
P3 mesostasis	10.69	5.05	-0.51	150	54.30	0.02	0.17	0.07	20.29	0.35	24.49	0.09	0.08	0.03	99.89
P4 oliv edge	7.04	1.87	-1.79	200	49.79	0.19	0.67	0.09	30.15	0.51	19.11	0.81	0.09	0.04	101.47
P5 oliv core	-3.73	-6.76	-4.82	250	39.35	0.00	0.00	0.01	18.90	0.19	42.84	0.02	0.00	0.00	101.31
1500ºC 32min #512															
P75 oliv interior	-1.80	-7.45	-6.51	0	39.36	0.00	0.00	0.03	16.63	0.23	44.58	0.00	0.00	0.00	100.79
P76 oliv interior	-2.28	-7.03	-5.85	25	39.42	0.00	0.00	0.00	17.88	0.21	43.30	0.01	0.02	0.00	100.83

P77 oliv interior	-2.40	-6.45	-5.20	45	39.55	0.02	0.00	0.03	17.88	0.20	43.61	0.03	0.01	0.00	101.28
P78 oliv core	-3.13	-5.42	-3.79	65	39.67	0.00	0.00	0.00	16.56	0.19	44.40	0.02	0.00	0.00	100.85
P79 oliv interior	-3.38	-5.02	-3.27	90	40.19	0.00	0.00	0.02	14.17	0.19	46.68	0.00	0.01	0.00	101.23
P82 oliv edge	12.53	7.34	0.83	160	40.56	0.00	0.00	0.01	13.22	0.18	47.57	0.02	0.00	0.00	101.55
P90 oliv interior	11.76	5.92	-0.20	0	40.62	0.00	0.00	0.01	13.88	0.21	46.97	0.04	0.00	0.00	101.71
P91 oliv edge	11.26	5.46	-0.40	30	40.30	0.00	0.00	0.00	14.50	0.25	46.54	0.00	0.01	0.00	101.61
P92 oliv edge	13.22	7.07	0.19	70	39.69	0.01	0.00	0.02	17.18	0.28	44.26	0.00	0.01	0.00	101.43
P93 melt grn pyx	13.55	7.14	0.09	105	50.41	0.85	4.79	0.04	32.09	0.65	4.84	5.97	0.02	0.00	99.62
P94 melt grn pyx	14.69	6.31	-1.33	140	50.24	0.81	2.64	0.06	37.61	0.34	4.91	2.67	0.00	0.00	99.22
P95 mesostasis	12.74	4.80	-1.83	175	50.75	0.07	0.51	0.01	27.96	0.51	19.75	0.70	0.00	0.00	100.25
P96 mesostasis	12.79	4.97	-1.69	205	55.31	0.46	3.12	0.02	24.22	0.60	11.29	3.61	0.00	0.00	98.62
P97 mesostasis (quench ol)	12.16	4.70	-1.63	230	39.70	0.00	0.00	0.04	17.71	0.22	43.61	0.02	0.00	0.00	101.26
P98 mesostasis (quench ol)	11.11	4.67	-1.11	265	39.61	0.03	0.00	0.00	17.01	0.15	44.00	0.01	0.00	0.00	100.80
P99 mesostasis (quench ol)	10.39	4.98	-0.43	300	39.47	0.00	0.01	0.02	17.85	0.18	43.62	0.00	0.00	0.00	101.13
100 oliv core	-2.66	-5.54	-4.15		39.51	0.00	0.00	0.01	18.21	0.18	43.39	0.00	0.00	0.00	101.30
83 melt grn pyx	-3.03	-5.90	-4.32		53.28	0.28	1.98	0.03	27.69	0.57	14.37	1.91	0.00	0.00	100.06
84 melt grn pyx	-2.07	-5.89	-4.81		53.02	0.28	2.15	0.03	28.31	0.64	12.95	2.64	0.00	0.00	99.98
1500ºC 16min #511															
P102 oliv edge	-2.83	-5.69	-4.22	0	39.02	0.02	0.07	0.00	18.85	0.19	42.42	0.00	0.00	0.01	100.57
P104 oliv core	-2.36	-5.93	-4.70	70	39.11	0.00	0.00	0.01	18.65	0.22	42.48	0.00	0.00	0.00	100.46
P105 oliv interior	-2.52	-6.20	-4.89	105	39.02	0.00	0.00	0.01	18.90	0.24	42.57	0.00	0.01	0.00	100.73
P106 oliv edge	-2.88	-6.29	-4.79	135	39.10	0.00	0.00	0.00	18.70	0.18	42.55	0.00	0.00	0.00	100.53
P107 oliv edge	6.83	0.02	-3.53	160	39.45	0.00	0.00	0.01	17.37	0.17	43.69	0.02	0.00	0.01	100.69
P108 mesostasis	9.53	7.22	2.27	170	57.89	0.00	0.01	0.09	13.02	0.22	35.00	0.01	0.00	0.00	106.15
P109 mesostasis	9.22	5.93	1.13	200	53.95	0.84	3.03	0.36	33.40	0.53	4.57	3.24	0.00	0.01	99.57
P110 mesostasis	11.90	6.09	-0.10	225	54.88	0.82	3.12	0.34	32.30	0.55	4.56	3.28	0.01	0.00	99.51
P111 oliv interior	6.09	0.28	-2.89	250	40.71	0.00	0.00	0.07	12.46	0.18	47.95	0.02	0.00	0.01	101.33
P112 oliv edge	0.79	-5.10	-5.51	275	39.25	0.00	0.00	0.03	17.97	0.14	43.18	0.02	0.00	0.00	100.56
P9 oliv edge	0.62	-5.70	-6.02	0	39.65	0.00	0.00	0.02	18.79	0.20	42.85	0.01	0.01	0.00	101.51

P10 oliv edge	-0.07	-5.76	-5.73	30	39.42	0.02	0.00	0.03	18.80	0.18	42.90	0.00	0.00	0.01	101.33
P11 oliv interior	-0.90	-6.10	-5.63	65	39.63	0.00	0.00	0.01	18.23	0.18	43.33	0.01	0.00	0.00	101.38
P12 oliv edge	6.88	-1.30	-4.87	90	40.18	0.00	0.00	0.06	15.48	0.18	44.26	0.03	0.02	0.00	100.15
P13 melt grn pyx	14.72	6.87	-0.79	115	53.02	0.00	0.00	0.15	14.67	0.25	33.74	0.00	0.02	0.01	101.70
P14 melt grn pyx	12.82	5.38	-1.28	140	54.42	0.03	0.04	0.16	14.11	0.23	31.32	0.04	0.00	0.00	100.19
P15 melt grn pyx	11.72	5.46	-0.64	165	55.94	0.00	0.06	0.19	14.43	0.25	30.29	0.05	0.00	0.00	101.02
P16 melt grn pyx	11.35	5.39	-0.51	190	57.44	0.06	0.04	0.19	14.15	0.22	28.13	0.04	0.01	0.00	100.10
P17 mesostasis	11.62	5.44	-0.60	220	54.59	0.06	0.24	0.32	21.54	0.43	23.15	0.24	0.00	0.00	100.24
P18 mesostasis	12.35	5.15	-1.27	245	53.94	0.11	0.54	0.48	23.64	0.56	19.41	0.53	0.00	0.00	98.73
P19 mesostasis	12.55	5.32	-1.20	270	52.96	0.21	0.95	0.52	26.37	0.57	18.59	1.05	0.02	0.01	100.72
P20 mesostasis	11.77	5.19	-0.93	295	50.78	0.32	1.31	0.62	32.30	0.61	12.15	1.59	0.00	0.00	99.05
23 melt grn oliv	-1.97	-5.65	-4.63		41.40	0.03	0.00	0.10	15.11	0.23	43.92	0.04	0.00	0.00	100.73
24 melt grn oliv	-3.28	-5.75	-4.04		40.42	0.04	0.00	0.10	14.31	0.24	46.32	0.02	0.00	0.00	101.35
114 melt grn pyx	10.04	5.63	0.41		58.24	0.01	0.02	0.08	13.59	0.26	28.84	0.05	0.01	0.00	101.00
115 melt grn pyx	10.38	5.97	0.57		54.68	0.00	0.03	0.12	14.98	0.29	30.14	0.05	0.00	0.00	100.18
117 melt grn pyx	-3.05	-5.84	-4.25		52.52	0.01	0.01	0.13	15.07	0.26	32.50	0.02	0.01	0.00	100.41
1500℃ 8min #510															
P118 oliv core	-2.04	-6.11	-5.05	0	38.75	0.00	0.00	0.02	19.00	0.15	41.97	0.04	0.00	0.00	99.92
P119 oliv core	-4.11	-6.14	-4.01	30	38.67	0.02	0.00	0.03	18.94	0.13	41.65	0.37	0.02	0.00	99.81
P120 oliv interior	-2.73	-5.86	-4.45	50	38.25	0.00	0.00	0.02	18.77	0.18	41.77	0.08	0.00	0.01	99.07
P121 oliv interior	-2.91	-5.63	-4.12	80	39.60	0.00	0.00	0.03	18.60	0.17	42.80	0.04	0.00	0.01	101.21
P123 oliv edge	2.57	-1.76	-3.09	135	40.38	0.00	0.00	0.04	13.80	0.21	46.26	0.00	0.00	0.00	100.65
P124 mesostasis	10.89	5.01	-0.65	165	58.01	0.01	0.13	0.12	19.19	0.33	22.72	0.10	0.00	0.01	100.49
P125 melt grn pyx	11.55	4.89	-1.11	195	54.99	0.03	0.06	0.07	18.55	0.32	26.44	0.06	0.00	0.01	100.45
P126 melt grn pyx	10.91	3.72	-1.95	225	51.33	0.89	3.56	0.25	16.45	0.40	24.69	3.14	0.01	0.00	100.47
P127 melt grn pyx	11.41	3.54	-2.39	260	53.66	0.00	0.01	0.05	14.28	0.25	32.40	0.00	0.00	0.00	100.61
P128 melt grn pyx	11.39	3.40	-2.52	280	52.67	0.00	0.02	0.07	15.75	0.27	32.56	0.04	0.00	0.00	101.32
129 oliv edge	-2.64	-6.06	-4.69		39.22	0.00	0.00	0.02	18.72	0.20	42.21	0.00	0.00	0.00	100.34
130 oliv interior	3.92	-0.98	-3.02		39.59	0.00	0.00	0.02	17.40	0.17	43.99	0.00	0.01	0.00	101.16
131 oliv core	-2.28	-5.95	-4.77		39.15	0.00	0.00	0.02	18.29	0.17	42.59	0.00	0.00	0.00	100.20

1500ºC 4min #507															
P176 oliv core	-2.04	-6.51	-5.45	0	39.72	0.00	0.00	0.02	18.40	0.19	42.80	0.03	0.00	0.00	101.14
P177 oliv interior	-3.15	-5.54	-3.91	40	40.42	0.01	0.00	0.03	14.76	0.21	46.07	0.00	0.01	0.00	101.49
P178 oliv edge	5.07	0.84	-1.79	80	44.24	0.36	2.95	0.02	39.23	0.74	6.72	5.07	0.01	0.00	99.32
P179 meso /melt grn oliv	12.57	6.68	0.14	120	47.09	0.54	3.54	0.02	34.96	0.73	6.57	5.17	0.05	0.01	98.65
P180 meso /melt grn oliv	11.80	5.70	-0.44	160	46.80	0.55	3.38	0.03	36.08	0.66	6.68	4.92	0.03	0.01	99.10
P181 meso /melt grn oliv	7.99	4.83	0.68	200	42.22	0.38	1.18	0.04	43.58	0.61	9.31	1.34	0.01	0.01	98.63
P182 meso /melt grn oliv	9.12	5.95	1.20	230	50.60	0.19	1.80	0.05	30.57	0.78	13.66	3.15	0.03	0.00	100.77
P183 meso /melt grn oliv	9.70	6.39	1.35	260	48.07	0.31	1.25	0.02	34.19	0.65	11.79	1.68	0.02	0.00	97.95
P184 meso /melt grn oliv	8.98	5.89	1.22	295	38.55	0.68	1.77	0.01	50.11	0.65	4.41	2.69	0.01	0.01	98.89
P185 meso /melt grn oliv	8.14	5.88	1.64	330	39.76	0.53	1.80	0.05	48.44	0.66	3.34	4.56	0.04	0.01	99.13
P186 meso /melt grn oliv	10.52	5.92	0.45	370	40.15	1.46	4.96	0.00	42.39	0.61	0.19	9.17	0.03	0.02	98.99
1500ºC 2min #508															
P154 oliv interior	-3.85	-6.12	-4.12	0	39.68	0.02	0.00	0.02	18.58	0.23	42.82	0.00	0.00	0.00	101.33
P155 oliv interior	-2.19	-5.69	-4.55	25	38.95	0.00	0.00	0.02	19.51	0.16	41.61	0.00	0.00	0.01	100.23
P156 oliv core	-1.64	-5.82	-4.97	45	37.91	0.00	4.96	0.01	18.05	0.14	39.26	0.02	0.00	0.00	100.34
P157 oliv core	-1.77	-6.24	-5.32	70	39.63	0.00	0.00	0.01	18.85	0.14	42.69	0.02	0.00	0.00	101.34
P158 oliv interior	-1.70	-4.83	-3.95	90	39.40	0.00	0.26	0.02	18.52	0.21	43.05	0.00	0.01	0.00	101.45
P159 oliv interior	-1.46	-4.90	-4.14	120	39.05	0.00	0.00	0.02	18.82	0.22	41.68	0.01	0.00	0.00	99.77
P160 oliv interior	-0.45	-5.64	-5.41	140	39.92	0.01	0.00	0.01	18.73	0.13	42.69	0.02	0.00	0.00	101.51
P161 oliv edge	-1.42	-4.38	-3.64	165	39.67	0.00	0.00	0.02	18.34	0.20	42.60	0.01	0.00	0.00	100.83
P162 melt grn oliv	11.13	8.01	2.22	190	40.33	0.00	0.00	0.09	15.62	0.23	45.67	0.00	0.02	0.00	101.86
P163 melt grn oliv	7.77	7.58	3.54	215	40.35	0.17	0.21	0.34	14.10	0.37	45.31	0.21	0.08	0.01	100.82
P164 melt grn oliv	6.29	7.46	4.19	240	40.50	0.00	0.00	0.21	13.92	0.31	46.53	0.00	0.01	0.00	101.28
P165 melt grn oliv	10.94	6.99	1.30	265	40.15	0.02	0.00	0.24	14.40	0.30	46.08	0.01	0.00	0.00	100.98
P166 melt grn oliv	10.54	6.32	0.83	290	40.53	0.01	0.00	0.21	13.70	0.32	46.30	0.00	0.00	0.00	100.86
167 melt grn oliv	10.61	4.97	-0.55		40.98	0.01	0.00	0.29	15.16	0.33	45.15	0.01	0.01	0.00	101.64
168 melt grn oliv	9.24	4.92	0.11		41.46	0.04	0.00	0.28	15.33	0.43	44.12	0.02	0.00	0.00	101.40
169 oliv core	-3.62	-5.78	-3.90		39.47	0.00	0.07	0.04	18.67	0.20	42.50	0.04	0.01	0.00	100.96
170 oliv core	-3.62	-6.11	-4.23		39.69	0.00	0.00	0.03	18.48	0.17	42.44	0.01	0.00	0.00	100.79

1500ºC 1min #502															
P1 oliv core	-2.73	-6.68	-5.26	0	39.25	0.00	0.06	0.01	19.15	0.19	42.54	0.00	0.00	0.01	101.20
P2 oliv interior	-2.87	-5.40	-3.91	90	39.35	0.02	0.00	0.01	19.09	0.22	42.70	0.00	0.00	0.00	101.39
P5 oliv edge	-3.78	-5.69	-3.73	120	40.46	0.04	0.00	0.03	12.52	0.28	48.11	0.05	0.00	0.00	101.49
P6 melt grn pyx	8.92	5.73	1.09	150	56.15	0.42	0.10	0.09	11.74	0.36	32.06	0.11	0.01	0.00	101.05
3 mesostasis	10.02	5.70	0.49		55.68	0.67	0.18	0.11	11.77	0.31	32.16	0.10	0.01	0.00	100.98
4 mesostasis	9.22	6.35	1.55		55.61	0.60	0.20	0.10	13.10	0.38	30.93	0.12	0.02	0.00	101.06
1500ºC 30sec #501															
P13 oliv interior	-4.26	-5.99	-3.78	0	39.15	0.00	0.00	0.02	18.66	0.22	42.84	0.02	0.00	0.00	100.91
P12 oliv interior	-4.04	-4.80	-2.70	100	39.22	0.00	0.19	0.01	18.53	0.18	42.79	0.02	0.01	0.00	100.95
P11 oliv interior	-4.34	-4.69	-2.43	200	38.94	0.00	0.00	0.03	19.56	0.20	42.01	0.05	0.00	0.00	100.81
P29 oliv edge	0.56	-6.30	-6.59	300	38.31	0.00	1.60	0.02	18.65	0.17	40.97	0.12	0.06	0.00	99.90
P2 oliv core	-2.45	-4.16	-2.89	0	39.23	0.00	0.00	0.02	18.38	0.16	42.45	0.04	0.01	0.00	100.29
P9 oliv core	-3.64	-4.66	-2.77	100	39.45	0.00	0.00	0.01	18.19	0.19	43.43	0.03	0.00	0.00	101.30
P10 oliv interior	-3.68	-5.47	-3.56	200	39.17	0.01	0.00	0.01	18.25	0.16	43.01	0.02	0.00	0.00	100.62
P28 oliv edge	0.81	-4.67	-5.09	300	39.11	0.00	0.00	0.02	18.61	0.18	42.80	0.05	0.00	0.00	100.78
1 oliv core	-1.87	-4.88	-3.91		38.95	0.01	0.01	0.02	18.51	0.17	42.98	0.11	0.00	0.00	100.75
5 mesostasis	9.87	0.96	-4.17		51.87	0.46	1.61	0.06	32.15	0.58	9.20	2.00	1.05	0.21	99.19
6 mesostasis	9.49	5.13	0.19		52.47	0.40	1.64	0.06	30.91	0.58	11.52	2.07	0.93	0.23	100.80
7 oliv core	-3.09	-7.40	-5.79		39.12	0.01	0.00	0.02	18.78	0.18	42.74	0.00	0.00	0.00	100.85
8 oliv core	-3.34	-6.19	-4.45		39.11	0.00	0.14	0.02	18.93	0.16	42.60	0.02	0.00	0.00	100.97
30 mesostasis	12.98	5.91	-0.84		51.85	0.17	0.86	0.10	24.07	0.62	21.71	0.84	0.22	0.03	100.48
3 melt grn pyx	10.52	6.17	0.70		56.65	0.02	0.08	0.08	12.06	0.37	32.05	0.12	0.01	0.00	101.45
4 melt grn pyx	7.84	2.78	-1.30		55.91	0.05	0.12	0.07	12.92	0.37	31.06	0.11	0.03	0.01	100.64
1515ºC 32min #530															
P1 oliv core	-1.98	-5.66	-4.63	0	39.28	0.01	0.00	0.02	18.76	0.18	42.89	0.05	0.01	0.00	101.19
P4 oliv interior	-3.38	-6.22	-4.46	70	38.90	0.01	0.01	0.03	18.76	0.20	42.45	0.07	0.00	0.00	100.43

P3 oliv interior	-2.76	-6.27	-4.84	110	39.40	0.02	0.02	0.04	18.85	0.20	41.67	0.13	0.00	0.00	100.33
P2 oliv edge	12.58	6.98	0.44	160	40.34	0.00	0.01	0.05	15.72	0.20	44.94	0.04	0.00	0.00	101.30
P5 mesostasis/melt grn pyx	8.39	4.33	-0.03	200	55.93	0.05	0.07	0.03	12.80	0.22	28.91	0.07	0.00	0.00	98.09
P6 mesostasis/melt grn pyx	8.26	4.21	-0.09	220	53.43	0.08	0.14	0.05	24.05	0.52	23.15	0.21	0.01	0.00	101.63
7 oliv edge	10.51	5.99	0.52		40.48	0.00	0.01	0.04	14.13	0.20	46.64	0.04	0.00	0.00	101.55
8 melt grn oliv	10.49	5.89	0.43		40.93	0.01	0.00	0.04	12.42	0.20	46.04	0.03	0.00	0.00	99.69
42 oliv edge	5.33	2.97	0.20		40.58	0.00	0.00	0.03	12.96	0.22	47.71	0.03	0.00	0.00	101.52
44 melt grn oliv	6.57	3.54	0.12		40.41	0.03	0.16	0.03	13.87	0.22	43.71	0.17	0.00	0.00	98.61
45 mesostasis	2.93	3.30	1.78		52.72	0.08	0.31	0.04	20.75	0.43	26.33	0.43	0.01	0.01	101.09
46 melt grn oliv	5.02	4.22	1.61		40.54	0.02	0.01	0.03	13.16	0.22	47.41	0.02	0.00	0.00	101.42
47melt grn oliv	7.20	4.31	0.57		40.90	0.01	0.00	0.02	13.32	0.23	47.36	0.01	0.00	0.00	101.87
1515ºC 8min #531															
P21 mesostasis	9.88	4.88	-0.26	0	50.71	0.15	0.62	0.35	22.06	0.57	25.24	0.82	0.00	0.00	100.17
P22 mesostasis	9.59	4.97	-0.02	45	51.25	0.19	1.02	0.32	21.83	0.57	23.22	1.28	0.01	0.00	99.36
P23 mesostasis	10.17	5.03	-0.26	85	50.95	0.18	0.69	0.37	23.05	0.57	24.29	0.80	0.00	0.00	100.53
P24 mesostasis	10.86	5.06	-0.58	130	51.53	0.06	0.43	0.23	21.01	0.49	26.48	0.51	0.01	0.00	100.50
P25 melt gr pyx/meso	10.75	4.88	-0.71	165	53.15	0.18	0.78	0.28	22.51	0.58	21.73	0.66	0.01	0.00	99.58
P26 melt grn pyx	13.67	5.95	-1.15	200	52.87	0.25	1.71	0.11	24.89	0.86	16.74	2.07	0.00	0.00	99.38
P27 oliv edge	-1.48	-5.06	-4.29	230	40.31	0.00	0.00	0.15	14.04	0.27	46.74	0.02	0.00	0.00	101.37
P28 oliv core	-2.83	-5.80	-4.32	260	39.13	0.00	0.01	0.02	19.36	0.20	42.27	0.01	0.01	0.00	100.99
P29 oliv core	-2.53	-6.03	-4.71	295	39.19	0.00	0.00	0.01	18.50	0.19	42.76	0.00	0.00	0.00	100.64
P30 oliv interior	-2.18	-6.05	-4.91	330	39.34	0.00	0.08	0.03	18.75	0.16	42.54	0.01	0.01	0.00	100.90
1515ºC 2min #532															
P71 oliv edge	-1.53	-5.93	-5.13	0	39.44	0.00	0.03	0.02	18.57	0.16	43.17	0.01	0.00	0.00	101.37
P72 oliv interior	-2.48	-6.11	-4.82	45	39.29	0.01	0.07	0.01	19.16	0.17	42.89	0.00	0.00	0.01	101.59
P73 oliv interior	-2.83	-6.05	-4.58	85	38.80	0.00	0.24	0.02	19.36	0.17	41.75	0.02	0.00	0.00	100.35
P74 oliv core	-2.42	-5.81	-4.56	130	39.06	0.01	0.24	0.02	19.48	0.24	41.56	0.02	0.01	0.01	100.62
P75 oliv core	-3.38	-5.81	-4.05	180	38.74	0.00	0.69	0.01	19.94	0.13	41.48	0.00	0.00	0.00	100.98
P76 oliv interior	-3.05	-6.13	-4.54	220	39.16	0.00	0.01	0.01	19.01	0.18	42.98	0.00	0.00	0.00	101.35
P77 oliv interior	-1.26	-3.93	-3.28	250	39.22	0.00	0.00	0.02	18.26	0.18	43.40	0.00	0.00	0.00	101.06

P78 oliv edge	9.82	5.37	0.26	280	39.36	0.00	0.00	0.02	18.50	0.13	43.43	0.00	0.00	0.00	101.42
P79 mesostasis	9.26	5.02	0.21	310	53.49	0.48	0.64	0.07	20.22	0.42	24.31	0.66	0.02	0.02	100.27
P80 mesostasis	9.54	5.05	0.09	365	51.76	0.31	0.39	0.06	20.40	0.44	26.82	0.44	0.02	0.02	100.60
P81 melt grn oliv	12.29	6.43	0.04	0	39.13	0.00	0.00	0.02	17.80	0.17	42.94	0.05	0.00	0.00	100.10
P82 melt grn oliv	8.78	3.40	-1.17	15	39.53	0.02	0.00	0.03	17.15	0.24	44.27	0.02	0.00	0.00	101.22
P83 oliv edge	-0.28	-3.90	-3.75	30	39.10	0.00	0.26	0.03	18.06	0.20	41.55	0.02	0.00	0.00	99.20
P84 oliv interior	-3.05	-5.79	-4.20	50	39.20	0.01	0.00	0.01	18.28	0.16	43.13	0.01	0.00	0.00	100.79

Notes:
Dist – distance along profile in microns

Table 4.4. Run conditions and analytical results of the dynamic crystallization experiments. All experiments remained at 1515ºC for 15 minutes before the initation of cooling cycle. All analyses are from the olivines. Unfortunately, no glass was analyzed.

Cooling rate (Duration) Exp #	$\delta^{18}O$	Dist	SiO_2	TiO_2	Al_2O_3	Cr_2O_3	FeO	MnO	MgO	CaO	Na_2O	K_2O	Total
2000ºC/hr (0.52 hrs) #563													
P1 oliv edge	9.41	15	39.58	0.00	0.00	0.03	17.20	0.18	43.34	0.04	0.01	0.00	100.36
P2 oliv interior	-2.32	50	39.54	0.00	0.00	0.02	18.58	0.17	42.41	0.03	0.00	0.00	100.73
P3 oliv interior	-2.32	85	39.33	0.00	0.00	0.02	18.15	0.15	42.52	0.01	0.01	0.00	100.16
1000ºC/hr (0.77 hrs) #562													
P1 oliv edge	2.00	30	39.85	0.00	0.00	0.03	15.01	0.20	44.91	0.01	0.01	0.00	99.99
P6 oliv interior	-2.84	65	39.24	0.00	0.00	0.03	18.63	0.16	42.10	0.04	0.00	0.01	100.17
P2 oliv core	-2.93	155	39.38	0.01	0.00	0.03	18.80	0.14	42.62	0.02	0.00	0.00	100.97
P3 oliv interior	-2.99	190	39.41	0.04	0.00	0.04	18.98	0.20	42.22	0.04	0.01	0.00	100.90
P4 oliv interior	-2.93	220	39.42	0.00	0.00	0.03	18.79	0.14	42.39	0.04	0.01	0.01	100.80
P5 oliv edge / melt grn oliv	9.97	255	39.59	0.00	0.00	0.02	18.70	0.16	42.07	0.02	0.00	0.00	100.53
500ºC/hr (1.28 hrs) #559													
P1 oliv edge	4.82	25	38.95	0.00	0.01	0.03	16.82	0.20	43.71	0.05	0.01	0.00	99.75
P2 oliv interior	-2.78	65	39.30	0.00	0.00	0.06	18.59	0.16	42.19	0.04	0.01	0.00	100.28
P5 oliv edge	-2.66	240	38.74	0.00	0.00	0.03	18.93	0.16	42.27	0.02	0.00	0.00	100.11
P4 oliv edge / melt grn oliv	9.09	265	39.26	0.03	0.74	0.03	15.38	0.17	44.56	0.00	0.00	0.00	100.15
P3 melt grn oliv	11.15	290	39.09	0.00	0.00	0.03	17.05	0.30	43.34	0.02	0.01	0.00	99.81
200ºC/hr (2.83 hrs) #560													
P1 oliv edge	10.74	20	39.26	0.00	0.00	0.26	17.75	0.29	42.97	0.01	0.01	0.00	100.29
P2 oliv interior	-2.70	55	39.57	0.02	0.00	0.09	17.93	0.18	42.98	0.07	0.01	0.00	100.75
P3 oliv interior	-2.33	90	39.38	0.00	0.00	0.05	18.60	0.16	42.72	0.04	0.01	0.01	100.92
P7 oliv core	-2.40	150	39.30	0.00	0.00	0.03	18.77	0.13	42.67	0.06	0.01	0.00	100.93
P6 oliv interior	-2.48	190	39.47	0.02	0.00	0.05	18.19	0.17	42.98	0.06	0.00	0.00	100.88
P5 oliv interior	0.18	230	39.68	0.00	0.00	0.25	16.25	0.25	44.44	0.05	0.01	0.00	100.68
P4 oliv edge	11.32	260	39.37	0.00	0.00	0.28	17.36	0.27	43.07	0.00	0.00	0.00	100.08

P11 oliv edge	4.60	10	39.56	0.00	0.00	0.10	17.06	0.17	43.54	0.00	0.00	0.00	100.33
P12 oliv interior	-2.44	40	39.35	0.00	0.04	0.04	18.84	0.18	42.28	0.03	0.00	0.00	100.73
P13 oliv interior	-2.72	70	39.27	0.02	0.00	0.02	18.63	0.20	42.76	0.00	0.00	0.00	100.88
P14 oliv interior	-2.80	100	39.36	0.03	0.00	0.02	18.67	0.25	42.63	0.02	0.00	0.00	100.96
P16 oliv interior	-2.64	320	39.14	0.02	0.00	0.03	18.30	0.18	42.86	0.01	0.00	0.00	100.51
P15 oliv edge	4.51	355	39.07	0.00	0.00	0.10	17.26	0.20	43.48	0.01	0.00	0.01	100.60
100ºC/hr (5.4 hrs) #566													
P1 oliv edge	9.42	15	39.67	0.00	0.00	0.02	16.44	0.24	44.43	0.04	0.02	0.01	100.84
P2 oliv interior	8.56	60	39.90	0.00	0.00	0.03	16.04	0.17	44.30	0.02	0.01	0.00	100.43
P3 oliv interior	5.21	115	40.12	0.03	0.00	0.03	16.14	0.13	44.51	0.00	0.01	0.00	100.95
P4 oliv core	-3.05	155	39.91	0.00	0.01	0.02	15.76	0.18	44.72	0.01	0.00	0.00	100.59
P5 oliv interior	-2.77	190	40.00	0.06	0.00	0.02	15.54	0.19	44.77	0.00	0.00	0.00	100.57
P6 oliv interior	-2.80	240	40.18	0.00	0.00	0.03	15.81	0.20	45.03	0.00	0.00	0.00	101.22
P7 oliv edge	10.14	280	40.21	0.00	0.00	0.02	16.39	0.25	44.25	0.06	0.00	0.00	101.15
P11 oliv edge	9.64	20	40.13	0.00	0.00	0.00	15.91	0.16	45.06	0.02	0.02	0.00	101.31
P12 oliv interior	4.52	55	40.07	0.02	0.00	0.03	15.74	0.19	44.80	0.03	0.01	0.00	100.85
P13 oliv core	-3.05	85	40.18	0.00	0.21	0.01	15.78	0.18	44.86	0.02	0.00	0.00	101.24
P14 oliv core	-2.99	130	40.21	0.01	0.00	0.05	15.45	0.13	44.94	0.00	0.02	0.00	100.76
P15 oliv interior	4.09	180	40.05	0.00	0.00	0.02	15.22	0.22	45.16	0.01	0.00	0.00	100.66
P16 oliv edge	10.26	220	39.98	0.00	0.00	0.01	15.85	0.25	44.56	0.03	0.00	0.00	100.67
50ºC/hr (10.55 hrs) #567													
P1 oliv edge	11.84	30	40.07	0.00	0.00	0.04	16.11	0.30	44.35	0.00	0.01	0.00	100.84
P3 oliv interior	6.27	55	39.96	0.00	0.00	0.06	15.26	0.26	45.17	0.03	0.00	0.00	100.69
P4 oliv interior	-2.52	90	40.07	0.00	0.00	0.04	15.82	0.31	44.79	0.01	0.00	0.01	101.01
P5 oliv interior	-2.71	155	39.83	0.01	0.00	0.04	16.83	0.32	43.71	0.02	0.01	0.00	100.72
P2 oliv core	-2.50	200	40.24	0.00	0.00	0.04	14.97	0.31	44.70	0.01	0.01	0.00	100.24
P6 oliv interior	-2.50	265	40.30	0.00	0.00	0.05	13.79	0.26	46.09	0.02	0.00	0.00	100.47
P7 oliv interior	-2.54	320	40.18	0.00	0.00	0.04	15.35	0.25	44.59	0.02	0.00	0.01	100.38
P8 oliv edge	-0.50	355	38.75	0.00	0.00	0.05	20.94	0.45	40.06	0.01	0.01	0.01	100.23

P11 oliv edge	11.64	35	40.22	0.00	0.00	0.04	15.07	0.21	45.20	0.03	0.00	0.00	100.73
P13 oliv interior	12.49	45	39.60	0.00	0.15	0.04	17.33	0.21	43.00	0.07	0.02	0.00	100.38
P12 oliv interior	12.07	65	39.24	0.00	0.00	0.06	18.62	0.22	42.25	0.08	0.00	0.00	100.40
P14 oliv core	12.22	100	39.46	0.02	0.00	0.05	18.67	0.16	42.02	0.09	0.00	0.00	100.42
P15 oliv core	12.66	140	39.49	0.00	0.00	0.06	18.75	0.16	42.34	0.09	0.00	0.00	100.83
P16 oliv interior	11.77	175	39.52	0.00	0.00	0.03	18.61	0.18	42.50	0.07	0.00	0.00	100.87
P17 oliv interior	12.37	205	39.53	0.00	0.01	0.07	18.01	0.18	42.54	0.08	0.00	0.00	100.35
P18 oliv edge	12.04	230	39.89	0.00	0.00	0.06	16.64	0.28	43.85	0.06	0.01	0.00	100.73
20ºC/hr (26.0 hrs) #565													
P1 oliv edge	9.81	20	38.76	0.00	0.00	0.01	18.90	0.27	42.15	0.03	0.03	0.00	100.13
P2 oliv interior	10.14	50	39.24	0.00	0.01	0.02	17.73	0.24	42.93	0.02	0.00	0.00	100.17
P3 oliv core	9.75	90	38.96	0.00	0.00	0.01	18.33	0.25	42.85	0.00	0.01	0.00	100.40
P4 oliv interior	9.83	120	39.38	0.00	0.00	0.01	17.77	0.21	43.05	0.01	0.00	0.00	100.42
P5 oliv edge	9.85	160	39.05	0.00	0.00	0.01	19.59	0.28	41.71	0.04	0.00	0.00	100.67
P11 oliv edge	9.77	30	39.09	0.01	0.00	0.02	20.04	0.24	41.93	0.03	0.00	0.00	101.34
P12 oliv core	9.95	150	39.78	0.00	0.00	0.03	16.26	0.20	44.37	0.00	0.01	0.00	100.61
P13 oliv edge	9.64	380	39.20	0.00	0.00	0.03	19.85	0.28	41.20	0.03	0.00	0.00	100.56
10ºC/hr (51.75 hrs) #568													
P1 oliv edge	9.44	30	39.65	0.00	0.00	0.00	16.73	0.33	44.21	0.04	0.00	0.01	100.96
P2 oliv interior	-2.77	80	39.41	0.00	0.00	0.00	17.05	0.20	44.32	0.00	0.01	0.01	101.00
P3 oliv core	-2.45	130	39.36	0.00	0.00	0.04	17.56	0.22	43.01	0.00	0.00	0.01	100.16
P4 oliv interior	-2.45	170	39.62	0.00	0.03	0.03	16.72	0.24	43.94	0.00	0.00	0.00	100.54
P5 oliv edge	0.53	215	39.69	0.02	0.00	0.02	16.52	0.22	43.82	0.01	0.00	0.00	100.27
5ºC (103.25 hrs) #569													
P1 oliv edge	5.63	20	40.78	0.00	0.00	0.03	12.87	0.19	47.21	0.05	0.00	0.00	101.11
P2 oliv interior	-3.78	80	40.80	0.00	0.00	0.02	12.66	0.21	47.34	0.06	0.00	0.00	101.07
P3 oliv core	-3.65	120	40.72	0.00	0.00	0.03	12.65	0.20	47.45	0.04	0.00	0.00	101.05
P4 oliv interior	-1.79	165	40.49	0.02	0.00	0.01	12.17	0.18	47.41	0.04	0.00	0.00	100.31
P5 oliv edge	9.21	210	40.82	0.00	0.00	0.01	12.14	0.24	47.52	0.04	0.01	0.00	100.77

P11 oliv edge	8.98	25	40.53	0.00	0.00	0.00	12.83	0.27	47.09	0.04	0.00	0.00	100.75
P12 oliv interior	9.03	60	40.21	0.01	0.00	0.00	12.58	0.22	47.49	0.04	0.01	0.01	100.57
P13 oliv core	9.17	100	40.47	0.00	0.00	0.00	11.96	0.18	47.89	0.02	0.00	0.00	100.52
P14 oliv interior	9.15	135	40.43	0.00	0.00	0.00	11.97	0.25	48.20	0.02	0.00	0.01	100.87
P15 oliv interior	9.32	160	40.23	0.00	0.00	0.00	12.02	0.23	47.51	0.02	0.00	0.00	100.03
P16 oliv edge	8.20	190	40.17	0.00	0.00	0.00	12.54	0.22	46.91	0.02	0.00	0.00	99.86

Figure 4.1a. 1500℃ down to 1425℃ at 3600℃ per hour, then air quench

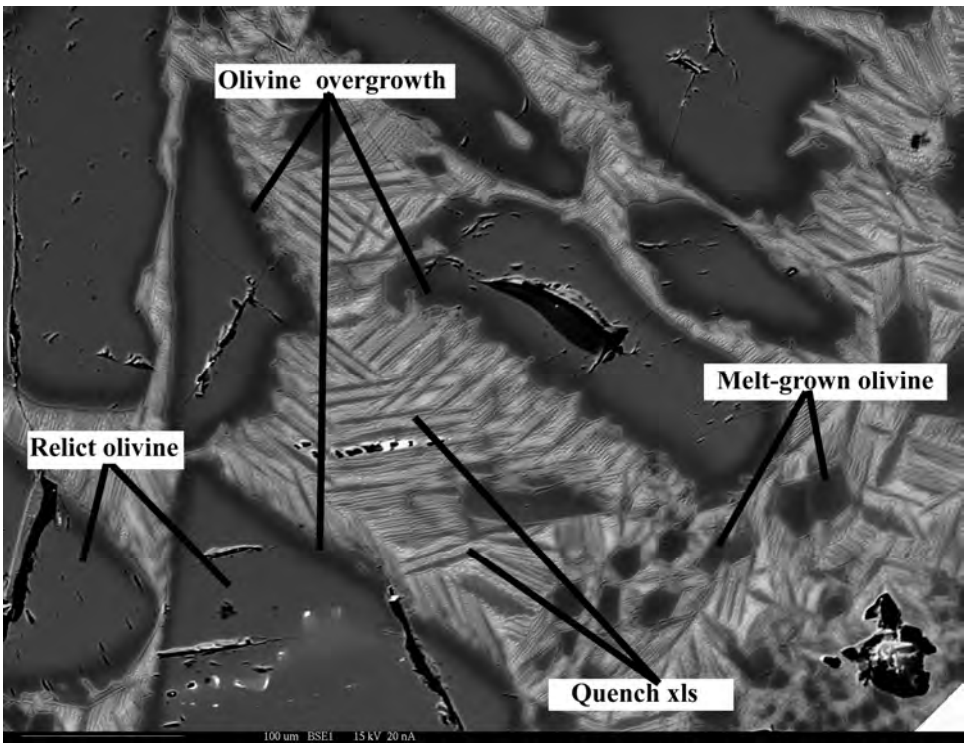

Figure 4.1b. 1500℃ and water quench

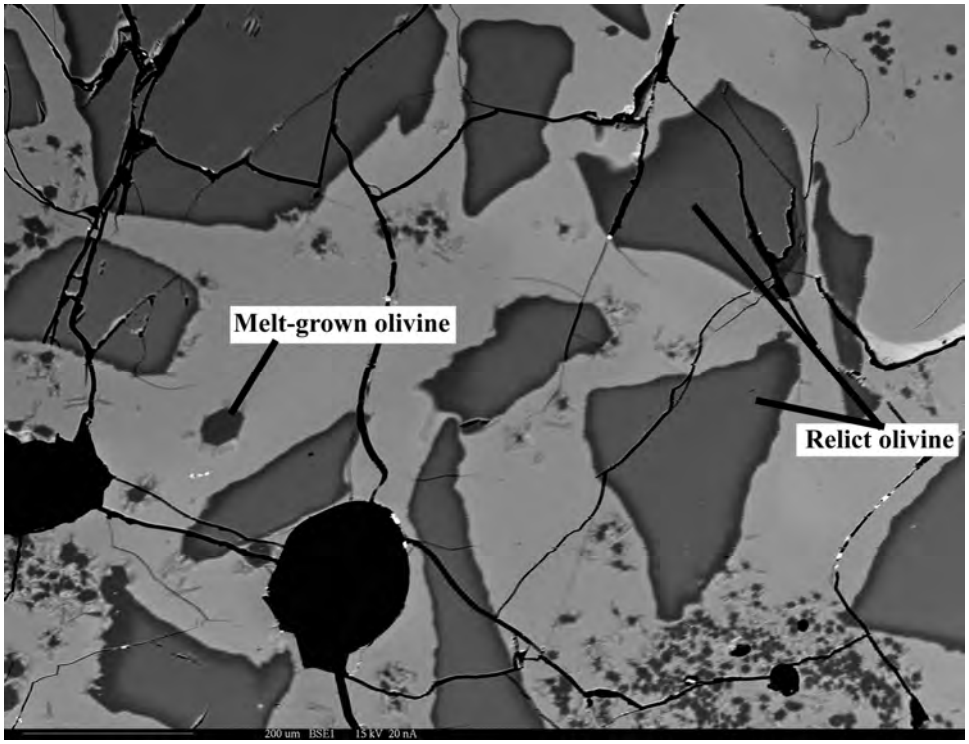

Figure 4.1c. 1500℃ down to 1425℃ at 3600℃ per hour, then water quench

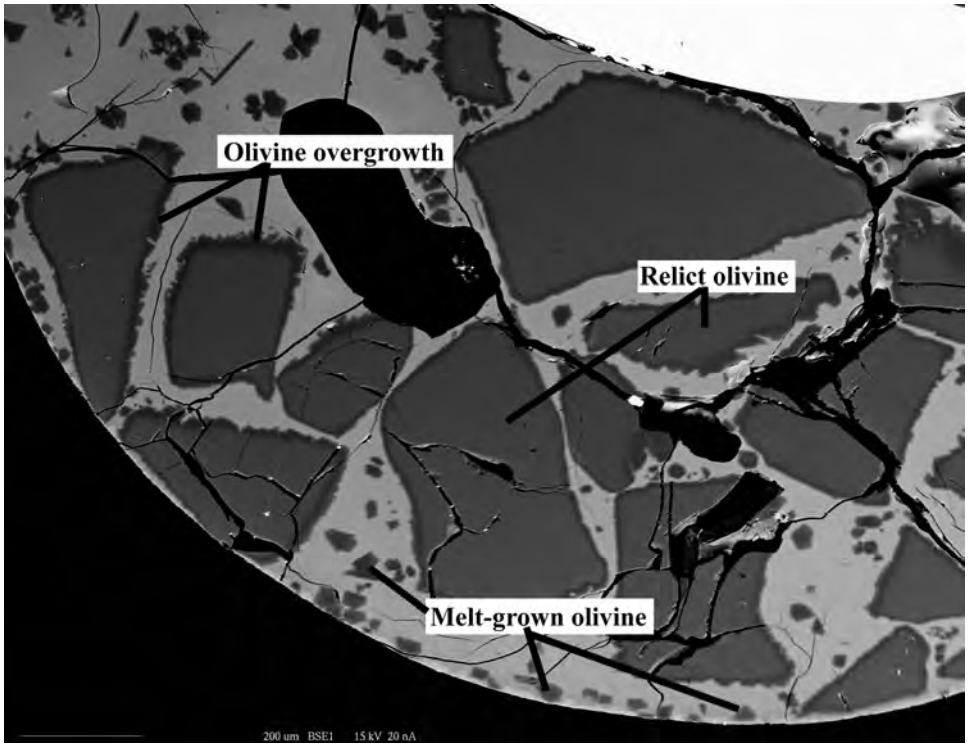

Figure 4.2a.
1300℃ 64min #521

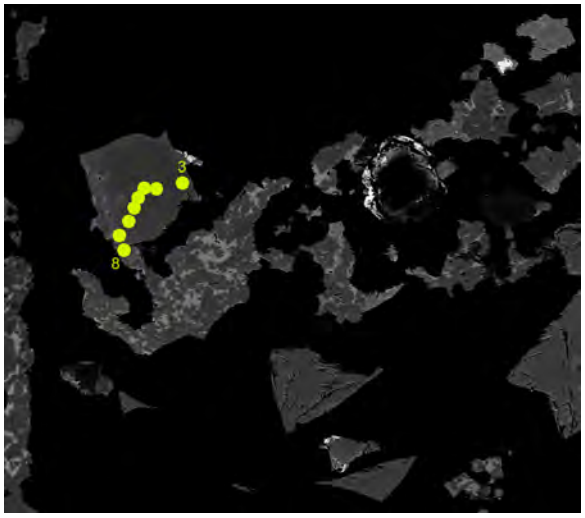

Figure 4.2b.
1300℃ 32min #520

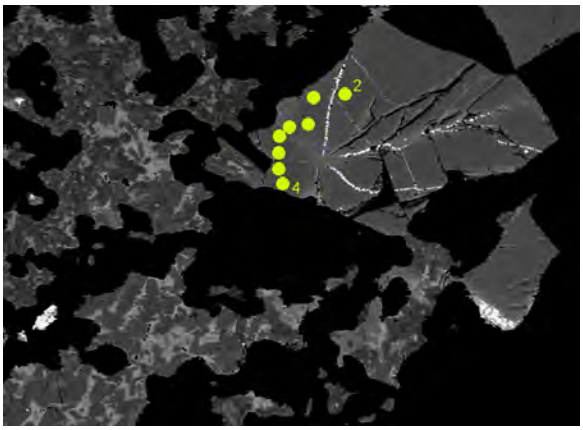

Figure 4.2c.
1300℃ 16min #519

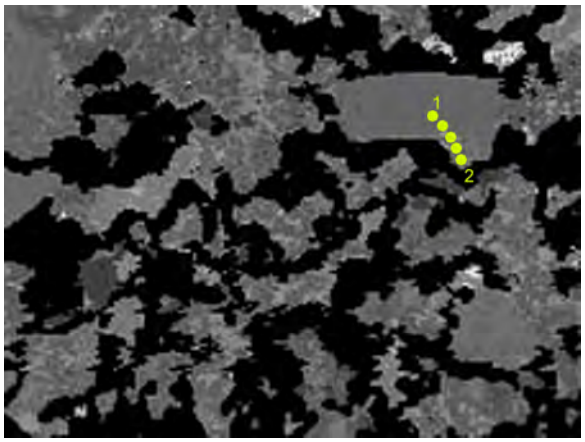

Figure 4.2d.
1400℃ 64min #529

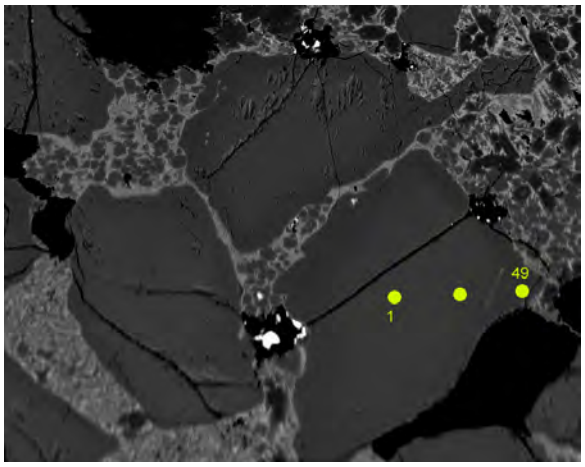

Figure 4.2e.
1400℃ 32min #528

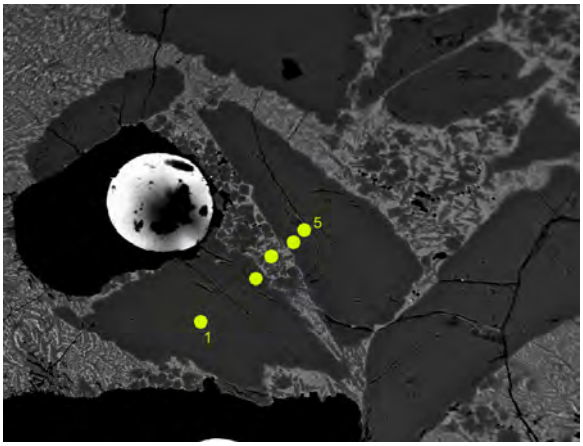

Figure 4.2f and g.
1500℃ 32min #512

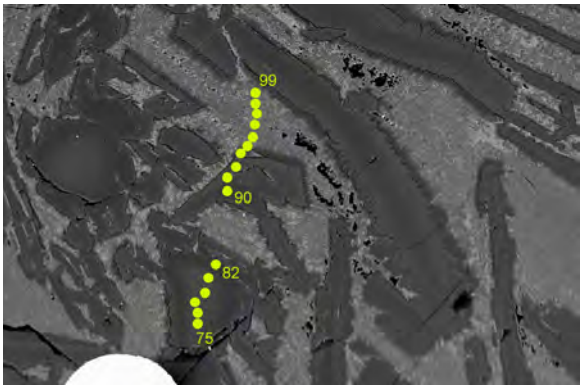

Figure 4.2h and i.
1500℃ 16min #511

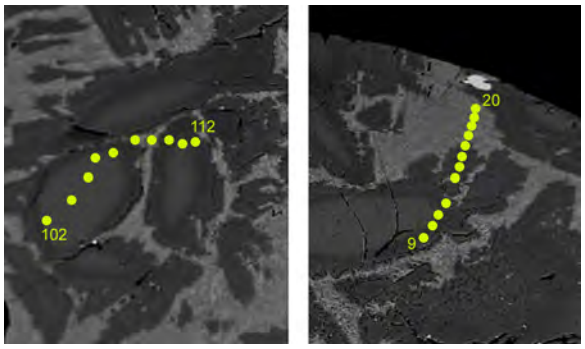

Figure 4.2j.
1500℃ 8min #510

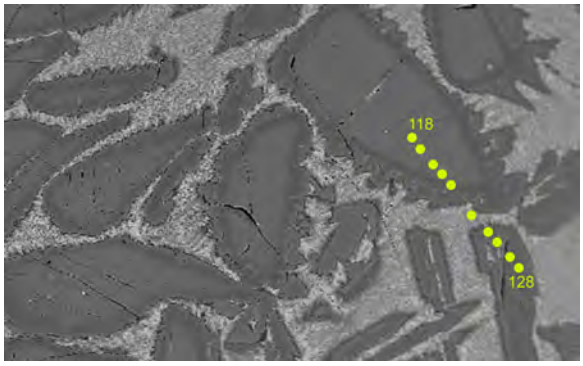

Figure 4.2k.
1500℃ 4min #507

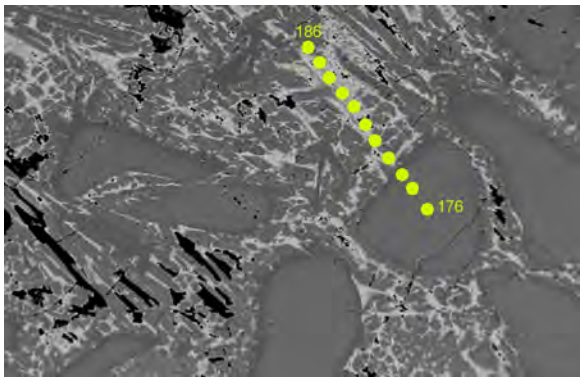

Figure 4.2l.
1500℃ 2min #508

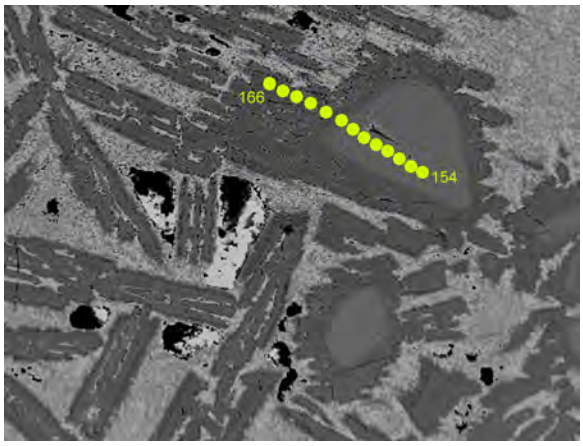

Figure 4.2m.
1500℃ 1 min #502

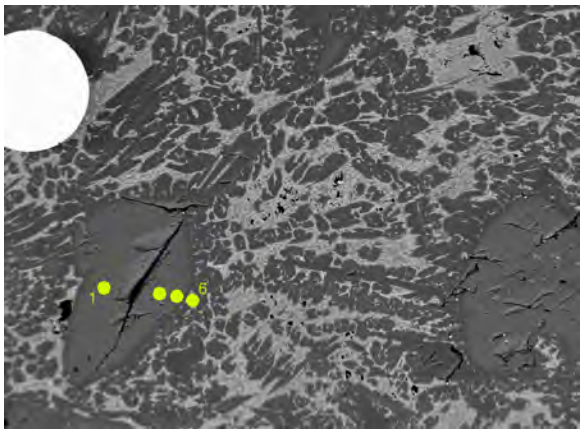

Figure 4.2n and o.
1500℃ 30sec #501

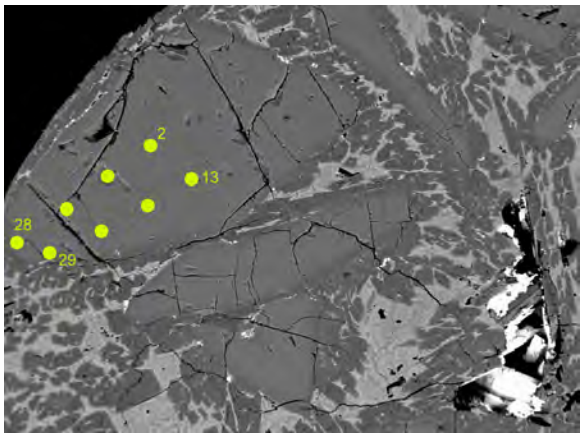

Figure 4.2p.
1515℃ 32min #530

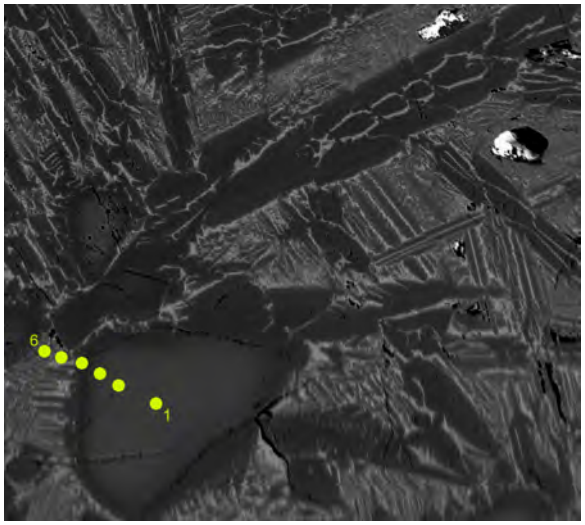

Figure 4.2q.
1515℃ 8min #531

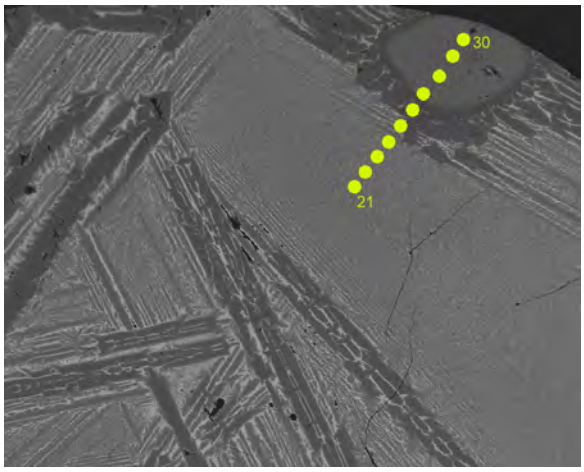

Figure 4.2r and s.
1515℃ 2min #532

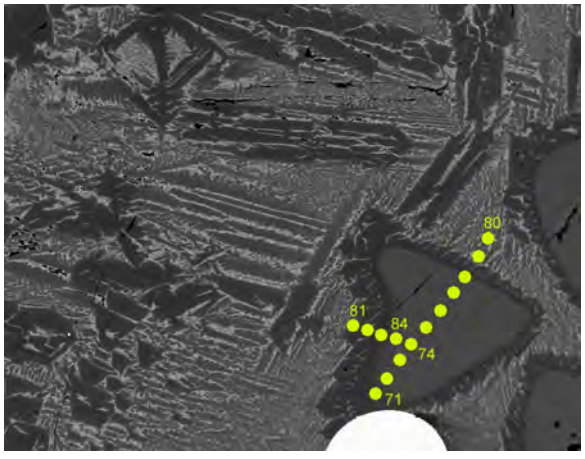

Figure 4.3a.

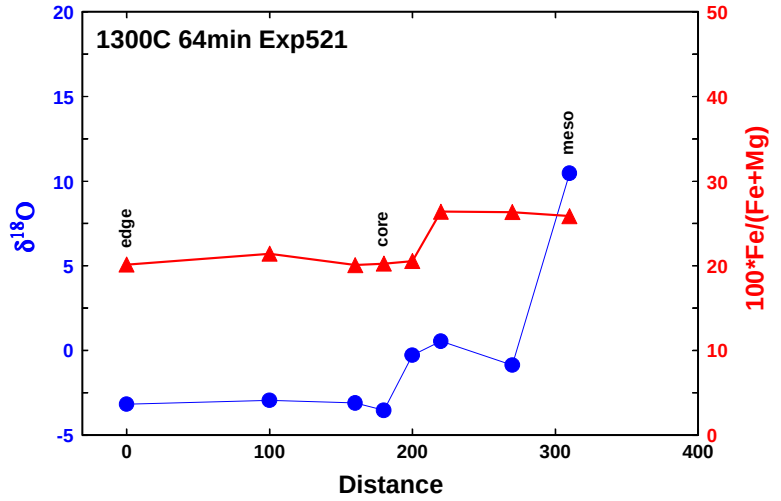

Figure 4.3b.

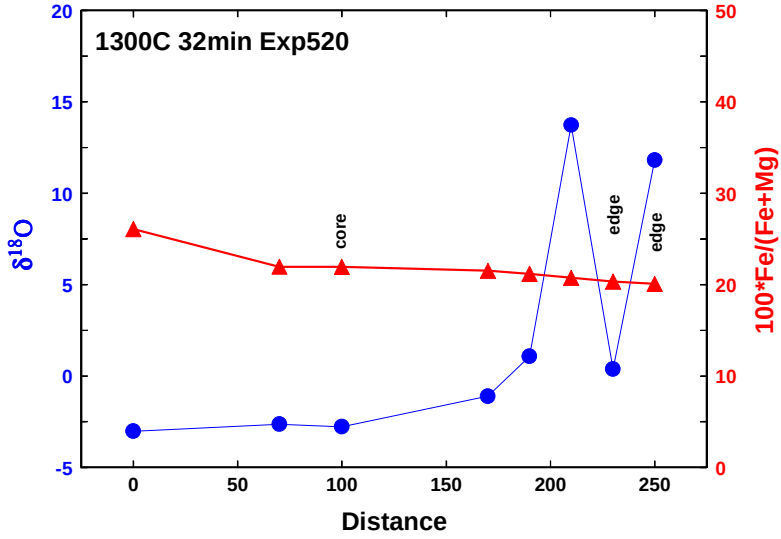

Figure 4.3c.

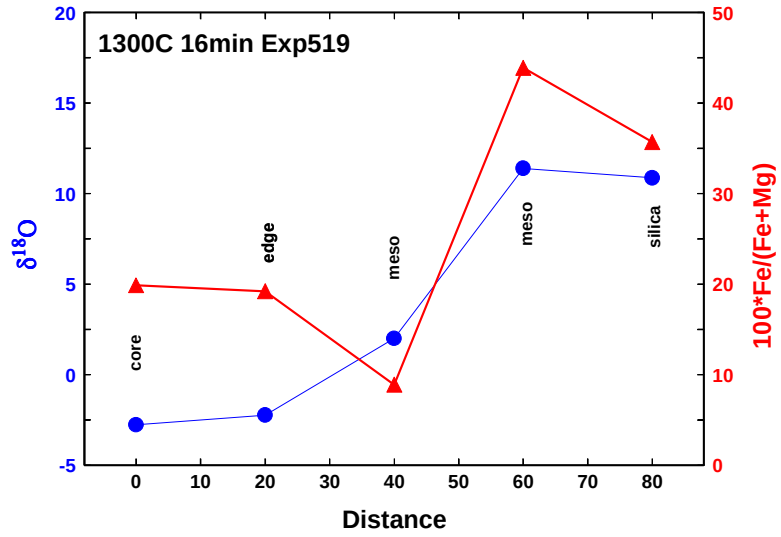

Figure 4.3d.

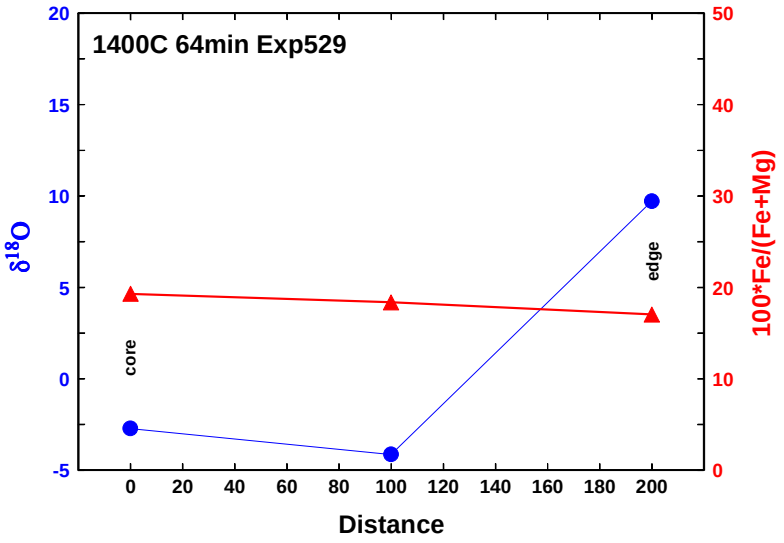

Figure 4.3e.

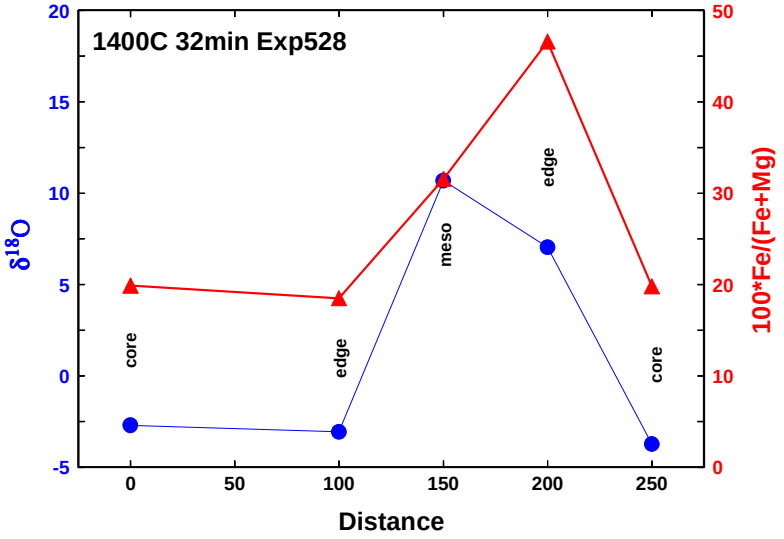

Figure 4.3f.

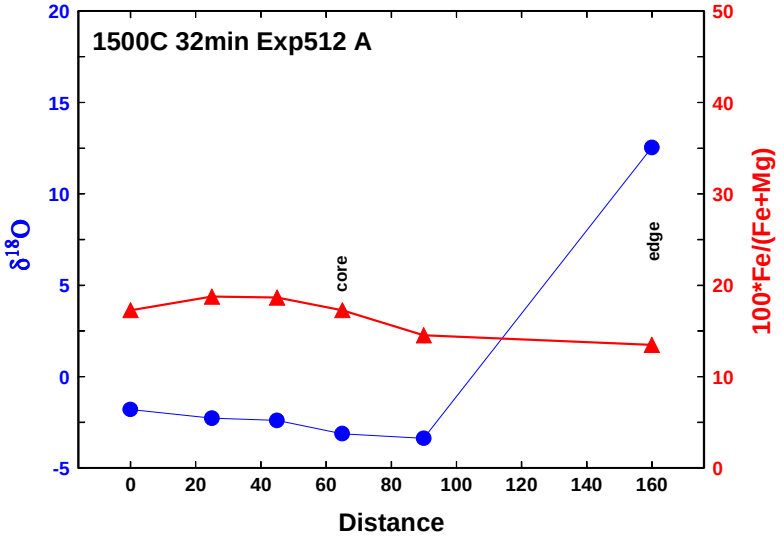

Figure 4.3g.

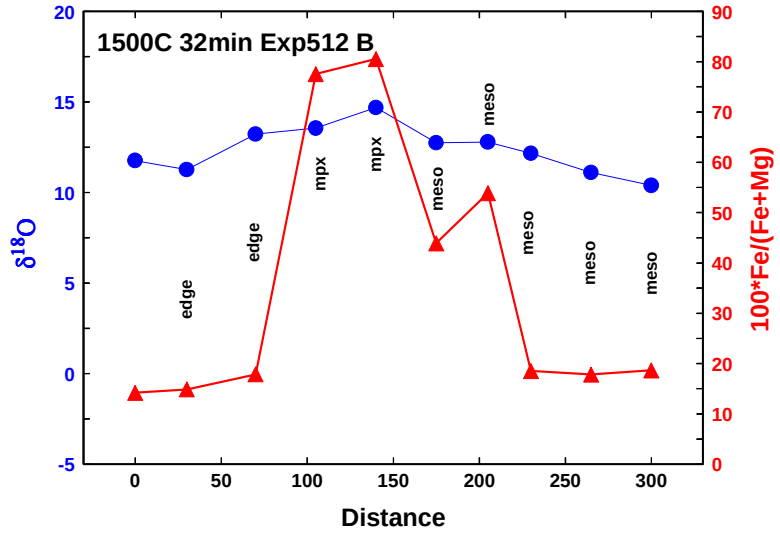

Figure 4.3h.

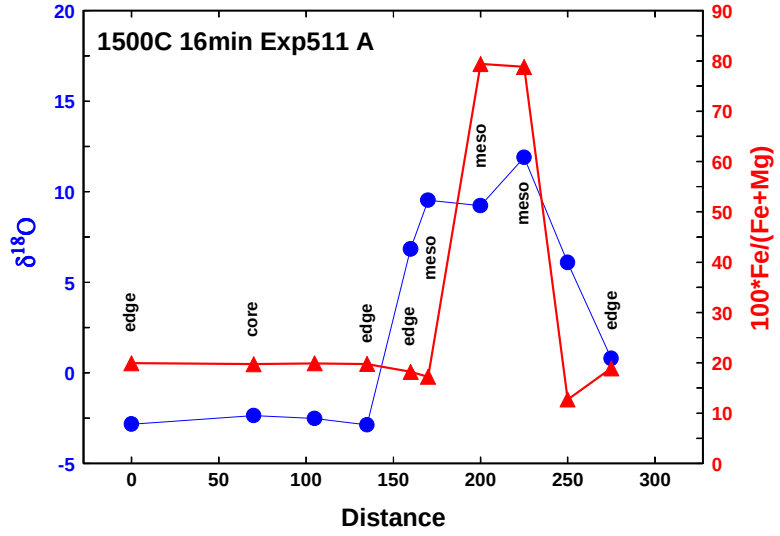

Figure 4.3i.

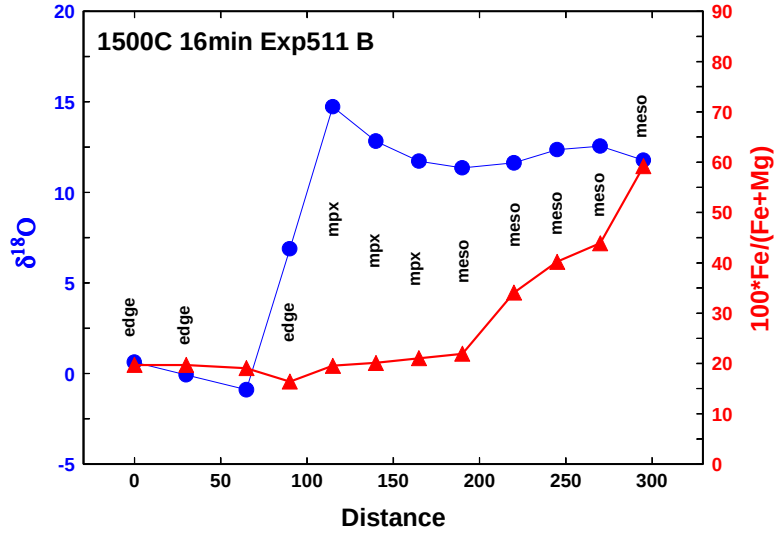

Figure 4.3j.

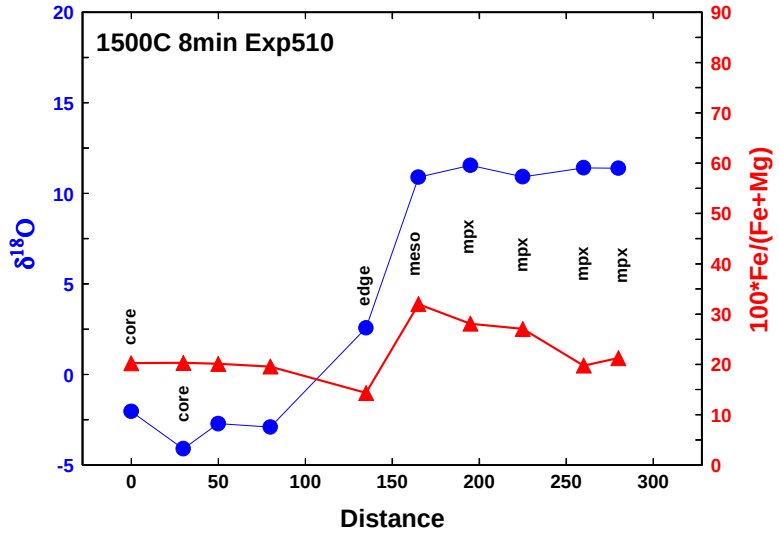

Figure 4.3k.

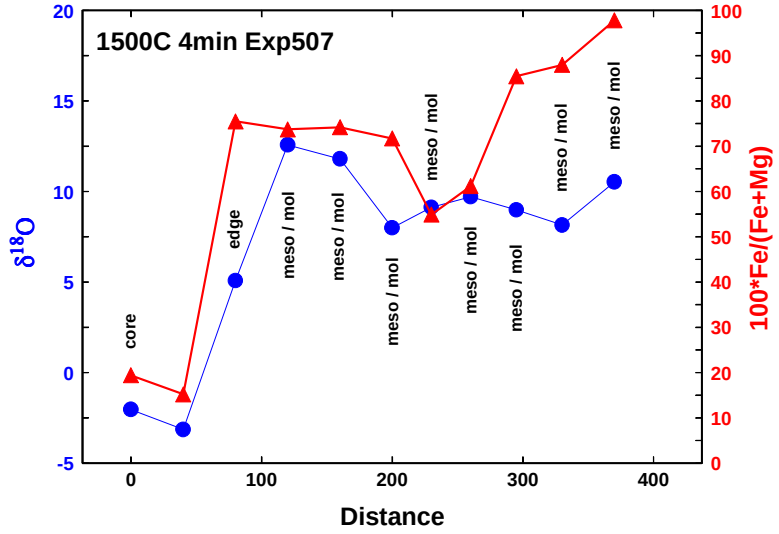

Figure 4.3l.

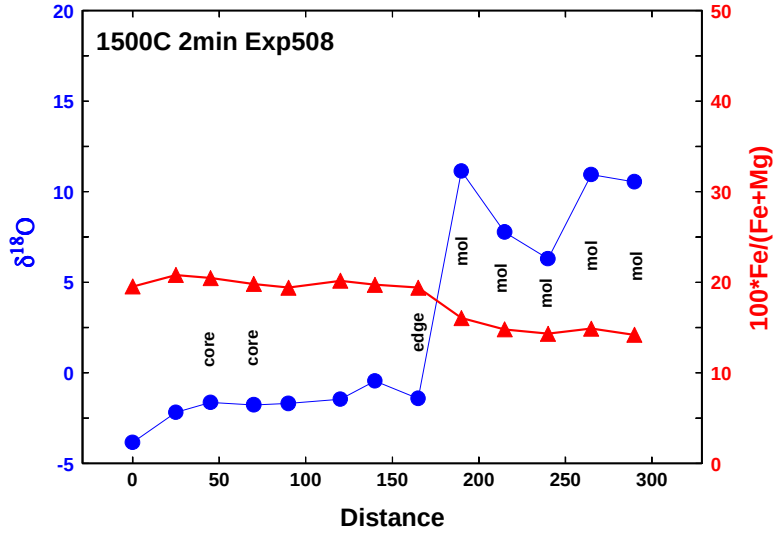

Figure 4.3m.

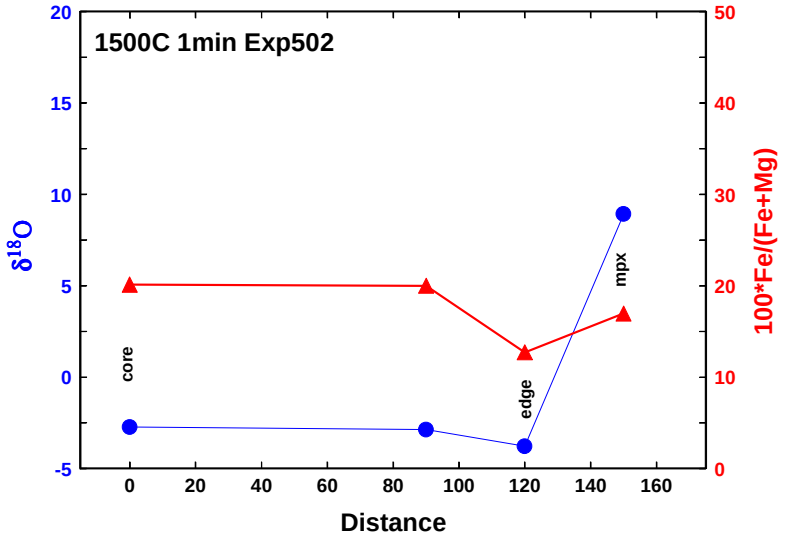

Figure 4.3n.

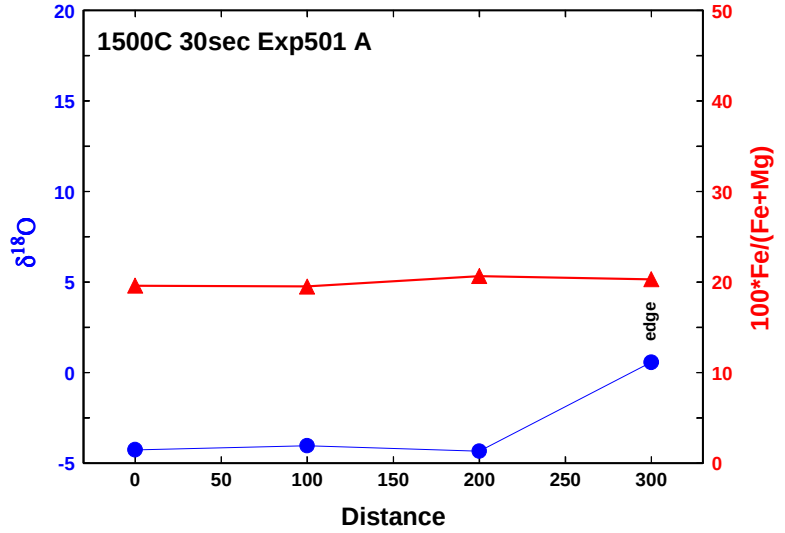

Figure 4.3o.

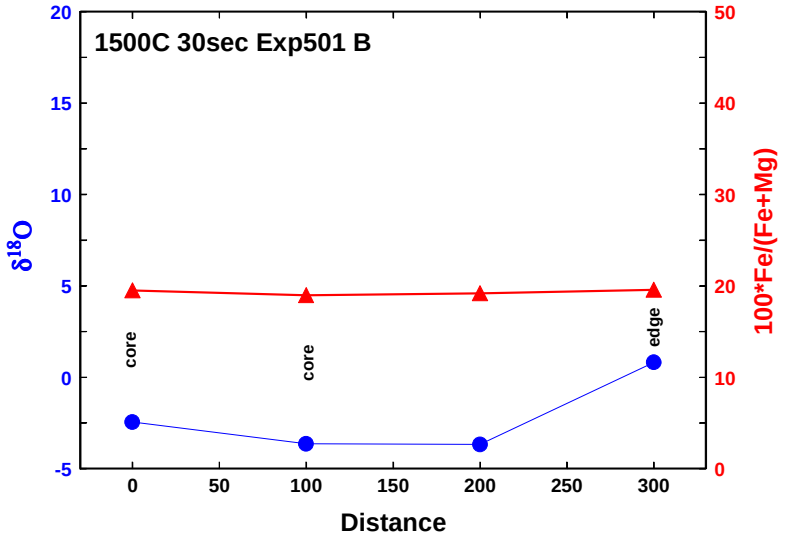

Figure 4.3p.

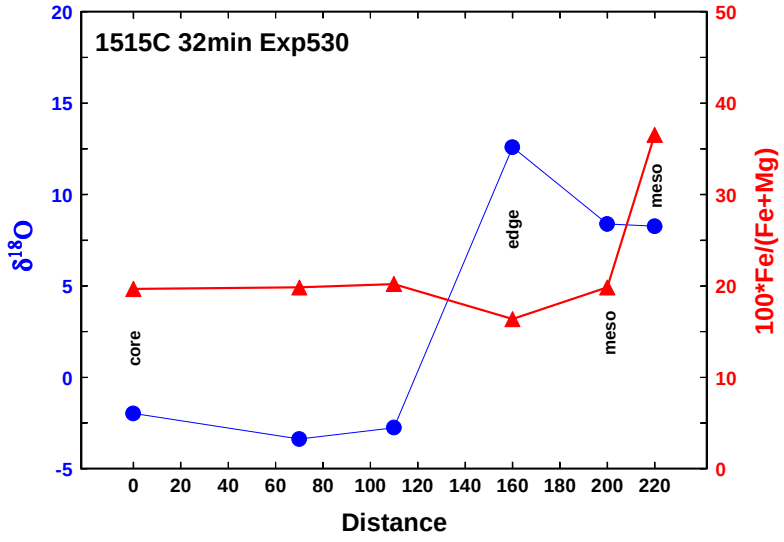

Figure 4.3q.

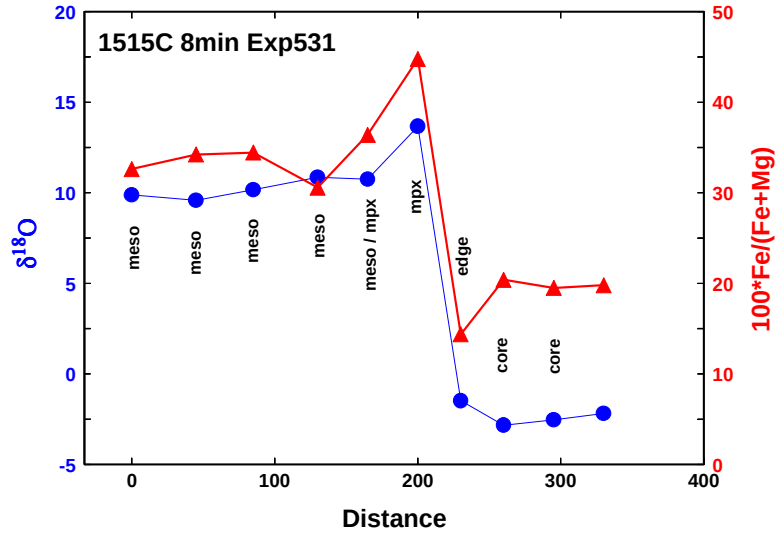

Figure 4.3r.

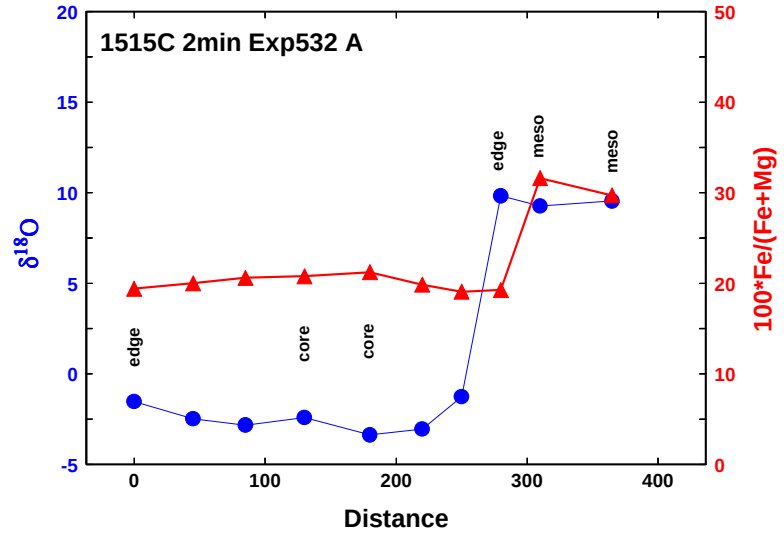

Figure 4.3s.

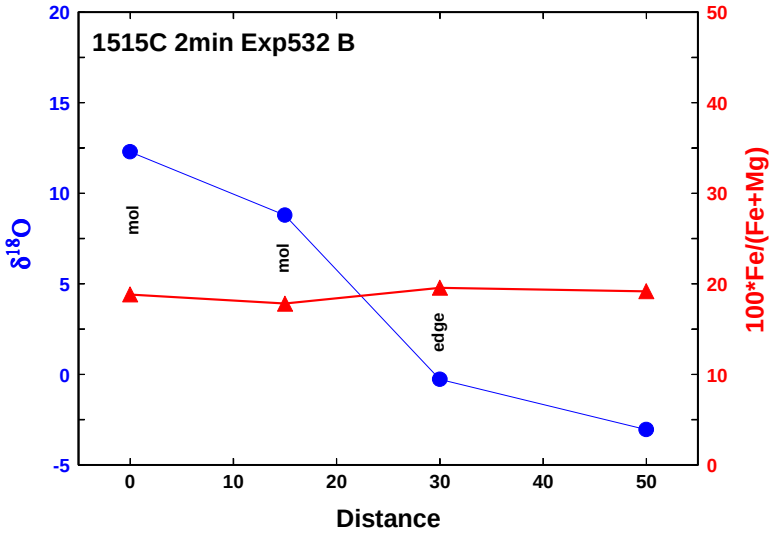
1515C 2min Exp532 B
δ18O
100*Fe/(Fe+Mg)
Distance
mol
mol
edge
20
15
10
5
0
-5
50
40
30
20
10
0
0
10
20
30
40
50

Figure 4.4a.
2000℃/hr #563

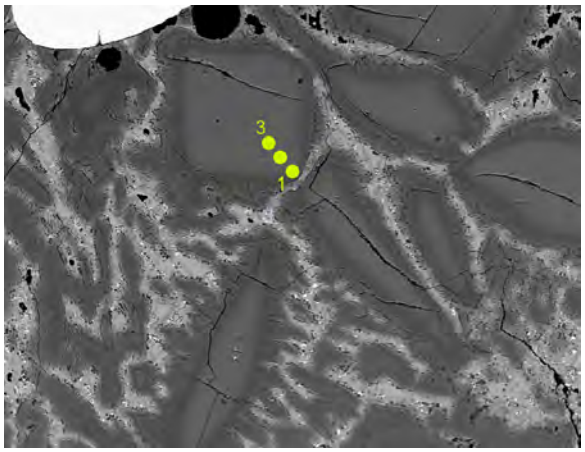

Figure 4.4b.
1000℃/hr #562

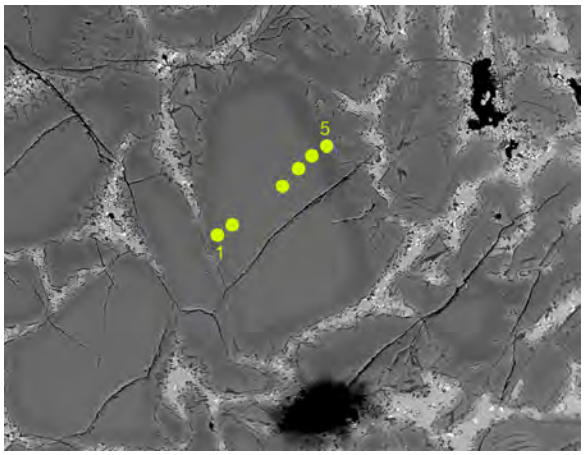

Figure 4.4c.
500℃/hr #559

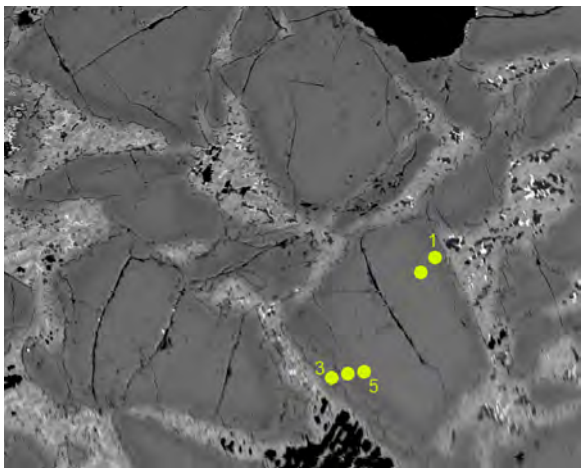

Figure 4.4d and e.
200℃/hr #560

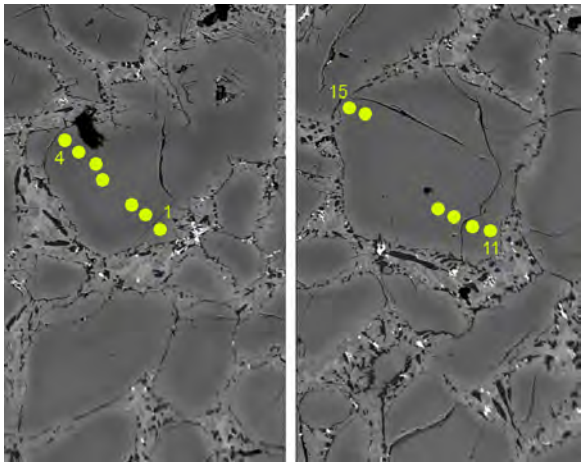

Figure 4.4f and g.
100℃/hr #566

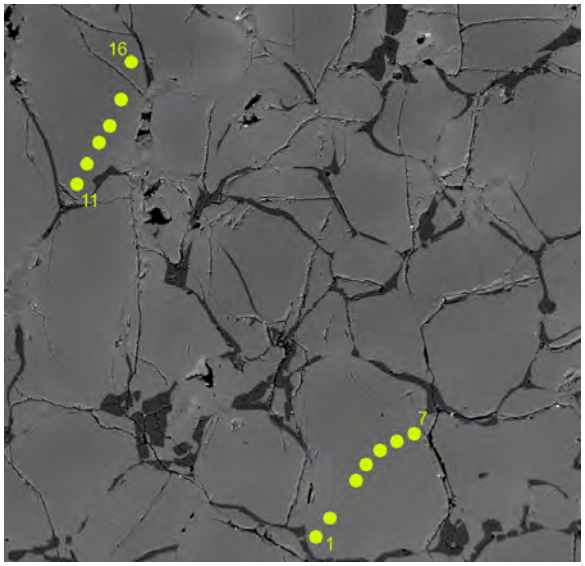

Figure 4.4h and i.
50℃/hr #567

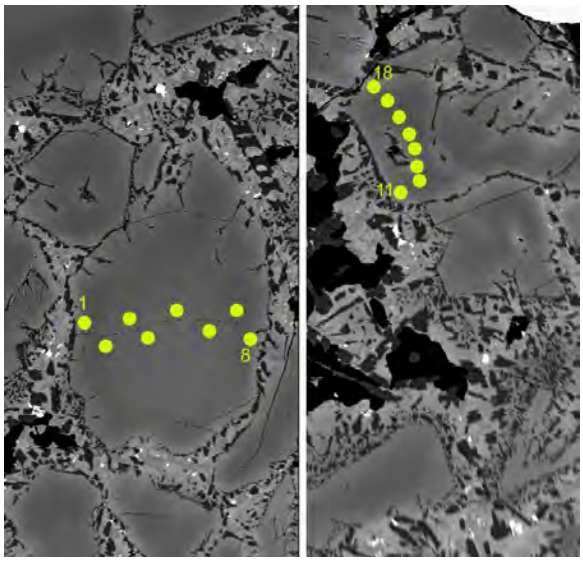

Figure 4.4j and k.
20℃/hr #565

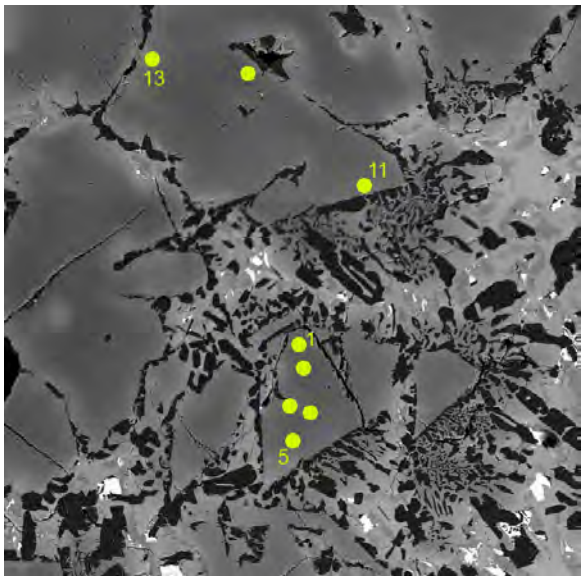

Figure 4.4l.
10℃/hr #568

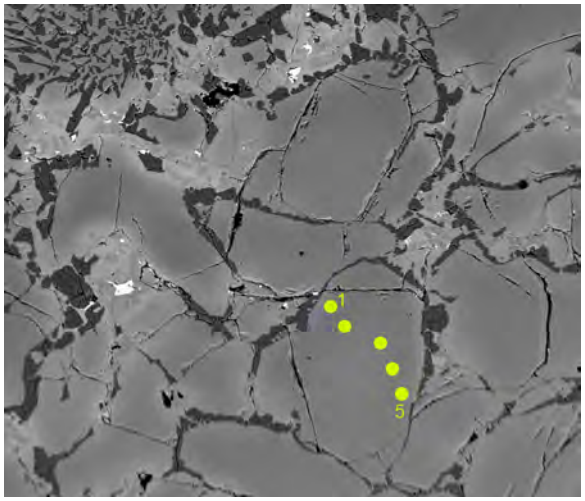

Figure 4.4m and n.
5℃/hr #569

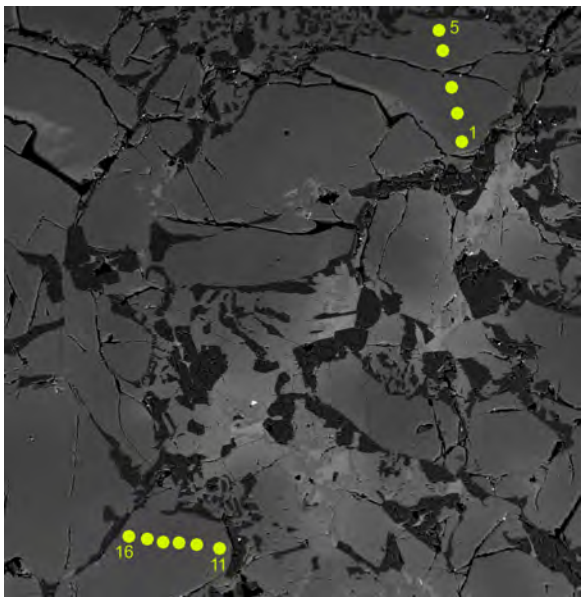

Figure 4.5a.

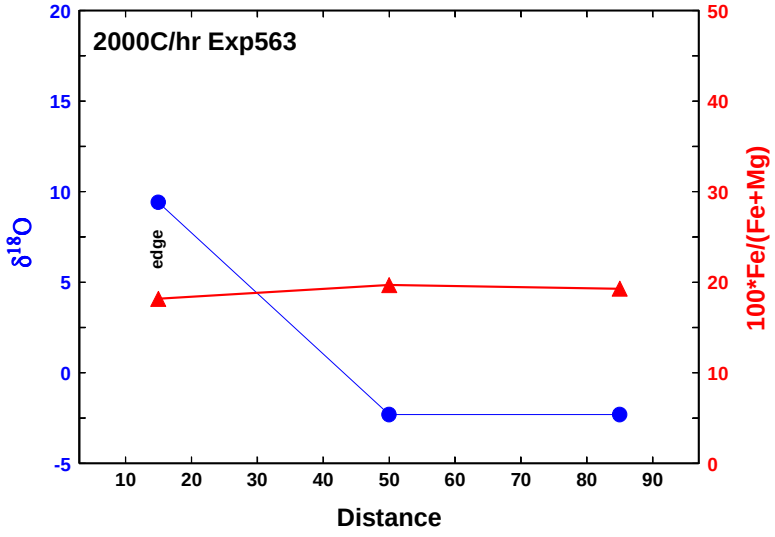

Figure 4.5b.

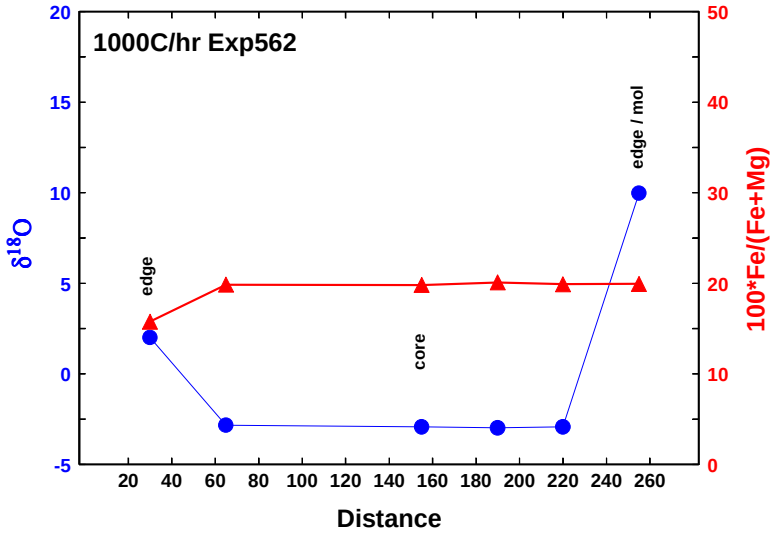

Figure 4.5c.

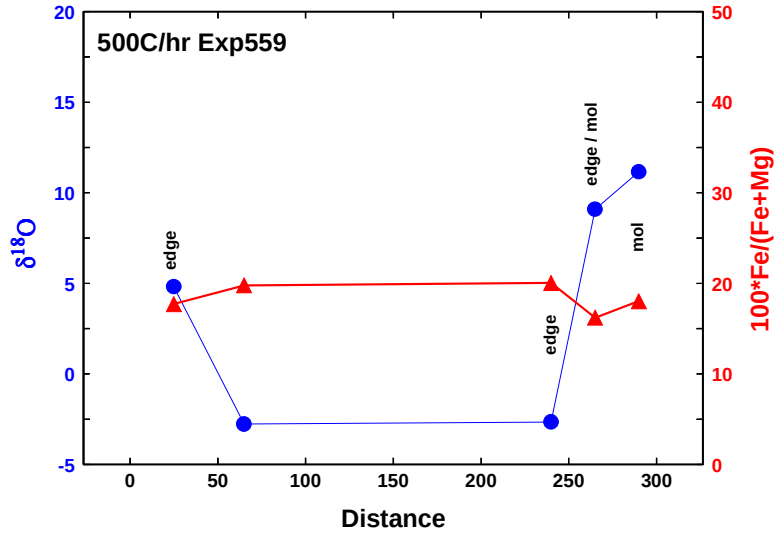

Figure 4.5d.

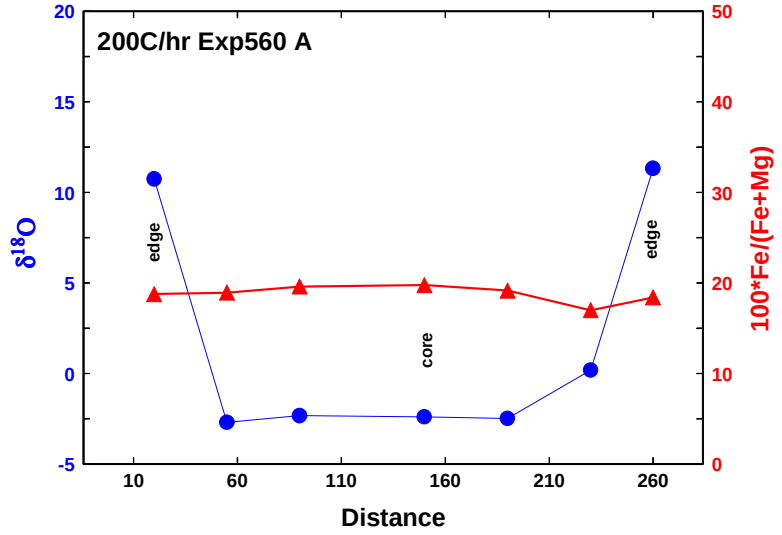

Figure 4.5e.

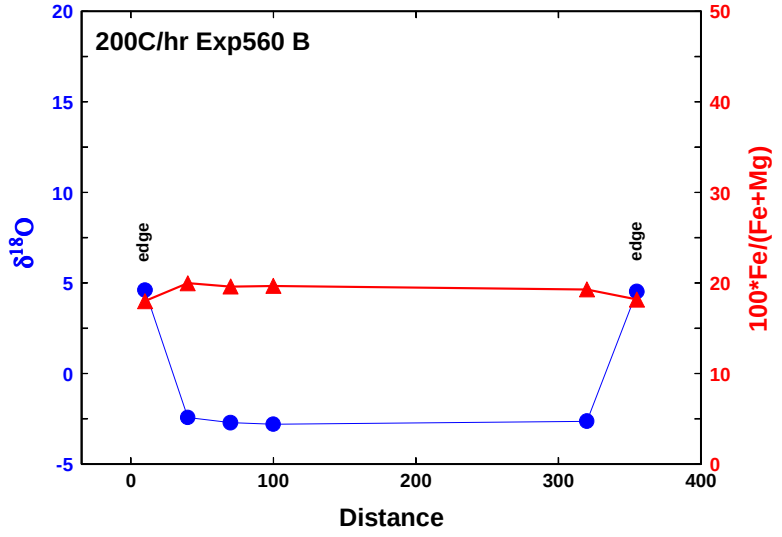

Figure 4.5f.

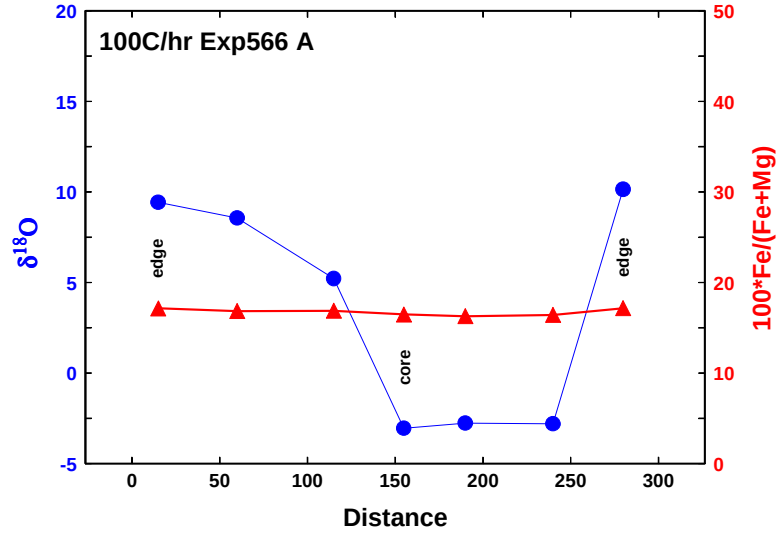

Figure 4.5g.

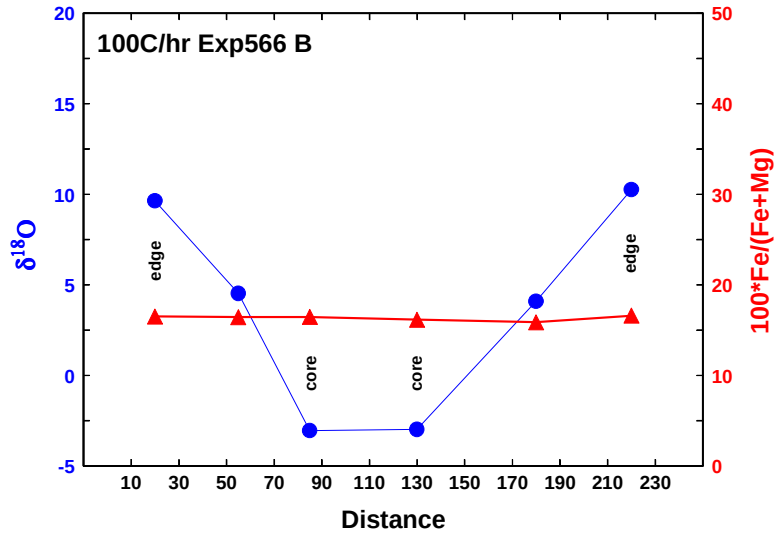

Figure 4.5h.

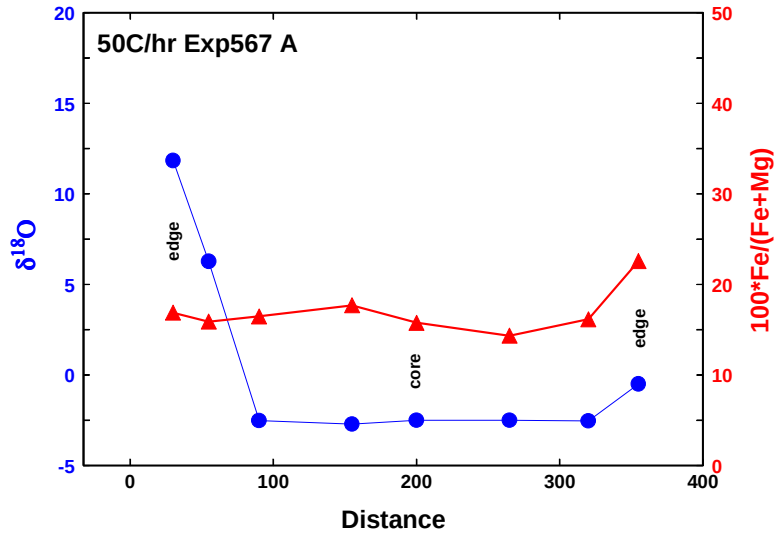

Figure 4.5i.

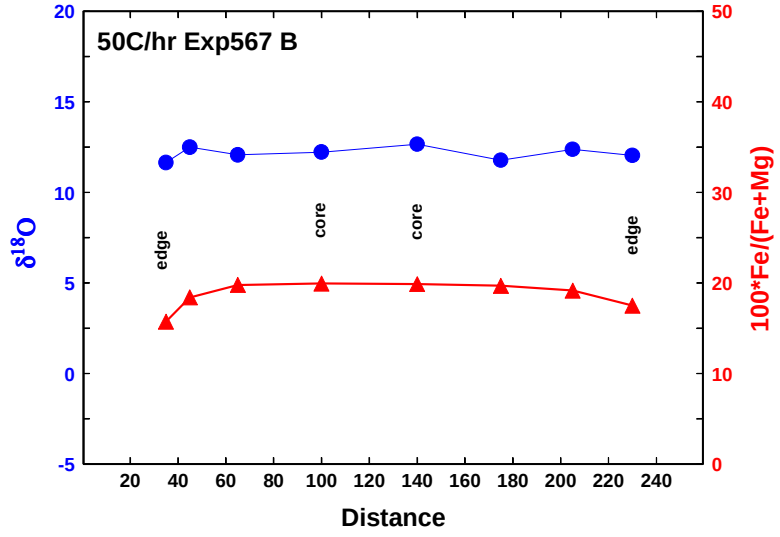

Figure 4.5j.

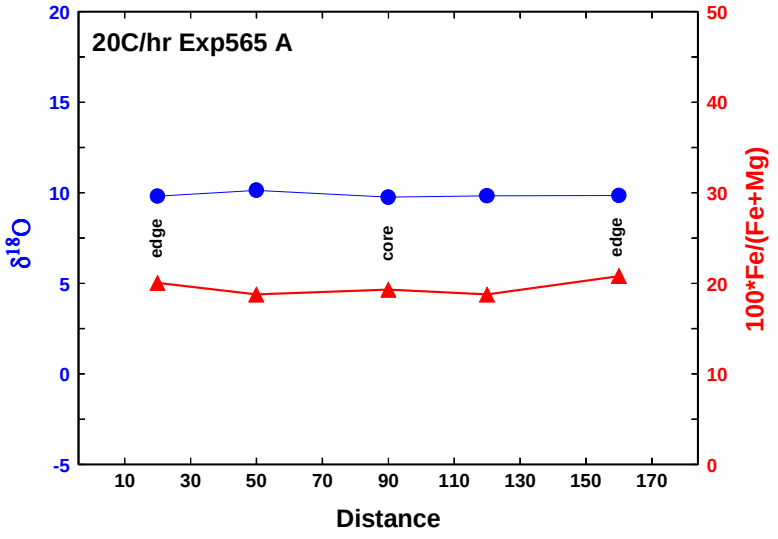

Figure 4.5k.

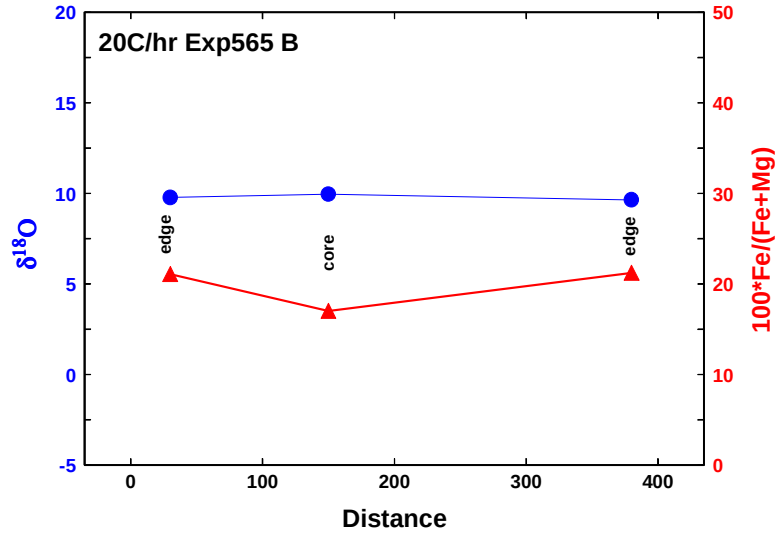

Figure 4.5l.

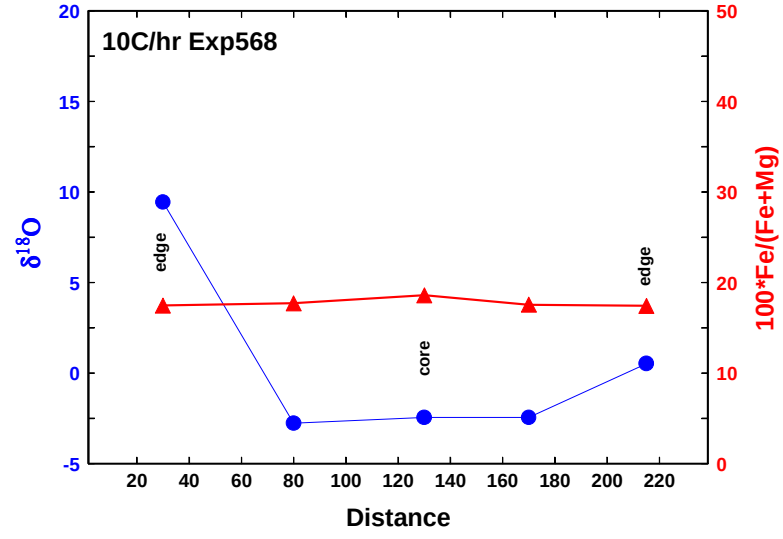

Figure 4.5m.

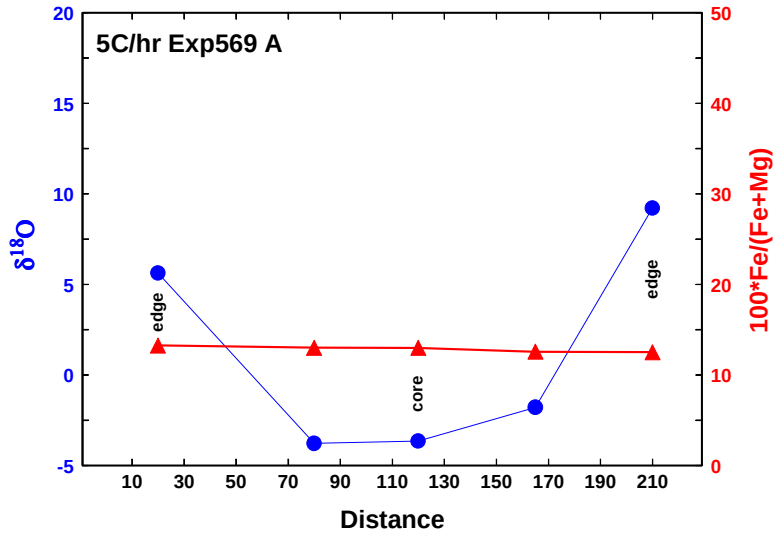

Figure 4.5n.

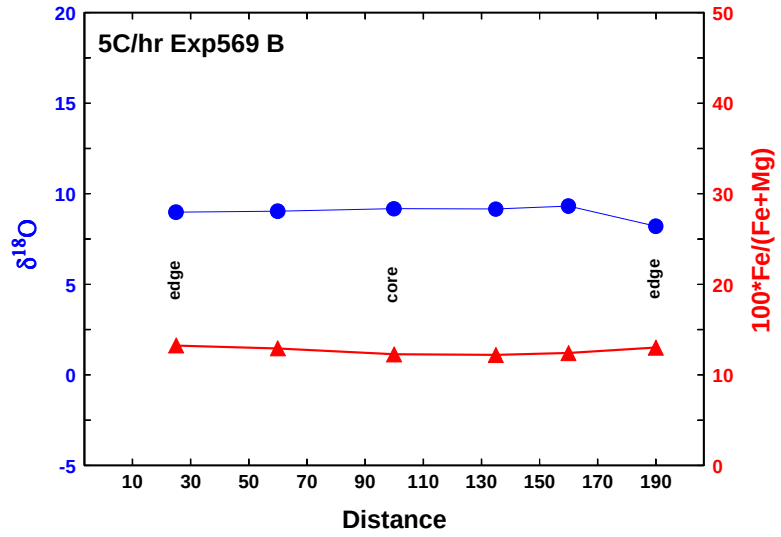

Figure 4.6.

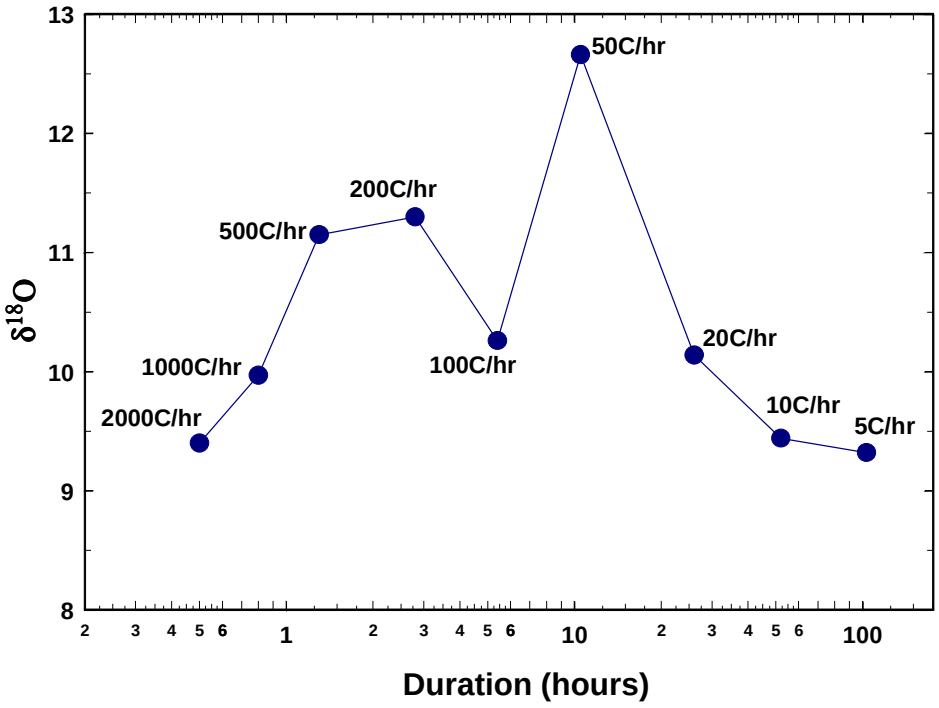
13
12
11
10
9
8
δ18O
50C/hr
200C/hr
500C/hr
20C/hr
1000C/hr
100C/hr
10C/hr
5C/hr
2000C/hr
2 3 4 5 6 1 2 3 4 5 6 10 2 3 4 5 6 100
Duration (hours)

Figure 4.7.

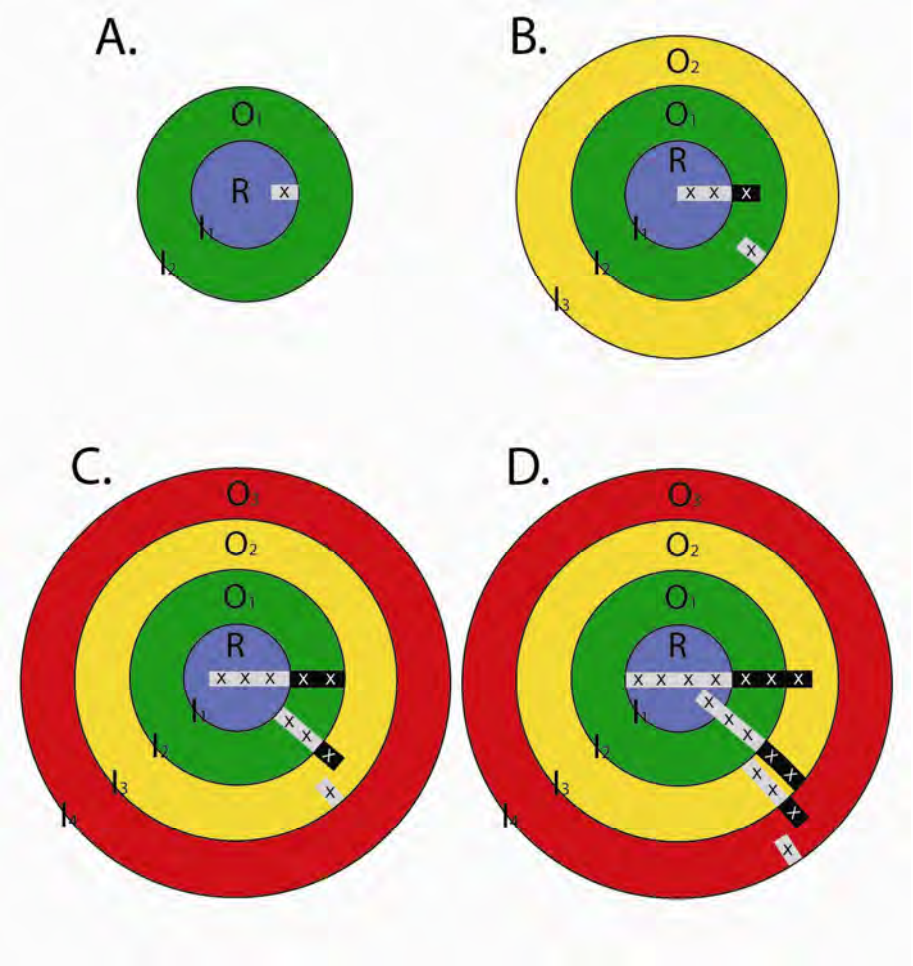

Figure 4.8.

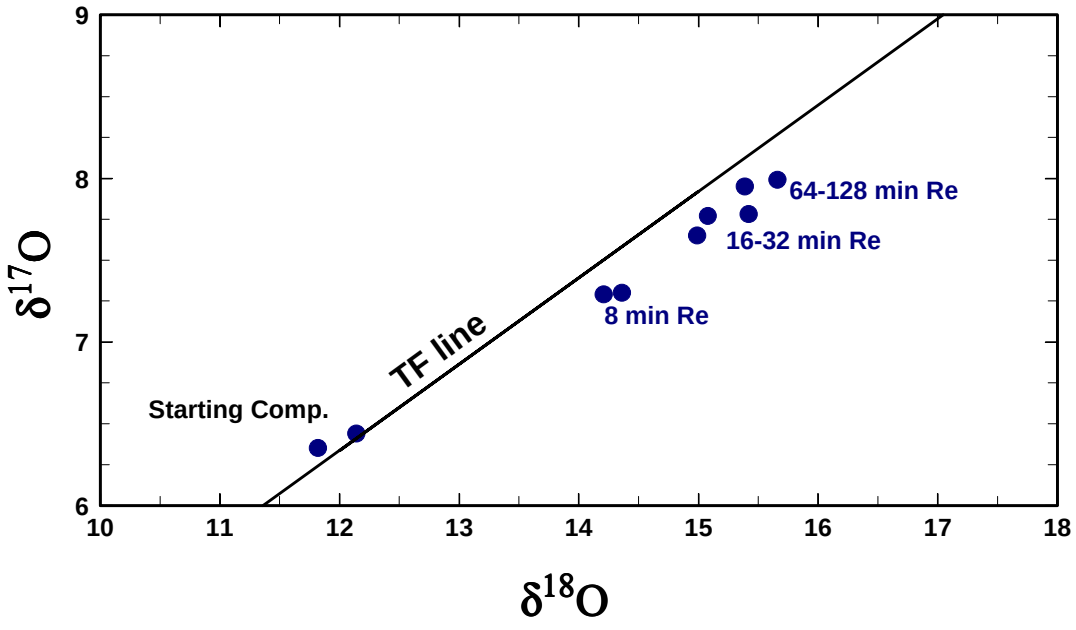
9
8
7
6
10
11
12
13
14
15
16
17
18
δ17O
δ18O
64-128 min Re
16-32 min Re
8 min Re
TF line
Starting Comp.

Appendix I. Chemical Analyses of Electron Microprobe Mineral Standards

Mineral	SiO_2	TiO_2	Al_2O_3	Cr_2O_3	FeO	MnO	MgO	CaO	Na_2O	K_2O	NiO	P_2O_5	Total	Ref.
Anorthite, Miyake Island, Japan	44.09	0.01	35.46	-	0.46	-	0.08	19.45	0.40	-	-	0.02	99.97	1
Anorthoclase, Kakanui, New Zealand, NMNH 133868	66.44	-	20.12	-	0.20	-	-	0.87	9.31	2.35	-	-	99.29	2
Orthoclase OR-1	64.39	-	18.57	-	-	-	-	-	1.14	14.92	-	-	99.02	3
Plagioclase (Labradorite), Lake County, OR, NMNH 115900	51.25	0.05	30.91	-	0.46	0.01	0.14	13.64	3.45	0.18	-	-	100.09	2
Tiburon Albite, CA	68.74	-	19.37	-	0.04	-	-	-	11.79	0.03	-	-	99.97	4
Olivine (Fo 90), San Carlos, Gils Co., AZ, NMNH 111312	40.81	-	-	-	9.55	0.14	49.42	0.05	-	-	0.37	-	100.34	2
Fayalite, Rockport, MA, NMNH 85276	29.22	0.04	-	-	67.55	2.14	-	-	-	-	-	-	99.65	2
Olivine 174.1, Kauai, Hawaii	40.50	-	-	-	9.35	0.13	49.20	-	-	-	0.36	-	99.54	5
Olivine, Quebec, Chibougamau, Canada	42.00	-	-	-	3.05	0.07	54.40	-	-	-	-	-	99.52	6
Augite, Kakanui, New Zealand, NMNH 122142	50.73	0.74	8.73	-	6.4	0.13	16.65	15.82	1.27	-	-	-	100.47	2
Diopside Glass, synthetic	55.48	-	-	-	-	-	18.62	25.90	-	-	-	-	100.00	7
Lunar Crater Augite, Nevada, NMNH 164905	50.48	0.51	7.53	0.85	4.69	0.12	17.32	17.30	0.84	-	-	-	100.14	2
Orthopyroxene 25-25	54.31	0.17	4.36	0.30	6.35	0.16	33.32	0.84	0.08	-	0.09	-	99.98	8
Hornblende, Kakanui, New Zealand, NMNH 143965	40.37	4.72	14.90	-	11.0	0.09	12.80	10.30	2.60	2.05	-	-	98.83	2
Rhodonite, Minas Gerais, Brazil	47.02	-	-	-	2.32	45.20	3.91	1.48	-	-	-	-	99.93	9
$MgCr_2O_4$	-	-	-	79.04	-	-	20.96	-	-	-	-	-	100.00	10
TiO_2, synthetic	-	100.00	-	-	-	-	-	-	-	-	-	-	100.00	11
Berlinite, synthetic	-	-	41.80	-	-	-	-	-	-	-	-	58.20	100.00	12
Wilberforce Apatite, Ontario	0.25	-	0.02	-	0.06	-	-	54.94	0.24	-	-	40.71	96.22	13

Source:

1 E. Mathez, AMNH
2 E. Jarosewich
3 Ingamells
4 University of California, Berkley
5 R. W. White
6 T. Frisch
7 F. R. Boyd
8 I. Charmichael
9 C. Klein
10 I. Ridley
11 unknown
12 G. Harlow, AMNH
13 C.M. Taylor

Appendix II. Vacuum Furnace Construction

The vacuum furnace consists of five main components 1) a standard, vertical tube, high temperature Deltech box furnace, 2) a alumina muffle tube assembly, 3) a quartz dome - gas inlet - support assembly, 4) the mechanical pump, turbopump and their respective vacuum gauges, and 5) the cooling heads and a water chiller.

The standard Deltech furnace (VT-31-OS) is a one atmosphere, high temperature furnace designed to achieve temperatures up to 1600ºC (Fig. A1). The furnace consists of an insulated steel box, 16 inches cubed, through which an alumina muffle tube passes vertically. Inside the insulation and encircling the ceramic tube are six molybdenum disilicide U-shaped heating elements (Kanthal). The heating elements are linked together at the top of the furnace using aluminum buss bars. The elements heat the furnace by conduction through the ceramic tube. Controls for the furnace are contained within a separate unit.

The muffle tube assembly consists of an Al_2O_3 ceramic tube onto which customized steel flanges are bonded (Fig. A2). The steel flanges facilitate the incorporation of and connection to the 10^{-6} torr vacuum system using standard CF and KF vacuum fittings. The original version of the muffle tube assembly (Yu et al., 2003) consisted of a 99.8% alumina tube bonded at the top to a custom KF50 steel flange/cooling head attachment and bonded at the bottom to a custom 1.33 inch CF flange (Fig. A3). The assembly was fabricated by Ceramaseal (New Lebanon, NY) using a metal-ceramic bonding method (unknown composition).

NOTE: There are two major types of seals used in vacuum systems: CF and KF. CF or conflat seals consist of two flat headed (typically 304 stainless steel) flanges which are tightened together using six to eight nuts and bolts. Between the two flanges, a copper or aluminum deformable O-ring is sandwiched and forms a high vacuum seal (Fig. A4). CF seals are good to 10^{-10} torr. KF or Kwik seals (sometimes denoted as NW) consist of two (typically 304 stainless steel) flanges, which have 15 degree angled outer edges, a Viton or Buna O-ring with a steel centering ring, and an aluminum C-shaped clamp which is closed using a single wingnut fastener (Fig. A5). The two flanges are placed together with the O-ring and centering ring between them. The clamp then encompasses both flanges and the O-ring is tightened, applying uniform pressure along the 15 degree inclined surface. The clamp allows rapid assembly and disassembly and is useful for applications up to 10^{-8} torr and temperatures near the clamp of 200ºC.

There were major drawbacks in the design of the Yu et al. (2003) assembly that necessitated changes to the furnace muffle tube and vacuum system. The changes became absolutely necessary because the ceramic tube slowly but steadily collapsed during early heating and evacuation tests to determine the dissolution rate of forsterite grains in a chondrule composition melt at 1500ºC (Fig. A6). The muffle tube imploded following run times of about 50 hours at high temperature. It is unclear why previous researchers in the same lab did not experience this type of muffle tube collapse, but it is hypothesized that, at high temperatures of the current experiments, the very low pressures employed were never achieved in practice by the previous researchers. This is either the result of basic design flaws (constrictions and obstacles) in their evacuation system or as discussed below inherent sealing problems with the earlier muffle tube supplied by the manufacturer.

Following the implosion, negotiations with the fabricator, Ceramaseal, began and attempts to produce a new muffle tube assembly were made. Repeated attempts failed as the engineer who originally built the first muffle tube had left the company, leaving no one who had sufficient experience to successfully complete the assembly. Ceramaseal could not reproduce their own original design of the KF flange-cooling head combination assembly. Because of the large mass of steel used in the seal construction, producing consistent leak tight seals became impossible to achieve. The thermal mass of the steel continually inhibited proper melting of the slurry used in making the metal-to-ceramic seal. Metal to ceramic seals within the cooling head were breaking before the metal-to-ceramic seal around the muffle tube could be achieved. Although a new tube was produced some 14 months later, it was of poor quality, having had microcracks introduced into the ceramic during assembly. Following 18 months of frustration with Ceramaseal, the author decided to find a new company.

Of the five companies contacted by the author, the most professional, accommodating and enthusiastic was Omley Industries (Grants Pass, Oregon). The author was quite fortunate in being able to deal directly with the vice president of the company, Dave Omley. Ironically, it was Dave Omley's father who had founded Ceramaseal back in the 1970's. However, in the 1980's, Dave's father sold the company, as it was moving towards mass production, while he wished to pursue custom fabrications.

After consultation with Dave Omley and his engineers about the layout and requirements of the furnace, vacuum system and muffle tube, several fundamental design changes were made to solve difficulties with the ceramic-to-metal brazing, as well as practical maintenance annoyances the author had discovered. The first redesign involved completely separating the upper furnace cooling head (which cools the metal-to-ceramic seal) from the muffle tube assembly (Fig. A7). This reduced the large mass of metal in contact with the ceramic to only simple stainless steel flanges, thus making it much easier to achieve an efficient seal. The flanges and extension rings required in making the seal were composed of either titanium or stainless steel (Fig. A8a-e). At the top of the muffle tube would be the KF50 flange, while the bottom flange would be altered from a CF 1.33 to a KF16 (Fig. A9). The change from CF to KF would make attachment to the vacuum system easier. Extension rings were used to lock the flanges in position. [The furnace-vacuum system is contained within a confined space beneath the furnace which limits the amount of torque and arc of rotation that can be used to tighten the CF bolts. This would not be of great concern if both the vacuum system and furnace were not made of fragile materials. In trying to produce a leak tight CF seal, ever present was the constant possibility of cracking the ceramic or injuring the user. Typically, the most common result was stripping the threads off the bolts and the skin from your knuckles. This problem was exacerbated by the fact that the vacuum system and furnace were intimately tied together. Whenever maintenance was performed on either the vacuum system or furnace, CF seals were required to be broken. Re-establishing a good seal was both extremely difficult and time consuming.]. Additionally, new detachable, cooling heads were designed by the author to snugly fit around the metal-to-ceramic seals that could be easily removed during maintenance (Fig. A10). The new cooling heads (both top and bottom) would be made separately by the Rutgers University Physics department from stainless steel. The metal-to-ceramic brazing between the flanges and muffle tube was achieved using a titanium-copper-silver alloy slurry and a ceramic tube composed of 99.6 wt% Al_2O_3, slightly less pure than the original, but easier to achieve a seal against. A ~10^{-6} torr seal could safely be maintained as long as the alloy did not reach a temperature above 350ºC. With the detachable cooling heads positioned in contact with the seal, there was little chance of ever approaching this temperature even when the hotspot of the furnace was at peak temperature (1550ºC). The redesign proved extremely flexible during maintenance to either the furnace or vacuum systems. The entire furnace could be taken apart and put back together by a single person within an hour without the use of any tools other than a simple level. The entire assembly also cost less than one-third of Ceramaseal's price.

Two assemblies were necessary to complete the oxygen experiments, as the first Omley tube eventually collapsed after 50 experiments as a result of exposure to the high temperature and vacuum conditions (Fig. A11). The first Omley tube lasted about 9 months, over which time the tube was at 1550ºC and ~10^{-5} torr over 250 accumulated hours, quite good considering the extreme conditions. Since 2003, Omley has produced four such muffle tube assemblies for the author, two of which are still unused.

Above the muffle tube assembly, sits the quartz dome, sample rod, gas inlet, and support structure (Fig. A12). The gas inlet is a five pound stainless steel unit which allows precise control of very low gas flowrates into the furnace. At its base and head, the muffle tube and quartz tube, respectively, are attached using KF50 flanges. The quartz dome is simply a 1.75 inch wide, quartz tube closed off on one end which attaches to the furnace muffle tube and allows sufficient space for the sample rod to insert and extract experiments. The sample rod is attached to a magnet system which allows the sample to be inserted and extracted from the furnace hotspot. Because there was some concern about the weight of the gas inlet bending or torquing the muffle tube when the furnace was at high temperature and high vacuum (at high temperature and vacuum, even alumina behaves plastically and deforms), a counterweight support structure was designed and constructed to remove any stress. The counterweight structure consists of a five pound weight and wire, which pass through a pulley and are attached to the gas inlet (Fig. A13).

The vacuum furnace contains two pumps: a mechanical pump and a turbopump. The mechanical pump is attached to the turbopump by KF16 flanges. Subsequently the turbopump attaches to the muffle tube by a T-adapter. The adapter has connections on three sides (Fig. A14). The muffle tube attaches to the upper vertical end of the T-adapter, the left arm connects to the turbopump, the right arm connects to the high and low vacuum gauges, and the lower vertical end is unused and sealed shut. The mechanical pump evacuates the muffle tube through the turbopump. The mechanical pump can achieve a maximum vacuum of 1.3 x 10^{-2} torr. Once the furnace has been pumped down by the mechanical pump (typical pump down time is 10 minutes, assuming the system is clean and has been used recently), the turbopump is switched on. Maximum vacuum attainable using the turbo (and mechanical) pump is 8 x 10^{-7} torr at room temperature or

3×10^{-4} torr at 1550ºC. Maximum vacuum can typically be achieved in about 8-12 hours, assuming the furnace and pumps are free of contamination. Vacuum measurements are made in a cold (50ºC) region of the furnace and recalculated for the temperature experienced by the sample in the hotspot. Vacuum gauge pressure readings are recorded by computer continuously (five times per second) throughout the experiment. A serial output port on the high vacuum gauge indicator allows a PC computer connection to the gauge using an analog-to-digital converter and a 9 pin bidirectional serial cable (Fig. A15). The gauge outputs voltages between 0-10 volts which have been calibrated against the vacuum readings of the system. A conversion chart, included with the vacuum indicator, correlates the recorded voltage to an actual pressure reading.

The final piece of the furnace is the water chiller (Fig. A16). The recirculating water chiller maintains a constant flow of 20ºC water to the cooling heads. The major task of the water supplied to the heads is to cool the metal-to-ceramic seals and any gases as they exit the furnace.

REFERENCES

Yu Y., Hewins R. H., Alexander C. M. O'D. and Wang J. (2003) Experimental study of evaporation and isotopic mass fractionation of potassium in silicate melts. *Geochimica et Cosmochimica Acta* **67**, 773-786.

FIGURE CAPTIONS

Figure A1. Photo showing the basic Deltech vertical muffle tube, high temperature, box furnace and controller unit.

Figure A2. Photo of the Ceramaseal muffle tubes with the KF – cooling head design at the top and the CF flange at its base.

Figure A3. Close-up photos showing the original design of the muffle tube used by Yu et al. (2003). Photo (a) shows the upper cooling head-KF flange combination, while photo (b) shows the base CF 1.33 flange.

Figure A4. CF flange system used on the original furnace and largely replaced on the new furnace design. A copper or aluminum gasket is fitted between the two flanges and compressed with six nuts and bolts.

Figure A5. KF flange system for upper (Fig A5a., KF50) and lower (Fig A5b., KF16) muffle tube.

Figure A6. Photo showing the plastic deformation that occurs to the central portion of the muffle tube following extended exposure to high temperatures and very low pressures.

Figure A7. General schematic diagram drawn by the engineers at Omley Industries of the redesigned muffle tube assembly shown with simple KF attachments

Figure A8. Detailed schematic diagrams drawn by the engineers at Omley Industries of the a) ceramic tube, b) upper KF50 flange, c) lower KF16 flange, d) ribbed extension ring, e) tube extension ring.

Figure A9. Close-up photos of the upper KF50 and lower KF16 flanges mounted on the muffle tube.

Figure A10. Schematic diagram drawn by the author detailing the cooling heads used on the furnace. In diagram (a), the views from the top and side of the cooling head are shown, while in (b), the side view is repeated with muffle tube shown in its proper position.

Figure A11. Full view photo of the first Omley muffle tube following its collapse.

Figure A12. Two photos of the top of the vacuum furnace showing the "sky hook" counterbalance support, the cooling heads, the quartz dome, the gas mixer, and the C-shaped clamps of KF flanges which attach the latter two parts to the muffle tube.

Figure A13. Schematic diagram of the vacuum furnace.

Figure A14. Close-up of the base of the muffle tube and the T-connection which attaches the turbo-pump to the muffle tube (left side of T) as well as the vacuum gauges (right side of T).

Figure A15. Another close-up showing the base of the muffle tube with the turbo-pump, vacuum gauges and the high vacuum gauge indicator (right). The indicator which can be linked to a PC using an analog-to-digital converter and the serial port in the back of the indicator.

Figure A16. Photo of the entire vacuum furnace and chiller.

Figure A1.

Figure A2.

Figure A3a.

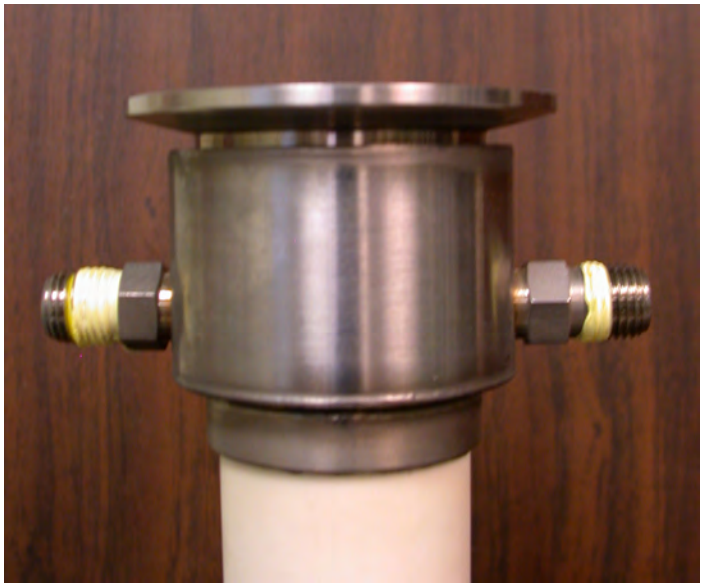

Figure A3b.

Figure A4.

Figure A5a.

Figure A5b.

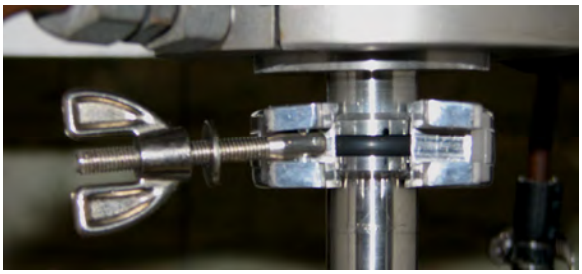

Figure A6.

Figure A7.

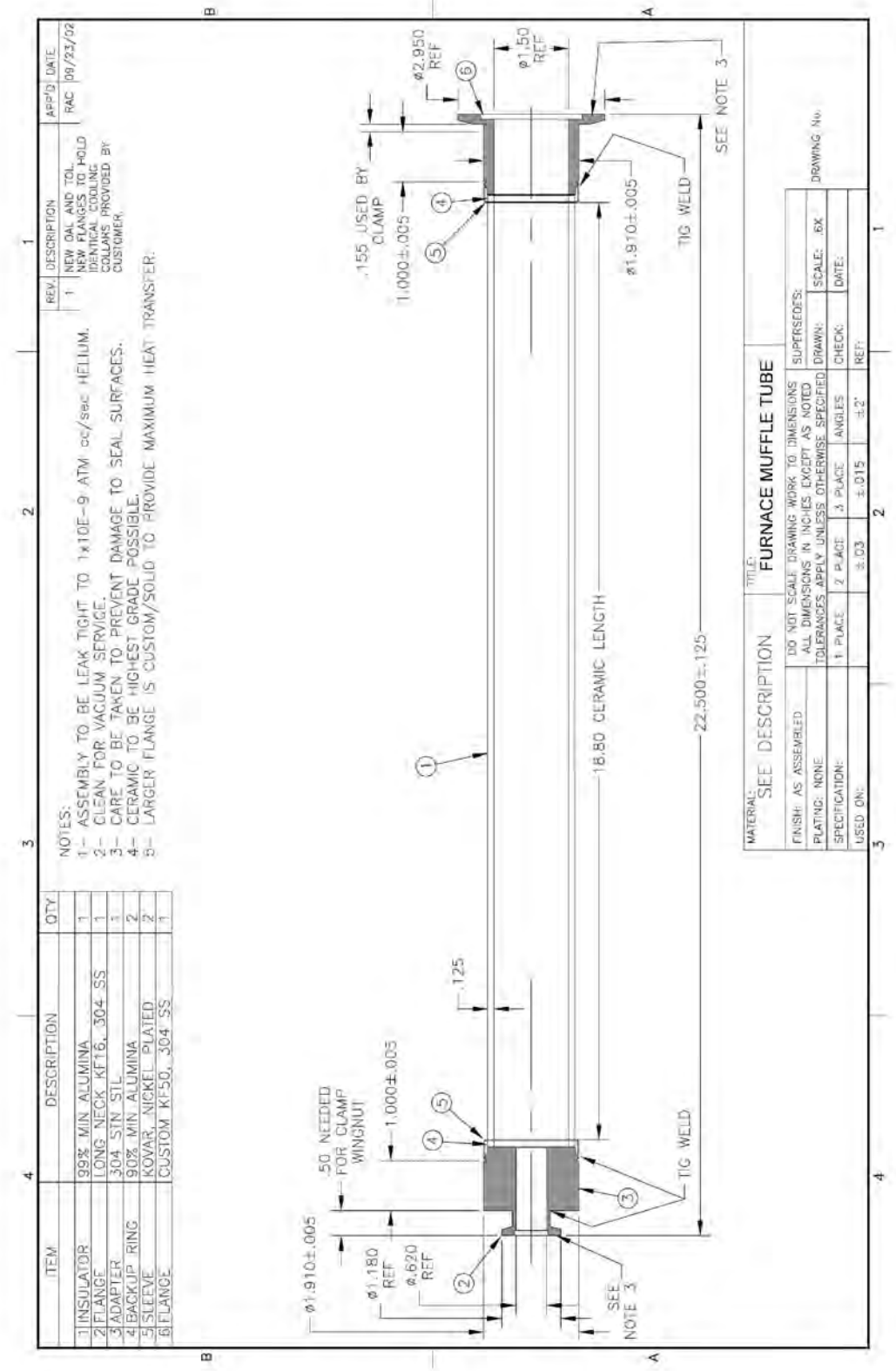
ITEM
DESCRIPTION
QTY
1 INSULATOR 99% MIN ALUMINA 1
2 FLANGE LONG NECK KF16, 304 SS 1
3 ADAPTER 304 STN STL 1
4 BACKUP RING 90% MIN ALUMINA 2
5 SLEEVE KOVAR, NICKEL PLATED 2
6 FLANGE CUSTOM KF50, 304 SS 1
NOTES:
1- ASSEMBLY TO BE LEAK TIGHT TO 1x10E-9 ATM cc/sec HELIUM.
2- CLEAN FOR VACUUM SERVICE.
3- CARE TO BE TAKEN TO PREVENT DAMAGE TO SEAL SURFACES.
4- CERAMIC TO BE HIGHEST GRADE POSSIBLE.
5- LARGER FLANGE IS CUSTOM/SOLID TO PROVIDE MAXIMUM HEAT TRANSFER.
REV.
DESCRIPTION
APP'D
DATE
1 NEW OAL AND TOL. NEW FLANGES TO HOLD IDENTICAL COOLING COLLARS PROVIDED BY CUSTOMER.
RAC
09/23/02
.155 USED BY CLAMP
1.000±.005
ø2.950 REF
ø1.50 REF
ø1.910±.005
TIG WELD
SEE NOTE 3
18.80 CERAMIC LENGTH
22.500±.125
.125
1.000±.003
.50 NEEDED FOR CLAMP WINGNUT
ø1.910±.005
ø1.180 REF
ø.620 REF
TIG WELD
SEE NOTE 3
MATERIAL: SEE DESCRIPTION
TITLE: FURNACE MUFFLE TUBE
FINISH: AS ASSEMBLED
PLATING: NONE
SPECIFICATION:
USED ON:
DO NOT SCALE DRAWING WORK TO DIMENSIONS
ALL DIMENSIONS IN INCHES EXCEPT AS NOTED
TOLERANCES APPLY UNLESS OTHERWISE SPECIFIED
1 PLACE
2 PLACE
3 PLACE
ANGLES
±.03
±.015
±2°
SUPERSEDES:
DRAWN:
CHECK:
REF:
SCALE: .6X
DATE:
DRAWING No.

Figure A8a.

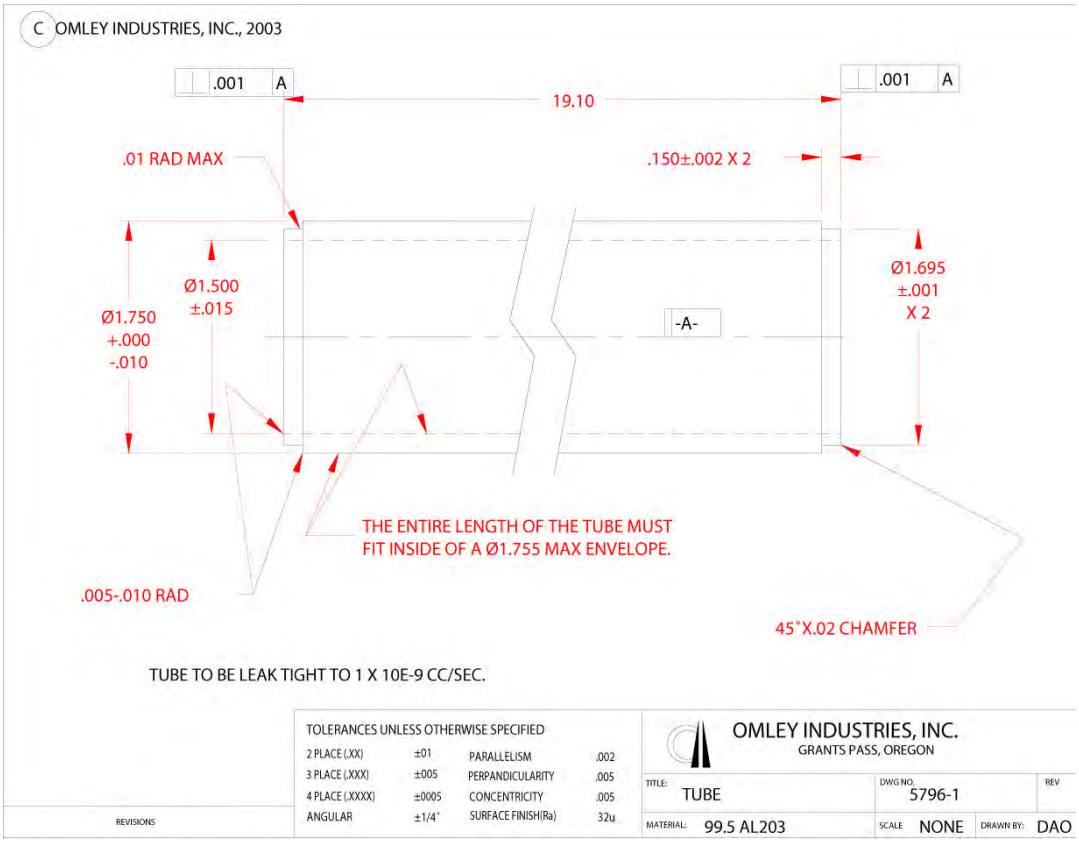
C OMLEY INDUSTRIES, INC., 2003
.001 A
19.10
.001 A
.01 RAD MAX
.150±.002 X 2
Ø1.500
±.015
Ø1.750
+.000
-.010
-A-
Ø1.695
±.001
X 2
THE ENTIRE LENGTH OF THE TUBE MUST
FIT INSIDE OF A Ø1.755 MAX ENVELOPE.
.005-.010 RAD
45°X.02 CHAMFER
TUBE TO BE LEAK TIGHT TO 1 X 10E-9 CC/SEC.
TOLERANCES UNLESS OTHERWISE SPECIFIED
2 PLACE (.XX) ±01
3 PLACE (.XXX) ±005
4 PLACE (.XXXX) ±0005
ANGULAR ±1/4°
PARALLELISM .002
PERPANDICULARITY .005
CONCENTRICITY .005
SURFACE FINISH(Ra) 32u
REVISIONS
OMLEY INDUSTRIES, INC.
GRANTS PASS, OREGON
TITLE: TUBE
DWG NO. 5796-1
REV
MATERIAL: 99.5 AL203
SCALE NONE
DRAWN BY: DAO

Figure A8b.

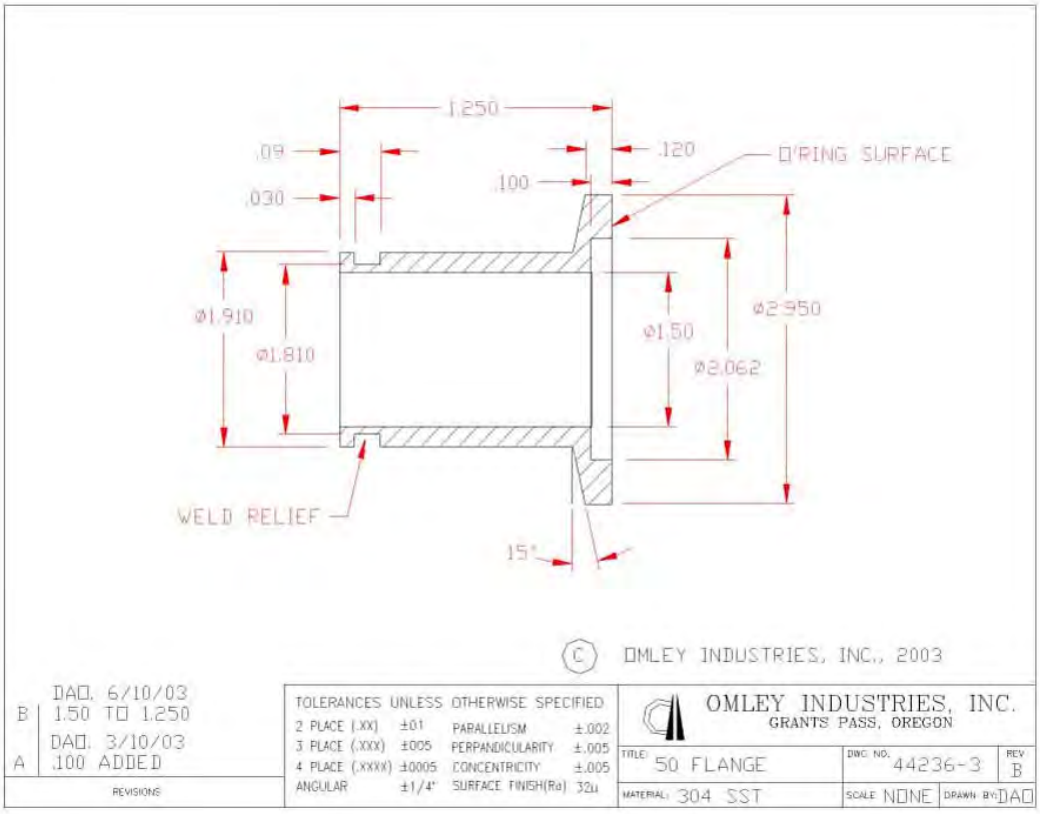
1.250
.09
.030
.100
.120
O'RING SURFACE
ø1.910
ø1.810
ø1.50
ø2.062
ø2.950
WELD RELIEF
15°
© OMLEY INDUSTRIES, INC., 2003
B DAO. 6/10/03 1.50 TO 1.250
A DAO. 3/10/03 .100 ADDED
REVISIONS
TOLERANCES UNLESS OTHERWISE SPECIFIED
2 PLACE (.XX) ±01
3 PLACE (.XXX) ±005
4 PLACE (.XXXX) ±0005
ANGULAR ±1/4°
PARALLELISM ±.002
PERPANDICULARITY ±.005
CONCENTRICITY ±.005
SURFACE FINISH(Ra) 32µ
OMLEY INDUSTRIES, INC.
GRANTS PASS, OREGON
TITLE: 50 FLANGE
DWG. NO. 44236-3
REV B
MATERIAL: 304 SST
SCALE NONE
DRAWN BY: DAO

Figure A8c.

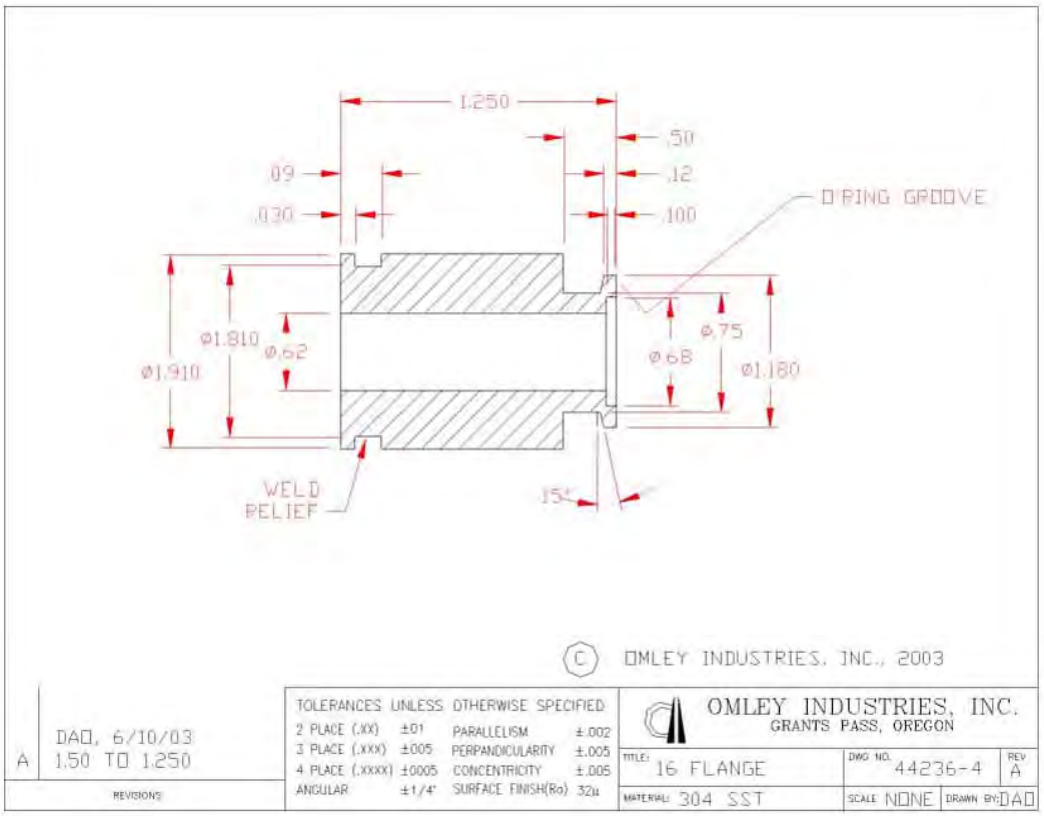
1.250
.50
.09
.12
.030
.100
O'RING GROOVE
Ø1.810
Ø.62
Ø1.910
Ø.75
Ø.68
Ø1.180
WELD
RELIEF
15°
© OMLEY INDUSTRIES, INC., 2003
A
DAO, 6/10/03
1.50 TO 1.250
REVISIONS
TOLERANCES UNLESS OTHERWISE SPECIFIED
2 PLACE (.XX) ±01
3 PLACE (.XXX) ±005
4 PLACE (.XXXX) ±0005
ANGULAR ±1/4°
PARALLELISM ±.002
PERPANDICULARITY ±.005
CONCENTRICITY ±.005
SURFACE FINISH(Ra) 32µ
OMLEY INDUSTRIES, INC.
GRANTS PASS, OREGON
TITLE: 16 FLANGE
DWG NO. 44236-4
REV A
MATERIAL: 304 SST
SCALE NONE
DRAWN BY: DAO

Figure A8d.

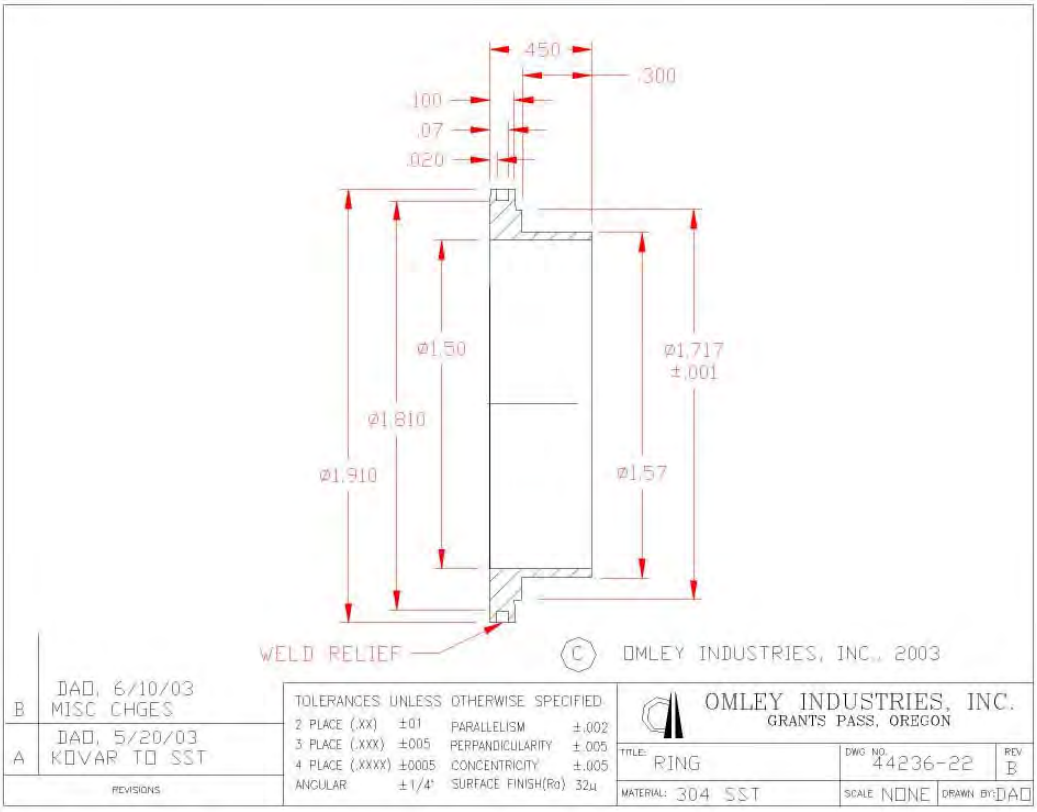
.450
.300
.100
.07
.020
ø1.50
ø1.717
±.001
ø1.810
ø1.910
ø1.57
WELD RELIEF
© OMLEY INDUSTRIES, INC., 2003
B DAD, 6/10/03 MISC CHGES
A DAD, 5/20/03 KOVAR TO SST
REVISIONS
TOLERANCES UNLESS OTHERWISE SPECIFIED
2 PLACE (.XX) ±01
3 PLACE (.XXX) ±005
4 PLACE (.XXXX) ±0005
ANGULAR ±1/4°
PARALLELISM ±.002
PERPANDICULARITY ±.005
CONCENTRICITY ±.005
SURFACE FINISH(Ra) 32µ
OMLEY INDUSTRIES, INC.
GRANTS PASS, OREGON
TITLE: RING
DWG NO. 44236-22
REV B
MATERIAL: 304 SST
SCALE NONE
DRAWN BY: DAD

Figure A8e.

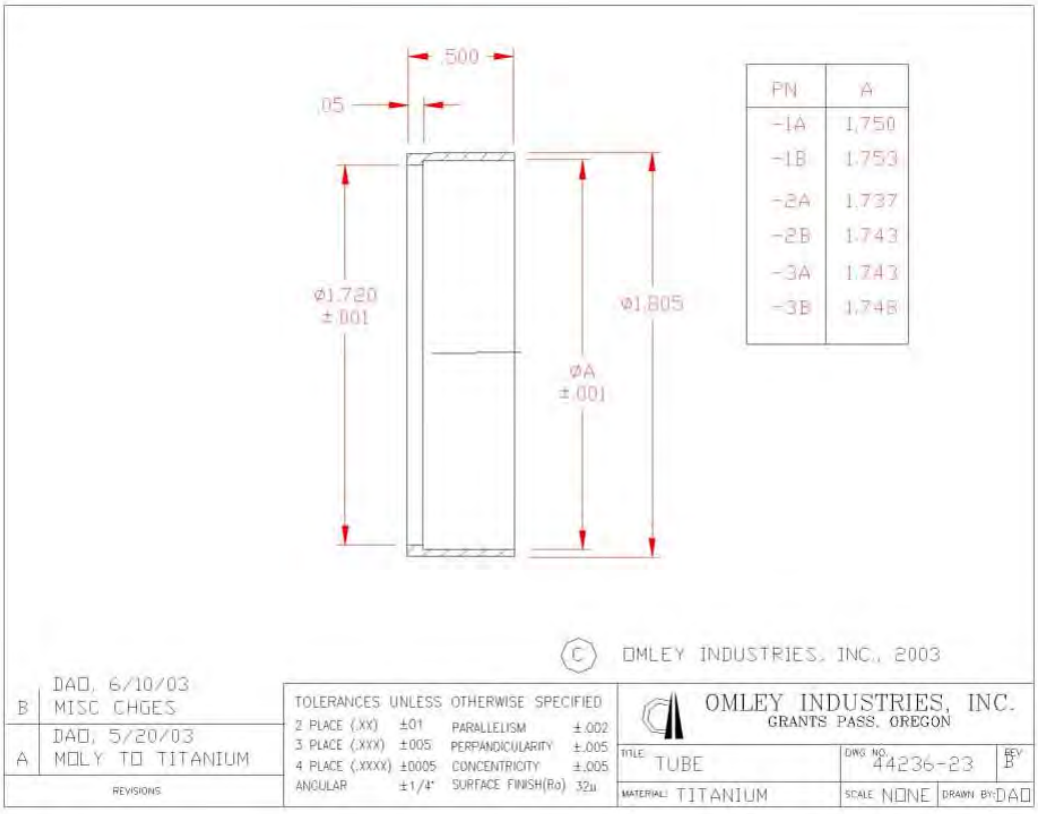
.500
.05
Ø1.720
±.001
ØA
±.001
Ø1.805
PN
A
-1A
1.750
-1B
1.753
-2A
1.737
-2B
1.743
-3A
1.743
-3B
1.746
© OMLEY INDUSTRIES, INC., 2003
B
DAD, 6/10/03
MISC CHGES
A
DAD, 5/20/03
MOLY TO TITANIUM
REVISIONS
TOLERANCES UNLESS OTHERWISE SPECIFIED
2 PLACE (.XX) ±01
3 PLACE (.XXX) ±005
4 PLACE (.XXXX) ±0005
ANGULAR ±1/4°
PARALLELISM ±.002
PERPANDICULARITY ±.005
CONCENTRICITY ±.005
SURFACE FINISH(Ra) 32µ
OMLEY INDUSTRIES, INC.
GRANTS PASS, OREGON
TITLE: TUBE
DWG NO. 44236-23
REV. B
MATERIAL: TITANIUM
SCALE: NONE
DRAWN BY: DAD

Figure A9a

Figure A9b.

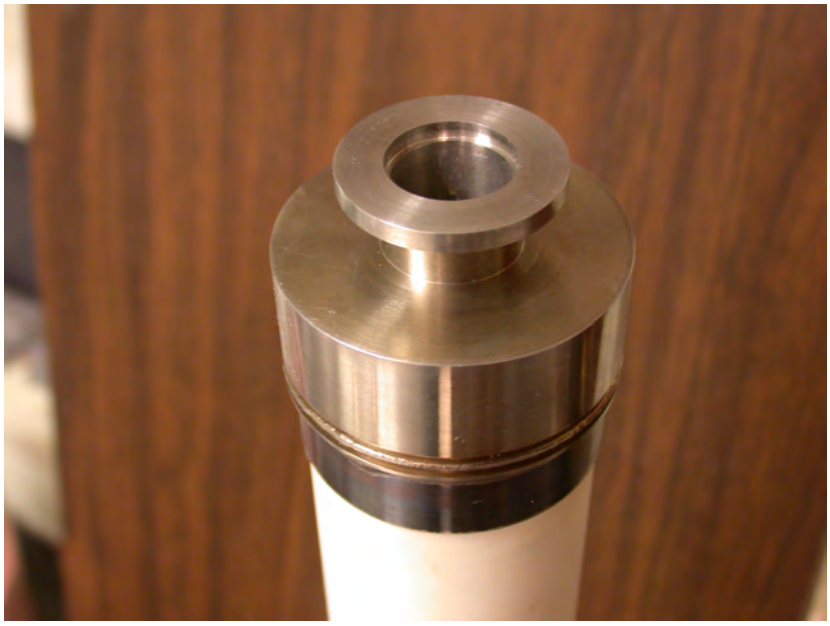

Figure A10a.

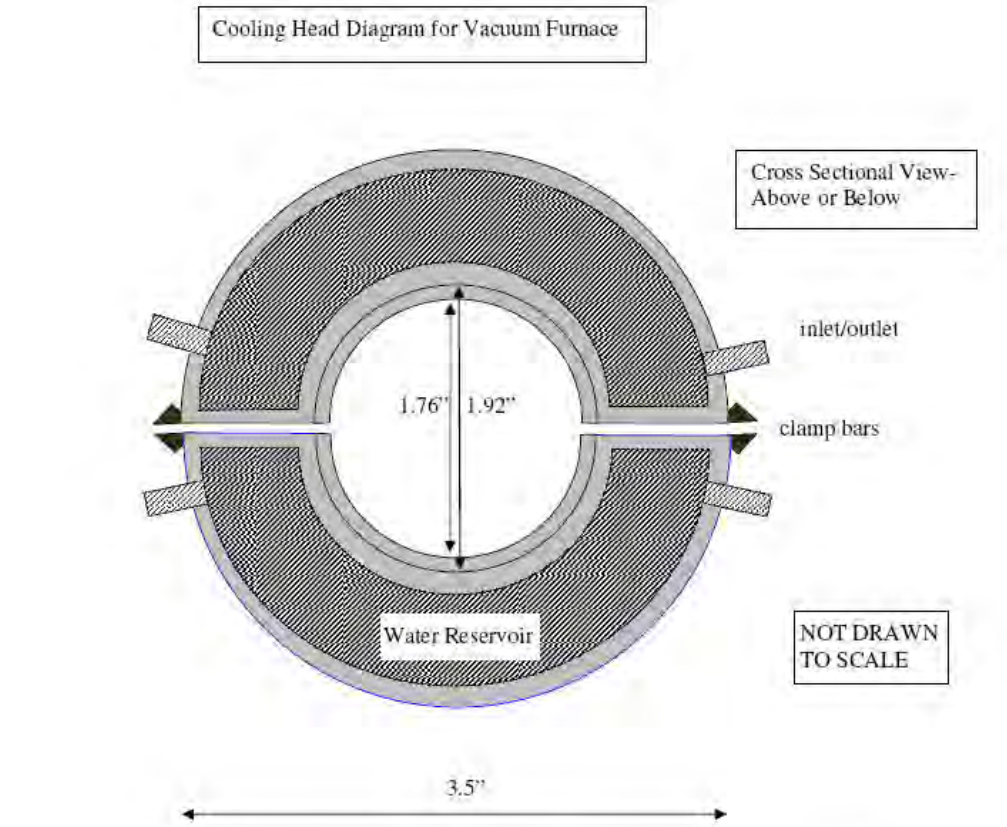

Cooling head is made of two identical halves. The complete cooling head is 3.5 inches in diameter and 2.50 inches high. The central hole changes its diameter from 1.92 inches in upper part to1.75 inches in the lower part. Each diameter extends for 1.25 inches in height. Each half cooling head has a water inlet and outlet. The two halves of the cooling head will be held together at the clamp bars using binder clips. This will allow for slight expansion of ceramic muffle tube.

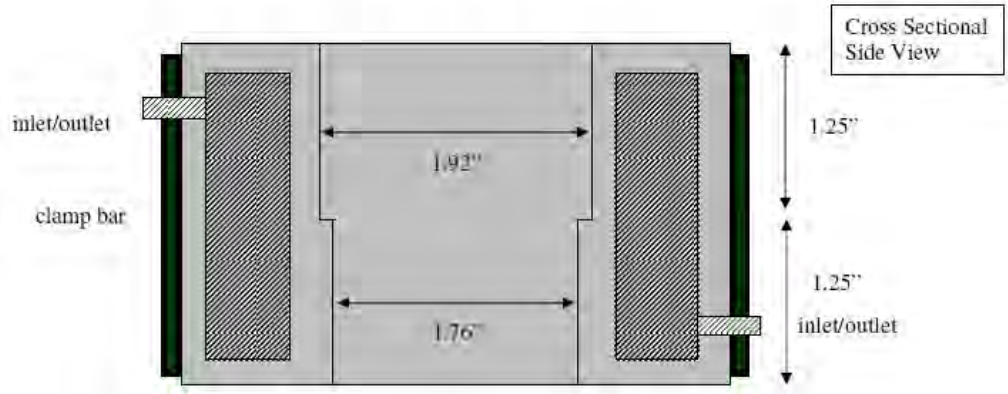

Figure A10b.

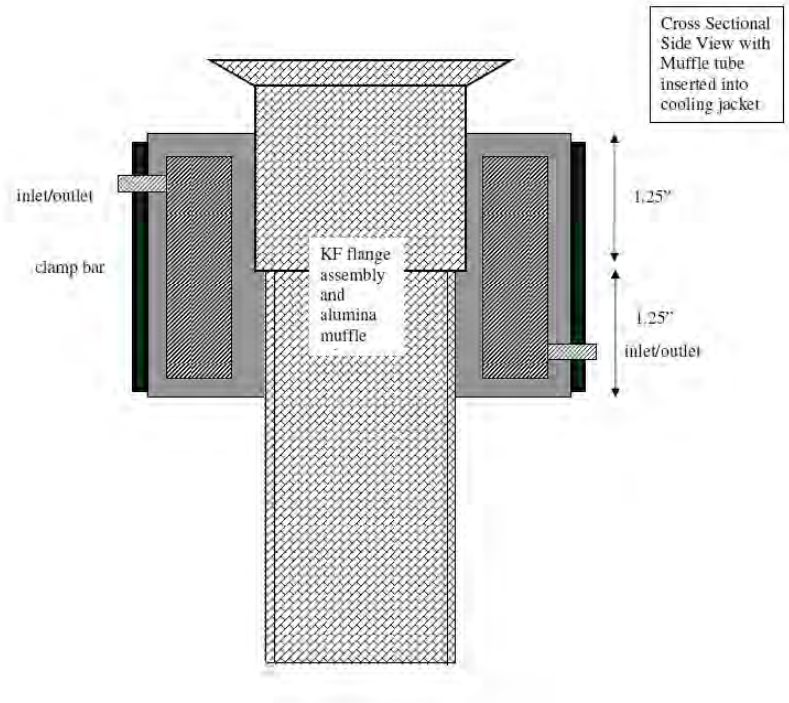

Figure A11.

Figure A12a.

Figure A12b.

Figure A13.

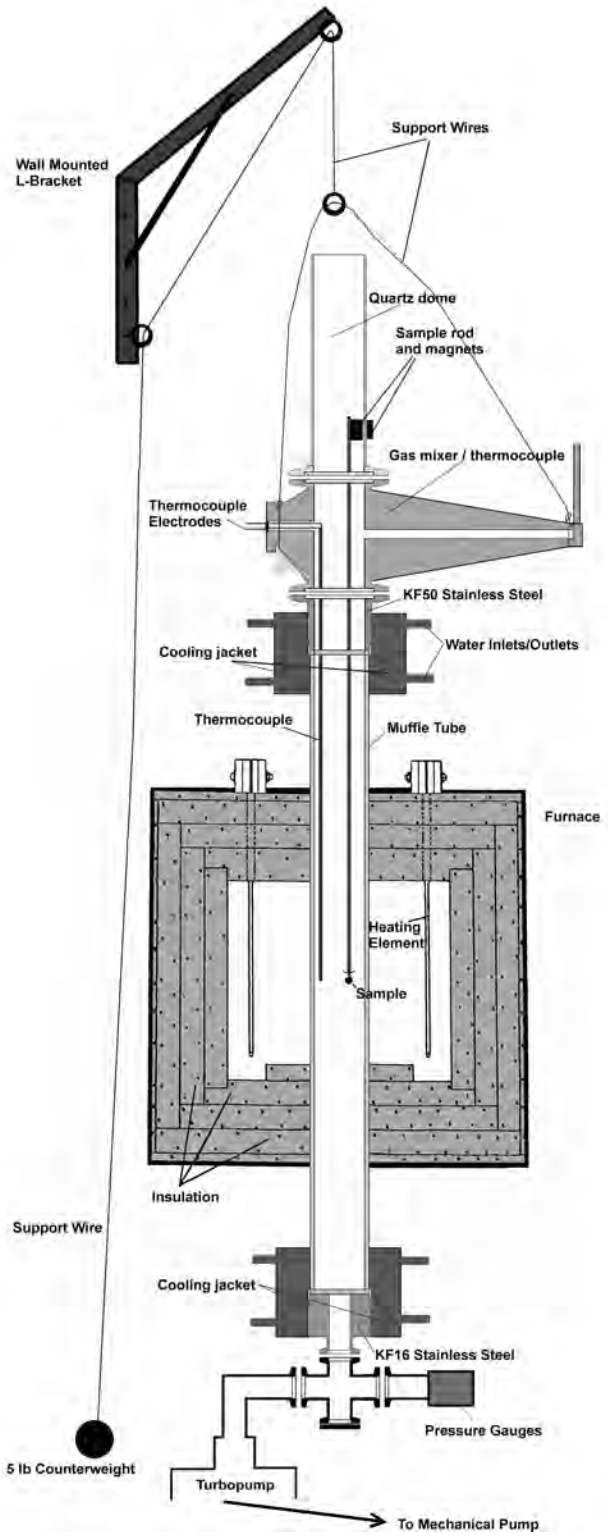
Support Wires
Wall Mounted
L-Bracket
Quartz dome
Sample rod
and magnets
Gas mixer / thermocouple
Thermocouple
Electrodes
KF50 Stainless Steel
Water Inlets/Outlets
Cooling jacket
Thermocouple
Muffle Tube
Furnace
Heating
Element
Sample
Insulation
Support Wire
Cooling jacket
KF16 Stainless Steel
Pressure Gauges
5 lb Counterweight
Turbopump
To Mechanical Pump

Figure A14.

Figure A15.

Figure A16.

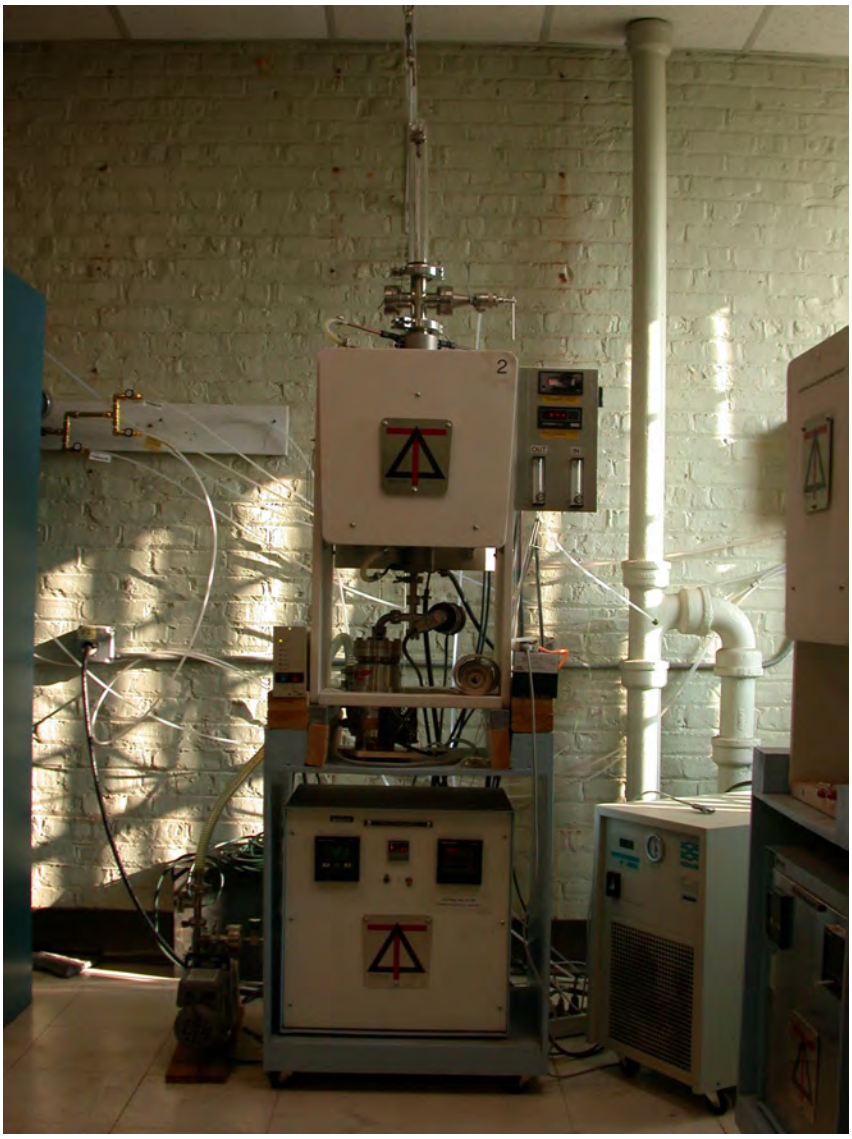

Appendix III. The calculated table used to determine the extent of Eagle Station olivine dissolved into the IIAB melt and the amount of FeO removed by either evaporation or loss to the platinum wire (in the isothermal experiments) (shown in Table 4.2). The table in section A shows the starting compositions of the IIAB melt, the alkali-free renormalized version of the IIAB melt and Eagle Station olivine. In section B, a percentage of Eagle Station olivine (noted at the top of each column) is added to the alkali-free IIAB melt and the total renormalized. In section C, the compositions shown in section B have had progressively higher amounts of FeO removed (from 5% to 30% of the total FeO) and were renormalized.

A.

	IIAB	**IIAB A-free**	**ES**
SiO2	50.92	51.81	38.21
TiO2	0.18	0.18	0
Al2O3	0.89	0.91	0
Cr2O3	0.4	0.41	0.03
FeO	21.52	21.89	19.01
MnO	0.42	0.43	0.16
MgO	22.89	23.29	42.23
CaO	1.07	1.09	0.03
Na2O	1.79		0
K2O	0.22		0
Total	100.3		99.67

B.

	Alkali-free (IIAB + %ES oliv.) & renormalized									
	1%	**2%**	**3%**	**4%**	**5%**	**10%**	**15%**	**20%**	**25%**	**50%**
SiO2	51.67	51.54	51.41	51.29	51.17	50.59	50.05	49.57	49.12	47.33
TiO2	0.18	0.18	0.18	0.18	0.17	0.17	0.16	0.15	0.15	0.12
Al2O3	0.90	0.89	0.88	0.87	0.86	0.82	0.79	0.75	0.72	0.60
Cr2O3	0.40	0.40	0.40	0.39	0.39	0.37	0.36	0.34	0.33	0.28
FeO	21.87	21.84	21.81	21.79	21.76	21.64	21.53	21.43	21.33	20.96
MnO	0.42	0.42	0.42	0.42	0.41	0.40	0.39	0.38	0.37	0.34
MgO	23.48	23.66	23.84	24.02	24.19	25.02	25.77	26.46	27.09	29.63
CaO	1.08	1.07	1.06	1.05	1.04	0.99	0.95	0.91	0.88	0.74

C.

					minus 5% FeO & renormalized					
SiO2	52.24	52.11	51.98	51.85	51.73	51.14	50.60	50.10	49.65	47.83
TiO2	0.18	0.18	0.18	0.18	0.18	0.17	0.16	0.15	0.15	0.12
Al2O3	0.91	0.90	0.89	0.88	0.87	0.83	0.80	0.76	0.73	0.61
Cr2O3	0.41	0.40	0.40	0.40	0.39	0.38	0.36	0.35	0.34	0.28
FeO	21.00	20.98	20.95	20.92	20.90	20.78	20.67	20.57	20.48	20.12
MnO	0.43	0.43	0.42	0.42	0.42	0.41	0.40	0.39	0.38	0.34
MgO	23.74	23.92	24.11	24.28	24.46	25.29	26.05	26.75	27.39	29.95
CaO	1.09	1.08	1.07	1.06	1.05	1.00	0.96	0.92	0.89	0.74
					minus 10% FeO & renormalized					
SiO2	52.83	52.69	52.56	52.43	52.30	51.70	51.16	50.65	50.19	48.34
TiO2	0.19	0.18	0.18	0.18	0.18	0.17	0.16	0.16	0.15	0.12
Al2O3	0.92	0.91	0.90	0.89	0.88	0.84	0.81	0.77	0.74	0.62
Cr2O3	0.41	0.41	0.40	0.40	0.40	0.38	0.37	0.35	0.34	0.29
FeO	20.12	20.09	20.07	20.04	20.02	19.91	19.80	19.71	19.62	19.26
MnO	0.43	0.43	0.43	0.43	0.42	0.41	0.40	0.39	0.38	0.35
MgO	24.00	24.19	24.37	24.55	24.73	25.57	26.34	27.04	27.69	30.27
CaO	1.10	1.09	1.08	1.07	1.06	1.01	0.97	0.93	0.90	0.75
					minus 15% FeO & renormalized					
SiO2	53.43	53.29	53.15	53.02	52.89	52.28	51.72	51.21	50.74	48.86
TiO2	0.19	0.19	0.18	0.18	0.18	0.17	0.16	0.16	0.15	0.13
Al2O3	0.93	0.92	0.91	0.90	0.89	0.85	0.81	0.78	0.75	0.62
Cr2O3	0.42	0.41	0.41	0.41	0.40	0.39	0.37	0.36	0.34	0.29
FeO	19.22	19.19	19.17	19.14	19.12	19.01	18.91	18.82	18.73	18.39
MnO	0.44	0.44	0.43	0.43	0.43	0.42	0.41	0.40	0.39	0.35
MgO	24.27	24.46	24.65	24.83	25.01	25.86	26.63	27.34	27.99	30.60
CaO	1.11	1.10	1.09	1.08	1.07	1.03	0.98	0.94	0.91	0.76

minus 20% FeO & renormalized

SiO2	54.04	53.90	53.76	53.63	53.49	52.87	52.31	51.79	51.31	49.40
TiO2	0.19	0.19	0.19	0.18	0.18	0.17	0.17	0.16	0.15	0.13
Al2O3	0.94	0.93	0.92	0.91	0.90	0.86	0.82	0.79	0.76	0.63
Cr2O3	0.42	0.42	0.41	0.41	0.41	0.39	0.37	0.36	0.35	0.29
FeO	18.29	18.27	18.25	18.22	18.20	18.09	18.00	17.91	17.83	17.50
MnO	0.44	0.44	0.44	0.44	0.43	0.42	0.41	0.40	0.39	0.35
MgO	24.55	24.74	24.93	25.11	25.29	26.15	26.93	27.64	28.30	30.93
CaO	1.13	1.12	1.11	1.10	1.09	1.04	0.99	0.95	0.92	0.77

minus 25% FeO & renormalized

SiO2	54.66	54.52	54.38	54.24	54.11	53.48	52.90	52.37	51.89	49.94
TiO2	0.19	0.19	0.19	0.19	0.18	0.18	0.17	0.16	0.15	0.13
Al2O3	0.95	0.94	0.93	0.92	0.91	0.87	0.83	0.80	0.77	0.64
Cr2O3	0.43	0.42	0.42	0.42	0.41	0.39	0.38	0.36	0.35	0.30
FeO	17.35	17.32	17.30	17.28	17.26	17.16	17.06	16.98	16.90	16.59
MnO	0.45	0.45	0.44	0.44	0.44	0.43	0.41	0.40	0.40	0.36
MgO	24.83	25.03	25.22	25.40	25.59	26.45	27.24	27.96	28.62	31.27
CaO	1.14	1.13	1.12	1.11	1.10	1.05	1.01	0.96	0.93	0.78

minus 30% FeO & renormalized

SiO2	55.30	55.16	55.01	54.88	54.74	54.10	53.51	52.97	52.48	50.50
TiO2	0.19	0.19	0.19	0.19	0.19	0.18	0.17	0.16	0.16	0.13
Al2O3	0.96	0.95	0.94	0.93	0.92	0.88	0.84	0.81	0.77	0.64
Cr2O3	0.43	0.43	0.42	0.42	0.42	0.40	0.38	0.37	0.35	0.30
FeO	16.38	16.36	16.34	16.32	16.30	16.20	16.11	16.03	15.95	15.65
MnO	0.45	0.45	0.45	0.45	0.44	0.43	0.42	0.41	0.40	0.36
MgO	25.12	25.32	25.51	25.70	25.88	26.75	27.55	28.28	28.95	31.62
CaO	1.15	1.14	1.13	1.12	1.11	1.06	1.02	0.98	0.94	0.79

Appendix IV. Dissolution Effect

a) Density of Fo80 relict = 3.45 gm/cm^3 = 3.45 mg/mm^3 (from Deer, Howie and Zussman, 1992)
b) Wt % Eagle Station dissolved in melt (at 1515ºC 32min – from Table 4.2) = 20% x 10 mg (total in experimental charge) = 2 mg
c) Volume of dissolved portion of Eagle Station = 2 mg / 3.45 mg/mm^3 = 0.580mm^3
d) Assuming that the 10mg of Eagle Station was added as a single sphere, its volume is 10mg / 3.45 mg/mm^3 = 2.889 mm^3
e) Amount of relict Eagle Station remaining after experiment = 2.889 - 0.580 = 2.319 mm^3
f) Radius of a sphere that has volume of 2.319 mm^3 = 4/3 π r^3 = 0.821 mm
g) Radius of a sphere of starting Eagle Station volume of 2.899 mm^3 = 4/3 π r^3 = 0.885 mm
h) Radius of dissolution 0.885-0.821 = 0.064 mm

Applying the same logic to a **100 um diameter relict Eagle Station sphere yields:**

a) Density 3.45 mg/mm^3
Volume of 100 micron sphere = 4/3 π r^3 = 5.217 x 10^{-4} mm^3
Mass of 100 micron Fo80 sphere = 3.45 mg/mm^3 x 5.23 x 10^{-4} mm^3 = 1.8x10^{-3} mg
b) Wt % Eagle Station dissolved in melt (at 1515ºC 32min) = 20% x 1.8x10^{-3} mg = 3.60 x 10^{-4} mg
c) Volume dissolved = 3.60 x 10^{-4} mg / 3.45 mg/mm^3 = 1.04 x 10^{-4} mm^3
d) Volume of 100 micron Eagle Station = 5.217 x 10^{-4} mm^3
e) Amount of relict Eagle Station remaining after experiment = 5.217 x 10^{-4} mm^3 - 1.04 x 10^{-4} mm^3 = 4.174 x10^{-4} mm^3
f) Radius of sphere that has volume of 4.174 x10^{-4} mm^3 = 4/3 π r^3 = 0.0464 mm
g) Radius of sphere of starting Eagle Station volume = 0.0500 mm
h) **Radius of dissolution** 0.0500 – 0.0464 = 0.0046 mm or **3.6 microns in 32 min at 1515ºC**

Appendix V. Diffusion Effect

A. Fe-Mg Diffusion Effect (Fixed boundary condition)

100 um diameter relict Eagle Station sphere

D of Fe-Mg in olivine (~Fo_{90}) (from Freer, 1981) (Data from Buening and Buseck, 1973)
$D = D_o \exp(-Q/RT)$ at 1515C (1788K)
$D = (3.71 \times 10^{-11}\ m^2/s) \exp[(-120.5 \times 10^3\ J/mol) / (8.314\ J/K\ mol)(1788K)] = 1.12 \times 10^{-14}\ m^2/s$

Diffusion distance of Fe-Mg in olivine in 32 minutes at 1515ºC is estimated by $x^2 \approx Dt$, where x is distance (meters) , and t is time (seconds).

$x^2 \approx (1.12 \times 10^{-14}\ m^2/s)\ (1920\ s)$
$x = 4.64 \times 10^{-6}$ m or **4.6 microns**

Fe-Mg diffusion barely exceeds crystal dissolution by ~20% in 32 minutes at 1515ºC

B. ^{18}O Diffusion Effect (Fixed boundary condition)

D of ^{18}O in olivine (~Fo_{90}) (from Freer, 1981) (Data from Jaoul et al., 1980)
$D = D_o \exp(-Q/RT)$ at 1515ºC (1788K)
$D = (1 \times 10^{-8}\ m^2/s) \exp[(-322 \times 10^3\ J/mol) / (8.314\ J/K\ mol)(1788K)] = 3.92 \times 10^{-18}\ m^2/s$

Diffusion distance of ^{18}O in olivine in 32 minutes at 1515C is estimated by $x^2 \approx Dt$, where x is distance (meters) , and t is time (seconds).

$x^2 \approx (3.92 \times 10^{-18}\ m^2/s)\ (1920\ s)$
$x = 8.67 \times 10^{-8}$ m or **0.09 microns**

Crystal dissolution far outpaces oxygen diffusion by more than a magnitude in 32 minutes at 1515ºC

CURRICULUM VITA

Joseph S. Boesenberg

Education:

University of Arizona, Tucson, AZ (1987)
Astronomy (18 credits)
Rutgers University, New Brunswick, NJ
Bachelor of Arts (1988-1992), Geological Sciences
Rutgers University, New Brunswick, NJ
Master of Science (1992-1995), Geological Sciences
Rutgers University, New Brunswick, NJ
Doctor of Science (2000-2007), Geological Sciences

Employment:

Senior Scientific Assistant III, American Museum of Natural History, Earth & Planetary Sciences, New York, NY 10024-5192 (9/94 - present)

- Meteorite collection manager
- Dept chemical laboratory manager
- Dept network/computer/web manager

Past Employment:

Adjunct Lecturer, Kingsborough College, Physical Sciences, Brooklyn, NY 11235 (2/00-6/00)

- Course instructed: Introduction to Earth Science 036 (lecture & laboratory)

Teaching Assistant, Rutgers University, Geological Sciences, Piscataway, NJ 08855 (8/92-5/94)

- Courses instructed: Geophysics Laboratory 312 & Introductory Geology Laboratory 103

Laboratory Assistant, Electron Microscopy Service Labs., Piscataway, NJ 08854 (5/91-10/92)

- Asbestos analysis laboratory.

Professional Societies:

American Geophysical Union
Meteoritical Society
Mineralogical Society of America

Grants:

Co-investigator - *Institute of Museum and Library Services* – American Museum of Natural History Cultural Property Risk Assessment 2004-2007 – risk assessment of Earth and Planetary Science collections

Awards:

ANSMET – Antarctic Search for Meteorites 2005-2006 team member

Publications:

Journal Articles

Boesenberg J. S. (2006) Wrought iron from the *U.S.S. Monitor*: Mineralogy, petrology and metallography. *Archaeometry* **48**, 613-631.

Boesenberg J. S., Prinz M., Weisberg M. K., Davis A. M., Clayton R. N. and Mayeda T. K. (2000) The pyroxene pallasites, Vermillion and Yamato 8451: Not quite a couple. *Meteoritics and Planetary Science* **35**, 757-769.

Boesenberg J. S. and Delaney J. S. (1997) A model composition of the basaltic achondrite planetoid. *Geochimica et Cosmochimica Acta* **61**, 3205-3225.

Journal Notes

Ebel D. S. and Boesenberg J. S. (2004) The new Arthur Ross Hall of Meteorites at the American Museum of Natural History, *Meteoritics and Planetary Science* **39**, 1761-1762.

Abstracts

Boesenberg J. S., Cosarinsky M., McKeegan K. D., Chaussidon M. and Hewins R. H. (2007) An experimental study of Fe-Mg and oxygen isotope exchange between relict olivine and chondrule melt. *Lunar and Planetary Science Conference* **XXXVIII**, 1621 (CD-ROM).

Mcfadden L. A., Ebel D. S., Loeffler M. J., Boesenberg J. S. and Baragiola R. A. (2007) Infrared spectroscopy of eucrite Juvinas under vacuum: IR absorption of water and organic species. *Lunar and Planetary Science Conference* **XXXVIII**, 2390 (CD-ROM).

Boesenberg J. S. and Delaney J. S. (2006) Elephant Moraine 87521: Two pyroxenes, two chromites, and two ilmenites, but only one fractionation series. *Lunar and Planetary Science Conference* **XXXVII**, 1680 (CD-ROM).

Boesenberg J. S., Young E. D., Ziegler K. and Hewins R. H. (2005) Evaporation and the absence of oxygen isotopic exchange between silicate melt and carbon monoxide gas at nebular pressures. *Meteoritics and Planetary Science* **40**, A22.

Boesenberg J. S., Hewins R. H. and Chaussidon M. (2004) Oxygen isotopic diffusion and exchange experiments on olivine and chondrule melts: Preliminary results. *Workshop on Chondrites and the Protoplanetary Disk*, 9047 (CD-ROM).

Boesenberg J. S., Ebel D. S. and Hewins, R. H. (2004) An experimental study of phosphoran olivine and its significance in Main Group pallasites. *Lunar and Planetary Science Conference* **XXXV**, 1366 (CD-ROM).

Boesenberg J. S. (2003) An oxygen isotope mixing model for the Northwest Africa 011 basaltic achondrite. *Lunar and Planetary Science Conference* **XXXIV**, 1239 (CD-ROM).

Murray J., Boesenberg J. S. and Ebel D. S. (2003) Unambiguous voids in Allende chondrules and refractory inclusions. *Lunar and Planetary Science Conference* **XXXIV**, 1999 (CD-ROM).

Nehru C. E., Weisberg M. K., Boesenberg J. S. and Kilgore M. (2003) Tafassasset: A metal-rich primitive achondrite with affinities to brachinites. *Lunar and Planetary Science Conference* **XXXIV**, 1370 (CD-ROM).

Weisberg M. K., Ebel D. S., Connolly H. C., Boesenberg J. S. and Castellano D. (2002) Petrologic-tomographic study of metal in the CR chondrites. *Meteoritics and Planetar Science* **37**, A149.

Weisberg M. K., Boesenberg J. S. and Ebel D. S. (2002) Gujba and origin of the bencubbin-like (CB) chondrites. *Lunar and Planetary Science Conference* **XXXIII**, 1551 (CD-ROM).

Ruzicka A., Kilgore M., Boesenberg J. S. and Prinz M. (2000) Portales Valley: Not just another "ordinary" chondrite. *Meteoritics and Planetary Science* **35**, A139-A140.

Ikeda Y., Prinz M., Nehru C. E., Boesenberg J. S. and Kita N. T. (1999) Petrology of the Dar Al Gani (DAG) 319 polymict ureilite. *NIPR Symp. Antarc. Meteorites* **XXIV**, 43-46.

Ruzicka, A., Boesenberg J. S., Snyder G. A., Prinz M. and Taylor L. A. (1999) Petrogenesis of the Lamont mesosiderite: Evidence from petrography and pyroxene clast zoning systematics. *Lunar and Planetary Science Conference* **XXX**, 1513 (CD-ROM).

Ruzicka, A., Boesenberg J. S., Snyder G. A., Prinz M. and Taylor L. A. (1999) Rare-earth-element abundances of clasts and matrix in the Lamont mesosiderite: Complex spatial variations. *Lunar and Planetary Science Conference* **XXX**, 1516 (CD-ROM).

Boesenberg J. S., Delaney J. S. and Prinz M. (1997) Magnesian megacrysts and matrix in the mesosiderite Lamont. *Lunar and Planetary Science Conference* **XXVIII**, 125-126.

Weisberg M. K., Prinz M., Boesenberg J. S., Kozhushko G., Clayton R. N., Mayeda T. K. and Ebihara M. (1996) A new petrologic and oxygen isotopic study of six Allende dark inclusions: Evaluation of nebular vs. asteroidal models for their origin. *Lunar and Planetary Science Conference* **XXVII**, 1407-1408.

Boesenberg J. S., Prinz M., Weisberg M. K., Davis A. M., Clayton R. N., Mayeda T. K. and Wasson J. T. (1995) Pyroxene pallasites: A new pallasite grouplet. *Meteoritics*, **30**, 488-489.

Weisberg M. K., Boesenberg J. S., Kozhushko G., Prinz M., Clayton R. N. and Mayeda T. K. (1995) EH3 and EL3 chondrites: A petrologic-oxygen isotopic study. *Lunar and Planetary Science Conference* **XXVI**, 1481-1482.

Boesenberg J. S. and Delaney J. S. (1994) Results of partial melting experiments on chondritic precursors of basaltic achondrites. *Meteoritics*, **29**, 445-446.

Boesenberg J. S. and Delaney J. S. (1994) Fe and Mn systematics in experimental analogues of Murchison and a 65% H chondrite-35% CM chondrite. *Lunar and Planetary Science Conference* **XXV**, 135-136.

Boesenberg J. S. and Delaney J. S. (1993) Preliminary results of Mn partitioning experiments on Murchison analogues. *Lunar and Planetary Science Conference* **XXIV**, 137-138.

Delaney J. S. and Boesenberg J. S. (1993) Fe/Mn constraints on precursors of basaltic achondrites. *Lunar and Planetary Science Conference* **XXIV**, 391-392.

Boesenberg J. S. and Delaney J. S. (1992) Lithic clasts in Elephant Moraine 87521 sample two VLT fractionation series. *Lunar and Planetary Science Conference* **XXIII**, 127-128.